Laser-Induced Cavitation for Controlling Crystallization from Solution

Nagalingam, Nagaraj

DOI
10.4233/uuid:17b93f25-8f3f-4ab4-b5f8-ba446d923b6d

Publication date
2024

Document Version
Final published version

Citation (APA)
Nagalingam, N. (2024). *Laser-Induced Cavitation for Controlling Crystallization from Solution*. [Dissertation (TU Delft), Delft University of Technology]. https://doi.org/10.4233/uuid:17b93f25-8f3f-4ab4-b5f8-ba446d923b6d

Laser-Induced Cavitation for Controlling Crystallization from Solution

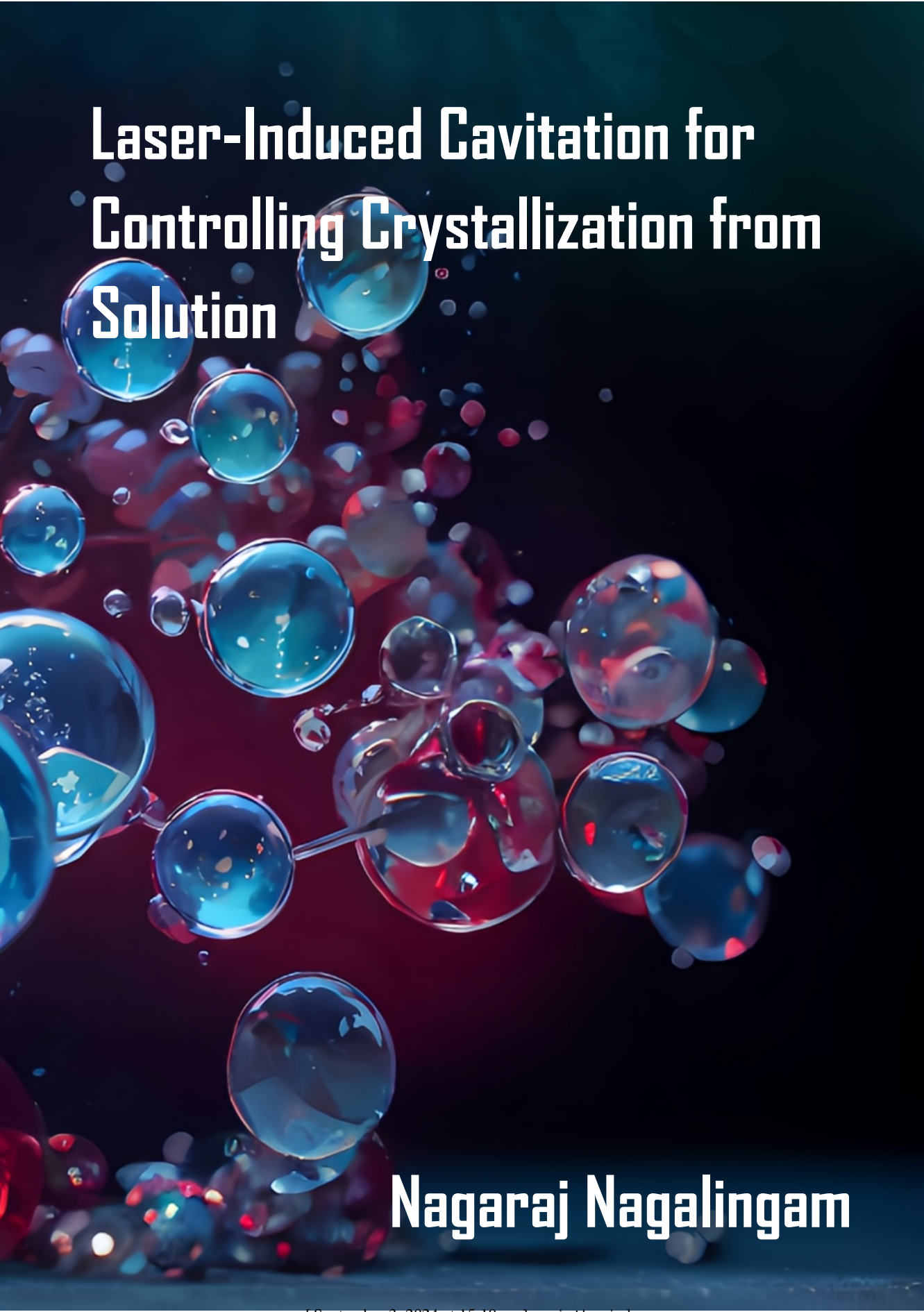

Nagaraj Nagalingam

Laser-Induced Cavitation for Controlling Crystallization from Solution

Dissertation

for the purpose of obtaining the degree of doctor
at Delft University of Technology
by the authority of the Rector Magnificus, prof.dr.ir. T.H.J.J. van der Hagen,
chair of the Board for Doctorates
to be defended publicly on
Monday 14 October 2024 at 10:00 o'clock

by

Nagaraj NAGALINGAM

Master of Science in Mechanical Engineering,
Delft University of Technology, the Netherlands,
born in Thevaram, India.

This dissertation has been approved by the promotors.
Composition of the doctoral committee:

Rector Magnificus,	chairperson
Dr. H. B. Eral	Delft University of Technology, promotor
Prof. dr. ir. J. T. Padding	Delft University of Technology, promotor
Dr. ir. R. M. Hartkamp	Delft University of Technology, copromotor
Independent members:	
Prof. dr. R. Pecnik	Delft University of Technology
Prof. dr. N. F. Shahidzadeh	University of Amsterdam
Prof. dr. W. L. Noorduin	University of Amsterdam
Dr. A. J. Alexander	The University of Edinburgh
Prof. dr. K. Hooman	Delft University of Technology, reserve member

This work was funded by LightX project under NWO Open Technology Programme (project number 16714).

Cover by: Nagaraj Nagalingam. Designed using software Canva, Fotor and Vmake AI.

Printed by: Ridderprint | www.ridderprint.nl

ISBN 978-94-6366-925-2
An electronic version of this dissertation is available at
http://repository.tudelft.nl/

to my family, teachers and humankind

— As the letter A is the first of all letters,
so is the eternal Sun for the world.
Thiruvalluvar

CONTENTS

SUMMARY

Primary nucleation control of crystals is central to achieve targeted crystal properties such as purity, size, morphology and polymorphic form. Non-photochemical laser-induced nucleation (NPLIN) from solution has gained attention due to its presumed absence of chemical reactions, non-invasive procedures, spatio-temporal control of the nucleation rate, and the ability to influence the polymorphic form of the crystals. Yet, the existing literature has no general agreement on the underlying mechanism and therefore lacks optimization to be applied at the industrial scale. The objective of this dissertation is to elucidate the dominant mechanism behind the direct interaction of the laser pulse(s) with a slightly supersaturated solution that result in crystallization.

This dissertation examines how solutions that are transparent to laser light (at least for most studied wavelengths of 532 and 1064 nm) can form vapor bubbles and subsequent crystals. Micron-sized transient vapor bubbles can be formed in solutions due to the absorption of the laser energy by intrinsic impurities or via optical cavitation by intentionally focusing the laser light. First of all, the crystallization in aqueous solutions of KCl is discussed, due to bubbles formed using focused laser light with nanoseconds pulse width. The results reveal enhanced solute accumulation above the saturation limit at the vapor-liquid interface (bubble surface). A numerical model employing the finite element method, validated against the bubble size evolution from experiments, is leveraged to estimate the mass transfer of the solute and, from this, the local supersaturation surrounding the bubble. The model shows the emergence of a more concentrated solute boundary layer in the liquid surrounding the bubble due to high solvent evaporation rates [$\sim 100\,\mathrm{kg/(m^2 s)}$] associated with the bubble growth. The experimentally recorded crystallization probability and crystal count are successfully correlated to the numerically estimated supersaturation at the vapor-liquid interface using classical nucleation theory.

The proposed mechanism to NPLIN of KCl via bubble formation is then extended to other aqueous solutes such as NH_4Cl, NaCl, KBr and CH_4N_2O. With the experiments performed for NH_4Cl and NaCl, similar to KCl as discussed above, a general analytical relation for supersaturation in the liquid surrounding the bubble is developed. This analytical relation is then used to rationalize the observed NPLIN activity of all above-mentioned solutes in experiments performed in literature employing an unfocused laser. An unfocused laser is expected to generate bubbles via energy absorption by impurities. The predicted bubble sizes surrounding impurities using Mie theory successfully correlate to the minimum necessary nucleation rate as a function of supersaturation at the vapor-liquid interface. Thus, the study on the laser-induced

bubbles provides understanding of a viable mechanism underlying NPLIN, necessary to engineer a laser-induced crystallizer.

Because single isolated bubbles are hardly present within an irradiated volume due to the random distribution of impurities, a study considering bubble-bubble interaction and its influence on crystallization is necessary. Moreover, unbounded liquid domains are absent in a continuous functioning system. Therefore, first, the dynamics of a single laser-induced bubble within diverse quasi-1D microchannel geometries is analyzed using both experiments and theory. The proposed analytical and scaling relations show a unified theory for dynamic bubble size and lifetime as a function of laser energy, including insights on a transitory flow instability - uncommon to low Reynolds flows (< 1000). This instability originates from the channel walls and exists due to the oscillating nature of the flow, with its origin and growth characterized by the Womersley number and convective timescale of the flow, respectively. Later, crystallization using laser-induced bubble pairs in a microchannel is demonstrated using supersaturated $KMnO_4$ as a model salt. A microjet emerging due to bubble-bubble hydrodynamic interaction is shown to alter the nucleation kinetics via the induced shear over the liquid surrounding the bubble due to jet impingement. Furthermore, the microjets allow crystallization at lower laser energy and solution supersaturation in the bulk compared to single bubbles. A concomitant numerical model is developed to study the bubble interactions employing the boundary integral element method. The inferred scaling relations from the model on the jet velocity successfully captures the observations in experiments and literature. The associated shear and the supersaturation in the liquid bulk are correlated to the recorded crystallization probabilities in experiments using classical nucleation theory. This study using confined bubbles and their interaction with each other suggests a novel pathway for crystal nucleation under laser light for solutes that might otherwise require large supersaturation and laser energies. Thus, using bubble pairs avoids the process difficulties associated with handling solutions with large supersaturation and usage of high-powered lasers that might potentially cause photochemistry.

Thus this dissertation demonstrates laser-induced cavitation as a viable mechanism for crystal nucleation. While direct measurement of the vapor bubble(s) in this work is achieved using focused laser light, in addition, the results are correlated to the bubble formation surrounding a nanometer sized impurity in solution. Together, the findings in this dissertation serve to *a priori* predict the non-photochemical laser-induced nucleation (NPLIN) activity of a solution, based on the laser intensity and physicochemical properties of the solute, solvent and intrinsic impurities.

SAMENVATTING

Primaire nucleatiebeheersing van kristallen is van cruciaal belang om gerichte kristaleigenschappen te bereiken, zoals zuiverheid, grootte, morfologie en polymorfe vorm. Niet-fotochemische lasergeïnduceerde nucleatie (NPLIN) uit oplossing heeft aandacht gekregen vanwege de veronderstelde afwezigheid van chemische reacties, niet-invasieve procedures, spatio-temporele controle van de nucleatiesnelheid en het vermogen om de polymorfe vorm van de kristallen te beïnvloeden. Toch bestaat er in de literatuur geen algemene overeenstemming over het onderliggende mechanisme en ontbreekt het daarom aan optimalisatie voor toepassing op industriële schaal. Het doel van dit proefschrift is het ophelderen van het dominante mechanisme achter de directe interactie van de laserpuls(en) met een enigszins oververzadigde oplossing met kristallisatie tot gevolg.

Dit proefschrift onderzoekt hoe oplossingen die transparant zijn voor laserlicht (althans voor de meest bestudeerde golflengten van 532 en 1064 nm) waterdampbellen en daaropvolgende kristallen kunnen vormen. Tijdelijke waterdampbellen van micrometer grootte kunnen zich vormen in oplossingen als gevolg van de absorptie van de laserenergie door intrinsieke onzuiverheden of via optische cavitatie door het laserlicht opzettelijk op een punt te concentreren. Allereerst wordt de kristallisatie in waterige oplossingen van KCl besproken, als gevolg van bellen die worden gevormd door middel van geconcentreerd laserlicht met een pulsbreedte van nanoseconden. De resultaten laten een verhoogde accumulatie van opgeloste stoffen zien boven de verzadigingslimiet op het damp-vloeistofgrensvlak (bellenoppervlak). Een numeriek model dat gebruik maakt van de eindige-elementenmethode, gevalideerd aan de hand van de evolutie van de belgrootte uit experimenten, wordt gebruikt om de massaoverdracht van de opgeloste stof te schatten en, op basis hiervan, de lokale oververzadiging rond de bel. Het model toont de vorming aan van een meer geconcentreerde grenslaag van opgeloste stoffen in de vloeistof rond de bel als gevolg van de hoge verdampingssnelheid van oplosmiddelen [$\sim 100\,\mathrm{kg/(m^2 s)}$] geassocieerd met de groei van bellen. De experimenteel bepaalde kristallisatiewaarschijnlijkheid en het aantal kristallen zijn met succes gecorreleerd met de numeriek geschatte oververzadiging aan het damp-vloeistofgrensvlak met behulp van klassieke nucleatietheorie.

Het voorgestelde mechanisme voor NPLIN van KCl via belvorming wordt vervolgens uitgebreid naar andere waterige opgeloste stoffen zoals NH_4Cl, NaCl, KBr en CH_4N_2O. Met de experimenten uitgevoerd voor NH_4Cl en NaCl, vergelijkbaar met KCl zoals hierboven besproken, wordt een algemeen analytisch verband voor oververzadiging in de vloeistof rond de bel ontwikkeld. Deze analytische relatie wordt

vervolgens gebruikt om de waargenomen NPLIN-activiteit van alle bovengenoemde opgeloste stoffen te rationaliseren voor experimenten die in de literatuur zijn uitgevoerd met behulp van een ongefocusde laser. Van een onfocusde laser wordt verwacht dat hij bellen genereert via energieabsorptie door onzuiverheden. De voorspelde belgroottes rond onzuiverheden met behulp van de Mie-theorie correleren met succes met de minimaal noodzakelijke nucleatiesnelheid als functie van oververzadiging aan het damp-vloeistofgrensvlak. Het onderzoek naar de door laser geïnduceerde bellen geeft dus inzicht in een realistisch mechanisme dat ten grondslag ligt aan NPLIN, noodzakelijk om een door laser geïnduceerde kristallisator te ontwikkelen.

Omdat afzonderlijke geïsoleerde bellen nauwelijks aanwezig zijn in een bestraald volume vanwege de willekeurige verdeling van onzuiverheden, is een onderzoek naar de interactie tussen bellen en bellen en de invloed ervan op kristallisatie noodzakelijk. Bovendien ontbreken onbegrensde vloeistofdomeinen in een continu functionerend systeem. Daarom wordt eerst de dynamiek van een enkele lasergeïnduceerde bel binnen diverse quasi-1D microkanaalgeometrieën geanalyseerd met behulp van zowel experimenten als theorie. De voorgestelde analytische en schalingsrelaties tonen een uniforme theorie aan voor de dynamische belgrootte en levensduur als een functie van laserenergie, inclusief inzichten over een transiënte stromingsinstabiliteit - ongebruikelijk voor lage Reynolds-stromingen (< 1000). Deze instabiliteit is afkomstig van de kanaalwanden en bestaat als gevolg van de oscillerende aard van de stroming, waarbij de oorsprong en groei ervan worden gekenmerkt door respectievelijk het Womersley-getal en de convectieve tijdschaal van de stroming. Later wordt kristallisatie met behulp van lasergeïnduceerde bellenparen in een microkanaal gedemonstreerd met behulp van oververzadigde $KMnO_4$ als modelzout. Er is aangetoond dat een microjet die tevoorschijn komt als gevolg van de hydrodynamische interactie tussen bel en bel, de kinetiek van de nucleatie verandert via de geïnduceerde schuifkracht over de vloeistof die de bel omringt als gevolg van de botsing van de jet. Bovendien maken de microjets kristallisatie bij lagere laserenergie en oververzadiging van de oplossing in de bulk mogelijk in vergelijking met enkele bellen. Er wordt een begeleidend numeriek model ontwikkeld om de belinteracties te bestuderen met behulp van de grensintegraalelementenmethode. De afgeleide schaalrelaties uit het model over de jetsnelheid geven met succes de observaties uit experimenten en literatuur weer. De bijbehorende afschuiving en de oververzadiging in de vloeibare bulk zijn gecorreleerd met de geregistreerde kristallisatiekansen in experimenten met behulp van de klassieke nucleatietheorie. Deze studie, waarbij gebruik wordt gemaakt van opgesloten bellen en hun interactie met elkaar, suggereert een nieuwe route voor kristalnucleatie onder laserlicht voor opgeloste stoffen die anders grote oververzadiging en laserenergieën zouden vereisen. Het gebruik van bellenparen vermijdt dus de procesproblemen die gepaard gaan met het hanteren

van oplossingen met grote oververzadiging en het gebruik van krachtige lasers die mogelijk fotochemie kunnen veroorzaken.

Dit proefschrift demonstreert dus laser-geïnduceerde cavitatie als een haalbaar mechanisme voor kristalnucleatie. Hoewel de directe meting van de waterdampbel(len) in dit werk wordt bereikt met behulp van geconcentreerd laserlicht, zijn de resultaten bovendien gecorreleerd met de belvorming rond een onzuiverheid van nanometerformaat in oplossing. Samen kunnen de bevindingen in dit proefschrift de niet-fotochemische lasergeïnduceerde nucleatieactiviteit (NPLIN) van een oplossing voorspellen, gebaseerd op de laserintensiteit en fysisch-chemische eigenschappen van de opgeloste stof, het oplosmiddel en de intrinsieke onzuiverheden.

SUMMARY (IN TAMIL)

தூய்மை, அளவு, உருவவியல் மற்றும் பாலிமார்பிக் வடிவம் போன்ற படிக பண்புகளை அடைய படிகங்களின் முதன்மை கரு கட்டுப்பாடு மையமாக உள்ளது. கரைசல்களில், ஒளி வேதியியல் அல்லாத லேசர் தூண்டப்பட்ட படிகக்கரு (NPLIN), அதன் இரசாயன எதிர்வினைகள் இல்லாமை, ஊடுருவற்ற நடைமுறைகள், படிகக்கரு வீதத்தின் இடஞ்சார்ந்த-நேரம்சார்ந்த கட்டுப்பாடு, மற்றும் படிகங்களின் பாலிமார்பிக் வடிவத்தை பாதிக்கும் திறன் ஆகியவற்றின் காரணமாக கவனத்தை ஈர்த்துள்ளது. ஆயினும்கூட, தற்போதுள்ள இலக்கியங்களில் அடிப்படை பொறிமுறையில் பொதுவான உடன்பாடு இல்லை, எனவே தொழில்துறை அளவில் பயன்படுத்துவதற்கான தொழில்நுட்பமும் இல்லை. இந்த ஆய்வறிக்கையின் நோக்கம் லேசர் மற்றும் கரைசலின் நேரடி தொடர்புக்கு பின்னால் உள்ள மேலாதிக்க பொறிமுறையை தெளிவுபடுத்துவதாகும்.

நீராவி குமிழ்கள் மற்றும் படிகங்கள் ஒளிபுகு கரைசல்களில் (குறைந்தபட்சம் 532 மற்றும் 1064 nm அலைநீளங்களுக்கு) எவ்வாறு உருவாக்குகின்றன என்பதை இந்த ஆய்வுக் கட்டுரை ஆராய்கிறது. மைக்ரான்-அளவிலான நிலையற்ற நீராவி குமிழ்கள் லேசர் ஆற்றலை உள்ளார்ந்த கரைசல் அசுத்தங்கள் மூலம் அல்லது லேசர் ஒளியை மையப்படுத்துவதன் மூலம் கரைசல்களில் உருவாகலாம். முதலில், நானோ விநாடிகள் (ns) கால அளவிலான மையப்படுத்தப்பட்ட லேசர் ஒளியைப் பயன்படுத்தி உருவாகும் குமிழ்கள் KCl இன் நீர் கரைசல்களில் படிகமயமாக்கல் விவாதிக்கப்படுகிறது. எண்ணியல் முறைகள் மூலம் அதிக கரைசல் ஆவியாதல் விகிதங்கள் காரணமாக [~100 kg/(m^2s)] நீராவி-திரவ இடைமுகத்தில் (குமிழி மேற்பரப்பு) நிறைவுற்ற அளவைவிட அதிக கரைபொருள் செறிவு வெளிப்படுகிறது. பரிசோதனை ரீதியாக பதிவுசெய்யப்பட்ட படிகமயமாக்கல் நிகழ்தகவு மற்றும் படிக எண்ணிக்கை ஆகியவை கிளாசிக்கல் நியூக்ளியேஷன் கோட்பாட்டைப் பயன்படுத்தி நீராவி-திரவ இடைமுகத்தில் எண்ணியல் ரீதியாக மதிப்பிடப்பட்ட அதிக நிறைவுற்ற கரைசலுடன் வெற்றிகரமாக தொடர்புபடுத்தப்பட்டுள்ளன.

பின்னர், குமிழி உருவாக்கம் வழியாக KCl NPLIN க்கு முன்மொழியப்பட்ட பொறிமுறை NH_4Cl, NaCl, KBr மற்றும் CH_4N_2O போன்ற பிற நீர்நிலைக் கரைசல்களுக்கு நீட்டிக்கப்படுகிறது. NH_4Cl மற்றும் NaCl க்கு நடத்தப்பட்ட பரிசோதனைகள், முன் விவாதிக்கப்பட்ட KCl போலவே குமிழியைச் சுற்றியுள்ள திரவத்தில் கரைபொருள் செறிவுக்கான பொதுவான பகுப்பாய்வு தொடர்பு உருவாக்கப்படுகிறது. இந்த பகுப்பாய்வு தொடர்பு, மையப்படுத்தப்படாத லேசரைப் பயன்படுத்தி இலக்கியத்தில் நிகழ்த்தப்பட்ட சோதனைகளில் மேலே குறிப்பிடப்பட்ட அனைத்து கரைசல்களின் கவனிக்கப்பட்ட NPLIN செயல்பாட்டை பகுத்தறிவு செய்ய

பயன்படுத்தப்படுகிறது. கரைசல் அசுத்தங்கள் மையப்படுத்தப்படாத லேசர் ஆற்றலை உள்ளார்ந்தது குமிழ்களை உருவாக்கும் என்று எதிர்பார்க்கப்படுகிறது. மீ கோட்பாட்டைப் பயன்படுத்தி அசுத்தங்களைச் சுற்றியுள்ள கணிக்கப்பட்ட குமிழி அளவுகள், நீராவி-திரவ இடைமுகத்தில் அதிக நிறைவுற்ற கரைசலின் செயல்பாடாக உருவாகும் குறைந்தபட்ச படிகக்கரு விகிதத்துடன் வெற்றிகரமாக தொடர்புபடுத்தப்படுகிறது. எனவே, லேசர் தூண்டப்பட்ட குமிழ்கள் பற்றிய ஆய்வு, லேசர் தூண்டப்பட்ட படிகமயமாக்குதலின் பொறியியலுக்குத் தேவையான NPLIN இன் அடிப்படை புரிதலை வழங்குகிறது.

கரைசல்களில், அசுத்தங்களின் சீரற்ற பரப்பு காரணமாக ஒரு தனிமைப்படுத்தப்பட்ட குமிழி அரிதாகவே இருக்கும், எனவே குமிழி-குமிழி இடைவினை மற்றும் படிகமயமாக்குதலில் அதன் தாக்கத்தை கருத்தில் கொள்வது அவசியம். மேலும், தொடர்ச்சியான உற்பத்தி செயல்முறை அமைப்பில் எல்லையில்லா திரவ களங்கள் இல்லை. எனவே, முதலில், பல்வேறு நுண்குழல்கள் வடிவவியலுக்குள் லேசர் தூண்டப்பட்ட ஒற்றை குமிழியின் இயக்கவியல் சோதனை மற்றும் கோட்பாட்டை பயன்படுத்தி பகுப்பாய்வு செய்யப்படுகிறது. முன்மொழியப்பட்ட பகுப்பாய்வில், லேசர் ஆற்றலின் செயல்பாடாக வெளிப்படும் குமிழி அளவு மற்றும் குமிழி ஆயுட்காலத்திற்கான ஒரு ஒருங்கிணைந்த கோட்பாடு பரிந்துரைக்கப்படுகின்றது, இதில் இடைநிலை திரவ ஓட்ட நிலையற்ற தன்மை பற்றிய நுண்ணறிவுகளும் அடங்கும் – ரெனால்ட்ஸ் எண் (<1000). இந்த திரவ நிலையற்ற தன்மை ஓட்டத்தின் ஊசலாடும் தன்மை காரணமாக நுண்குழல் சுவர்களில் இருந்து உருவாகிறது. அதன் தோற்றம் மற்றும் வளர்ச்சி வோமர்ஸ்லி எண் மற்றும் ஓட்டத்தின் வெப்பச்சலன நேர அளவு ஆகியவற்றால் வகைப்படுத்தப்படுகிறது. பின்னர், நுண்குழாய்களுக்குள் லேசர் தூண்டப்பட்ட குமிழி ஜோடிகளைப் பயன்படுத்தி $KMnO_4$ நீர் கரைசலில் படிகமயமாக்கல் நிரூபிக்கப்படுகிறது. குமிழி-குமிழி நீர் இயக்கக் தொடர்பு காரணமாக வெளிப்படும் நீர்த்தாரை குமிழியைச் சுற்றியுள்ள திரவத்தின் சந்திப்பின் போது படிகக்கரு இயக்கவியலை மாற்றுவதாகக் காட்டப்படுகிறது. மேலும், ஒற்றை குமிழிகளுடன் ஒப்பிடும்போது நீர்த்தாரைகள் குறைந்த லேசர் ஆற்றல் மற்றும் குறைந்த நிறைவுற்ற கரைசலை கொண்டு படிகமயமாக்குதலை சாத்தியப்படுத்துகிறது. பௌண்டரி இன்டெக்ரல் எலிமெண்ட் முறையைப் பயன்படுத்தும் குமிழி இடைவினைகளைப் படிக்க ஒரு இணையான எண்ணியல் உருவாக்கப்பட்டது. கிளாசிக்கல் நியூக்ளியேஷன் கோட்பாட்டைப் பயன்படுத்தி பரிசோதனைகளில் பதிவுசெய்யப்பட்ட படிகமயமாக்கல் நிகழ்தகவுகளுடன் கரைசலின் நிறைவுற்று மற்றும் நீர்த்தாரை உருவாக்கும் கத்தரிப்பு விசை தொடர்புபடுத்தப்படுகின்றன. எனவே குமிழ்கள் மற்றும் அவற்றின் இடைவினை ஆகியவற்றைப் பயன்படுத்தி இந்த ஆய்வு லேசர் ஒளியின் காரணமாக படிகக்கரு உருவர்க்கதிக்கு ஒரு புதிய பாதையை பரிந்துரைக்கிறது, இல்லையெனில் மிக அதிக நிறைவுற்ற கரைசல் மற்றும் லேசர் ஆற்றல் தேவைப்படலாம். எனவே, குமிழி ஜோடிகளைப் பயன்படுத்துவது, மிக அதிக நிறைவுற்ற கரைசல்களைக் கையாள்வது

மற்றும் ஒளி வேதியியலை ஏற்படுத்தக்கூடிய அதிக ஆற்றல் கொண்ட லேசர்களின் பயன்பாடு ஆகியவற்றுடன் தொடர்புடைய செயல்முறை சிக்கல்களைத் தவிர்க்கிறது.

எனவே இந்த ஆய்வுக்கட்டுரையானது லேசர் தூண்டப்பட்ட குமிழ்கள் மூலம் படிகக்கரு உருவாக்கத்திற்கு ஒரு சாத்தியமான பொறிமுறையை நிரூபிக்கிறது. இந்த கட்டுரையில் நீராவி குமிழி(கள்) மையப்படுத்தபட்ட லேசர் ஒளியைப் பயன்படுத்தி அடையப்படுகிறது, கூடுதலாக, ஆய்வு முடிவுகள் கரைசலில் நானோமீட்டர் (nm) அளவிலான அசுத்தங்களை சுற்றி உருவாகும் குமிழியை தொடர்புபடுத்துகிறது. ஆகமொத்தம், இந்த ஆய்வறிக்கையில் உள்ள கண்டுபிடிப்புகள் லேசர் ஆற்றல், கரைசல் மற்றும் அசுத்தங்களின் இயற்பியல் வேதியியல் பண்புகளை கொண்டு அடிப்படையில் ஒளிவேதியியல் அல்லாத லேசர் தூண்டப்பட்ட படிகக்கரு செயல்பாட்டைக் கணிக்க உதவும்.

PART I

1

INTRODUCTION

Crystallization is abundant in nature and industrial practice. A plethora of indispensable products ranging from agrochemicals and pharmaceuticals to battery materials, are produced in crystalline form in industrial practice. Yet, our control over the crystallization process across scales, from molecular to macroscopic crystals, is far from complete. This bottleneck not only hinders our ability to engineer the properties of crystalline products essential for maintaining our quality of life but also hampers progress toward a sustainable circular economy in resource recovery. In recent years, approaches leveraging light have emerged as promising alternatives to manipulate crystallization. This dissertation is focused on the advancement in the crystallization processes by clarifying the physicochemical mechanism behind this recent discovery. This chapter begins with the motivation for this work, followed by background on non-photochemical laser-induced nucleation, the research questions and objective of this work, and outline of this dissertation.

This chapter is based on the article:
V. Korede* and N. Nagalingam* et al. "A Review of Laser- Induced Crystallization from Solution." In: *Crystal Growth & Design* 23.5 (2023), pp. 3873–3916.
* denotes equal contribution.

1.1 Motivation

Crystalline materials are omnipresent in nature and commodities including minerals, functional materials, agro-based products, pharmaceuticals and high value fine chemicals [1, 2]. Thus the studies on crystallization process have an extended scope spanning across geology, biology and engineering, necessary to understand the mineral morphogenesis and characterize the self-organized crystalline structures [3, 4], see Fig. 1.1. Consequently, crystallization is the most widely used separation/purification process in industrial practice. Despite its widespread use, the majority of the state-of-art techniques rely on trial-error approaches to ensure desired crystal qualities, such as, crystal size distribution, crystal shape, polymorphic form and purity [5]. Furthermore, the conventional operations are batch-wise, which is sub-optimal in terms of operation costs, energy-usage, quality control and safety [6, 7]. Thus the dependency on "out-of-date" technologies by industries is a bottleneck with immediate consequences pertaining to stringent product requirements, high production costs and fast changing market conditions [8].

Figure 1.1: (a) Gypsum crystals in Naica's crystal cave (credit: Javier Trueba/MSF/Science Source). (b) Urea as a plant fertilizer (credit: FertigHy, EIT InnoEnergy). (c) Carbonate-silica coprecipitation patterns imaged using scanning electron microscopy (image source: reprinted with permission from C. N. Kaplan et al., *Science*, 2017). (d) Exoskeletons of mollusks from calcification (credit: Mandy Disher, Scientific American). (e) Pharmaceutical drugs (credit: Trade Brains).

Non-photochemical laser-induced nucleation of crystals is a promising yet not-completely-understood physiochemical phenomenon - where an intense nanosecond

laser pulse induces almost instantaneous crystallization in solutions of low supersaturation that would otherwise take weeks to nucleate. Thus the laser light is capable of directly manipulating nucleation energy barriers and therefore has the potential to carry the industrial engineering beyond the-state-of-the-art. This calls for a study to fundamentally understand the mechanism behind this underexplored physiochemical phenomenon and develop a continuously operated crystallization/seed generation system [9]. The contributions will significantly advance the industrial-scale synthesis of tailored crystalline materials, including high quality, "first time right" crystals, for which no additional particle modification or recrystallization steps will be required.

1.2 Background

1.2.1 Nucleation in solutions

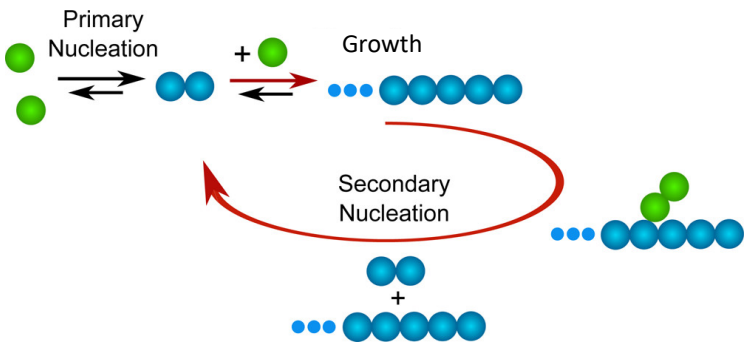

Figure 1.2: Primary nucleation, growth and secondary nucleation of crystals. Primary nucleation involves the aggregation of single solute molecules in solution. Secondary nucleation involves molecules of solute on the surface of an already existing aggregate of the same solute. Image source: reprinted with permission from P. Arosio et al., *JACS*, 2013.

The formation of a crystal is a two-step phenomenon consisting of nucleation and growth. Nucleation is the emergence of an ordered structure of solute molecules from a solution. The Szilard mechanism of successive attachments and detachments of single solute molecules in solution leads to small molecular clusters of various sizes. These clusters upon reaching a critical size called nuclei, grow into a macroscopic crystal, see Fig. 1.2. The driving potential for nucleation and growth of one-component crystals in a liquid environment is the supersaturation of the solution defined as,

$$S = C/C_{sat}. \tag{1.1}$$

C is the concentration in the bulk of solution, and C_{sat} is the saturation concentration at a given temperature (also known as the solubility). The nucleation and/or growth of

the crystals is possible only when the solution is supersaturated, $S > 0$. The solution is, saturated or undersaturated when $S = 0$ or $S < 0$, respectively.

Classical nucleation theory (CNT) is an analytical model proposed to rationalize the nucleation process [2]. It explains nucleation as a competition between the tendency to form a new phase against the energy cost associated with forming a new surface. CNT is widely used due to its analytical simplicity and describes nucleation as a one-step stochastic process dictated by the overall Gibbs free energy change as [10],

$$\Delta G = 4\pi r^2 \sigma_{sl} - \frac{4\pi r^3 k_B T \log S}{3\nu_0}, \tag{1.2}$$

where r is the cluster radius, σ_{sl} is the solute-solution interfacial tension, k_B is the Boltzmann constant, T is the temperature and ν_0 the molecular volume. On the right hand side of the above equation, the first and second term correspond to the change in free energy for the phase transformation and the surface formation, respectively. For one-component nucleation, this allows determination of the supersaturation dependence of the rate of nucleation, J, e.g., the number of nuclei formed per unit volume per unit time, as [11]

$$J = AS \exp\left[-16\pi\nu_0^2\sigma_{sl}^3/(3k_B^3T^3\log^2(S))\right], \tag{1.3}$$

in which A is a pre-exponential kinetic parameter.

The currently employed industrial crystallizers are predominantly large mixed vessels in which a number of physical phenomena take place simultaneously, such as, heat and mass transfer, generation of supersaturation, crystal nucleation, crystal growth, and dissolution. Thus the control and optimization of the product quality in the presence of a plethora of complex phenomena is highly challenging [12]. For example, in classic approaches using large cooling vessels, high temperature gradients and consequently high supersaturation gradients are inevitable. The steep exponential dependence of the rate of nucleation on supersaturation result in process instability and unpredictable product quality, e.g., polymorphism and morphology. Furthermore, while primary nucleation occurs from clear (crystal free) supersaturated solutions, secondary nucleation can emerge from the attrition and coalescence of the primary crystals [13]. Therefore nucleation, growth, and such secondary physical phenomena collectively dictate the crystal quality. Hence a process that is continuous, scalable and capable of producing commercially viable high-quality "first time right" crystals is utmost necessary.

1.2.2 Non-photochemical laser induced nucleation : Introduction

Controlling crystallization from solution, which is central to technological applications thus is still challenging our understanding of nucleation [17–19]. Among the

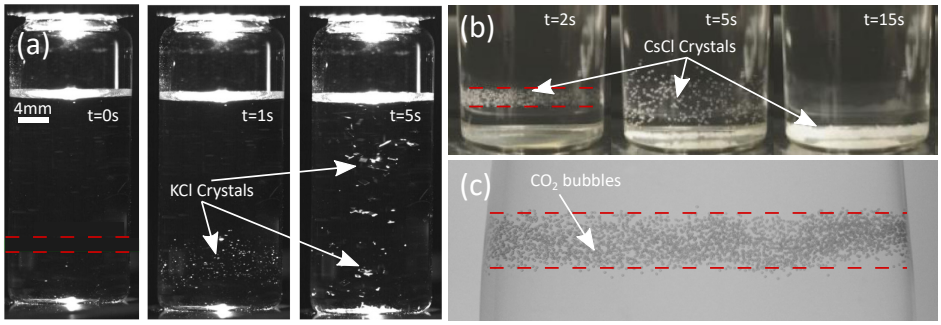

Figure 1.3: Phase separation using a laser pulse with 532 nm wavelength and $5-7$ ns pulse duration. Supersaturated solutions of (a) KCl [14], (b) CsCl [15], and (c) CO_2 [16]. The path of the laser beam is indicated using the red dashed lines. All images are reprinted with permission.

strategies proposed to control kinetics and emerging crystal properties [20–22], non-photochemical laser-induced nucleation (NPLIN), where one or more unfocused laser pulses trigger accelerated nucleation in supersaturated solutions [23–25], emerged as a promising approach due to its presumed non-chemical nature and ability to influence polymorphic form [26, 27], see Fig. 1.3. At the reported laser pulse duration (~ns), wavelengths (532/1064 nm) and laser intensity (~MW/cm^2), neither the solute nor the solvent have sufficiently strong absorption bands to induce photochemical effects. Various solutes, including small organics [28–32] (urea, glycine, L-histidine, carbamazepine, and sulfathiazole), metal halides [33] (potassium chloride, potassium bromide), dissolved gases [16, 34] (carbon dioxide) and a macromolecule - lysozyme [35] have been reported to undergo NPLIN. There is so far limited information on the list of solutions that do *not* undergo NPLIN. So far, only acetamide and sodium chlorate were reported to not undergo NPLIN [36, 37].

Several putative mechanistic hypotheses, ranging from molecular phenomena relying on (an)isotropic polarization and isotropic electronic polarizability of solute clusters [38] to microscale phenomena based on impurity heating and consequent cavitation, have been proposed in an attempt to explain the observations [39]. However, the exact mechanism behind NPLIN remains elusive [39]. Below in brief the proposed NPLIN mechanisms and their corresponding shortcomings are discussed.

Optical Kerr effect (OKE)

The first ever observation of NPLIN was made by Garetz et al. [23] in 1996. They reported the formation of needle-like urea crystals aligned with the polarization plane of the laser, suggesting an electric-field-induced origin of the underlying mechanism. Therefore the first hypothesized mechanism was based on the optical Kerr effect. This

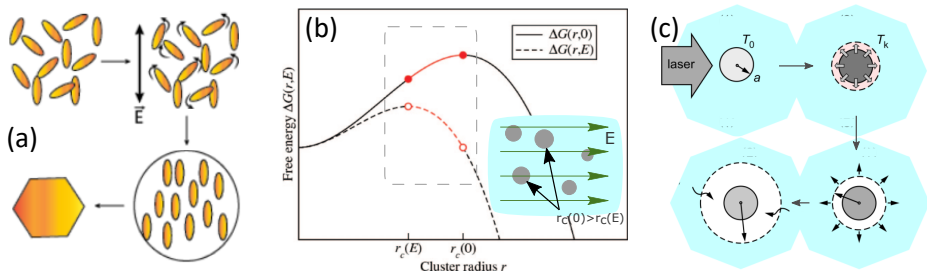

Figure 1.4: (a) Field-induced alignment of molecules - optical Kerr effect. (b) Stabilization of otherwise subcritical clusters under electric field [16] - dielectric polarization (where $r_c(0)$ and $r_c(E)$ are the critical cluster radius in the absence and presence of laser light, respectively). (c) Evaporation of solvent surrounding a nanoparticle due to local heating - impurity heating.

hypothesis states that the laser produces a weak torque that aligns all anisotropically polarizable molecules (or clusters of molecules) with their most polarizable axis parallel to the direction of polarization of the incident light. For instance, the observed alignment of urea crystals to the laser direction by Garetz et al. was argued based on the urea molecule's ability to align their C_2 axes parallel to an applied laser's electric field. Consequently, it was proposed that the electric-field-induced alignment reduces the free energy barrier for nucleation, see Fig. 1.4 (a). However, the permanent dipole moment of a molecule does not contribute to the Kerr effect since the rotational timescales of solute molecules [40] are much larger than the duration of the change in the electric field of the laser ($\sim 10^{-14}$ s).

The whole basis of the Kerr effect lies in the ability of laser light to polarize a solute molecule, yet the NPLIN of solutes without anisotropic polarizability, such as metal halides, lacks explanation. Thus, below the dielectric polarization hypothesis is presented that attempts to explain the observed NPLIN of potassium halides such as KCl [41] and KBr [33].

Dielectric polarization (DP)

The dielectric polarization mechanism suggests that isotropic polarization of prenucleating clusters by an electric field modifies the cluster's free energy by which it becomes stable, see Fig. 1.4 (b). This means that a dielectrically homogeneous cluster smaller than the critical size can be stabilized by an electric field if its dielectric constant exceeds that of the surrounding medium. Unlike OKE which works on induced polarization of solutes under laser light, DP stems from differences in the dielectric permittivity of solutes compared to solvents.

The dielectric polarization model successfully predicts the linear relation of the nucleation probability to low laser intensity for KCl [33]. By doing so, it also hypoth-

esizes a mechanism under which ionic solutes such as KCl and KBr [33], that have no preferred orientation under laser, can nucleate under NPLIN. Yet the model fails to answer the observed minimum required (threshold) laser intensity for crystallization, crystallization probability dependence on laser pulse duration and wavelength, and the polymorph selectivity under different laser polarizations [29, 30, 42]. Moreover, NPLIN of dissolved gases in which the dissolved gas phase has a lower dielectric constant than water cannot be explained by the dielectric polarization hypothesis. To explain the observed NPLIN of dissolved gases and the effect of impurities on NPLIN probabilities of NH_4Cl [36], the impurity heating hypothesis is presented below, which attempts to explain NPLIN as a function of inherent impurities rather than the solute-laser interaction.

Impurity heating (IH)

The impurity heating hypothesis suggests that the interaction of the laser irradiation with impurities plays a significant role in NPLIN. This hypothesis emerged from the inability of the OKE and DP mechanisms to explain certain observations common in NPLIN experiments, particularly the existence of a threshold below which no nucleation is observed and the pronounced effect of filtration on NPLIN [36, 43]. In a nutshell, this hypothesis assumes a scenario where insoluble impurities such as nanoparticles absorb laser energy at the wavelength of irradiation and rapidly heat and evaporate the surrounding solution, see Fig. 1.4 (c). Consequently, a region of high solute concentration at the vapor-liquid interface is expected to emerge, due to the solvent that evaporated. This increased solute concentration at the vapor-liquid interface is expected to contribute to a higher local supersaturation and therefore trigger nucleation.

1.2.3 Non-photochemical laser induced nucleation : Discussion

Owing to the work of a large number of research groups, a considerable number of observations has been accumulated in the literature [44]. Table 1.1 provides a visual summary of observation and the extent to which each proposed mechanism can explain a given observation. As one can immediately see in, none of the proposed mechanisms explains all observations.

Any contribution going beyond the proposed mechanisms has to explain both observations on NPLIN active systems as well as rationalize why some systems do *not* undergo NPLIN. The ability to exploit potential advantages of NPLIN in industrial settings requires figuring out how laser-matter interaction(s), such as laser-solute interaction, laser-impurity interaction, or both, dictate the NPLIN phenomena. The answer to this question holds the key to explaining the observations. Below, an effort is

Table 1.1: Observation and mechanism summary for NPLIN (inspired by Barber [37]). OKE = optical Kerr effect, DP = dielectric polarization, IH = impurity heating. Meaning of symbols: ✓- can be explained; x - cannot be explained; ? - needs more insight/analysis.

	Observation		**OKE**	**DP**	**IH**
1	NPLIN is reported for a broad range of systems	Small organics	✓	✓	✓
		Metal halides	x	✓	✓
		Gases	x	x	✓
2	Not all solutions undergo NPLIN		x	x	?
3	Probability dependence on laser intensity and solution super-saturation		✓	✓	✓
4	Probability dependence on laser pulse duration		✓	x	✓
5	Probability dependence on laser wavelength		?	x	?
6	Product count dependence on laser intensity	Crystals	✓	✓	✓
		Bubbles	x	x	✓
7	Polymorph selectivity under different laser polarizations		✓	x	?
8	Existence of laser intensity threshold		x	x	✓
9	Probability dependence on solution aging		✓	✓	✓
10	Effect of filtration and nanoparticle doping		x	?	✓
11	Observed crystal alignment with laser		✓	x	x
12	Effect of irradiation pathway		✓	✓	✓
13	Direct solution-laser interaction matters		✓	✓	✓

made to rationalize the observations so far, by classifying them into laser and solution parameters from a pragmatic application point of view.

Laser parameters

For the reported aqueous solutions, irrespective of the solute type, increasing the laser intensity and pulse duration have been observed to enhance NPLIN probability [36]. For both conditions, it is evident that the amount of laser-matter interaction increases. However, the reported weak dependance of the laser wavelength on the nucleation probability, and its role in laser-matter interaction is less conclusive [14, 28, 33]. The absorption of near-infrared laser light by water does explain the reported lower NPLIN probabilities for 1064 nm wavelength in aqueous solutions [45]. But the relatively high probability for 355 nm wavelengths compared to 532 nm still lacks explanation [14].

The observed increase in the number of crystals/gas bubbles with increasing laser intensity can be rationalized by all proposed mechanisms [16, 46–48]. However, the DP mechanism when applied to glycine, the values of the experimental parameters such as laser intensity and supersaturation were not comparable to the theoretically calculated values [48]. Similarly, the OKE mechanism fails to explain the observations for KCl since dissolved KCl lacks directional polarization under laser light. Furthermore, for small organic solutes, the effect of laser polarization on the polymorph formed is still under debate [30–32, 42, 45, 49].

The lack of understanding of laser-matter interactions in NPLIN leaves us with an unanswered question: why is there a laser intensity threshold to NPLIN below which no nucleation occur ? [23, 28, 33, 42, 49] As the existence of this threshold cannot be explained by the OKE and DP mechanisms, this observation may hold the key to solving the puzzle of laser-matter interaction in NPLIN. Since the nucleation probability increases with laser intensity above this threshold, one may pragmatically ask if rather any supersaturated solution, regardless of its chemical identity, may be forced to nucleate at high enough laser intensities.

Solution parameters

For a fixed laser intensity above a threshold, the observed increase in NPLIN probability with solution supersaturation can be explained using the increase in the average size of the pre-nucleating clusters with supersaturation - favoring stable nucleus formation. The observed increase in nucleation probability with aging for small organics is also in line with the attempted explanation [48, 50]: the more time available for the solution to progress towards equilibrium before the laser irradiation, the higher the likelihood of the formation of large pre-nucleating clusters. Since the equilibrium timescale for a solution would depend on the solute's diffusivity, the reported higher diffusion coefficient for metal halides [51] compared to small organics [52] could be a possible reason why aging of metal halides is less significant for NPLIN probability [41].

Within a solution, in addition to the intended solute and solvent, there are often impurities that a laser can interact with. The majority of authors have overlooked the composition of the impurities present in their solution. The role of impurities in NPLIN has been demonstrated by Ward et al. [36] who observed a decrease in NPLIN probability with filtration. The reported increase in the nucleation probability with laser intensity and pulse duration can be rationalized using the increase in the energy available to heat up a nano-impurity for triggering nucleation. In addition, the reported laser intensity threshold in NPLIN could be reasoned as the minimum energy required to form a significant vapor bubble surrounding a nano-impurity. Thus the light absorption spectra of impurities based on their size and composition could

be a deciding factor. This approach to energy absorption could explain the weak dependence of crystallization probability on wavelength as a function of impurity's light absorption efficiency.

Although the majority of the NPLIN observations can be explained using the nano-impurity heating hypothesis, there exist only a few theoretical works that explore the mechanism [53, 54]. These theoretical works are largely phenomenological and lack the ability to quantify and predict the experimentally observed correlation between laser intensity and crystallization probability. Nonetheless, predicted qualitative trends from simulations offer a means to compare experiments and theory. Hopefully, further efforts from both the theoretical and the experimental side can answer questions on the exact nature and role of these nano-impurities. This extended understanding can answer questions such as what are the physical properties of a given nano-impurity (physicochemical state- soluble or colloidal, size, chemical composition, and more) that make it NPLIN active? Furthermore, the reported zero nucleation probability by Kacker et al. [14] for samples that masked the laser entry within the solution further strengthens the argument on the role of direct light-solution interaction in NPLIN. Thus, clear evidence on the type of light-solution interaction occurring in NPLIN will help in establishing a concrete theory for predicting the NPLIN activity of a solution.

1.3 Research questions and Objective

Despite the ever-growing list of systems exhibiting NPLIN, some basic questions remain unanswered.

- Can one *a priori* predict whether a solution is NPLIN active or not, based on the physicochemical properties of the solute, solvent and impurities ?
- For a given solution, what are the critical laser parameters for triggering NPLIN ?

The answers to the above questions lie with the development of a mechanistic understanding of NPLIN. In other words, more effort is required to extend the current understanding of NPLIN from both the theoretical and the experimental side.

The objective of this dissertation is to study on how the NPLIN reduces the energy barrier for crystal nucleation in solutions. The impurity heating hypothesis is tested since it explains majority of the observations summarized in Table 1.1. Therefore the detection of microbubble is necessary to study the early nucleation stage of solute crystals. Due to the random distribution of impurities within the solution, the precise location of the micron-sized cavitation bubbles with very small lengthscale [$O(100\,\mu m)$] and timescale [$O(10\,\mu s)$] forming nano- to micro- seconds after laser

irradiation are hard to study [55]. Therefore, in this dissertation, the following changes will be made compared to traditional NPLIN experiments to test the impurity heating hypothesis:

- use of microfluidics to enable in-situ observation of the micron-sized cavitation bubble and early nucleation of solute crystals
- utilizing high-speed microscopy to access relevant length and time scales
- depending on the solution and analysis requirement, addition of a ppm level soluble impurity to ensure that the absorbed laser energy by solution is consistent
- fix the position of bubble formation by focusing the laser to achieve in-situ recording of both the bubble and crystal(s).

However, obtaining direct and comprehensive insight into the molecular structure, local dynamics, and nucleation mechanisms is prohibited by the spatial and temporal resolution of the experimental techniques.

Simulations have proven to be a powerful way to complement experiments and help to interpret experimental measurements. Thus a concomitant numerical study will confirm experimental results and provide a solid basis for guiding the experimental studies with predictions. Unfortunately, the developed simulation technique should bridge the length and timescales of both the bubble evolution and crystal nucleation [56]. Such as technique should also include heat, mass, momentum and solute transfer, which makes the modelling difficult. Therefore a compromise will be made on the studies at molecular level. Instead the continuum models will be employed to estimate the parameter value such as temperature, velocities and solute concentration surrounding the bubble. More specifically, the estimated supersaturation will be used to quantitatively determine the rate of nucleation using the analytical relation from classical nucleation theory. Thereby, the theoretically determined rate of nucleation can be compared to the observed crystal counts and crystallization probabilities from experiments.

1.4 Dissertation Outline

This dissertation presents a range of techniques involving the use of laser-induced cavitation bubble(s) for crystallization from solutions. The work limits itself to the presumed non-photochemical methods and discusses various phenomenon (mechanism) that would lead to crystal nucleation following the vapor bubble(s) evolution.

The experimental setup

Chapter 2 delineates the construction of a dedicated optical setup for performing laser-induced cavitation experiments inside a microfluidic device. The setup design presents flexibility with customization of optical components based on the study. In addition, the use of only the necessary optics modules and component specific choice in the manufacturer allows the construction of a budget friendly equipment.

Is cavitation a plausible mechanism for NPLIN?

Chapter 3 discusses the role of solute accumulation in the liquid immediately surrounding a laser-induced vapor bubble within supersaturated solutions of KCl. A laser pulse of 532 nm and 4 ns duration is employed for this study. With complementing experiments and numerical simulations the chapter provides a quantitative evidence on the supersaturation profiles at and around the vapor-liquid interface.

Can the above proposed cavitation mechanism be applied to all solute-solvent systems?

Following Chapter 3, Chapter 4 extends the application of the developed experimental technique to other salts such as NH_4Cl and NaCl. The experiments are performed using 1064 nm laser pulse with 6 ns duration including in solutions of KCl to compare against the results from Chapter 3. In addition, the chapter also discusses analytical relations to estimate the supersaturation at the vapor-liquid interface, necessary to predict the NPLIN activity of a solution.

The dynamics of a bubble within microchannels and the role of bubble-bubble interactions in NPLIN

Unbounded liquid domains necessary to produce 3-D spherical bubble(s) are hardly present in nature and engineering systems. Moreover, even bubble-bubble interaction can affect the symmetry associated with the bubble dynamics. Therefore, first a single laser-induced vapor bubble dynamics within diverse quasi-1D microchannel geometries is analyzed using experiments and theory in Chapter 5. The study provides insights on precise and rapid flow control, and flow stability, necessary to *a priori* design a cavitation powered microsystem. Following which, Chapter 6 discusses the experiments with bubble pairs in a circular microchannel containing supersaturated solutions of a model salt, $KMnO_4$. Liquid microjet emerge from the vapor-liquid interface due to bubble-bubble hydrodynamic interaction. The characteristics and role of a microjet in crystallization is studied using experiments, classical nucleation theory and boundary integral element method.

Conclusions

Finally, Chapter 7 provides the overall conclusions made from the studies performed in this dissertation.

REFERENCES

[1] Allan S. Myerson. Second Edition. Woburn: Butterworth-Heinemann, 2002. ISBN: 978-0-7506-7012-8.

[2] D Kashchiev. Vol. 1. Butterworth-Heinman, 2000. ISBN: 0-7506-4682-9.

[3] J. M. García-Ruiz, S. T. Hyde, A. M. Carnerup, A. G. Christy, M. J. Van Kranendonk, and N. J. Welham. "Self-Assembled Silica-Carbonate Structures and Detection of Ancient Microfossils." In: *Science* 302.5648 (2003), pp. 1194–1197.

[4] Ivan V Markov. *Crystal Growth for Beginners*. 2nd. WORLD SCIENTIFIC, 2003.

[5] Alison Lewis, Marcelo Seckler, Herman Kramer, and Gerda van Rosmalen. *Industrial Crystallization: Fundamentals and Applications*. Cambridge University Press, 2015.

[6] K. Plumb. "Continuous Processing in the Pharmaceutical Industry: Changing the Mind Set." In: *Chemical Engineering Research and Design* 83.6 (2005). 7th World Congress of Chemical Engineering, pp. 730–738. ISSN: 0263-8762.

[7] Jie Chen, Bipul Sarma, James M. B. Evans, and Allan S. Myerson. "Pharmaceutical Crystallization." In: *Crystal Growth & Design* 11.4 (2011), pp. 887–895.

[8] Salvatore Mascia, Patrick L Heider, Haitao Zhang, Richard Lakerveld, Brahim Benyahia, Paul I Barton, Richard D Braatz, Charles L Cooney, James MB Evans, Timothy F Jamison, et al. "End-to-end continuous manufacturing of pharmaceuticals: integrated synthesis, purification, and final dosage formation." In: *Angewandte Chemie* 125.47 (2013), pp. 12585–12589.

[9] Vikram Korede et al. "Design and Validation of a Droplet-based Microfluidic System To Study Non-Photochemical Laser-Induced Nucleation of Potassium Chloride Solutions." In: *Crystal Growth & Design* 23.8 (2023), pp. 6067–6080.

[10] J. W. Mullin. *Crystallization*. Oxford: Butterworth-Heinemann, 2001.

[11] D. Kashchiev and G. M. van Rosmalen. "Review: Nucleation in solutions revisited." In: *Crystal Research and Technology* 38.7-8 (2003), pp. 555–574.

[12] H.J.M. Kramer and P.J. Jansens. "Tools for Design and Control of Industrial Crystallizers – State of Art and Future Needs." In: *Chemical Engineering & Technology* 26.3 (2003), pp. 247–255.

[13] Gregory D. Botsaris. “Secondary Nucleation — A Review.” In: *Industrial Crystallization*. Ed. by J. W. Mullin. Boston, MA: Springer US, 1976, pp. 3–22. ISBN: 978-1-4615-7258-9.

[14] Rohit Kacker, Sanjana Dhingra, Daniel Irimia, Murali Krishna Ghatkesar, Andrzej Stankiewicz, Herman J. M. Kramer, and Huseyin Burak Eral. “Multiparameter Investigation of Laser-Induced Nucleation of Supersaturated Aqueous KCl Solutions.” In: *Crystal Growth & Design* 18.1 (2018), pp. 312–317.

[15] Yao Liu, Qingqing Qiu, Guohua Ding, and Weixiong You. “Effect of Acidic Polymers on the Morphology of Laser-Induced Nucleation of Cesium Chloride.” In: *ACS Omega* 6.4 (2021), pp. 2699–2706.

[16] Martin R. Ward, William J. Jamieson, Claire A. Leckey, and Andrew J. Alexander. “Laser-induced nucleation of carbon dioxide bubbles.” In: *Journal of Chemical Physics* 142.14 (2015). ISSN: 00219606.

[17] Cédric Schoonen and James F. Lutsko. “Crystal Polymorphism Induced by Surface Tension.” In: *Phys. Rev. Lett.* 129 (24 Dec. 2022), p. 246101.

[18] James F. Lutsko. “How crystals form: A theory of nucleation pathways.” In: *Science Advances* 5.4 (2019), eaav7399.

[19] Valentino Bianco, P. Montero de Hijes, Cintia P. Lamas, Eduardo Sanz, and Carlos Vega. “Anomalous Behavior in the Nucleation of Ice at Negative Pressures.” In: *Phys. Rev. Lett.* 126 (1 Jan. 2021), p. 015704.

[20] Romain Grossier, Zoubida Hammadi, Roger Morin, and Stéphane Veesler. “Predictive Nucleation of Crystals in Small Volumes and Its Consequences.” In: *Phys. Rev. Lett.* 107 (2 July 2011), p. 025504.

[21] Grisell Díaz Leines and Jutta Rogal. “Template-Induced Precursor Formation in Heterogeneous Nucleation: Controlling Polymorph Selection and Nucleation Efficiency.” In: *Phys. Rev. Lett.* 128 (16 Apr. 2022), p. 166001.

[22] Masoud Bozorg Bigdeli and Peichun Amy Tsai. “Making Photonic Crystals via Evaporation of Nanoparticle-Laden Droplets on Superhydrophobic Microstructures.” In: *Langmuir* 36.17 (2020). PMID: 32309954, pp. 4835–4841.

[23] B. A. Garetz, J. E. Aber, N. L. Goddard, R. G. Young, and A. S. Myerson. “Nonphotochemical, Polarization-Dependent, Laser-Induced Nucleation in Supersaturated Aqueous Urea Solutions.” In: *Phys. Rev. Lett.* 77 (16 Oct. 1996), pp. 3475–3476.

[24] Mohammed Noorul Hussain, Jeroen Jordens, Simon Kuhn, Leen Braeken, and Tom Van Gerven. “Ultrasound as a tool for polymorph control and high yield in flow crystallization.” In: *Chemical Engineering Journal* 408 (2021), p. 127272. ISSN: 1385-8947.

[25] Carla Duffus, Philip J. Camp, and Andrew J. Alexander. “Spatial Control of Crystal Nucleation in Agarose Gel.” In: *Journal of the American Chemical Society* 131.33 (2009). PMID: 19645467, pp. 11676–11677.

[26] Bruce A. Garetz, Jelena Matic, and Allan S. Myerson. “Polarization Switching of Crystal Structure in the Nonphotochemical Light-Induced Nucleation of Supersaturated Aqueous Glycine Solutions.” In: *Phys. Rev. Lett.* 89 (17 Oct. 2002), p. 175501.

[27] Yao Liu, Mees H. van den Berg, and Andrew J. Alexander. “Supersaturation dependence of glycine polymorphism using laser-induced nucleation, sonocrystallization and nucleation by mechanical shock.” In: *Phys. Chem. Chem. Phys.* 19 (29 2017), pp. 19386–19392.

[28] Jelena Matic, Xiaoying Sun, Bruce A. Garetz, and Allan S. Myerson. “Intensity, wavelength, and polarization dependence of nonphotochemical laser-induced nucleation in supersaturated aqueous urea solutions.” In: *Crystal Growth & Design* 5.4 (2005), pp. 1565–1567. ISSN: 15287483.

[29] Bruce A. Garetz, Jelena Matic, and Allan S. Myerson. “Polarization Switching of Crystal Structure in the Nonphotochemical Light-Induced Nucleation of Supersaturated Aqueous Glycine Solutions.” In: *Physical Review Letters* 89.17 (2002), pp. 1–4. ISSN: 10797114.

[30] Xiaoying Sun, Bruce A. Garetz, and Allan S. Myerson. “Polarization switching of crystal structure in the nonphotochemical laser-induced nucleation of supersaturated aqueous L-histidine.” In: *Crystal Growth & Design* 8.5 (2008), pp. 1720–1722. ISSN: 15287483.

[31] Aziza Ikni, Bertrand Clair, Philippe Scouflaire, Stéphane Veesler, Jean Michel Gillet, Nouha El Hassan, Françoise Dumas, and Anne Spasojević-De Biré. “Experimental demonstration of the carbamazepine crystallization from non-photochemical laser-induced nucleation in acetonitrile and methanol.” In: *Crystal Growth & Design* 14.7 (2014), pp. 3286–3299. ISSN: 15287505.

[32] Wenjing Li, Aziza Ikni, Philippe Scouflaire, Xiaoxuan Shi, Nouha El Hassan, Pascale Gémeiner, Jean Michel Gillet, and Anne Spasojević-De Biré. “Non-Photochemical Laser-Induced Nucleation of Sulfathiazole in a Water/Ethanol Mixture.” In: *Crystal Growth & Design* 16.5 (2016), pp. 2514–2526. ISSN: 15287505.

[33] Martin R. Ward and Andrew J. Alexander. “Nonphotochemical Laser-Induced Nucleation of Potassium Halides: Effects of Wavelength and Temperature.” In: *Crystal Growth & Design* 12.9 (2012), pp. 4554–4561.

[34] Brandon C. Knott, Jerry L. LaRue, Alec M. Wodtke, Michael F. Doherty, and Baron Peters. "Communication: Bubbles, crystals, and laser-induced nucleation." In: *The Journal of Chemical Physics* 134.17 (2011), p. 171102.

[35] In Sung Lee, James M.B. Evans, Deniz Erdemir, Alfred Y. Lee, Bruce A. Garetz, and Allan S. Myerson. "Nonphotochemical laser induced nucleation of hen egg white lysozyme crystal." In: *Crystal Growth & Design* 8.12 (2008), pp. 4255–4261. ISSN: 15287483.

[36] Martin R. Ward, Alasdair M. Mackenzie, and Andrew J. Alexander. "Role of Impurity Nanoparticles in Laser-Induced Nucleation of Ammonium Chloride." In: *Crystal Growth & Design* 16.12 (2016), pp. 6790–6796. ISSN: 15287505.

[37] Eleanor Rose Barber. "Non-photochemical laser-induced nucleation (NPLIN): an experimental investigation via real-time imaging and product analysis." PhD thesis. 2022.

[38] Andrew J. Alexander and Philip J. Camp. "Single Pulse, Single Crystal Laser-Induced Nucleation of Potassium Chloride." In: *Crystal Growth & Design* 9.2 (2009), pp. 958–963.

[39] Andrew J. Alexander and Philip J. Camp. "Non-photochemical laser-induced nucleation." In: *The Journal of Chemical Physics* 150.4 (2019), p. 040901.

[40] Deepak Ojha and Amalendu Chandra. "Urea in Water: Structure, Dynamics, and Vibrational Echo Spectroscopy from First-Principles Simulations." In: *The Journal of Physical Chemistry B* 123.15 (2019). PMID: 30905162, pp. 3325–3336.

[41] Andrew J. Alexander and Philip J. Camp. "Single Pulse, Single Crystal Laser-Induced Nucleation of Potassium Chloride." In: *Crystal Growth & Design* 9.2 (2009), pp. 958–963.

[42] Xiaoying Sun and Bruce A Garetz. "Supersaturation and Polarization Dependence of Polymorph Control in the Nonphotochemical Laser-Induced Nucleation (NPLIN) of Aqueous Glycine Solutions, volume = 6, year = 2006." In: *Crystal Growth & Design* 3 (), pp. 684–689.

[43] Nadeem Javid, Thomas Kendall, Iain S. Burns, and Jan Sefcik. "Filtration suppresses laser-induced nucleation of glycine in aqueous solutions." In: *Crystal Growth & Design* 16.8 (2016), pp. 4196–4202. ISSN: 15287505.

[44] V. Korede and N. Nagalingam, Frederico Marques Penha, Noah van der Linden, Johan T. Padding, Remco Hartkamp, and Huseyin Burak Eral. "A Review of Laser-Induced Crystallization from Solution." In: *Crystal Growth & Design* 23.5 (2023), pp. 3873–3916.

[45] Daniel Irimia, Jenkins Jose Shirley, Anshul S. Garg, Davey P.A. Nijland, Antoine E. D. M. van der Heijden, Herman J. M. Kramer, and Huseyin Burak Eral. “Influence of Laser Parameters and Experimental Conditions on Non-photochemical Laser-Induced Nucleation of Glycine Polymorphs.” In: *Crystal Growth & Design* 21.1 (2021), pp. 631–641.

[46] Carla Duffus, Philip J. Camp, and Andrew J. Alexander. “Spatial control of crystal nucleation in agarose gel.” In: *Journal of the American Chemical Society* 131.33 (2009), pp. 11676–11677. ISSN: 00027863.

[47] Tianyi Hua, Omar Gowayed, Danielle Grey-Stewart, Bruce A. Garetz, and Ryan L. Hartman. “Microfluidic Laser-Induced Nucleation of Supersaturated Aqueous KCl Solutions.” In: *Crystal Growth & Design* 19.6 (2019), pp. 3491–3497.

[48] Tianyi Hua, Celymar Valentín-Valentín, Omar Gowayed, Seongha Lee, Bruce A. Garetz, and Ryan L. Hartman. “Microfluidic Laser-Induced Nucleation of Supersaturated Aqueous Glycine Solutions.” In: *Crystal Growth & Design* 20.10 (2020), pp. 6502–6509.

[49] Yao Liu, Mees H. Van Den Berg, and Andrew J. Alexander. “Supersaturation dependence of glycine polymorphism using laser-induced nucleation, sonocrystallization and nucleation by mechanical shock.” In: *Physical Chemistry Chemical Physics* 19.29 (2017), pp. 19386–19392. ISSN: 14639076.

[50] Julien Zaccaro, Jelena Matic, Allan S. Myerson, and Bruce A. Garetz. “Non-photochemical, Laser-Induced Nucleation of Supersaturated Aqueous Glycine Produces Unexpected gamma-Polymorph.” In: *Crystal Growth & Design* 1.1 (2001), pp. 5–8.

[51] Victor M.M. Lobo, Ana C.F. Ribeiro, and Luis M.P. Verissimo. “Diffusion coefficients in aqueous solutions of potassium chloride at high and low concentrations.” In: *Journal of Molecular Liquids* 78.1 (1998). Proceedings of the 25th International Conference on Solution Chemistry, pp. 139–149. ISSN: 0167-7322.

[52] Shyam P. Khanal, Yadav Prasad Kandel, and Narayan P. Adhikari. “Transport properties of zwitterion glycine, diglycine, and triglycine in water.” In: *AIP Advances* 9.6 (2019), p. 065303.

[53] Niklas Hidman, Gaetano Sardina, Dario Maggiolo, Henrik Ström, and Srdjan Sasic. “Numerical Frameworks for Laser-Induced Cavitation: Is Interface Supersaturation a Plausible Primary Nucleation Mechanism?” In: *Crystal Growth & Design* 20.11 (2020), pp. 7276–7290.

[54] Julien O. Sindt, Andrew J. Alexander, and Philip J. Camp. “Effects of nanoparticle heating on the structure of a concentrated aqueous salt solution.” In: *The Journal of Chemical Physics* 147.21 (2017), p. 214506.

[55] Linglong Wang, Yingchun Wu, Xuecheng Wu, and Kefa Cen. “Measurement of dynamics of laser-induced cavitation around nanoparticle with high-speed digital holographic microscopy.” In: *Experimental Thermal and Fluid Science* 121 (2021), p. 110266. ISSN: 0894-1777.

[56] K. M. Mohamed and A. A. Mohamad. “A review of the development of hybrid atomistic–continuum methods for dense fluids.” In: *Microfluidics and Nanofluidics* 8.3 (Mar. 2010), pp. 283–302. ISSN: 1613-4990.

2

THE EXPERIMENTAL SETUP

Optofluidic devices have revolutionized the manipulation and transportation of fluid at smaller length scales ranging from micrometers to millimeters. This chapter describes a dedicated optical setup for studying laser-induced cavitation inside a microfluidic device. In a typical experiment, a tightly focused laser beam is used to locally evaporate the solution laced with a dye resulting in the formation of a microbubble. The evolving bubble interface is tracked using high-speed microscopy and digital image analysis. In essence, a complete guide for constructing a fluorescence microscope from scratch using standard optical components is presented with flexibility in the design, and at a lower cost (≈65 % less) compared to its commercial analogues.

This chapter is based on the article:
N. Nagalingam* and A. Raghunathan* et al. "Low-cost fluorescence microscope with microfluidic device fabrication for optofluidic applications." In: *HardwareX* 14 (2023), e00415.
* denotes equal contribution

2.1 Hardware in context

The evolution of optical microscopy has been sparked by the recent advancements in digital image processing and machine vision that have led to improved mobility and flexibility with microscopes through the use of open hardware and software [1]. A fluorescence microscope is a non-invasive, visualization and optical measurement tool widely employed in the field of life sciences over the past several decades [2]. In recent times, a microscope combined with an excitation laser has gained traction in the optofluidics domain with an increasing number of applications that include cell sorting [3], micro-robotics [4], microparticle synthesis [5, 6], droplet drying [7], optical micromanupulation [8], fluid microfilms and nanofilms [9] and other microfluidic systems [10, 11]. Despite its widespread use, commercially available microscopes often entail huge costs (€ $100,000 - 150,000$ depending on the options and manufacturer) and offer limited flexibility with the design. Moreover, with rapid technological advancements, microscopes come with sophistications that require technical expertise for operation and maintenance [12].

Several microscope designs have been developed in literature specifically to perform laser-induced cavitation studies in microfluidic systems [13–15]. For example, Rau et al. [16] studied the hydrodynamic effects of cell lysis using a pulsed Nd:YAG laser beam. In this setup, the source beam is bisected using a beamsplitter to both lyse the cell and illuminate the sample. Zwaan et al. [17] performed controlled cavitation experiments to study the planar bubble dynamics within different lab-on-a-chip device geometries fabricated using Polydimethylsiloxane (PDMS). In application to cavitation based micropump, Dijkink et al. [18] investigated the effect of PDMS wall compliance together with the flow fields visualization using the conventional Particle Image Velocimetry (PIV) technique. Besides single component systems (e.g., aqueous dye), laser-induced cavitation has also been employed for triggering crystal nucleation in thin layers of supersaturated aqueous solution [19]. Furthermore, techniques such as fluorescence-based thermometry [20], high-speed micro-PIV [21] and microparticle tracking velocimetry [22] when combined with cavitation experiments have proven to help with the characterization of the phenomena using the measurement of the associated parameters such as temperature and flow fields. Although many distinct microscopy configurations have been reported in the literature to perform laser-induced cavitation and PIV experiments, very limited emphasis is given to the design details and assembly of the experimental setup.

This chapter delineates the architecture and construction of a low-cost customizable microscope using optomechanical components in conjunction with a pulsed laser to primarily study laser-induced microbubble dynamics. The hardware design is limited to the basic models of commercially available counterparts. However, with dedicated customization, its applications can be extended beyond the addressed laser-induced

cavitation, e.g., PIV analyses and fluorescence-based thermometry. In order to emphasize the flexibility of the constructed setup, an example alteration is made to equip the setup for fluorescence-PIV.

2.2 Hardware description

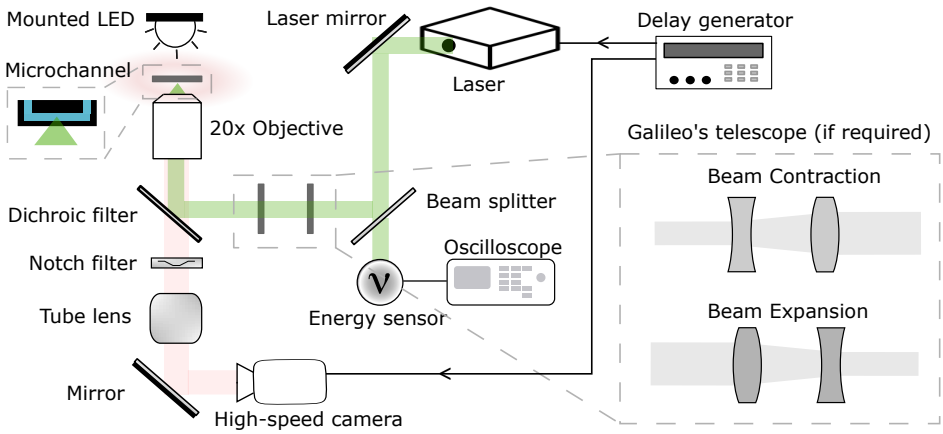

Figure 2.1: Architecture of the experimental setup.

A schematic of the optical architecture is provided in Fig. 2.1. Micron-sized vapor bubble is generated within the microchannel using a 532 nm, frequency-doubled, pulsed Nd:YAG laser having a beam diameter of 4 mm and a pulse duration of 4 ns. The beam path is guided from the laser source using a fully reflecting mirror and a partially reflecting beamsplitter. An energy meter connected to an oscilloscope is used to measure the pulse energy transmitted by the beamsplitter. The reflected laser pulse from the dichroic filter is directed towards a 3-axis translation stage where the microfluidic device is positioned. Depending on the desired laser beam diameter, a Galilean telescope arrangement (a set of convex and concave lenses separated by the sum of their focal lengths) can be constructed to either increase or decrease the laser beam diameter as indicated in Fig. 2.1. Alternatively, a beam expander with the required magnification range can be used for this purpose but is relatively more expensive. The flexibility of the design allows the placement of the telescope at any position between the source laser and the dichroic filter. For this study the laser beam was expanded from 4 mm to 8 mm to roughly have the same size as the entrance pupil diameter (10 mm) of the 20x objective (Plan Fluor, Nikon).

An inverted microscope arrangement consisting of an infinity-corrected 20x objective with a numerical aperture (NA) of 0.5 is used to focus the laser and form a mi-

crobubble. The energy intensity of the laser at the focal spot is estimated to be in the order of GW/cm^2. In the setup, the same objective is also used to image the sample. A red LED light of 625 nm wavelength is used to illuminate the sample. In contrast to conventionally used white light, red light offers some advantages. Firstly, the entire light can pass through the dichroic filter having transmission band of $580 - 650$ nm, thereby providing better illumination at a lower intensity. Furthermore, the spectral response of the camera is found to be the highest for this particular wavelength. A notch filter provided beneath the dichroic filter protects the camera by completely blocking the reflected or scattered laser light. The sample using the objective is imaged over the camera's sensor with a tube lens. The high-speed camera operating at 264,000 frames per second (fps) is used to record the events that occur at microsecond timescales.

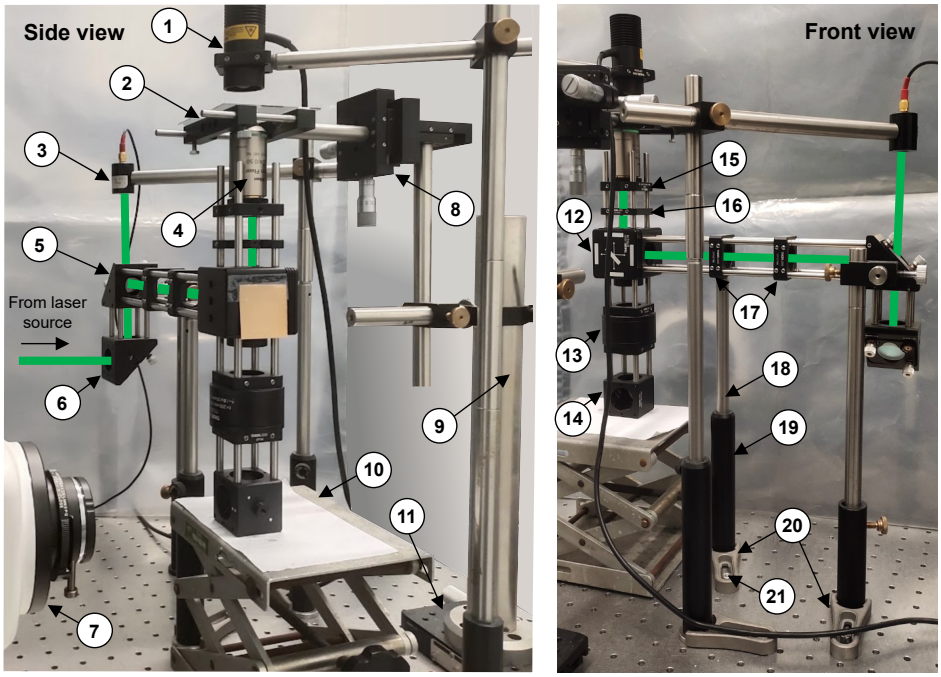

Figure 2.2: Annotation of components in the experimental setup. 1. Mounted LED, 2. Sample holder, 3. Energy sensor, 4. 20x objective, 5. Right-angle kinematic mirror mount with round beamsplitter, 6. Right-angle kinematic mirror mount with laser mirror, 7. Camera, 8. 3-axis travel stage, 9. Damped post, 10. Lab jack, 11. Linear translation stage 12. Kinematic fluorescence filter cube with dichroic and notch filters, 13. Tube lens with cage plates (tube lens) and threading adapters, 14. Cage cube with rectangular mirror, 15. Cage plate (objective) with threading adapter, 16. Cage system iris diaphragm, 17. Cage plates (lens), 18. Optical post, 19. Pedestal post holder, 20. Clamping fork, 21. Cap screw. The green track indicates the laser path.

The laboratory view of the experimental setup is depicted in Fig. 2.2. To illustrate the working of the setup a microchannel having a rectangular cross-section is used. Laser-induced cavitation is implemented in the microchannels using a solution of aqueous red dye (DR81, Sigma-Aldrich). The 3-axis translation stage (13 mm range with a least count of 10 μm) that holds the sample is mounted over a linear translation stage (50 mm range and with a least count of 10 μm) to have a larger travel range along the microchannel axis. The microchannels were fabricated in-house using PDMS and offer several advantages over commercially available plastic microfluidic chips [23]. For instance, the permeability of PDMS to gases can be exploited to remove residual gas bubbles and improve the functionality of the device in view of the cavitation experiments [24]. Furthermore, the elastomeric nature of PDMS can mimic vascular pressure-driven flows which can also aid in providing a real-time flow representation [25].

2.3 Bill of materials and Build instructions

The bill of materials summary and step-by-step build instructions are provided in Appendix A.1 and A.2, respectively. The Appendix provides the complete procedure for the assembly of the experimental setup using discrete optomechanical components. The main emphasis is laid on the ease of alignment and the quality of imaging. In addition to the assembly and alignment of the setup for performing laser-induced cavitation experiments, a procedure to equip the setup for fluorescence-PIV with minimal alterations is also demonstrated. This demonstration is included only to emphasises the flexibility of the setup to modification in the optics assembly. Therefore neither this chapter nor the other chapter in this dissertation employ fluorescence-PIV.

2.4 Operation and Validation

Operation

Transient micro-vapor bubbles are produced by focusing the laser within aqueous solutions containing a red dye. Since water is transparent to 532 nm wavelength, a dye is used to facilitate the solution's absorbance to produce thermo-cavitation [10]. The red dye (Direct Red 81, Sigma Aldrich) with a concentration of 0.5 wt% and an absorption coefficient of 173.47 cm^{-1} is used in this study.
The laser (Nano L 50-50 PIV, Litron) is operated in a pulsed mode using the delay generator to produce single laser pulses on demand. The flash lamp and Q-switch are triggered externally using two TTL pulses (4V) with 96 μs time delay. This delay between the flash lamp and Q-switch can vary based on the laser model and the oscillator

(for twin-headed lasers). The digital delay generator is set to externally trigger the camera at least 5 image frames before the Q-switch is triggered. Before pulsing the laser, the settings for the camera which include the field of view in pixels, frame rate and trigger options for recording are assigned accordingly using the Photron FASTCAM Viewer (PFV) 4 software [26]. After the laser pulse is shot, the created vapor bubble exists for tens of microseconds depending on the energy supplied. The recorded images are saved in '.MRAW' file format as it can then be converted to any desired format using the same software. Further details regarding the absorbance measurements, calibration of the camera, and experiment protocols for sample preparation and setup operation can be found in report by Raghunathan [27].

Validation

The microchannel filled with aqueous red dye solution is placed on the slide holder and the laser pulse with an energy of 118.1 μJ is focussed at the channel centre to produce a vapor bubble. The images of the vapor bubble captured using the high-speed camera are represented in Fig. 2.3 (a). Only the central part of the bubble is imaged due to lower number of pixels available for recording at the operated high frame rate (264,000 fps).

The time evolution of the vapor bubble after processing the images is presented in Fig, 2.3 (b). X is the half-size of the bubble and t is the time from laser irradiation. Figure 2.3 (c) shows the non-dimensionalized parameters with respect to the channel hydraulic diameter (d), and collapse time of the bubble (t_{col}) - defined as the time taken by the bubble to collapse from maximum size to zero. This non-dimensionalization allows the comparison of results with the existing literature. From Fig. 2.3 (c), the dimensionless time associated with the dimensionless size of the bubble is in good agreement with the experiments reported by Hellman et al. [28] and Quinto-Su et al. [29]. The values of the parameters used to plot Fig. 2.3 (c) are provided in Table 2.1 below.

Table 2.1: Parameter values used in the analysis of laser-induced cavitation experiments.

Author(s)	Marker	Channel Dimensions (μm)	d (μm)	t_{col} (μs)
This work	□	100 × 250	143	30
Hellman et al. [28]	◯	50 × 100	66.7	25
Hellman et al. [28]	◊	50 × 200	80	15
Quinto-Su et al. [29]	△	30 × 50	37.5	17

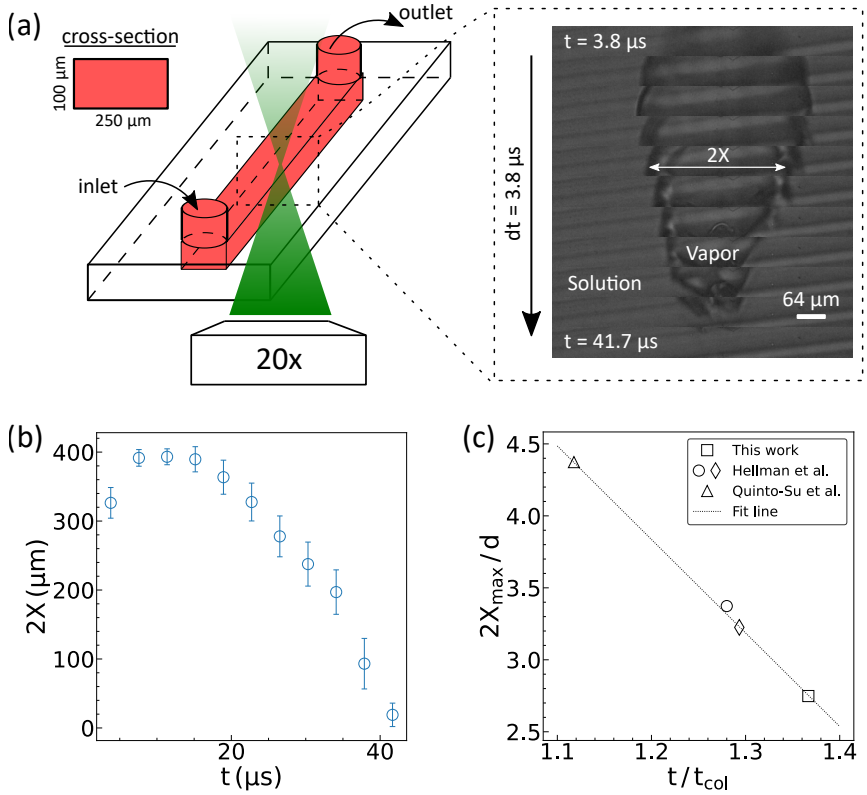

Figure 2.3: Laser-induced cavitation experiments. (a) Experimentally obtained bubble images recorded using the high-speed camera operated at 264,000 fps. The supplied laser pulse energy is 118.1 µJ. (b) Bubble evolution obtained from the post-processed experimental images. The error bars represent the standard error for 5 trials. (c) The non-dimensionalized parameter values compared against the experiments from literature [28, 29]. $2X_{max}$ represents the maximum size of the bubble. The coefficient of determination for the fit line is $R^2 = 0.997$.

2.5 Conclusions

To conclude, the chapter provides a guide for building a low-cost microscope from scratch dedicated to laser-assisted optofluidic studies with fully customized optics. Experiments on laser-induced cavitation bubbles within microchannel were performed to validate and exhibit the working functionality of the system. With dedicated adaptations, the proposed design can be utilized for a vast range of applications, e.g., in microfluidics [30, 31] and laser-induced crystallization research [32].

REFERENCES

[1] Jesus Salido, Gloria Bueno, Jesus Ruiz-Santaquiteria, and Gabriel Cristobal. "A review on low-cost microscopes for Open Science." In: *Microscopy research and technique* 85.10 (2022), pp. 3270–3283.

[2] Jeff W Lichtman and José-Angel Conchello. "Fluorescence microscopy." In: *Nature methods* 2.12 (2005), pp. 910–919.

[3] Kazunori Takahashi, Akihiro Hattori, Ikurou Suzuki, Takanori Ichiki, and Kenji Yasuda. "Non-destructive on-chip cell sorting system with real-time microscopic image processing." In: *Journal of Nanobiotechnology* 2.1 (June 2004), p. 5. ISSN: 1477-3155.

[4] Ivan Rehor, Charlie Maslen, Pepijn G. Moerman, Bas G.P. van Ravensteijn, Renee van Alst, Jan Groenewold, Huseyin Burak Eral, and Willem K. Kegel. "Photoresponsive Hydrogel Microcrawlers Exploit Friction Hysteresis to Crawl by Reciprocal Actuation." In: *Soft Robotics* 8.1 (2021). PMID: 32320334, pp. 10–18.

[5] Rumen N. Georgiev, Sara O. Toscano, William E. Uspal, Bram Bet, Sela Samin, René van Roij, and Huseyin Burak Eral. "Universal motion of mirror-symmetric microparticles in confined Stokes flow." In: *Proceedings of the National Academy of Sciences* 117.36 (2020), pp. 21865–21872.

[6] Ivan Rehor, Sophie van Vreeswijk, Tina Vermonden, Wim E. Hennink, Willem K. Kegel, and Huseyin Burak Eral. "Biodegradable Microparticles for Simultaneous Detection of Counterfeit and Deteriorated Edible Products." In: *Small* 13.39 (2017), p. 1701804.

[7] Tadashi Kajiya, Daisaku Kaneko, and Masao Doi. "Dynamical Visualization of "Coffee Stain Phenomenon" in Droplets of Polymer Solution via Fluorescent Microscopy." In: *Langmuir* 24.21 (2008), pp. 12369–12374.

[8] V Garbin, D Cojoc, Enrico Ferrari, E Di Fabrizio, MLJ Overvelde, SM Van Der Meer, N De Jong, Detlef Lohse, and Michel Versluis. "Changes in microbubble dynamics near a boundary revealed by combined optical micromanipulation and high-speed imaging." In: *Applied physics letters* 90.11 (2007), p. 114103.

[9] Anna Hoang, Guillaume Berteloot, Pooria Sharif-Kashani, and H Pirouz Kavehpour. "Dynamic measurement of microfilms and nanofilms of fluids using fluorescence microscopy." In: *Experiments in fluids* 52.6 (2012), pp. 1657–1662.

[10] Kai Zhang, Aoqun Jian, Xuming Zhang, Yu Wang, Zhaohui Li, and Hwa-yaw Tam. “Laser-induced thermal bubbles for microfluidic applications.” In: *Lab Chip* 11 (7 2011), pp. 1389–1395.

[11] Pei-Yu Chiou, Ting-Hsiang Wu, Sung-Yong Park, and Yue Chen. “Pulse laser driven ultrafast micro and nanofluidics system.” In: *Biosensing III*. Ed. by Hooman Mohseni and Manijeh Razeghi. Vol. 7759. International Society for Optics and Photonics. SPIE, 2010, 77590Z.

[12] Md Mehedi Hasan, Mohammad Wajih Alam, Khan A Wahid, Sayem Miah, and Kiven Erique Lukong. “A low-cost digital microscope with real-time fluorescent imaging capability.” In: *PLoS One* 11.12 (2016), e0167863.

[13] Siew-Wan Ohl and Claus-Dieter Ohl. “Acoustic Cavitation in a Microchannel.” In: *Handbook of Ultrasonics and Sonochemistry*. Singapore: Springer Singapore, 2016, pp. 99–135. ISBN: 978-981-287-278-4.

[14] Pedro A. Quinto-Su, Kang Y. Lim, and Claus-Dieter Ohl. “Cavitation bubble dynamics in microfluidic gaps of variable height.” In: *Phys. Rev. E* 80 (4 Oct. 2009), p. 047301.

[15] Chao Sun, Edip Can, Rory Dijkink, Detlef Lohse, and Andrea Prosperetti. “Growth and collapse of a vapour bubble in a microtube: the role of thermal effects.” In: *Journal of Fluid Mechanics* 632 (2009), 5–16.

[16] Kaustubh R. Rau, Pedro A. Quinto-Su, Amy N. Hellman, and Vasan Venugopalan. “Pulsed Laser Microbeam-Induced Cell Lysis: Time-Resolved Imaging and Analysis of Hydrodynamic Effects.” In: *Biophysical Journal* 91.1 (2006), pp. 317–329. ISSN: 0006-3495.

[17] Ed Zwaan, Séverine Le Gac, Kinko Tsuji, and Claus-Dieter Ohl. “Controlled Cavitation in Microfluidic Systems.” In: *Phys. Rev. Lett.* 98 (25 June 2007), p. 254501.

[18] Rory Dijkink and Claus-Dieter Ohl. “Laser-induced cavitation based micropump.” In: *Lab Chip* 8 (10 2008), pp. 1676–1681.

[19] Anamaria Soare, Rory Dijkink, Marcos Rodriguez Pascual, Chao Sun, Peter W. Cains, Detlef Lohse, Andrzej I. Stankiewicz, and Herman J. M. Kramer. “Crystal Nucleation by Laser-Induced Cavitation.” In: *Crystal Growth & Design* 11.6 (2011), pp. 2311–2316.

[20] Pedro A. Quinto-Su, Madoka Suzuki, and Claus-Dieter Ohl. “Fast temperature measurement following single laser-induced cavitation inside a microfluidic gap.” In: *Scientific Reports* 4.1 (June 2014), p. 5445. ISSN: 2045-2322.

[21] Kyosuke Shinohara, Yasuhiko Sugii, Arata Aota, Akihide Hibara, Manabu Tokeshi, Takehiko Kitamori, and Koji Okamoto. "High-speed micro-PIV measurements of transient flow in microfluidic devices." In: *Measurement science and Technology* 15.10 (2004), p. 1965.

[22] Claus-Dieter Ohl, Manish Arora, Rory Dijkink, Vaibhav Janve, and Detlef Lohse. "Surface cleaning from laser-induced cavitation bubbles." In: *Applied Physics Letters* 89.7 (Aug. 2006), p. 074102. ISSN: 0003-6951.

[23] Jinwen Zhou, Dmitriy A Khodakov, Amanda V Ellis, and Nicolas H Voelcker. "Surface modification for PDMS-based microfluidic devices." In: *Electrophoresis* 33.1 (2012), pp. 89–104.

[24] Andreas Volk, Massimiliano Rossi, Christian J. Kähler, Sascha Hilgenfeldt, and Alvaro Marin. "Growth control of sessile microbubbles in PDMS devices." In: *Lab Chip* 15 (24 2015), pp. 4607–4613.

[25] Hao Chong, Jiongcheng Lou, Kath M. Bogie, Christian A. Zorman, and Steve J. A. Majerus. "Vascular Pressure–Flow Measurement Using CB-PDMS Flexible Strain Sensor." In: *IEEE Transactions on Biomedical Circuits and Systems* 13.6 (2019), pp. 1451–1461.

[26] Photron. *Photron FASTCAM Viewer Software*. https://photron.com/photron-support/. [Online; accessed 03-May-2024].

[27] Aswin Raghunathan. "Exploring laser-induced cavitation for primary nucleation control: An experimental study." MSc thesis. Delft University of Technology, 2022.

[28] Amy N. Hellman, Kaustubh R. Rau, Helen H. Yoon, Stephanie Bae, James F. Palmer, K. Scott Phillips, Nancy L. Allbritton, and Vasan Venugopalan. "Laser-Induced Mixing in Microfluidic Channels." In: *Analytical Chemistry* 79.12 (2007). PMID: 17508715, pp. 4484–4492.

[29] Pedro A. Quinto-Su, Hsuan-Hong Lai, Helen H. Yoon, Christopher E. Sims, Nancy L. Allbritton, and Vasan Venugopalan. "Examination of laser microbeam cell lysis in a PDMS microfluidic channel using time-resolved imaging." In: *Lab Chip* 8 (3 2008), pp. 408–414.

[30] Fatma Ibis, Tsun Wang Yu, Frederico Marques Penha, Debadrita Ganguly, Manzoor Alhaji Nuhu, Antoine E. D. M. van der Heijden, Herman J. M. Kramer, and Huseyin Burak Eral. "Nucleation kinetics of calcium oxalate monohydrate as a function of pH, magnesium, and osteopontin concentration quantified with droplet microfluidics." In: *Biomicrofluidics* 15.6 (2021), p. 064103.

[31] Sameer D. Shingte, Olav Altenburg, Peter J. T. Verheijen, Herman J. M. Kramer, and Huseyin Burak Eral. “Microfluidic Platform with Serpentine Geometry Providing Chaotic Mixing in Induction Time Experiments.” In: *Crystal Growth & Design* 22.7 (2022), pp. 4072–4085.

[32] Daniel Irimia, Jenkins Jose Shirley, Anshul S. Garg, Davey P.A. Nijland, Antoine E. D. M. van der Heijden, Herman J. M. Kramer, and Huseyin Burak Eral. “Influence of Laser Parameters and Experimental Conditions on Non-photochemical Laser-Induced Nucleation of Glycine Polymorphs.” In: *Crystal Growth & Design* 21.1 (2021), pp. 631–641.

3

KCL CRYSTALLIZATION USING A SINGLE BUBBLE

This chapter demonstrate that a cavitation bubble initiated by a Nd:YAG laser pulse below breakdown threshold induces crystallization from supersaturated aqueous solutions with supersaturation and laser-energy dependent nucleation kinetics. Combining high-speed video microscopy and simulations, it is argued that a competition between the dissipation of absorbed laser energy as latent and sensible heat dictates the solvent evaporation rate and creates a momentary supersaturation peak at the vapor-liquid interface. The number and morphology of crystals correlate to the characteristics of the simulated supersaturation peak.

This chapter is based on the article:
N. Nagalingam et al. "Laser-Induced Cavitation for Controlling Crystallization from Solution." In: *Phys. Rev. Lett.* 131 (12 Sept. 2023), p. 124001.

3.1 Introduction

Transient micro vapor bubbles can be created in liquid environments with the absorption of laser pulses by dyes [1] and nanoparticles [2, 3]. The impurity heating hypothesis suggests that laser energy absorbed by inherent insoluble impurities (such as nanoparticles) locally evaporates its surrounding solvent - consequently triggering solute nucleation. However, no direct measurements of this hypothesized phenomenon was reported. Most reported NPLIN experiments only quantify the crystallization probability seconds to minutes after laser irradiation [4]. Moreover, the large exposed volumes [$O(cm^3)$] and uncertainties in concentration and chemical nature of impurities limit the observation of micron-sized cavitation bubbles within microseconds after laser irradiation. Thus the attempts to test the impurity heating hypothesis using numerical modeling have had limited success due to lack of concomitant experimental data [5].

Using high-speed microscopy experiments and 1D finite element simulations, a momentary supersaturation rise surrounding a laser-induced cavitation bubble is demonstrated to trigger crystallization in supersaturated aqueous solutions of potassium chloride (KCl). A frequency-doubled Nd:YAG pulsed laser with 532 nm wavelength and 4 ns pulse duration is used. Unlike the traditional NPLIN experiments, the laser is focused to fix the location of bubble formation with the solution intentionally doped using a light-absorbing soluble impurity. 32.6 μg potassium permanganate ($KMnO_4$) per g of water, is added to facilitate bubble formation below the optical breakdown threshold via thermocavitation [6] (see Appendix B.1). The laser focal spot resembles an impurity being heated up and a consequent cavitation bubble formation, establishing the connection between NPLIN experiments conducted with unfocussed laser and this study. The added $KMnO_4$ is comparable to the impurities level in traditional NPLIN experiments [$O(10\,ppm)$] [7], and therefore does not alter the solubility of KCl (see Appendix B.2). Thus, this work differentiates itself from cavitation-induced crystallization experiments via multiphoton absorption using focused ultrashort laser pulse (~fs) that might involve photochemistry [8]. Moreover, it captures the size of cavitation bubbles [$O(100\,\mu m)$] [3] surrounding the nanoparticles for the inferred magnitude of laser energies and impurity sizes in NPLIN experiments [7] (see Appendix B.3 for calculations).

Experiments were performed to record the size of the vapor bubbles created, the resulting number and morphology of crystal(s) formed, and the cumulative nucleation probability at a fixed time lag. Subsequently, using simulations, the local temperature, solute concentration, and solute supersaturation surrounding the bubble are estimated to complement the experiments. The quantitative agreement between experimental and simulated bubble dynamics validates the proposed model. Leveraging the model, it is argued that a competition between the dissipation of absorbed laser energy as

latent and sensible heat dictates the instantaneous solvent evaporation rate. A spike in evaporation rate during the cavitation bubble expansion creates a momentary supersaturation peak at the vapor-liquid interface (hereinafter referred to as "interface"). The experimentally acquired nucleation probabilities, number, and morphology of crystals formed correlate with the characteristics of the short-lived [$O(\mu s)$] supersaturation peak surrounding the bubble from simulations. For the first time, this work quantitatively correlate the likelihood of crystal formation due to an increase in the solute concentration at the interface through laser-induced bubble formation with no expected photochemical reaction.

3.2 Materials and Methods

Solution preparation

Ultrapure water (18.2 MΩ cm, ELGA Purelab) was used to prepare the supersaturated KCl (P9541, Sigma-Aldrich) solutions in a 8 ml vial (SF8, BGB). 30 µl $KMnO_4$ (223468, Sigma-Aldrich) of 7.6592 mg per g of H_2O was added to 7 ml KCl solution to improve its light absorbance at 532 nm. After preparation, the solution was placed in the oven maintained at 338 K overnight for complete dissolution.

Sample preparation

The microfluidic device (microwell) side walls were fabricated using polydimethylsiloxane (PDMS, Sylgard™ 184, Dow) and a cover glass with a thickness of $0.13 - 0.16$ mm was attached to the bottom side. The device was hydrophobized with trichloro(1H,1H,2H,2H-perfluoroctyl)-silane to prevent PDMS from triggering heterogeneous nucleation. During the experiments, before transferring the solution to the microfluidic device, the solution was removed from the oven (maintained at 323 K) and stirred at 1000 rpm for 1 min using a magnetic stirrer over a hotplate maintained at 323 K. The solution was then transferred to the microwell using a micro-pipette while it was still warm to avoid spontaneous nucleation while handling. Immediately, silicone oil (378321, Sigma-Aldrich) was pipetted over the solution to avoid evaporation. The device once placed on the microscopic travel stage was allowed to cool down for approximately 7 min to let the solution reach room temperature (298 K). Prior to shooting the laser, the bottom of the microfluidic device was scanned thoroughly to ensure the absence of any crystals. The entire scanning took around 5 min.

Optics/laser parameters

For imaging, a red LED light ($\lambda_{LED} = 625$ nm) and an infinity-corrected 40x objective (LUCPLFLN40X, Olympus) with 0.6 numerical aperture (*NA*) and 4.5 mm focal length (f) were used. The resolution of the objective is $\lambda_{LED}/(2\,NA) = 0.52$ µm. A red LED was chosen since the dichroic filter (MD568, Thorlabs) used in the setup has a transmission band of $580 - 650$ nm, and in addition, the high-speed camera (FASTCAM NOVA S16, Photron) has its maximum spectral response at this particular wavelength. The resolution of the image was measured using a test target (R1L1S1N, Thorlabs), and was found to be 0.5076 µm/px (for the high-speed camera) and 0.2016 µm/px (for the low-speed camera).

Pulsed Nd:YAG laser (Nano L 50:50 PIV, Litron) with 532 nm wavelength (λ), 4 ns pulse duration (t_L) and 4 mm beam diameter (D_L) was used. The estimated laser spot size diameter, $2w_0 = 0.762$ µm, is calculated using the expression $4M^2\lambda f/(\pi D_L)$, where λ is the laser wavelength and the beam quality parameter $M^2 = 1$ (assuming a perfect Gaussian profile). The depth of field (DOF) of the focused laser beam is $2\pi w_0^2/(M^2\lambda) = 1.71$ µm.

CHAPTER 3

3.3 Results and Discussions

3.3.1 Experiments

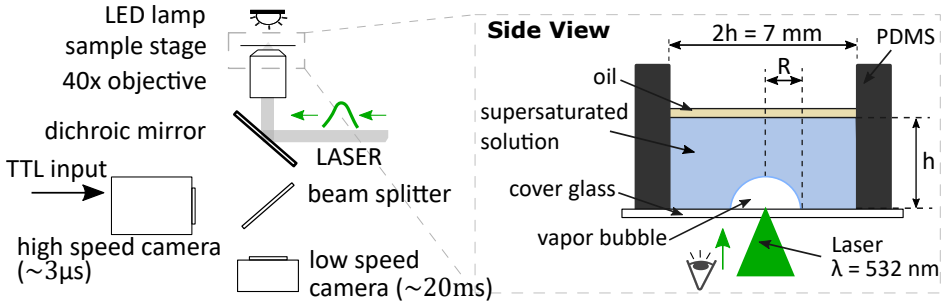

Figure 3.1: Sketch of the experimental setup to generate a microbubble. The green arrow indicates the direction of laser pulse.

In the experiments, KCl solutions with a supersaturation range of $0.999 - 1.029$ were used (solubility = 0.3597 g/g-H_2O at 298 K) with no pre-treatment for dissolved gases or filtration. A 40x objective (numerical aperture=0.6) is employed to both focus the laser and image the sample. Fig. 3.1 shows the architecture of the inverted microscope which employs two cameras: a high-speed camera operated at 330,000 frames per second (fps) to record the evolution of the bubble size and a low-speed camera op-

erated at 50 fps which records the appearance of crystals. A 1.23 mm layer of silicone oil (density = 930 kg/m^3) floating on top of the supersaturated solution prevents evaporation of the solution. The laser is focused to a point within 10 µm above the bottom surface (cover glass). The standoff distance to the bottom surface is maintained below 0.05 to prevent surface erosion [9]. In addition, all formed hemispherical bubbles in this work have, $h/R_{max} > 10$, to prevent the effect of side walls on the bubble dynamics [10]. Thus the cover glass acts as a plane of symmetry for the semi-unbounded fluid surrounding the hemispherical bubble, allowing one to analyze the bubble as spherically unbound - a 3D bubble. Since the negatively buoyant crystals sediment to the bottom, the adapted experimental technique allows in-situ recording of both the bubble and crystal(s).

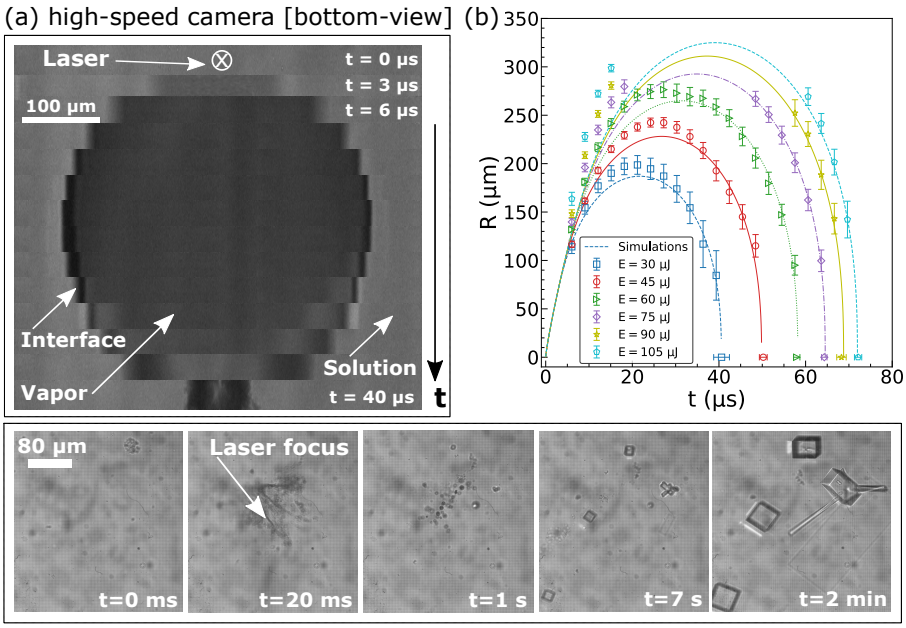

Figure 3.2: (a) Primary vapor bubble formation using a focused laser pulse of 30 µJ recorded at 330,000 fps with a reduced spatial resolution. (b) Dynamic radius of the hemispherical bubble for different laser energies E. The error bars represent the standard error on the mean of at least 20 independent trials. A bubble radius beyond $\approx$ 300 µm exceeded the field of view of the camera. The symbols and lines correspond to experiments and simulations, respectively. (c) Secondary bubbles and emergence of crystals after collapse of the primary vapor bubble surrounding the laser focal spot visualized at 50 fps using the low-speed camera. The experiment is for $E = 75$ µJ and $S_\infty = 1.019$.

Figure 3.2 (a) depicts the primary bubble formation, its subsequent expansion, and collapse immediately after laser irradiation. The primary bubble then disintegrates into secondary bubbles followed by the emergence of crystals surrounding the laser focal point (Fig. 3.2 (c)). After the primary bubble collapsed, a complex flow pattern that transports secondary bubbles and crystals was observed. The direction of the resulting flow was observed to be random, consistent with previous observations [11]. Figure 3.2 (b) displays a clear increase in the maximum radius (R_{max}) and bubble lifetime with the supplied laser energy (E). For details on the experimental validity of the bubble shape, see Appendix B.4.

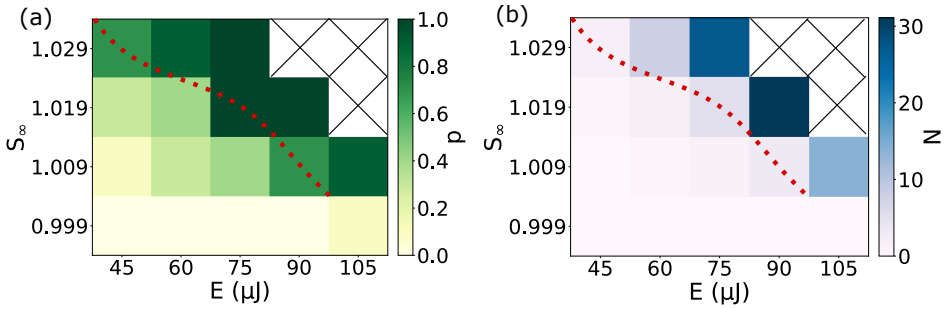

Figure 3.3: Experimentally observed nucleation statistics: (a) Cumulative nucleation probability (p) and (b) Mean crystal count (N), for different laser energies (E) and solution supersaturation in the bulk (S_∞). The results are for 10 trials, each with a fixed lag of 2 minutes from the time of laser irradiation. The red dotted curve is a guide to the eye representing the threshold where the crystallization probability is $\geqslant 0.5$. See Appendix B.5 for recorded morphologies.

Crystallization is quantified by plotting nucleation probability and crystal count for varying laser energy and supersaturation in the bulk, Fig. 3.3. The cumulative nucleation probability (p) is defined as the number of trials that resulted in crystal formation two minutes after laser irradiation to the number of trials performed. Overall, the nucleation probability increases with increasing laser energy and solution supersaturation in the bulk (S_∞). From Fig. 3.3 (a), a minimum threshold laser energy is observed for crystal formation related to S_∞ and vice versa, an observation repeatedly reported in NPLIN experiments [4]. A very low crystallization probability ($p \leqslant 0.1$) was recorded for roughly saturated solution ($S_\infty = 0.999$) as the lack of supersaturation would inhibit crystal growth. The non-zero p value is attribued to the uncertainty in S_∞ [$O(10^{-3})$] pertaining to the variation in room temperature ($297.8 - 299.1$ K). No experiment was performed beyond $S_\infty = 1.029$ as it was difficult to keep the solution stable during handling. In Fig. 3.3 (b), similar to the nucleation probability, an increase in the number of crystals formed (N) with both laser energy and bulk supersaturation above the minimum laser intensity threshold is recorded. Within these ex-

periments, cubic crystals were observed predominantly with the probability of finding a rectangle or needle-like crystal increasing with E and S_∞ (see Appendix B.5). This observed change in morphology aligns with previous observations [12, 13], deduced using limited solvent availability per nuclei. The local fluid properties surrounding the bubble in experiments, such as temperature and solute concentration, cannot be measured due to the small length and time scales involved. Therefore, numerical simulation is employed to calculate temporal and spatial values of these variables while the experimentally measured bubble radii and crystal count are used to validate the fluid flow and local supersaturation, respectively.

3.3.2 Numerical Simulations

The numerical simulations are solved for combined momentum, heat, and solute transport. For each phenomenon, the governing equations for an unbound 3D sphere are used due to the plane of symmetry offered by the cover glass. The Rayleigh-Plesset equation [14] is employed to solve for the momentum surrounding the bubble,

$$R\frac{d^2R}{dt^2}+\frac{3}{2}\left(\frac{dR}{dt}\right)^2=\frac{1}{\rho_L}\left(p_V-p_\infty-\frac{2\sigma_{gl}}{R}-\frac{4\mu_L}{R}\frac{dR}{dt}\right), \tag{3.1}$$

where $\rho_L = 1175\,\mathrm{kg/m^3}$ is the solution density, $p_\infty = 1.013\,\mathrm{bar}$ is the ambient pressure and p_V is the pressure within the bubble, σ_{gl} is the surface tension, μ_L is the dynamic viscosity of the solution and R the distance of the interface from the laser focal point. The spherically symmetric heat dissipation surrounding the bubble is modeled using,

$$\frac{\partial T}{\partial t}+\frac{R^2}{r^2}\frac{dR}{dt}\frac{\partial T}{\partial r}=\frac{1}{r^2}\frac{\partial}{\partial r}\left(r^2\alpha\frac{\partial T}{\partial r}\right), \tag{3.2}$$

in which T is the temperature, α is the thermal diffusivity of the solution and r ($> R$) the radial position from the bubble center. For solute transport, an analogous equation to Eq. 3.2 is used by substituting T with $\widehat{C}$, the solute concentration in g/g of the solution, and α with D, the mass diffusivity of the solute.

For simplicity, the bubble is assumed to be a lumped system with an energy balance given by

$$\frac{d(m_V c_{pV} T_V)}{dt}+\frac{dm_V}{dt}H_L=A_V k\left(\frac{\partial T}{\partial r}\right)_{r=R}, \tag{3.3}$$

where m_V, A_V, and c_{pV} are the mass, surface area, and specific heat capacity of the vapor bubble, respectively. H_L is the latent heat of vaporization and k the thermal conductivity of the solution. At the interface, the boundary condition $T_V = T|_{r=R}$ is

enforced at all times, where T_V is the bubble temperature. The change in mass of the bubble is estimated using the corrected Hertz-Knudsen equation [15], $dm_V/dt = -(16A_V/9\sqrt{2\pi R_g T})[p_V - p_{sat}(T|_{r=R})]$, where R_g is the specific gas constant for water vapor and $p_{sat}(T|_{r=R})$ the saturation pressure of the solution at the interface. The p_V is estimated using the ideal gas law, $p_V V_V = m_V R_g T_V$, where V_V is the bubble volume.

At $t = 0$ the bubble is assumed to be saturated with zero interface velocity, and the surrounding solute concentration is assumed to be same as in the bulk. System energy is imposed by initializing a thermal boundary layer profile surrounding the bubble. The initial temperature distribution is $T(\xi) = T_\infty + (T_V - T_\infty)\exp\left[-(\xi/\delta_T)^{25}\right]$, where T_∞ is the ambient temperature, δ_T is the thermal boundary layer thickness and $\xi = r - R$, is the radial distance from the interface. A high exponent of 25 is used to approximate a step function, while still being smooth enough to avoid numerical instabilities near $\xi \approx \delta_T$. The thermal energy supplied in the simulation is transformed into latent heat (vapor), sensible heat (vapor and liquid), and kinetic energy of the solution. Thus, the control parameter in simulation, δ_T, characterizes the energy available for a bubble to grow. The initial bubble temperature is chosen to be 650 K - the spinodal temperature [16], with the radius 0.5 μm calculated using theoretical laser spot dimensions. For details on the numerical model and parameter values solved, refer Appendix B.6.

Figure 3.2 (b) shows the numerically obtained bubble size for $\delta_T = 21$, 25.5, 29.5, 32.5, 34.5 and 36 μm, corresponding to the increasing laser energy values from experiments (see Appendix B.6 for calculations). The deviation between experiments and simulations in R for higher energies ($E \geqslant 90$ μJ) can be attributed to non-linear absorption [17, 18] with possible plasma formation. The plasma can initiate high pressures, leading to higher interface velocities [19]. The probability of bubble incidence with and without $KMnO_4$ in water was investigated for non-linear absorption, which supports the reasoning made for deviations in R (see Appendix B.1). Moreover, the increase in interface velocities will only enhance the solvent accumulation at the interface supporting the proposed hypothesis (see Appendix B.6).

To get insight into the crystal formation surrounding the bubble, the factors affecting the solute supersaturation is investigated using simulation. Figure 3.4 (a,b) shows the temporal evolution of the solute concentration and temperature at the dynamic interface for three different laser energies at fixed bulk supersaturation. Initially, the temperature drops abruptly, in conjunction with a steep rise in concentration due to high evaporation rates, $O(100\,kg/(m^2 s))$. Then, the decrease in temperature is more gradual, while the decrease in concentration is steep. The drop in temperature can be attributed to heat diffusion away from the interface and advection resulting from bubble dynamics. Similarly, for the solute, there is dilution occurring at the interface due to condensation of the vapor in addition to diffusion and advection. During the latter

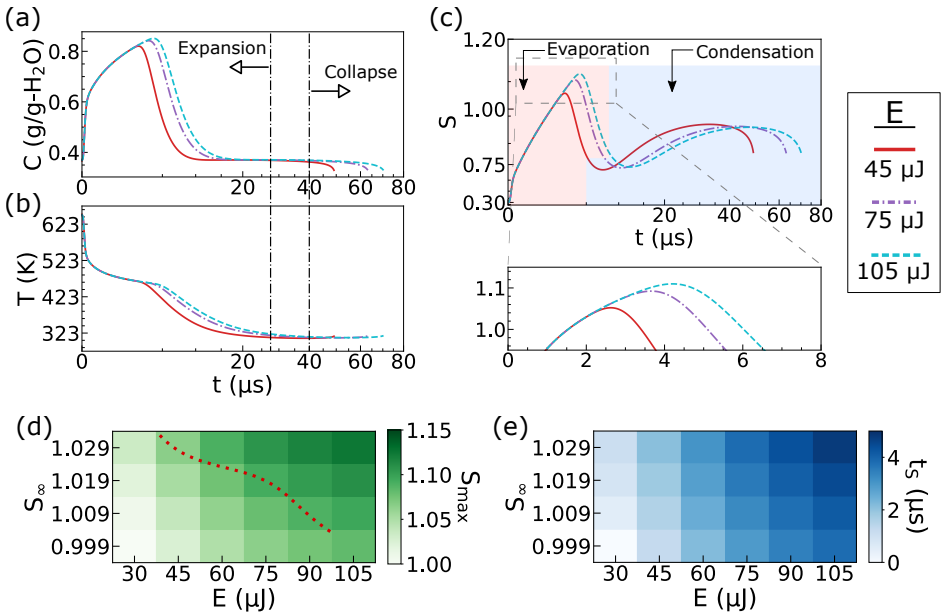

Figure 3.4: (a,b) Simulated temporal change in solute concentration (C) and temperature (T) at the interface for $S_\infty = 1.019$ (at 298 K). Since the laser pulse duration (4 ns) is negligible compared to the time scale of the phenomena (µs), the energy transfer from the laser (E) to the solution is considered to be instantaneous at $t = 0$ (x-axis is scaled quadratically). (c) The supersaturation ratio calculated using the concentration and temperature plotted in (a) and (b), respectively. The x-axis scale is quadratic, while the y-axis scale is cubic. t_S represents the time period for which $S > 1$. (d) The simulated maximum S values obtained for all the conditions in this work, similar to the examples from (c). The red dotted curve is the guide to the eye from Fig. 3.3, representing the crystallization probability $\geqslant 0.5$ in experiments. (e) The time period for which the simulated $S > 1$, similar to the examples from (c).

half of the bubble lifetime, the concentration and temperature have minimal change due to lower driving potentials and short time range, O(10 µs). The temperatures during bubble collapse estimated from the simulations are in good agreement with the empirical calculations from literature (see Appendix B.4).

Figure 3.4 (c) shows the temporal supersaturation at the interface calculated using profiles given in Fig. 3.4 (a,b). A peak in the local supersaturation ratio is observed when the bubble is rapidly expanding, after which the supersaturation decreases and the interface stays undersaturated ($S < 1$) within the bubble lifetime. This observation of a momentarily supersaturated state ($S > 1$), highlighted in the close-up in Fig. 3.4 (c), is a favorable condition for crystal nucleation. Moreover, both the peak supersaturation (S_{max}) and the time during which the interface remains supersaturated (t_S) increase with increasing E. In the above analysis, only the interface is investi-

gated since heat diffuses faster than the solute and thus the maximum supersaturation ratio can exist only in the region closest to the bubble, i.e., at the interface. The estimated supersaturated layer thickness increases with E and is O(10 nm), consistent with literature [5]. However, this supersaturation ratio at the interface is dynamic and is quantified only when the bubble exists. The induced flow and resulting temperature and solute distribution surrounding the laser focal point after the bubble collapses are complex and outside the scope of this work. The simulated trends observed in Fig. 3.4 (d,e) agree well with the presented experimental results in Fig. 3.3.

Subsequently, the simulated crystallization parameters, S_{max} and t_S, are correlated with the experimentally acquired parameter, N (Fig. 3.3 b). The nucleation rate (the number of nuclei formed per unit time per unit volume) can be expressed as [20],

$$J \propto S \exp\left[-16\pi\nu^2\sigma_{sl}^3/(3k_B^3T^3\log^2(S))\right]. \tag{3.4}$$

where σ_{sl} is the solute-solution interfacial tension, k_B is Boltzmann's constant and ν_0 the molecular volume, with $J \propto N/t_S$. Since the size of the bubbles for the time region where $S > 1$ are almost the same within the range of energies used, the shell volume surrounding the interface is ignored in the proportionality for J. Using the slope from Fig. 3.5 (a), σ_{sl} in Eq. (3.4) is estimated to be $3.7^{+0.47}_{-0.65}$ mJ/m^2 (at $\approx 458 - 464$ K). This value, when calculated for 298 K (3.51 mJ/m^2), is within the reported values of 2.19-5.283 mJ/m^2 for NPLIN [21–23] (see Appendix B.7 for calculation). Note that

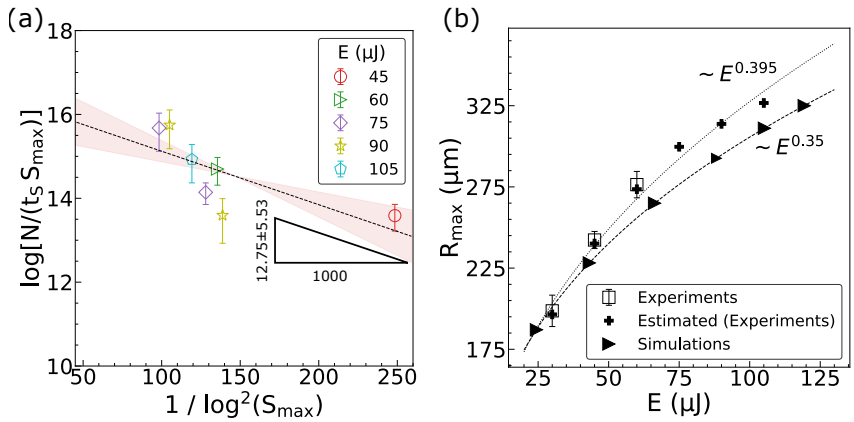

Figure 3.5: (a) Estimate of nucleation rate J against simulated peak supersaturation (S_{max}). $J \propto N/t_S$, where N is the mean crystal count from experiments and t_S is the time for which $S > 1$ in simulations. (b) Maximum vapor bubble radius plotted against the energy supplied. The dotted and dashed lines represent the power law fit for the data from experiments and simulations, respectively. Error bars represent the standard error on the mean.

the elevated temperature is also a favorable condition for crystal nucleation in addition to supersaturation (Eq. 3.4).

Figure 3.5 (b) is an equivalent representation of Fig. 3.2 (b), showing the dependence of maximum bubble size (R_{max}) for varying supplied energies. The estimate of the R_{max} in experiments was made using the bubble lifetime [24, 25] (see Appendix B.8). The closely matching trends between experiments and simulations support the reliability of the boundary conditions and assumptions employed in the simulation.

3.4 Conclusions

In summary, the primary nucleation in supersaturated aqueous KCl solution is demonstrated to be triggered by thermocavitation induced by a single Nd:YAG laser pulse below the optical breakdown threshold. The nucleation probability as well as the number and morphology of crystals formed depends on bulk supersaturation and laser energy used. Combining high-speed microscopy experiments and finite element simulations, a nucleation mechanism based on the solute accumulation at the interface due to solvent evaporation into the growing bubble is proposed. Simulations reveal a momentary spike in supersaturation with a lifetime [$O(\mu s)$] proportional to the bulk supersaturation and the supplied laser energy to facilitate nucleation.

The proposed mechanism is distinct from other speculated routes to crystal nucleation in laser-induced cavitation experiments, for example, due to photochemistry [26] and shock waves [27]. The intentional addition of $KMnO_4$ enabled bubble formation via thermocavitation avoiding photochemistry - that otherwise might exist due to plasma in cavitation via optical breakdown. Furthermore, the calculations reveal the lengthscale of a shockwave influencing crystallization [$O(10\,\mu m)$] matches the thermal boundary layer thickness surrounding the bubble (see Appendix B.8). Therefore, no formation of crystals is expected due to shockwaves because of the lower supersaturation ratio associated with higher temperatures. Thus, the proposed mechanism, verified by combining experiments and simulations, may shed light on the discussion of the working mechanism(s) behind NPLIN and sonocrystallization via cavitation [28, 29].

REFERENCES

[1] Ed Zwaan, Séverine Le Gac, Kinko Tsuji, and Claus-Dieter Ohl. "Controlled Cavitation in Microfluidic Systems." In: *Phys. Rev. Lett.* 98 (25 June 2007), p. 254501.

[2] Y. Arita, M. Antkowiak, V. Venugopalan, F. J. Gunn-Moore, and K. Dholakia. "Dynamics of primary and secondary microbubbles created by laser-induced breakdown of an optically trapped nanoparticle." In: *Phys. Rev. E* 85 (1 Jan. 2012), p. 016319.

[3] Linglong Wang, Yingchun Wu, Xuecheng Wu, and Kefa Cen. "Measurement of dynamics of laser-induced cavitation around nanoparticle with high-speed digital holographic microscopy." In: *Experimental Thermal and Fluid Science* 121 (2021), p. 110266. ISSN: 0894-1777.

[4] V. Korede and N. Nagalingam, Frederico Marques Penha, Noah van der Linden, Johan T. Padding, Remco Hartkamp, and Huseyin Burak Eral. "A Review of Laser-Induced Crystallization from Solution." In: *Crystal Growth & Design* 23.5 (2023), pp. 3873–3916.

[5] Niklas Hidman, Gaetano Sardina, Dario Maggiolo, Henrik Ström, and Srdjan Sasic. "Numerical Frameworks for Laser-Induced Cavitation: Is Interface Supersaturation a Plausible Primary Nucleation Mechanism?" In: *Crystal Growth & Design* 20.11 (2020), pp. 7276–7290.

[6] Jelle J. Schoppink, Jan Krizek, Christophe Moser, and David Fernandez Rivas. "Cavitation induced by pulsed and continuous-wave fiber lasers in confinement." In: *Experimental Thermal and Fluid Science* 146 (2023), p. 110926. ISSN: 0894-1777.

[7] Rohit Kacker, Sanjana Dhingra, Daniel Irimia, Murali Krishna Ghatkesar, Andrzej Stankiewicz, Herman J. M. Kramer, and Huseyin Burak Eral. "Multiparameter Investigation of Laser-Induced Nucleation of Supersaturated Aqueous KCl Solutions." In: *Crystal Growth & Design* 18.1 (2018), pp. 312–317.

[8] Teruki Sugiyama and Shun-Fa Wang. "Manipulation of nucleation and polymorphism by laser irradiation." In: *Journal of Photochemistry and Photobiology C: Photochemistry Reviews* 52 (2022), p. 100530. ISSN: 1389-5567.

[9] Fabian Reuter, Carsten Deiter, and Claus-Dieter Ohl. "Cavitation erosion by shockwave self-focusing of a single bubble." In: *Ultrasonics Sonochemistry* 90 (2022), p. 106131. ISSN: 1350-4177.

[10] Outi Supponen, Danail Obreschkow, Marc Tinguely, Philippe Kobel, Nicolas Dorsaz, and Mohamed Farhat. "Scaling laws for jets of single cavitation bubbles." In: *Journal of Fluid Mechanics* 802 (2016), 263–293.

[11] Pedro A. Quinto-Su, Kang Y. Lim, and Claus-Dieter Ohl. "Cavitation bubble dynamics in microfluidic gaps of variable height." In: *Phys. Rev. E* 80 (4 Oct. 2009), p. 047301.

[12] J. Kardum, Aleksandra Sander, and A Glasnoviae. "Batch Crystallization of KCl: the Influence of the Cooling and Mixing Rate on the Granulometric Properties of Obtained Crystals." In: *Chemical and Biochemical Engineering Quarterly* 19 (Mar. 2005).

[13] An-Chieh Cheng, Hiroshi Masuhara, and Teruki Sugiyama. "Evolving Crystal Morphology of Potassium Chloride Controlled by Optical Trapping." In: *The Journal of Physical Chemistry C* 124.12 (2020), pp. 6913–6921.

[14] M S Plesset and A Prosperetti. "Bubble Dynamics and Cavitation." In: *Annual Review of Fluid Mechanics* 9.1 (1977), pp. 145–185.

[15] Jonathan Barrett and Charles Clement. "Kinetic evaporation and condensation rates and their coefficients." In: *Journal of Colloid and Interface Science* 150.2 (1992), pp. 352–364. ISSN: 0021-9797.

[16] R. Thiéry and L. Mercury. "Explosivity Conditions of Aqueous Solutions." In: *Journal of Solution Chemistry* 38.7 (July 2009), pp. 893–905. ISSN: 1572-8927.

[17] J. Noack and A. Vogel. "Laser-induced plasma formation in water at nanosecond to femtosecond time scales: calculation of thresholds, absorption coefficients, and energy density." In: *IEEE Journal of Quantum Electronics* 35.8 (1999), pp. 1156–1167.

[18] Wenjun Sun, Zhongyang Liu, and Haijiao Zhou. "Study on Nonlinear Absorption Effect of Nanosecond Pulse Laser Irradiation for GaAs." In: *Journal of Nanoscience and Nanotechnology* 16.4 (2016), pp. 3895–3898. ISSN: 1533-4880.

[19] A. Vogel, S. Busch, and U. Parlitz. "Shock wave emission and cavitation bubble generation by picosecond and nanosecond optical breakdown in water." In: *The Journal of the Acoustical Society of America* 100.1 (1996), pp. 148–165.

[20] D. Kashchiev and G. M. van Rosmalen. "Review: Nucleation in solutions revisited." In: *Crystal Research and Technology* 38.7-8 (2003), pp. 555–574.

[21] Ke Fang, Stephen Arnold, and Bruce A. Garetz. "Nonphotochemical Laser-Induced Nucleation in Levitated Supersaturated Aqueous Potassium Chloride Microdroplets." In: *Crystal Growth & Design* 14.5 (2014), pp. 2685–2688.

[22] Andrew J. Alexander and Philip J. Camp. “Single Pulse, Single Crystal Laser-Induced Nucleation of Potassium Chloride.” In: *Crystal Growth & Design* 9.2 (2009), pp. 958–963.

[23] Martin R. Ward and Andrew J. Alexander. “Nonphotochemical Laser-Induced Nucleation of Potassium Halides: Effects of Wavelength and Temperature.” In: *Crystal Growth & Design* 12.9 (2012), pp. 4554–4561.

[24] Bing Han, Karsten Köhler, Kerstin Jungnickel, Robert Mettin, Werner Lauterborn, and Alfred Vogel. “Dynamics of laser-induced bubble pairs.” In: *Journal of Fluid Mechanics* 771 (2015), 706–742.

[25] Kaustubh R. Rau, Pedro A. Quinto-Su, Amy N. Hellman, and Vasan Venugopalan. “Pulsed Laser Microbeam-Induced Cell Lysis: Time-Resolved Imaging and Analysis of Hydrodynamic Effects.” In: *Biophysical Journal* 91.1 (2006), pp. 317–329. ISSN: 0006-3495.

[26] Tetsuo Okutsu, Kenji Furuta, Motoaki Terao, Hiroshi Hiratsuka, Akihito Yamano, Natalie Ferté, and Stéphane Veesler. “Light-Induced Nucleation of Metastable Hen Egg-White Lysozyme Solutions.” In: *Crystal Growth & Design* 5.4 (2005), pp. 1393–1398.

[27] B. Lindinger, R. Mettin, R. Chow, and W. Lauterborn. “Ice Crystallization Induced by Optical Breakdown.” In: *Phys. Rev. Lett.* 99 (4 July 2007), p. 045701.

[28] Judy Lee, Kyuichi Yasui, Muthupandian Ashokkumar, and Sandra E. Kentish. “Quantification of Cavitation Activity by Sonoluminescence To Study the Sonocrystallization Process under Different Ultrasound Parameters.” In: *Crystal Growth & Design* 18.9 (2018), pp. 5108–5115.

[29] Adrien Bussonnière, Qingxia Liu, and Peichun Amy Tsai. “Cavitation Nuclei Regeneration in a Water-Particle Suspension.” In: *Phys. Rev. Lett.* 124 (3 Jan. 2020), p. 034501.

4

GENERAL RELATIONS FOR CRYSTALLIZATION USING A SINGLE BUBBLE

The discussion on the underlying mechanism in presumed non-photochemical crystallization of supersaturated solutions upon laser irradiation remains unsettled in literature for over three decades. The dominant mechanism is identified to involve generation of microns-sized vapor bubbles due to interaction of the laser with solutions. Using high-speed microscopy and theory the evolution of a vapor bubble is quantified upon laser irradiation and analytical relations are proposed for the local supersaturation in the liquid around such bubbles. The crystallization is correlated to the enhanced solute accumulation above the saturation limit at the vapor-liquid interface due to solvent evaporation associated with the bubble growth. Aqueous solutions of KCl, NH_4Cl and NaCl are used to test the proposed model based on laser-induced bubble formation (cavitation). The model is then used to explain the literature observations for aqueous solutions of KBr and CH_4N_2O, including KCl and NH_4Cl. The findings will serve to *a priori* predict the non-photochemical laser-induced nucleation activity of a solution, based on the supplied laser energy as well as the physicochemical properties of the solute, solvent and impurities.

This chapter is based on the article:
N. Nagalingam et al. "General Framework for Non-photochemical Laser-Induced Crystallization via Cavitation." In: *(under preparation)* (2024).

4.1 Introduction

In the previous chapter, the pathway to crystal nucleation due to the laser-induced vapor bubble was attributed to the potential enhancement of solute at the vapor-liquid interface during the bubble lifetime. However, the parameter space for the reported phenomena based on interfacial solute accumulation was limited to aqueous KCl irradiated with 532 nm laser [1], and therefore lacks a comprehensive study necessary to engineer a continuous laser-induced crystallizer.

In this chapter, combining high- and low-speed microscopy and theory, general analytical relations are proposed for crystallization in the vicinity of a laser-induced vapor bubble due to solvent evaporation. The validity of the proposed analytical model is first tested against experiments using supersaturated aqueous solutions of NH_4Cl, KCl and NaCl, in which the vapor bubbles are formed intentionally using a focused laser. All these salts have an increasing solubility with temperature, however with different changes in saturation concentration with respect to changes in temperature. The experimentally recorded bubble size and crystallization probability are correlated to the supersaturation surrounding the bubble estimated using theory. The analytical model is then applied to the experiments performed in literature employing classical NPLIN technique using a single unfocussed laser pulse for aqueous solutions of KBr and CH_4N_2O, including KCl and NH_4Cl. The predictions using the model show good agreement with the experiments.

4.2 Materials and Methods

Solution preparation

Ultrapure water (18.2 MΩ cm, ELGA Purelab) was used to prepare the supersaturated solutions in a 8 ml vial (SF8, BGB). The solutes used in this work are as follows,

- NH_4Cl (213330, Sigma-Aldrich), with solubility 0.3879 g/100g-H_2O at 298 K
- KCl (P9541, Sigma-Aldrich), with solubility 0.3578 g/100g-H_2O at 298 K
- NaCl (S3014, Sigma-Aldrich), with solubility 0.3593 g/100g-H_2O at 298 K

After preparation, the solution was stirred at 1000 rpm over a hot plate maintained at 333 K for one hour to accelerate the dissolution. Then the solution was transferred to an oven maintained at 323 K overnight ($>$ 12 hours) for complete dissolution. During experiments the vials were placed over a hot plate maintained at 333 K and constantly stirred at 700 rpm. However, only for NaCl the solution was stirred at 350 rpm with a fan heater blowing air at 333 K over the vial. The NaCl solutions stirred at 700 rpm was unstable (crystallized) during transfer to the microwells.

Optical setup

For sample illumination a red LED light (625 nm) was used. An infinity corrected 20x objective (Plan Fluor, Nikon) with 0.5 numerical aperture was used for both laser focusing and imaging. The imaging was performed with resolution $\approx$ 1 µm/px for high-speed camera (FASTCAM NOVA S16, Photron) and $\approx$ 0.37 µm/px for low-speed camera (Imager Pro LX 16M, LaVision). The laser was pulsed Nd:YAG (Nano L 90-100 with TEM_{00}, LaVision) generating 1064 nm laser pulse with 6 ns pulse width. The diameter of the laser at the source and before objective were 4 mm and 9.3 mm, respectively.

4.3 Results and Discussions

4.3.1 Experiments

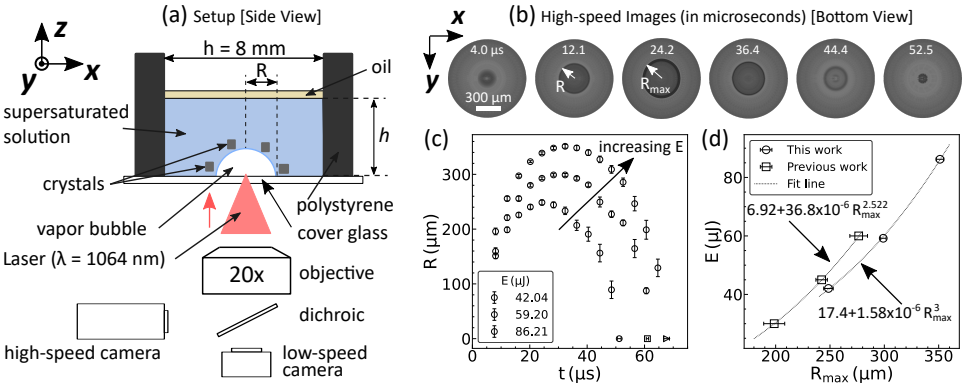

Figure 4.1: (a) The formation of a hemispherical vapor bubble with the sketch of the experimental setup and (b) the bubble evolution recorded using a high-speed camera at 247,500 frames per second. (c) Time evolution of bubble radius, R. (d) The laser energy supplied (E) and the corresponding maximum bubble radius (R_{max}) recorded. The previous work (previous chapter) corresponds to experiments with 532 nm laser using a 40x objective (numerical aperture = 0.65) [1]. The silicone oil (SigmaAldrich, 378321) floating on top prevents the evaporation of the solution. Oil thickness = 1.6 mm.

In the experiments, a 500 µL of supersaturated solution is loaded in a microwell (ThermoFisher, 155411PK) with a laser pulse (1064 nm, 6 ns) focused 20 µm above the bottom surface, see Figure 4.1 (a). A 20x objective with 0.5 numerical aperture is used to focus the laser and image the formed crystals. The non-linear absorption of laser due to high laser intensity (~GW/cm^2) at the focus creates a vapor bubble that expands and collapses over time [2]. The bubble is hemispherical due to the location

of inception, yet it behaves as a 3-D spherical bubble due to the symmetry offered by the bottom surface [3]. The boundaries of the liquid volume are sufficiently far ($h/(2R_{max}) > 10$) to not affect the bubble dynamics [4]. The dynamic bubble radius is denoted using R, see Figure 4.1 (b), with R_{max} as the maximum bubble radius. Figures 4.1 (c) and (d) display an increase in the bubble size with the supplied laser energy, E. The observed cubic power index of R_{max} in relation to E is in agreement with others [2, 5] and the previous chapter employing a 532 nm laser [1]. It is to be noted that for the range of supersaturation and laser energy discussed in this work, the bubble evolution was independent of the solutes used. For details on the experimental protocol, refer to Appendix C.1.

Figure 4.2 (a) illustrates the formation of secondary bubbles and crystals following the bubble collapse. The position and direction of the crystals are always random but the crystals are consistently surrounding the laser's focal spot. All the experiments performed are summarized in Figure 4.2 (b) and (c). An increase is seen in the crystallization probability and crystal count with E (or R_{max}) and supersaturation in the bulk, S_∞ (with respect to 298 K). The probability (p) is defined as the number of trials that crystallized within 2 minutes after the laser irradiation to the total number of trials. For the trials that didn't crystallize, the samples lasted at least an hour before they were discarded. The crystallization results suggest different reference values for S_∞ and a corresponding threshold (minimum) laser energy for significant crystallization ($p \geqslant 0.5$) to occur based on the solute. This observation is consistent with the reported values for classical NPLIN experiments where NH_4Cl [8] demands higher S_∞ and E compared to KCl [9, 10]. While NaCl is a new candidate to NPLIN, the values of the parameters are identified to be lower than for KCl. Thus, the observed order of S_∞ for crystallization is $NH_4Cl > KCl > NaCl$ for similar E. The solubility data in Fig. 4.2 (d) with C_{sat} as the saturation concentration provides a subtle hint on this observed order with NH_4Cl having the highest solubility slope and NaCl the least. However, further analysis is required to delineate the role of solubility in NPLIN. Furthermore, the illustrated probabilities for KCl in Fig. 4.2 (b) are in agreement for the same R_{max} and S_∞ in similar experiments reported in the previous chapter using a 532 nm laser pulse [1]. This suggests the crystallization phenomenon to be primarily governed by the bubble dynamics ($\propto R_{max}$) and solution supersaturation in the bulk (S_∞) with both dictating the mass, momentum, heat and solute transport in the vicinity of the bubble.

4.3.2 Theory

The creation of a supersaturation at the vapor-liquid interface (hereinafter referred to as "interface") can be analyzed using two parameters: (i) the temperature surround-

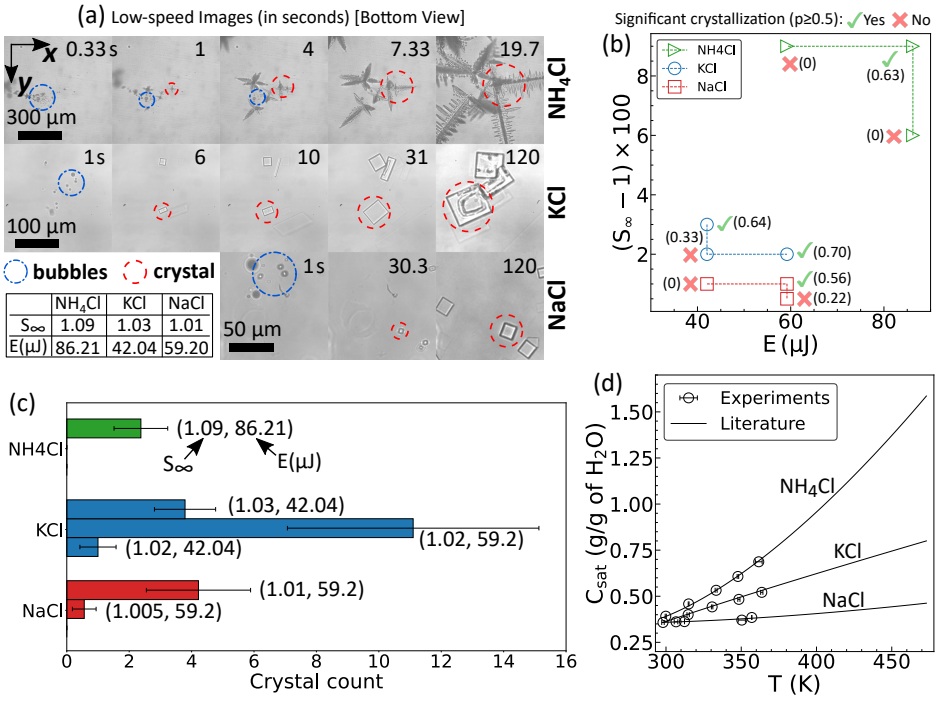

Figure 4.2: (a) Representative images of crystals recorded using the low-speed camera. The values of the solution supersaturation in the bulk (S_∞) and laser energy supplied (E) are tabulated for each solute. (b) Relative bulk supersaturation ($S_\infty - 1$) and laser energy dependent crystal nucleation probability. The values in the brackets adjoining the markers correspond to the probabilities (p). The tick and cross marks illustrate the $p \geqslant 0.5$ and $p < 0.5$, respectively. The crystallization was determined with a standard observation time of 2 minutes following the laser irradiation. The data points consist of 8 trails each. (c) The recorded crystal count corresponding to the experimental data shown in (b). The error bars represent the standard error on the mean. (d) Experimentally measured solubility data, where C_{sat} is the saturation concentration and T is the corresponding temperature. The solubility experiments were performed by measuring turbidity at different temperatures (Crystal16, Technobis Crystallization Systems), using 1.5 ml vials constantly stirred at 700 rotations per minute. The data from the literature is used since it covers a wide range of temperatures [6, 7].

ing the bubble, and (ii) the increase in solute concentration in the liquid surrounding the bubble due to the evaporation of solvent. The very high Péclet number [$\geqslant O(10^4)$] for heat and solute transfer surrounding the bubble suggests a convection dominated temperature and solute dissipation. The convection, inferred using the kinetic energy is a derivative of the bubble's potential energy - characterized using R^3_{max} [2, 5]. Thus, the rise in temperature of the liquid surrounding the bubble ΔT is correlated with R_{max} as the E concentrated (or absorbed) over the laser focus can depend on the solution absorption, laser wavelength and objective's numerical aperture [5]. The derivation

of analytical relation for ΔT using the Fourier law [11] is provided in Appendix C.2 with

$$\Delta T \approx \frac{\lambda_T p_\infty^{5/4}}{3\sqrt{0.915 k_L c_{pL} \rho_L^{3/2}}} \sqrt{R_{max}}. \tag{4.1}$$

k_L, c_{pL} and ρ_L are the thermal conductivity, specific heat capacity and density of the solution, respectively. p_∞ is the ambient pressure and λ_T is a proportionality constant. The temperature at the interface, therefore, can be estimated using $T = 298 + \Delta T$ K.

Analogously, the concentration C of solute in liquid surrounding the bubble is derived in Appendix C.2 with

$$\frac{C}{1+C} - \frac{\lambda_C C_\infty (1 - \Gamma C/M) p_V^\circ p_\infty^{1/4} \sqrt{R_{max}}}{3 R_g T \sqrt{0.915 D \rho_L^{5/2}}} = \frac{C_\infty}{1+C_\infty}. \tag{4.2}$$

C_∞ is the solute concentration in the bulk (in g/g-H_2O), λ_C is a proportionality constant, Γ is the relative molar vapor pressure lowering, M is the molar mass of solute, p_V° is the saturation pressure of pure water at temperature T, R_g is the specific gas constant, and D is the mass diffusivity of solute. The above relation (Eq. 4.2) is a quadratic equation in C and is solved using the quadratic formula [12]. The supersaturation at the interface, therefore, can be estimated as, $S = C/C_{sat}$. Thus, the above analysis provides an estimate of S at the interface as a function of R_{max} - a characteristic bubble parameter dependent on the supplied laser energy (E), and C_∞ - a parameter controlled during solution preparation.

While the experiments in this work involve the intentional formation of a vapor bubble using a focused laser, a quantitative estimate of the vapor bubble surrounding an impurity in classical NPLIN experiments is required for determining R_{max}. The relationship between the R_{max} and the insoluble iron (Fe_3O_4) nanoparticle is correlated using the empirical relation [13]

$$R_{max,R_p} \propto (Q_{abs} R_p^2 I_0)^{(1/3)}. \tag{4.3}$$

where I_0 is the laser intensity, R_p is the nanoparticle radius, and Q_{abs} is the absorption efficiency calculated using the Mie theory [14, 15]. The Mie theory employs R_p and complex refractive index of nanoparticle for the estimation of Q_{abs}. It is to be noted that complex refractive index is a function of laser wavelength [16]. From the classical NPLIN experiments in the literature, the R_p is determined using the Dynamic Light Scattering (DLS) data if provided, otherwise the R_p is matched to the filter pore size employed during solution preparation. In literature, a few of the experiments involve the intentional addition of impurities (extrinsic) for which the composition is known.

Table 4.1: Experimental Conditions for NPLIN from the literature, performed using a single laser pulse. Impurity origin: [a]intrinsic, [b]extrinsic. The I_0 in this table corresponds to the values at $p = 0.5$. The Q_{abs} of the nanoparticle (impurity) is calculated with a refractive index of 1.33 for the surrounding medium.

Solute	Impurity	R_p (nm)	Wavelength (nm)	Refractive index	Q_{abs}	S_∞	I_0 (MW/cm^2)
NH_4Cl [8]	Fe_3O_4[b]	350	1064	$2.1112 + i0.3698$ [17]	1.374	1.186	12
KCl [18]	Fe_3O_4[a]	225	532	$2.3456 + i0.0926$ [17]	0.983	1.054	13
KCl [18]	Fe_3O_4[a]	225	1064	$2.1112 + i0.3698$ [17]	1.173	1.054	8.5
CH_4N_2O [19]	Au[b]	60	532	$0.54386 + i2.2309$ [20]	2.034	1.57	100
KBr [10]	Fe_3O_4[a]	110	532	$2.3456 + i0.0926$ [17]	0.544	1.034	12
KBr [10]	Fe_3O_4[a]	110	1064	$2.1112 + i0.3698$ [17]	0.582	1.034	15

However, in the rest of the experiments, the nature of impurities is intrinsic and therefore their composition is deduced using the manufacturer's specification sheet of the solute. The chemical composition of the major impurity in the specification sheet is chosen for calculations. The source of the intrinsic impurities are attributed to solute instead of solvent since all the chosen experiments from the literature used ultrapure water (18.2 MΩcm). The nature of the intrinsic impurity can depend on the manufacturer, solute material and production process. Table 4.1 contains the parameter values required for the estimation of R_{max} surrounding an impurity, R_{max,R_p}.

The necessary condition for a crystal nucleus to form or grow is $S > 1$ [21]. With this supersaturation condition established, the number of nuclei formed per unit volume per unit time is determined using the nucleation rate as [22],

$$J = \Lambda S \exp\left[-16\pi v_0^2 \sigma_{sl}^3/(3k_B^3 T^3 \log^2(S))\right]. \tag{4.4}$$

Where v_0 is the molecular volume of solute, σ_{sl} is the interfacial tension, k_B is the Boltzmann's constant. $v_0 = M/(\rho_S N_A)$, in which M is the molar mass of solute, ρ_S is the crystal density and N_A the Avogadro constant. Λ is a pre-exponential kinetic parameter given by [21],

$$\Lambda = \left(\frac{4\pi}{3v_0}\right)^{1/3} \left(\frac{\sigma_{sl}}{k_B T}\right)^{1/2} D\left(\frac{C\rho_L N_A}{(1+C)M}\right) \tag{4.5}$$

for homogeneous nucleation. The above equation should be multiplied by 1000 if ρ_L is in kg/m^3.

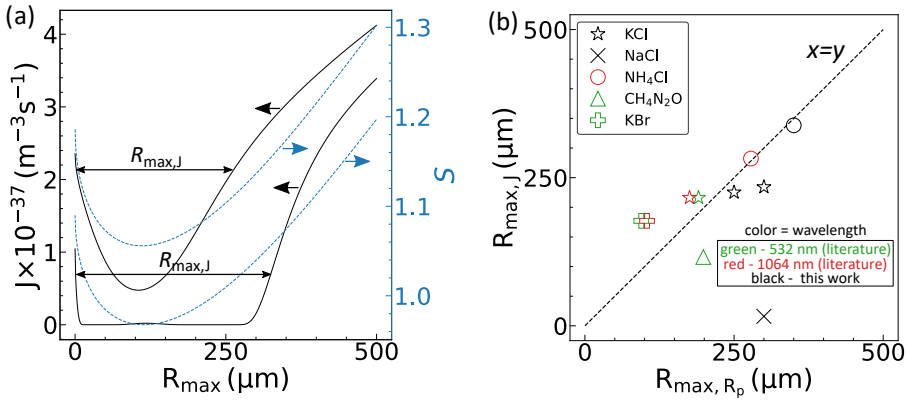

Figure 4.3: (a) The nucleation rate (J) calculated using Eq. 4.4 for NH_4Cl. $R_{max,J}$ is the R_{max} value at which the J increases above the initial value (at $R_{max} = 0$). The illustrations are for $S_\infty = 1.09$ and 1.186. $S = S_\infty$ at at $R_{max} = 0$. (b) The threshold bubble radius ($R_{max,J}$) estimated for different solutions in literature. The bubble size surrounding an impurity (R_{max,R_p}) is estimated using Eq. 4.3. The colors of the markers correspond to the laser wavelength used in literature as follows: green - 532 nm and red - 1064 nm. The black markers represent the experiments performed in this work. The marker shapes are assigned to the solutes as presented in the legend. The parameter values used for calculations are presented in Table 4.1 and Appendix C.3.

In Eq. 4.4, using the solution properties and analytically calculated S from Eqs. 4.1 and 4.2 the J can be calculated as a function of R_{max}. Figure 4.3 (a) shows the calculated J values for NH_4Cl with $S_\infty = 1.09$ and 1.186 for illustration. With laser irradiation, there exists a minimum (threshold) R_{max} only above which the J increases beyond the value before irradiation (at $R_{max} = 0$). This theoretically calculated R_{max} threshold is denoted as, $R_{max,J}$. The values above $R_{max,J}$ simply indicate the increased tendency of the solution to crystallize. This estimation agrees with the classical NPLIN experimental observations for all solutes from literature, where there exists a minimum necessary laser intensity I_0 ($\propto E$) to have significant crystallization with $p \geqslant 0.5$ [8, 10, 18, 19, 23, 24]. Thus, correspondingly there exists a minimum $R_{max} \propto E$. In addition, this threshold $R_{max,J}$ decreases with increasing S_∞ (see Fig. 4.3 (a)), similar to literature where crystallization probability increases with increasing S_∞ for a fixed laser energy [25].

Figure 4.3 (b) shows the estimations of the $R_{max,J}$ against the R_{max,R_p} for the experiments performed in this work and the classical NPLIN experiments from literature. The shape and color of the markers represent the solute and laser wavelength used, respectively. The values of the constant of proportionality $\lambda_T = 30$ and $\lambda_C = 3.9$ are determined based on the best fit of the data points to the $x = y$ line. The values

for the solution parameters necessary for calculating J using Eq. 4.4 are provided in Appendix C.3 with S_∞ taken from Table 4.1. It is to be noted that the tabulated S_∞ and the corresponding I_0 values in Table 4.1 were chosen for crystallization probabilities $p \approx 0.5$ from classical NPLIN experiments performed using a single laser pulse in literature. $p \approx 0.5$ is established as the minimum necessary condition for significant crystallization to occur, as in Fig. 4.2 (b). For the experiments performed in the work R_{max,R_p} is substituted with R_{max} and the S_∞ is taken for $0.5 < p < 0.7$, see Fig. 4.2 (b). Thus, from Fig. 4.3 (b) a good agreement is seen between the determined $R_{max,J}$ and R_{max,R_p} estimated using the control parameters S_∞ and I_0 (or E), respectively, with the exception of NaCl. While $R_{max,J}$ and R_{max,R_p} provide quantitative insight into the proposed underlying mechanism in classical NPLIN experiments, S_∞ and I_0 (or E) are the measurable parameter in experiments necessary to quantify crystallization using probability and crystal count [25].

The following are the discussions derived from the Fig. 4.3. It is to be noted that the term threshold in this work is defined at $p = 0.5$, while in literature the terminology might be used to refer p slightly greater than zero.

1. Threshold laser energy for crystallization

The theoretical analysis made using laser-induced cavitation quantitatively predicts the observed threshold laser energy for crystallization for the experiments performed in this work and from the literature. For a given solute, the threshold energy is a function of supersaturation, laser wavelength, and impurity parameters such as size and chemical composition.

2. Does all solutions undergo NPLIN?

In principle all solutions should undergo NPLIN provided the minimum (threshold) required laser energy is supplied. Thus the reported absence of NPLIN for aqueous CH_3CONH_2 [8] and $NaClO_3$ [26] could be due to the insufficient energy supplied corresponding to the employed supersaturation.

3. Crystallization dependence on wavelength

The $R_{max,J}$ (minimum bubble size) necessary to crystallize a given solution with fixed supersaturation can be generated using lower laser energy for impurities with higher Q_{abs}. Kacker et al. [18] in their experiments using KCl reported the energy threshold to vary based on the laser wavelength for a given supersaturation. The reported energy threshold was the least for 355 nm followed by 1064 nm and 532 nm. This order of wavelength corresponds to the calculated Q_{abs} for $R_p < 200$ µm presented in Fig. 4.4 for Fe_3O_4 nanoparticle - major impurity determined from the manufacturer specification sheet for KCl employed in their work (P9541, SigmaAldrich).

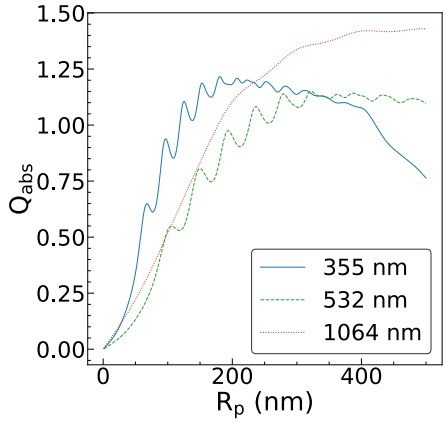

Figure 4.4: Absorption efficiency for different wavelengths calculated using the Mie theory for Fe_3O_4 nanoparticle (impurity). R_p is the radius of the nanoparticle. The Q_{abs} of the nanoparticle (impurity) is calculated with a refractive index of 1.33 for the surrounding medium.

This range of R_p is in agreement with the filter pore radius of 225 nm employed in their work and thus further validates the proposed model.

In the experiments by Ward et al. [10] for KCl, the 532 nm laser was reported to exhibit an almost similar laser energy threshold when compared to 1064 nm. This contradicts the observations by Kacker et al. [18]. The contradiction arises due the difference in impurity radius, estimated to be 110 nm in the work of Ward et al. and 225 nm for Kacker et al. From Fig. 4.4, it can been that Q_{abs} below 150 μm is almost same for 532 nm and 1064 nm, consistent with the observations by Ward et al.

4. Crystal count dependence on S_∞ and I_0 (or E)

The theoretically calculated increase in J value above a threshold R_{max} ($R_{max,J}$) with laser energy (E or I_0) is consistent with the experimentally observed increase in the number of crystals or crystallization probability with laser energy. Since this $R_{max,J}$ decreases with increasing S_∞, the number of crystals formed can be increased by increasing S_∞ for a fixed E (or I_0).

4.4 Conclusions

In summary, the proposed analytical model quantitatively relates the experimental observed crystallization probabilities and crystal counts to the local supersaturation S in the liquid immediately surrounding the bubble. The experiments were performed by intentionally forming a vapor bubble by focusing the laser over the desired location. With supersaturation in the bulk S_∞ and supplied laser energy E (or I_0) as control pa-

rameters in experiments, the model successfully correlates the theoretical minimum (threshold) required bubble size $R_{max,J}$ to the measured bubble size in experiments that resulted in crystallization probability of ≈ 0.5. Furthermore, for the experiments performed in literature employing classical NPLIN technique using an unfocused laser, the estimated bubble size surrounding an impurity R_{max,R_p} is in agreement with $R_{max,J}$.

While the effect of laser energy, laser wavelength, solution supersaturation in the bulk and physicochemical properties of impurities on crystallization probability and crystal count are already discussed, the reported polymorph selectivity under laser [27–30] needs further analysis. Potentially, different polymorphs could be a result of a different local supersaturation generated at the interface. However, this is a mere speculation and lacks concomitant study. While the crystallization probabilities for metal halides were reported to be invariant to the solution aging [9], the experiments performed with aqueous $C_2H_5NO_2$ exhibited zero crystallization probabilities without aging [31, 32]. This suggests the inability of the intrinsic impurities within the solutions of $C_2H_5NO_2$ - a small organic solute, to absorb the laser energy necessary to form a vapor bubble of significant size. However, upon aging, the detected emergence of nanoclusters [31] could agglomerate the impurities together with the solute and solvent, thereby increasing the laser energy absorbed.

Thus this work establishes a mechanistic understanding of NPLIN of salts from solutions, necessary to settle the discussions on the dominant underlying mechanism in NPLIN in literature.

REFERENCES

[1] Nagaraj Nagalingam, Aswin Raghunathan, Vikram Korede, Christian Poelma, Carlas S. Smith, Remco Hartkamp, Johan T. Padding, and Hüseyin Burak Eral. "Laser-Induced Cavitation for Controlling Crystallization from Solution." In: *Phys. Rev. Lett.* 131 (12 Sept. 2023), p. 124001.

[2] Werner Lauterborn and Alfred Vogel. "Shock Wave Emission by Laser Generated Bubbles." In: *Bubble Dynamics and Shock Waves*. Ed. by Can F. Delale. Berlin, Heidelberg: Springer Berlin Heidelberg, 2013, pp. 67–103. ISBN: 978-3-642-34297-4.

[3] Pedro A. Quinto-Su, Kang Y. Lim, and Claus-Dieter Ohl. "Cavitation bubble dynamics in microfluidic gaps of variable height." In: *Phys. Rev. E* 80 (4 Oct. 2009), p. 047301.

[4] Outi Supponen, Danail Obreschkow, Marc Tinguely, Philippe Kobel, Nicolas Dorsaz, and Mohamed Farhat. "Scaling laws for jets of single cavitation bubbles." In: *Journal of Fluid Mechanics* 802 (2016), 263–293.

[5] Vasan Venugopalan, Arnold Guerra, Kester Nahen, and Alfred Vogel. "Role of Laser-Induced Plasma Formation in Pulsed Cellular Microsurgery and Micromanipulation." In: *Phys. Rev. Lett.* 88 (7 Feb. 2002), p. 078103.

[6] James R Wood. "Thermodynamics of brine-salt equilibria — II. The system NaCl-KCl-H2O from 0 to 200°C." In: *Geochimica et Cosmochimica Acta* 40.10 (1976), pp. 1211–1220. ISSN: 0016-7037.

[7] Huang Lin and Vishal Lagad. "Evaluating Ammonium Chloride Corrosion Potential with Water Partial Pressure." In: vol. All Days. NACE CORROSION. Mar. 2017, NACE–2017–8960.

[8] Martin R. Ward, Alasdair M. Mackenzie, and Andrew J. Alexander. "Role of Impurity Nanoparticles in Laser-Induced Nucleation of Ammonium Chloride." In: *Crystal Growth & Design* 16.12 (2016), pp. 6790–6796. ISSN: 15287505.

[9] Andrew J. Alexander and Philip J. Camp. "Single Pulse, Single Crystal Laser-Induced Nucleation of Potassium Chloride." In: *Crystal Growth & Design* 9.2 (2009), pp. 958–963.

[10] Martin R. Ward and Andrew J. Alexander. "Nonphotochemical Laser-Induced Nucleation of Potassium Halides: Effects of Wavelength and Temperature." In: *Crystal Growth & Design* 12.9 (2012), pp. 4554–4561.

[11] Matevž Dular and Olivier Coutier-Delgosha. “Thermodynamic effects during growth and collapse of a single cavitation bubble.” In: *Journal of Fluid Mechanics* 736 (2013), 44–66.

[12] Po-Shen Loh. *A simple proof of the quadratic formula*. 2019. arXiv: 1910.06709.

[13] Linglong Wang, Yingchun Wu, Xuecheng Wu, and Kefa Cen. “Measurement of dynamics of laser-induced cavitation around nanoparticle with high-speed digital holographic microscopy.” In: *Experimental Thermal and Fluid Science* 121 (2021), p. 110266. ISSN: 0894-1777.

[14] Christian Matzler. “MATLAB functions for Mie scattering and absorption.” In: *IAP Res Rep* 8 (July 2002).

[15] Andrea Baldi. *Mie Scattering and Absorption Sphere*. https://github.com/andrea-baldi/Mie_Scattering_and_Absorption_Sphere. 2022.

[16] Mikhail N. Polyanskiy. “Refractiveindex.info database of optical constants.” In: *Scientific Data* 11.1 (Jan. 2024), p. 94. ISSN: 2052-4463.

[17] Marvin R Querry. *Optical constants*. Tech. rep. Missouri Univ-Kansas City, 1985.

[18] Rohit Kacker, Sanjana Dhingra, Daniel Irimia, Murali Krishna Ghatkesar, Andrzej Stankiewicz, Herman J. M. Kramer, and Huseyin Burak Eral. “Multiparameter Investigation of Laser-Induced Nucleation of Supersaturated Aqueous KCl Solutions.” In: *Crystal Growth & Design* 18.1 (2018), pp. 312–317.

[19] Pingping Cui, Vikram Korede, Pepijn van Tooren, Nagaraj Nagalingam, Runze Wang, Qiuxiang Yin, Antoine E.D.M. van der Heijden, Herman J.M. Kramer, and Huseyin Burak Eral. “Influence of Nanoparticle Properties on Non-Photochemical Laser-Induced Nucleation.” In: *(to be submitted)* (2024).

[20] P. B. Johnson and R. W. Christy. “Optical Constants of the Noble Metals.” In: *Phys. Rev. B* 6 (12 Dec. 1972), pp. 4370–4379.

[21] D. Kashchiev and G. M. van Rosmalen. “Review: Nucleation in solutions revisited.” In: *Crystal Research and Technology* 38.7-8 (2003), pp. 555–574.

[22] J. W. Mullin. *Crystallization*. Oxford: Butterworth-Heinemann, 2001.

[23] Daniel Irimia, Jenkins Jose Shirley, Anshul S. Garg, Davey P.A. Nijland, Antoine E. D. M. van der Heijden, Herman J. M. Kramer, and Huseyin Burak Eral. “Influence of Laser Parameters and Experimental Conditions on Non-photochemical Laser-Induced Nucleation of Glycine Polymorphs.” In: *Crystal Growth & Design* 21.1 (2021), pp. 631–641.

[24] Mélody Briard, Clément Brandel, Sandrine Morin-Grognet, Gérard Coquerel, and Valérie Dupray. “Potassium Sulfate: A New Candidate to Explore Non-Photochemical Laser-Induced Nucleation Mechanisms.” In: *Crystals* 11.12 (2021). ISSN: 2073-4352.

[25] V. Korede and N. Nagalingam, Frederico Marques Penha, Noah van der Linden, Johan T. Padding, Remco Hartkamp, and Huseyin Burak Eral. “A Review of Laser-Induced Crystallization from Solution.” In: *Crystal Growth & Design* 23.5 (2023), pp. 3873–3916.

[26] Eleanor Rose Barber. “Non-photochemical laser-induced nucleation (NPLIN): an experimental investigation via real-time imaging and product analysis.” PhD thesis. 2022.

[27] Xiaoying Sun and Bruce A Garetz. “Supersaturation and Polarization Dependence of Polymorph Control in the Nonphotochemical Laser-Induced Nucleation (NPLIN) of Aqueous Glycine Solutions, volume = 6, year = 2006.” In: *Crystal Growth & Design* 3 (), pp. 684–689.

[28] Xiaoying Sun, Bruce A. Garetz, and Allan S. Myerson. “Polarization switching of crystal structure in the nonphotochemical laser-induced nucleation of supersaturated aqueous L-histidine.” In: *Crystal Growth & Design* 8.5 (2008), pp. 1720–1722. ISSN: 15287483.

[29] Aziza Ikni, Bertrand Clair, Philippe Scouflaire, Stéphane Veesler, Jean Michel Gillet, Nouha El Hassan, Françoise Dumas, and Anne Spasojević-De Biré. “Experimental demonstration of the carbamazepine crystallization from non-photochemical laser-induced nucleation in acetonitrile and methanol.” In: *Crystal Growth & Design* 14.7 (2014), pp. 3286–3299. ISSN: 15287505.

[30] Wenjing Li, Aziza Ikni, Philippe Scouflaire, Xiaoxuan Shi, Nouha El Hassan, Pascale Gémeiner, Jean Michel Gillet, and Anne Spasojević-De Biré. “Non-Photochemical Laser-Induced Nucleation of Sulfathiazole in a Water/Ethanol Mixture.” In: *Crystal Growth & Design* 16.5 (2016), pp. 2514–2526. ISSN: 15287505.

[31] Tianyi Hua, Celymar Valentín-Valentín, Omar Gowayed, Seongha Lee, Bruce A. Garetz, and Ryan L. Hartman. “Microfluidic Laser-Induced Nucleation of Supersaturated Aqueous Glycine Solutions.” In: *Crystal Growth & Design* 20.10 (2020), pp. 6502–6509.

[32] Julien Zaccaro, Jelena Matic, Allan S. Myerson, and Bruce A. Garetz. “Non-photochemical, Laser-Induced Nucleation of Supersaturated Aqueous Glycine Produces Unexpected gamma-Polymorph.” In: *Crystal Growth & Design* 1.1 (2001), pp. 5–8.

5

SINGLE BUBBLE DYNAMICS WITHIN QUASI-1D MICROCHANNELS

Oscillatory flow in confined spaces is central to understanding physiological flows and rational design of synthetic periodic-actuation based micromachines. Using theory and experiments on oscillating flows generated through a laser-induced cavitation bubble, this chapter associates the dynamic bubble size (fluid velocity) and bubble lifetime to the laser energy supplied - a control parameter in experiments. Employing different channel cross-section shapes, sizes and lengths, the characteristic scales for velocity, time and energy is demonstrated to depend solely on the channel geometry. Contrary to the generally assumed absence of instability in low Reynolds number flows (< 1000), a momentary flow distortion is reported to originate due to the boundary layer separation near channel walls during flow deceleration. The emergence of distorted laminar states is characterized using two stages. First the conditions for the onset of instabilities is analyzed using the Reynolds number and Womersley number for oscillating flows. Second the growth and the ability of an instability to prevail is analyzed using the convective time scale of the flow. The findings inform rational design of microsystems leveraging pulsatile flows via cavitation-powered microactuation.

This chapter is based on the article:
N. Nagalingam et al. "Unified framework for laser-induced transient bubble dynamics within microchannels." In: *Scientific Reports* 14.1 (Aug. 2024), p. 18763.

5.1 Introduction

Micromachines with few mechanical components have revolutionized the areas of microelectromechanical systems (MEMS) [1–3]. The potential of bubble-powered micromachines was first realized in ink-jet printing [4], later also finding other applications that require precise flow control and rapid actuation [5–7]. Oscillatory flows are not limited to synthetic devices, but also invariably exist in nature, e.g., in cardiovascular and respiratory flows [8]. Yet characterization and optimization of pulsated oscillatory flow is underexplored compared to steady flows [2]. Therefore, a unified understanding will inform both synthetic and physiological systems, encompassing particle manipulation [9, 10], rheology [11, 12], emulsification [13], cell lysis [14, 15], prilling [16], needleless injection [17, 18] and gas embolotherapy [19].

Laser-induced cavitation allows localization of high temperature and large flow velocities due to the growth and collapse of short-lived vapor bubbles. Thus, laser light can be implemented to induce flow in processes with only need for optical access [20]. For confined geometries, the arrested directions of flow and increase in bubble lifetime due to strong confinement-induced momentum dissipation allows for a simplified theoretical and experimental approach [21, 22]. Yuan et al. [23] laid the theoretical foundation for the dynamics of a vapor bubble in a narrow channel with a circular cross-section. They reported the internal vapor pressure of the bubble to be insignificant after the initial 10 % of the bubble's lifetime. Thus, the dynamics of the bubble is largely governed by the wall resistance of the microchannel, ambient pressure, and inertia of the liquid shortly after bubble formation. Using experiments and a numerical model, Sun et al. [22] showed the role of absorbed laser energy in bubble evolution within circular microchannels with internal diameters of 25 and 50 μm.

The key to rational control of thermocavitation driven flows hinges on understanding the dynamics of the transient bubble, the bubble lifetime, and its dependence on the laser energy supplied. The findings could potentially be applied to any microsystem that employs a periodic actuation source to transfer momentum to the fluid much faster than the timescale of flow oscillation. Given application-specific requirements, e.g., flow rates, droplet production rate and mixing [24], valve actuation time [25], etc., there is a need for a unified framework with which one could *a priori* design the channel geometry (cross-section shape, size and length), provided that the fluid properties such as viscosity, density and light absorbance are known. Beyond the design of *lab-on-a-chip* devices, characterizing the flow and instabilities will help in the study and engineering of physiological systems, such as flows in arteries and bronchioles, by additionally incorporating the effects of channel wall compliance [26]. Furthermore, the fundamental understanding developed can be utilized in laser-induced crystallization via thermocavitation [27–29], as the bubble dynamics will dictate hydrodynamic flows around nucleated crystals.

Combining high-speed microscopy and an analytical approach, this chapter demonstrates a universal dependence of the magnitude and duration of the induced flow on the laser energy supplied in microchannels with circular, square, and rectangular cross-sections. Prior works discussed undistorted laminar flows [22, 30–32], which is a convenient assumption for low Reynolds numbers ($Re < 1000$) [33]. Nevertheless, the occurrence of a transient flow instability is observed even at $Re < 1000$, and is delineated by characterizing two dimensionless numbers: (i) the Reynolds number (Re), contingent on the peak mean flow velocity and channel hydraulic diameter, and (ii) the Womersley number (Wo), contingent on the bubble lifetime and channel hydraulic diameter. This momentary instability emerges due to the oscillatory nature of the flow [34, 35], and results in momentary unsteady velocity profiles due to the disruption of the momentum boundary layer near the channel walls [36].

This chapter first details the experiments for quantifying the dynamic bubble size and lifetime as the function of its maximum bubble size. Then the associated theoretical framework is presented to explain underlying physics. Following which, a general empirical correlation between maximum bubble size and laser energy supplied, and the minimum threshold laser energy for bubble formation is discussed. Finally, using the established theoretical framework and experiments, the flow transition limits and nature of the distorted laminar flow are characterized.

5.2 Materials and Methods

Laser setup

Frequency-doubled Nd:YAG pulsed laser with 532 nm wavelength, 4 mm beam diameter and 4 ns pulse duration. A $20\times$ objective (numerical aperture = 0.5) is used to focus the laser within the microchannel and simultaneously used for imaging [37]. The images are recorded at 112,500 frames per second using a high-speed camera.

Working fluid

An aqueous solution of red dye (RD81, Sigma-Aldrich) with 0.5 wt % is used to have higher absorbance to light at 532 nm. The absorption coefficient (β) was measured to be 173 cm^{-1} using a spectrometer (DR6000, Hach). The liquid was not pretreated for dissolved gases.

Channel geometry

The hydraulic diameter (d) of the channels range from 66.7 μm to 300 μm, with the maximum bubble half-size, $X_{max} \in [d/2, 2\,d]$ (see Fig. 5.1). Two different capillary

lengths, L = 25 and 50 mm, were used for all cases with the laser always focused at the geometric center. The channel specifications used in this chapter are summarized in Table 5.1.

Table 5.1: Microchannel specifications used in this work. Material: Borosilicate; Tolerance +/- 10%; Manufacturer: CM Scientific.

Cross-section	hydraulic diameter (μm)	Inner diameter (μm)	Wall thickness (μm)
Circular	100	100	35
Circular	200	200	65
Circular	300	300	50
Square	100	100	50
Square	200	200	100
Square	300	300	150
Rectangle	66.7	50×100	50
Rectangle	126	80×300	56

5.3 Results and Discussions

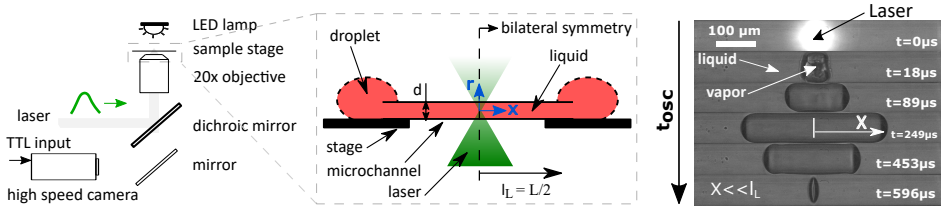

Figure 5.1: A sketch of the experimental setup with representative images of bubble dynamics from inception to collapse - one oscillation cycle. X represents the bubble size and t_{osc} is the bubble lifetime.

Dynamic bubble size

Since the midpoint of the capillary and the bubble coincides, in the theoretical model only half the geometric domain is analyzed owing to the bilateral symmetry, see Fig. 5.1. Thus, the length of the liquid column under analysis (l_L) is half the total length of the channel used, and the half-size of the bubble (X) is determined by the position of the vapor-liquid interface from the center as illustrated in Fig. 5.1. In the

post-processing of the images the parameter X was estimated by dividing the bubble volume with the area of the channel cross-section (see Appendix D.1). This approach of determining X rules out the effects of bubble end curvatures, furthermore allowing one to estimate the liquid velocities as a function of rate of volume displaced. The liquid droplets at either end of the channel act as reservoirs, thus compensating for the liquid displaced by the vapor bubble. In addition, these droplets also ensure that the evaporation of the liquid to the ambient surrounding doesn't deplete the liquid within the channel.

After attaining the capillary diameter (d), the vapor bubble elongates along the axial (along x) direction with the cross-section as that of the channel. Thus, for an elongated bubble, when $X \ll l_L$, the equation of motion of the liquid column within the channel is [22]

$$l_L \rho_L \frac{d^2X}{dt^2} = p_V(t) - p_\infty - \mathfrak{R}\,\frac{dX}{dt}, \tag{5.1}$$

where ρ_L is the liquid density, $p_V(t)$ is the pressure inside bubble, p_∞ is the ambient pressure and $\mathfrak{R}$ the hydraulic resistance of the channel. Due to strong confinement in two directions, the resulting flow is quasi-1D along the longitudinal axis x, which justifies the use of a one-dimensional model. The expressions of the steady state hydraulic resistance derived using laminar flow theory for different cross-sections are [38]: $32\mu_L l_L/a^2$ (circle); $28.4\mu_L l_L/a^2$ (square) and $\approx 12\mu_L l_L/[(1-0.63b/a)b^2]$ (rectangle), where μ_L is the dynamic viscosity of the liquid and a, b are the cross-section's edge lengths with $b < a$. For circular and square cross-sections $d = a$, and for a rectangular cross-section $d = 2ab/(a+b)$. By non-dimensionalizing Eq. 5.1, the characteristic velocity (v) and timescale (τ) for the channel geometry are obtained as $v = (p_\infty - p_V(t))/\mathfrak{R}$ and $\tau = (l_L \rho_L)/\mathfrak{R}$, respectively.

Since $p_V(t)$ is reported to be significant only during the first $\approx 10\,\%$ of the bubble's lifetime [23], the problem is simplified by dropping this term ($p_V(t) = 0$). Thus, the liquid initially gains momentum from the impulse offered by the vapor pressure. Subsequently, the bubble continues to grow due to the liquid's inertia, even though the pressure inside the bubble is much less than the ambient pressure [22]. At the end of the growth phase, the liquid momentum is fully dissipated by the resistance of the channel walls, following which the ambient pressure collapses the bubble. The bubble growth and collapse is described by solving the ordinary differential equation (ODE) from Eq. 5.1, resulting in the following dimensionless equation for the dynamic bubble size:

$$\widehat{X}_{max} - \widehat{X} = \widehat{t} + \exp(-\widehat{t}) - 1, \tag{5.2}$$

where $\widehat{X} = X/(v\tau)$ and $\widehat{t} = (t - t_0)/\tau$ are the dimensionless bubble size and time, respectively. The ODE is solved using the boundary condition $X = X_{max}$ at $t = t_0$,

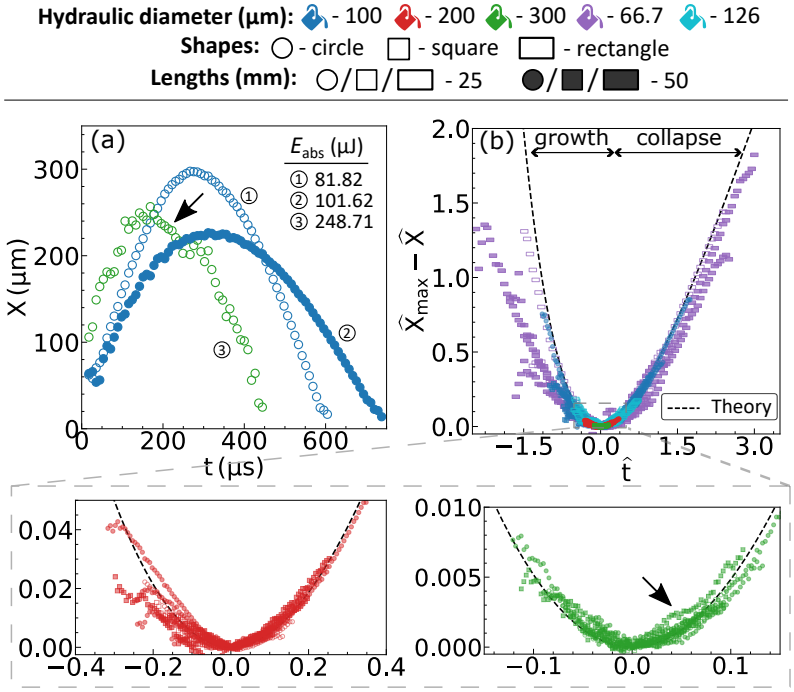

Figure 5.2: (a) Representative bubble dynamics for different channel geometries. (b) Universal motion of bubbles within channels with different size, shape and length. The dashed line represents the developed theory, Eq. 5.2. The marker colors represent the hydraulic diameters and the shapes represent the cross-section. The non-filled and filled markers represent the channel lengths L = 25 and 50 mm, respectively. The graphical marker symbols and colors established here are followed throughout this chapter. The black arrow represents the region of deviation(s) from the expected dynamics.

where X_{max} is the maximum bubble size. Fig. 5.2 (a) shows the representative bubble dynamics from experiments for different channel cross-sections and lengths. The bubble's maximum size, lifetime and the growth/collapse velocities vary significantly for different microchannel geometries. Fig. 5.2 (b) shows the experiments to follow the derived general expression for dynamic bubble size when non-dimensionalized using the characteristic scales (see Appendix D.1 for unscaled results).

In most cases, a deviation is seen in the bubble size from theory in the first 10% of the bubble's lifetime, as expected. This can be attributed to the significant vapor pressure inside the bubble due to instantaneous phase change during formation (~ 100 bar) which then decreases abruptly due to rapid change in the bubble volume [22]. Following the phase change, in the time range of O(μs) the vapor pressure is reported to be still very high ~ 8 bar corresponding to a saturation temperature of ~ 170 °C [22]. After which the change in pressure and therefore the corresponding

saturation temperature is rapid, 0.15 bar/μs or 2 °C/μs approximately. Moreover, the force exerted by the channel wall during the radial (r, see Fig. 5.1) growth of the bubble appearing during this first 10% of the bubble's lifetime will also influence its dynamics [19]. Thus a more sophisticated theoretical model incorporating the rapid change in pressure/temperature, change in the bubble geometry from spherical to elongated, and wall forces in radial direction is necessary to accurately match the observed bubble dynamics in experiments. This work therefore overlook's the accuracy within this time regime as its effect over the calculation of the characteristic parameters such as bubble lifetime, Womersley and Reynolds numbers are not large enough, discussed in detail in the following (sub)sections.

In Fig. 5.2 (a), for $d = 300\,\mu m$, a rapid acceleration is seen during the start of the bubble collapse (pointed using a black arrow). Similarly, in Fig. 5.2 (b), there is also a deviation seen from theory during the start of bubble collapse becoming more significant with increasing hydraulic diameter ($d \geqslant 200\,\mu m$). These are attributed to instabilities, discussed in detail under the section "Emergence of instabilities" later in this chapter.

Bubble lifetime

While the dynamic size of the vapor bubble quantifies the liquid velocity or flow rate, the lifetime of the oscillating bubble governs the oscillatory time period of flow. In this work, only the primary expansion and collapse of the bubble is studied and therefore ignore the bubble rebound caused by high pressures and temperatures [39]. Thus, the lifetime of the bubble is the time taken for one oscillation, t_{osc}. In Eq. 5.2, by substituting $\widehat{X} = 0$, the bubble's time of formation and collapse are obtained. The analytical prediction of the bubble's lifetime is

$$\widehat{t}_{osc} = t_{osc}/\tau = W_0(-e^{-\xi}) - W_{-1}(-e^{-\xi}), \tag{5.3}$$

where W_0 is the principal branch of the Lambert W function and W_{-1} its only other real branch, and $\xi = 1 + \widehat{X}_{max}$. The dimensionless times $W_{-1}(-e^{-\xi}) + \xi$ and $W_0(-e^{-\xi}) + \xi$ correspond to the time span of bubble expansion and collapse, respectively. It is to be noted that the dimensionless time in Figure 5.2 (b) is negative due to the choice of time zero at the maximum bubble size.

Figure 5.3 (a) illustrates the relation between the dimensionless bubble lifetime and maximum bubble size. A good agreement is seen between the experiments and the theoretical prediction from Eq. 5.3. See Appendix D.1 for unscaled data presented in Fig. 5.3 (a). There is a decrease in the bubble lifetime with an increase in the hydraulic diameter for a fixed channel length and X_{max}. This is caused by the decrease in hydraulic resistance with increasing hydraulic diameter, resulting in faster bubble dynamics. While the exact solution to the Lambert W function in Eq. 5.3 accurately cap-

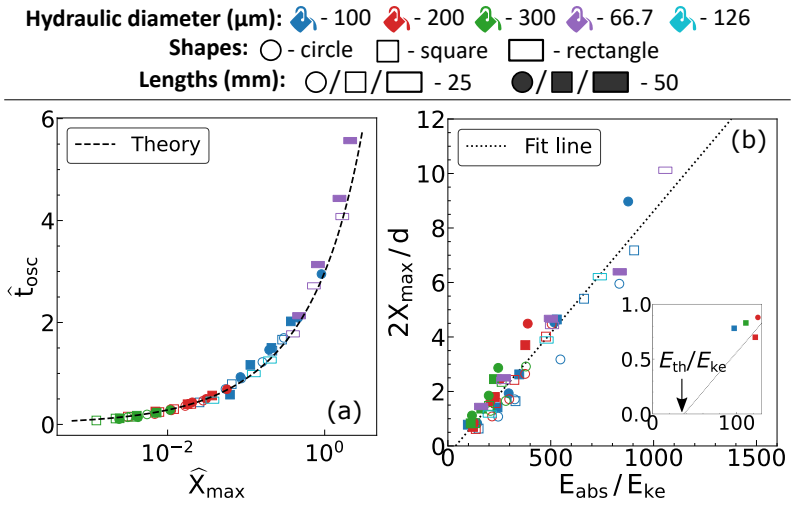

Figure 5.3: (a) Experimentally determined dimensionless lifetime ($\hat{t}_{osc}$) against maximum size ($\hat{X}_{max}$) of the bubble (markers) and comparison with the theoretical prediction from Eq. 5.3 (dashed line). (b) General linear relation between the non-dimensionalized experimentally determined maximum bubble size (X_{max}) and laser energy absorbed by the liquid (E_{abs}). The size and energy are non-dimensionalized using the channel hydraulic diameter (d) and unitary kinetic energy (E_{ke}) - calculated using the channel geometry and liquid properties. The inset illustrates the intercept in the plot which corresponds to the threshold laser energy for bubble formation (E_{th}). The coefficient of determination for the fit line is $R^2 = 0.928$.

tures the experiments, an approximation of this equation is discussed in Appendix D.1 to help solve the equation with more commonly used mathematical functions. The approximation however does decrease the accuracy of the results.

The above sections discuss the theory for dynamic bubble size ($X(t)$, Eq. 5.2) and lifetime (t_{osc}, Eq. 5.3). The proposed theory demands X_{max} as the only necessary parameter to compare with experiments. Thus it is necessary to have an estimate of X_{max} as a function of the laser energy supplied - a control parameter in experiments.

Energy Balance

Figure 5.3 (b) represents a general scaling law using empirical correlation for the maximum bubble size (X_{max}) against the absorbed laser energy, E_{abs}. The parameters X_{max} and E_{abs} are non-dimensionalized with respect to the hydraulic diameter and kinetic energy of the liquid with unitary velocity, respectively. The liquid kinetic energy with unitary velocity (E_{ke}) is calculated as

$$E_{ke} = A l_L \rho_L, \tag{5.4}$$

where A is the cross-sectional area of the channel. This approach to determine X_{max} via empirical correlation avoids the need for a more sophisticated numerical model with energy balances and phase transition [39].

For a certain cross-sectional shape, the energy required to achieve a certain X_{max} increases with the hydraulic diameter and length of the channel (see Appendix D.1 for unscaled results of Fig. 5.3 (b)). In Fig. 5.3 (b) the E_{abs} is at least two orders of magnitude higher than the E_{ke}. This observation is in agreement with the numerical simulations by Sun et al. [22], where most of the absorbed laser energy heats up the liquid directly surrounding the bubble, rather than transforming into the kinetic energy of the liquid.

In the experiments, the amount of laser energy absorbed by the liquid depends on the liquid properties and channel geometry. Based on the Beer-Lambert law [40], the absorption coefficient of the liquid and the distance the light travels through the liquid is used to estimate the amount of light absorbed, E_{abs}. Furthermore, the channel's wall thickness, material, cross-section shape and dimension can influence the laser energy available for the liquid to absorb. Thus the energy absorbed by the liquid in experiments was calibrated by measuring the difference of energy transmitted with the microchannel containing water and water-dye mixture (working fluid). Since water has very low absorption coefficient ($< 0.001\,\mathrm{cm}^{-1}$) for the laser wavelength used (532 nm) [41], the measured energy difference is attributed to the laser energy absorbed by the dye.

For rectangular channels, the longer edge length was used for supporting the channel over the stage (see Fig. 5.1), while the laser light was passed along the shorter edge. The details on the energy absorption measurement technique can be found in Appendix D.2. The estimated absorption coefficient of liquid, β, is $86.54\,\mathrm{cm}^{-1}$. This estimated value is different from measurements from the spectrometer (DR6000, Hach), $173\,\mathrm{cm}^{-1}$, which employs an unfocused and continuous light source. The difference in the absorption coefficient is attributed to the non-linear absorbance (saturable absorption) of the liquid due to high energy intensities ($\sim$ GWcm^{-2}) as the laser is focused and has short laser pulse duration (4 ns).

The fit in Fig. 5.3 (b) has an intercept for E_{abs}, implying there exists a threshold absorbed energy (E_{th}) only above which a vapor bubble forms. For a bubble to form, the spinodal temperature of water is theoretically used as the necessary condition [42] - the temperature at which water explosively turns into vapor. Thus, a sensible heat corresponding to $\Delta T = 279\,\mathrm{K}$ (at 1 atm and with respect to room temperature of 298 K) and a latent heat proportional to enthalpy of vaporization (H_L) is minimum required at the laser spot for bubble formation. Appendix D.2 provides the derivation

for analytical expression of E_{th} based on the energy balance for liquid. The threshold absorbed laser energy is,

$$E_{th} = (1 - 10^{-\beta d_L}) \frac{\pi w_0^2 \rho_L (c_{pL} \Delta T + H_L)}{\beta \log(10) 10^{-\beta (d_L/2)}}. \tag{5.5}$$

Where w_0 is the laser spot radius, c_{pL} is the specific heat and d_L is the distance the light will travel through the liquid. d_L is equal to the hydraulic diameter (d) for circular and square channels. For rectangles it is the shorter edge length of the cross-section. The parameter values for the calculation of Eq. 5.5 are presented in Table 5.2.

Table 5.2: Parameter values for theoretical calculation of the threshold energy for bubble formation using Eq. 5.5.

Parameter	Description	Value
ΔT	temperature rise	279 K (with respect to room temperature of 298 K)
c_{pL}	specific heat	4200 J/(kg K)
H_L	latent heat of vaporization	1377.6 kJ/kg (at 577 K)
ρ_L	liquid density	1000 kg/m^3
β	liquid absorption coefficient	86.54 cm^{-1} (measured experimentally, see Appendix D.2)

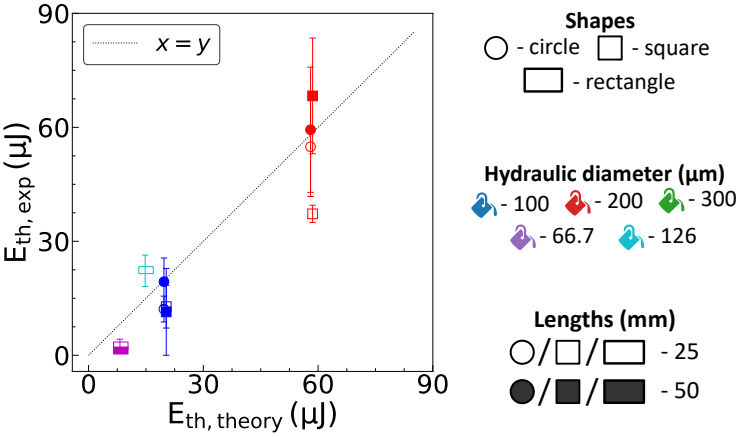

Figure 5.4: The threshold laser energy absorbed for bubble formation estimated from experiments ($E_{th,exp}$) against theory ($E_{th,theory}$) presented in Eq. 5.5.

In Eq. 5.5, the other necessary parameter for calculation is the laser spot diameter, $2w_0$. Theoretically, the laser spot diameter is calculated using the expression

$2w_0 = 4M^2\lambda f/(\pi D_L) = 1.69\,\mu m$. Where $\lambda = 532\,nm$ is the laser wavelength, $f = 10\,mm$ is the objective lens focal length, $D_L = 4\,mm$ is the laser beam diameter and the beam quality parameter $M^2 = 1$ (assuming a perfect Gaussian profile). The depth of field (DOF) of the focused laser beam is $2\pi w_0^2/(M^2\lambda) = 8.47\,\mu m$. However, these theoretical calculation for spot size and DOF can be different in experiments due to the optical aberrations caused by the channel walls [43]. From Fig. 5.4, a good agreement is seen between experiments ($E_{th,exp}$) and theory ($E_{th,theory}$) presented in Eq. 5.5 for the threshold laser energy absorbed by the liquid for bubble formation. The laser spot diameter used in the analytical expression is $9\,\mu m$, which is estimated based on the best fit of the theory to the experiments. This value of the laser spot diameter is same order of magnitude as the theoretically calculated value, thus emphasizing its validity. Furthermore, in Fig. 5.4 a deviation is seen in the threshold laser energy absorbed. The deviation is attributed to the laser aberrations due to channel wall curvature and thickness that can influence the laser spot diameter and therefore the threshold laser energy. In addition, the r position of the laser spot can also be affected by the confinement wall curvature and thickness, resulting in a larger E_{th} as the laser spot moves towards $r = d_L/2$. The channel specifications used in this work are summarized in Table 5.1.

The above analysis thus provides with an expression for bubble formation as a function of the energy absorbed by the liquid - a parameter that can be measured in experiments. The estimation of the laser energy threshold is one of the key design parameters necessary to choose the range of the laser energy required based on the channel geometry, liquid properties and objective lens specification.

Emergence of instabilities

In Fig. 5.5 (a), for $d \geqslant 200\,\mu m$ the bubble dynamics is seen to deviate from an expected bell curve like profile. Interestingly, the deviation occurs before X_{max} for $d = 200\,\mu m$ and after X_{max} for $d = 300\,\mu m$. Furthermore, Fig. 5.5 (b) shows that for $d = 200\,\mu m$ the deviation disappears for larger X_{max}. The observed deviations are hypothesized to occur due to the boundary layer instabilities near channel walls. These instabilities emerge due to the oscillating nature of the flow and unlike unidirectional flows it cannot be characterized only using the Reynolds number. Thus, the flow instability in oscillating channel flow is characterized using a peak oscillatory Reynolds number $Re_{osc} = \rho_L U_{max} d/\mu_L$ and a Womersley number $Wo = d/2\sqrt{\omega\rho_L/\mu_L}$ [44, 45]. U_{max} is the maximum mean flow velocity during the bubble growth, which on average occurs in the middle of the duration of growth, and $\omega = 2\pi/t_{osc}$ is the angular frequency of oscillation. Fig. 5.5 (c) shows these dimensionless numbers for the experiments performed in this work.

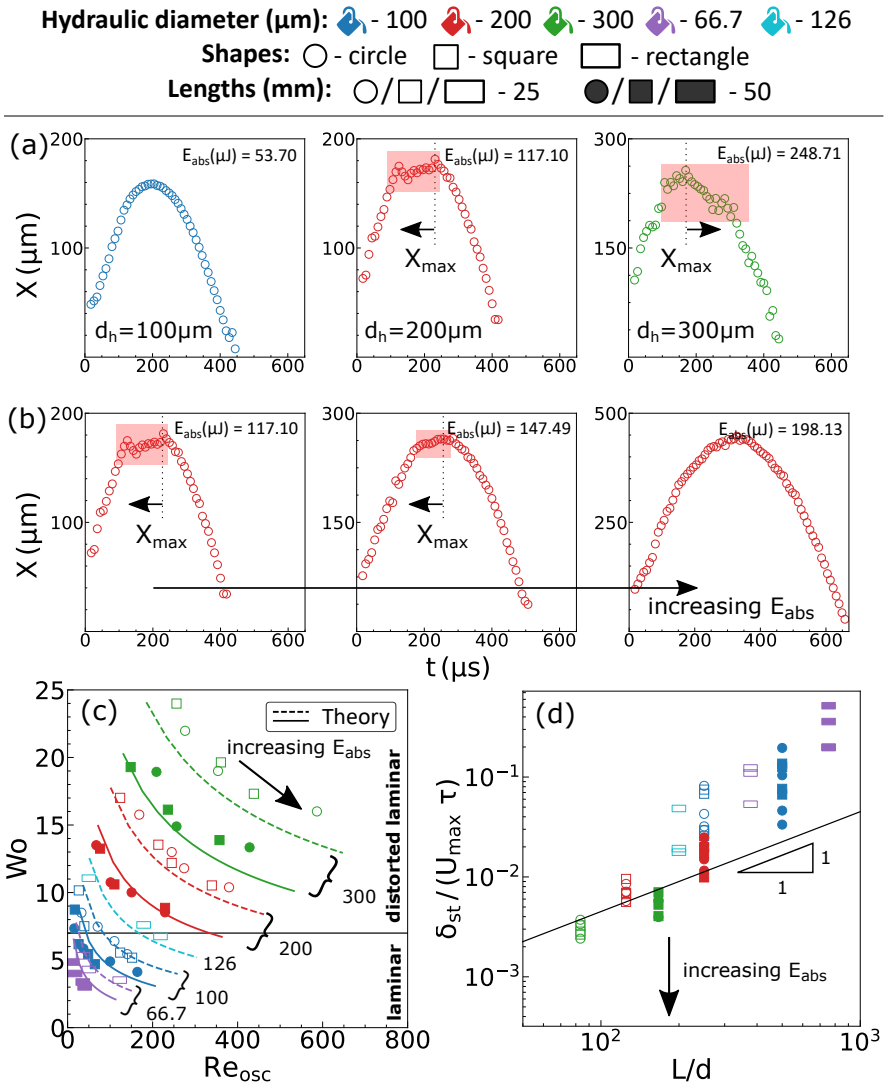

Figure 5.5: (a,b). Representative dynamic bubble size curves illustrating the emergence of instabilities. The zones of the instabilities are highlighted using a shaded rectangular area. The arrows represent if the instabilities occur before or after X_{max}. (a) Illustrates the experimental data for different d with similar oscillation time. The instabilities emerge with increasing d. (b) Illustrates the data for $d = 200$ μm with increasing laser energies. The instabilities disappear with increasing E_{abs}. (c) Flow stability diagram with the transition line at $Wo = 7$ [34]. The markers represent the experiments and the lines represent the analytical estimate. The numbers correspond to the channel hydraulic diameters (in μm) with the dashed and solid lines representing the channel lengths L = 25 and 50 mm, respectively. (d) The dimensionless convective timescale against the L/d aspect ratio. The partition line is a linear relation between the x and y axes with 45×10^{-6} as the slope and the origin as the intercept.

A simple approach to estimate the flow velocity, U, using theory can be formulated by using the analytical expression for t_{osc} (Eq. 5.3) and differentiating Eq. 5.2 with respect to time. The resulting dimensionless flow velocity is

$$U/v = -1 + \exp(-\widehat{t}). \tag{5.6}$$

By substituting half the bubble growth time $[W_{-1}(-e^{-\xi}) + \xi]/2$ for $\widehat{t}$, a corresponding maximum mean flow velocity U_{max} and Re_{osc} are calculated.

The lines in Fig. 5.5 (c) represent the analytical prediction of the dimensionless flow parameters for varying X_{max} in all channel geometries. A good agreement between the experiments and the analytical estimate are seen. The horizontal line in the figure, $Wo = 7$, represents the empirically observed laminar to distorted laminar transition value from literature for a perfectly oscillating flow with sinusoidal pressure gradient [34]. To predict the transition, the onset and growth of instability is determined using the parameters: (i) the position of the point of inflection, and (ii) the convective timescale, respectively. Das et al. [46], using pulsatile flow theory with a sinusoidal mean velocity profile [8], showed the dimensionless position of the point of inflection to be independent of the *Wo* above a critical Stokes parameter, $d/(2\delta_{st}) = Wo/\sqrt{2} \approx 3.6$, where $\delta_{st} = \sqrt{2\mu_L/(\rho_L\omega)}$ is the Stokes layer thickness. This theoretical critical value of $Wo \approx 5$ is below the empirically observed critical transition value of $Wo = 7$. Thus, the aforementioned analysis of instability using δ_{st} demonstrates the critical *Wo* in flow transition to be independent of the position of the point of inflection. However, the source of instability can still be attributed to the inflection of the velocity profiles near channel walls occurring due to the flow reversal (boundary layer separation) during the deceleration phase of the liquid. To further emphasize the observed deviation in Fig. 5.5 (a) as a cause of instability and not due to assumptions underlying the theory under consideration, it is compared to laminar flow due to an oscillating pressure gradient. Just before the bubble attains its maximum size, detachment of the boundary layer at the confining walls has been reported for flows between parallel plates based on numerical analysis [47]. The flow detachment exists due to the mismatch between the direction of the pressure gradient ($\partial p/\partial x > 0$) and fluid flow ($U > 0$). In accordance, the estimated flow profiles using theory with oscillating pressure gradient for microchannels [48] also predict a flow reversal occurring close to the channel walls (see Appendix D.3), similar to others [49]. However, the flow reversal near walls should decelerate the flow as the bubble begins to collapse - opposite to what is observed in experiments (in Fig. 5.5 (a), $d = 300\ \mu m$). This is a consequence of the instabilities causing flow distortion.

While the inflection in velocity profile near channel walls can lead to the onset of instabilities, the growth and therefore the time of emergence of instabilities is governed by the convective timescale. Fig 5.5 (d) shows the dimensionless convective

timescale from experiments, $\delta_{st}/(U_{max}\tau)$, for different L/d ratios. Small characteristic timescales of the channels (τ) compared to convective timescale (δ_{st}/U_{max}) would correspond to large resistance to flow offered by the channel walls as $\tau \propto 1/\mathfrak{R}$. Large resistance ($\mathfrak{R}$) in other words would mean a viscosity-dominated flow that effectively would dampen any perturbations/instabilities. However, as τ increases the instability would develop during the deceleration phase and prevail in the acceleration phase [46]. This argument on instability evolution explains the observed orientation of flow distortion relative to X_{max} in Fig 5.5 (a), when analyzed using the partition line depicted in Fig 5.5 (d). The partition line is adapted based on the experiments from this work which emphasizes the time of emergence of instabilities. As a data point approaches the partition line, the instabilities die out due to the motion-less state (zero velocities) at X_{max}, while below the partition line the instabilities sustain and prevail due to larger kinetic energies ($\propto U_{max}$).

In summary, the observed deviations in the dynamic bubble size from a bell curve like profile can be attributed to the disruption of the momentum boundary layer near channel walls [36] that would alter the channel hydraulic resistance and hence the mean velocities. However, these distorted laminar states are transient and therefore revert (decay) to laminar flow over time [36, 44]. Consequently, there exists a momentary deviation in dynamic bubble size as seen from the representative images in Fig. 5.5 (a).

5.4 Conclusions

By combining experiments and theory, this chapter demonstrated a universal behavior of fluid flows and transitions caused by transient laser-induced bubbles within microchannels of different geometries. This generalized approach to flow characteristics will aid the optimization of channel design and laser energy based on the application specific functionality. Contrary to the general assumption of undistorted laminar flow due to low Reynolds numbers ($Re < 1000$) in bubble-powered micro-systems, flow instability is reported. The instability originates due to the oscillating nature of the flow when the boundary layer separation occurs near channel walls during flow deceleration. During deceleration, the inflection point in the velocity profile near channel walls becomes unstable for larger flow oscillation frequencies ($Wo > 7$). Following the onset of instability, the time of emergence as distorted laminar states is discussed using the convective timescale associated with the flow. However, the distorted laminar states due to the growth of instability are transient and therefore decay rapidly compared to the overall flow oscillation time.

While this work is first to argue the existence of flow distortion in cavitation actuated flows in microfluidic channels, the measurement of such distortions in piston

actuated flows in channels with cross-sectional edge length of $O(10\,\mathrm{mm})$ have been extensively documented in the literature. The adapted measurement techniques in literature involve hot-wire anemometry [34, 44, 50, 51], laser doppler anemometry [51–54], particle image velocimetry [55] and flow visualization using dyes [46] for liquids, while for gases the techniques involve the use of transpiring walls [36] and smoke [50] for flow visualization. This work therefore does not employ any dedicated measurement technique to study flow distortion. However the argument on flow distortion is supported by characterizing the flow using the dimensionless numbers: Reynolds (Re) and Womersley (Wo) numbers, and order of magnitude analysis using convective time of the flow $\delta_{st}/(U_{max}\tau)$. In future, for studies that might examine the flow distortion in detail in the proposed system, the use of laser doppler anemometry, micro-particle image velocimetry and dyes are recommended since the presence of the hot-wire probe can promote flow distortion [51].

This study may also be relevant to explain a new phenomenon in the field of vesicle/cell deformation due to flow instability, challenging prior understanding based on resonance [56] and undistorted laminar shear [47, 57]. Thus the findings inform rational design of oscillatory pulsatile flows in engineering systems with potential applications to cavitation powered actuators [5, 20, 24, 58], confinement-induced acoustic cavitation [59] and biomimetic micromachines [60].

This work employs a simplified Darcy-Brinkman equation [48] for pure fluids with transient flow equations assuming steady-state hydraulic resistance. Therefore, by additionally incorporating the Darcy number, effective viscosity and porosity [61], this work can conveniently be extended to study flows within porous ducts with application to heat transfer in refrigeration [62] and biology [63].

REFERENCES

[1] Liwei Lin. "Microscale Thermal Bubble Formation: Thermophysical Phenomena and Applications." In: *Microscale Thermophysical Engineering* 2.2 (1998), pp. 71–85.

[2] Brian Dincau, Emilie Dressaire, and Alban Sauret. "Pulsatile Flow in Microfluidic Systems." In: *Small* 16.9 (2020), p. 1904032.

[3] Ivan Rehor, Charlie Maslen, Pepijn G. Moerman, Bas G.P. van Ravensteijn, Renee van Alst, Jan Groenewold, Huseyin Burak Eral, and Willem K. Kegel. "Photoresponsive Hydrogel Microcrawlers Exploit Friction Hysteresis to Crawl by Reciprocal Actuation." In: *Soft Robotics* 8.1 (2021). PMID: 32320334, pp. 10–18.

[4] RR Allen, JD Meyer, and WR Knight. *Hewlett-Packard Journal*. 1985.

[5] Seyedali Seyedmirzaei Sarraf, Farzad Rokhsar Talabazar, Ilayda Namli, Mohammadamin Maleki, Araz Sheibani Aghdam, Ghazaleh Gharib, Dmitry Grishenkov, Morteza Ghorbani, and Ali Koşar. "Fundamentals, biomedical applications and future potential of micro-scale cavitation-a review." In: *Lab Chip* 22 (12 2022), pp. 2237–2258.

[6] Vicente Robles, Juan Carlos Gonzalez-Parra, Natanael Cuando-Espitia, and Guillermo Aguilar. "The effect of scalable PDMS gas-entrapping microstructures on the dynamics of a single cavitation bubble." In: *Scientific Reports* 12.1 (Nov. 2022), p. 20379. ISSN: 2045-2322.

[7] Paul Delrot, Miguel A. Modestino, Fran çois Gallaire, Demetri Psaltis, and Christophe Moser. "Inkjet Printing of Viscous Monodisperse Microdroplets by Laser-Induced Flow Focusing." In: *Phys. Rev. Appl.* 6 (2 Aug. 2016), p. 024003.

[8] J. R. Womersley. "Method for the calculation of velocity, rate of flow and viscous drag in arteries when the pressure gradient is known." In: *Journal of Physiology* 127.3 (1955), pp. 553–563.

[9] J. Liam McWhirter, Hiroshi Noguchi, and Gerhard Gompper. "Flow-induced clustering and alignment of vesicles and red blood cells in microcapillaries." In: *Proceedings of the National Academy of Sciences* 106.15 (2009), pp. 6039–6043.

[10] Ido Frenkel and Avi Niv. "Light generated bubble for microparticle propulsion." In: *Scientific Reports* 7.1 (June 2017), p. 2814. ISSN: 2045-2322.

[11] Pedro A. Quinto-Su, Claudia Kuss, Peter R. Preiser, and Claus-Dieter Ohl. "Red blood cell rheology using single controlled laser-induced cavitation bubbles." In: *Lab Chip* 11 (4 2011), pp. 672–678.

[12] Justin C. Luo, Herman Ching, Bryce G. Wilson, Ali Mohraz, Elliot L. Botvinick, and Vasan Venugopalan. "Laser cavitation rheology for measurement of elastic moduli and failure strain within hydrogels." In: *Scientific Reports* 10.1 (Aug. 2020), p. 13144. ISSN: 2045-2322.

[13] Ralf Seemann, Martin Brinkmann, Thomas Pfohl, and Stephan Herminghaus. "Droplet based microfluidics." In: *Reports on Progress in Physics* 75.1 (Dec. 2011), p. 016601.

[14] Pedro A. Quinto-Su, Hsuan-Hong Lai, Helen H. Yoon, Christopher E. Sims, Nancy L. Allbritton, and Vasan Venugopalan. "Examination of laser microbeam cell lysis in a PDMS microfluidic channel using time-resolved imaging." In: *Lab Chip* 8 (3 2008), pp. 408–414.

[15] Paul Prentice, Alfred Cuschieri, Kishan Dholakia, Mark Prausnitz, and Paul Campbell. "Membrane disruption by optically controlled microbubble cavitation." In: *Nature Physics* 1.2 (Nov. 2005), pp. 107–110.

[16] Yavuz Emre Kamis, Huseyin Burak Eral, and Wim-Paul Breugem. "Active control of jet breakup and droplet formation using temperature modulation." In: *Phys. Rev. Fluids* 6 (10 Oct. 2021), p. 103903.

[17] Katharina Cu, Ruchi Bansal, Samir Mitragotri, and David Fernandez Rivas. "Delivery Strategies for Skin: Comparison of Nanoliter Jets, Needles and Topical Solutions." In: *Annals of Biomedical Engineering* 48.7 (July 2020), pp. 2028–2039. ISSN: 1573-9686.

[18] Jan Krizek, Paul Delrot, and Christophe Moser. "Repetitive regime of highly focused liquid microjets for needle-free injection." In: *Scientific Reports* 10.1 (Mar. 2020), p. 5067. ISSN: 2045-2322.

[19] Tao Ye and Joseph L. Bull. "Direct Numerical Simulations of Micro-Bubble Expansion in Gas Embolotherapy." In: *Journal of Biomechanical Engineering* 126.6 (Feb. 2005), pp. 745–759. ISSN: 0148-0731.

[20] Siew-Wan Ohl and Claus-Dieter Ohl. "Acoustic Cavitation in a Microchannel." In: *Handbook of Ultrasonics and Sonochemistry*. Singapore: Springer Singapore, 2016, pp. 1–37. ISBN: 978-981-287-470-2.

[21] E. Ory, H. Yuan, A. Prosperetti, S. Popinet, and S. Zaleski. "Growth and collapse of a vapor bubble in a narrow tube." In: *Physics of Fluids* 12.6 (2000), pp. 1268–1277.

[22] Chao Sun, Edip Can, Rory Dijkink, Detlef Lohse, and Andrea Prosperetti. "Growth and collapse of a vapour bubble in a microtube: the role of thermal effects." In: *Journal of Fluid Mechanics* 632 (2009), 5–16.

[23] H. Yuan, H.N. Oguz, and A. Prosperetti. "Growth and collapse of a vapor bubble in a small tube." In: *International Journal of Heat and Mass Transfer* 42.19 (1999), pp. 3643–3657. ISSN: 0017-9310.

[24] Khashayar Khoshmanesh, Abdullah Almansouri, Hamad Albloushi, Pyshar Yi, Rebecca Soffe, and Kourosh Kalantar-zadeh. "A multi-functional bubble-based microfluidic system." In: *Scientific Reports* 5.1 (Apr. 2015), p. 9942. ISSN: 2045-2322.

[25] Kai Zhang, Aoqun Jian, Xuming Zhang, Yu Wang, Zhaohui Li, and Hwa-yaw Tam. "Laser-induced thermal bubbles for microfluidic applications." In: *Lab Chip* 11 (7 2011), pp. 1389–1395.

[26] Christopher J. Morris and Fred K. Forster. "Oscillatory flow in microchannels." In: *Experiments in Fluids* 36.6 (June 2004), pp. 928–937. ISSN: 1432-1114.

[27] Nagaraj Nagalingam, Aswin Raghunathan, Vikram Korede, Christian Poelma, Carlas S. Smith, Remco Hartkamp, Johan T. Padding, and Hüseyin Burak Eral. "Laser-Induced Cavitation for Controlling Crystallization from Solution." In: *Phys. Rev. Lett.* 131 (12 Sept. 2023), p. 124001.

[28] V. Korede and N. Nagalingam, Frederico Marques Penha, Noah van der Linden, Johan T. Padding, Remco Hartkamp, and Huseyin Burak Eral. "A Review of Laser-Induced Crystallization from Solution." In: *Crystal Growth & Design* 23.5 (2023), pp. 3873–3916.

[29] Tianyi Hua, Omar Gowayed, Danielle Grey-Stewart, Bruce A. Garetz, and Ryan L. Hartman. "Microfluidic Laser-Induced Nucleation of Supersaturated Aqueous KCl Solutions." In: *Crystal Growth & Design* 19.6 (2019), pp. 3491–3497.

[30] Zhizhong Yin and Andrea Prosperetti. "A microfluidic 'blinking bubble' pump." In: *Journal of Micromechanics and Microengineering* 15.3 (Jan. 2005), p. 643.

[31] Erik D. Torniainen, Alexander N. Govyadinov, David P. Markel, and Pavel E. Kornilovitch. "Bubble-driven inertial micropump." In: *Physics of Fluids* 24.12 (2012), p. 122003.

[32] Hongchen Li, Jian Huang, Xianqian Wu, Jian Zhang, Jingzhu Wang, Yiwei Wang, and Chenguang Huang. "Dynamic behaviors of a laser-induced bubble and transition mechanism of collapse patterns in a tube." In: *AIP Advances* 10.3 (2020), p. 035210.

[33] Marc Avila, Dwight Barkley, and Björn Hof. “Transition to Turbulence in Pipe Flow.” In: *Annual Review of Fluid Mechanics* 55.1 (2023), pp. 575–602.

[34] Munekazu Ohmi, Manabu Iguchi, Koichiro Kakehashi, and Tetsuya Masuda. “Transition to Turbulence and Velocity Distribution in an Oscillating Pipe Flow.” In: *Bulletin of JSME* 25.201 (1982), pp. 365–371.

[35] Duo Xu, Atul Varshney, Xingyu Ma, Baofang Song, Michael Riedl, Marc Avila, and Björn Hof. “Nonlinear hydrodynamic instability and turbulence in pulsatile flow.” In: *Proceedings of the National Academy of Sciences* 117.21 (2020), pp. 11233–11239.

[36] Joseph Majdalani, James Barron, and William K. Van Moorhem. “Inception of Turbulence in the Stokes Boundary Layer Over a Transpiring Wall.” In: *Journal of Fluids Engineering* 124.3 (Aug. 2002), pp. 678–684. ISSN: 0098-2202.

[37] N. Nagalingam and A. Raghunathan, Vikram Korede, Edwin F.J. Overmars, Shih-Te Hung, Remco Hartkamp, Johan T. Padding, Carlas S. Smith, and Huseyin Burak Eral. “Low-cost fluorescence microscope with microfluidic device fabrication for optofluidic applications.” In: *HardwareX* 14 (2023), e00415. ISSN: 2468-0672.

[38] Henrik Bruus. “Chapter 1 Governing Equations in Microfluidics.” In: *Microscale Acoustofluidics*. The Royal Society of Chemistry, 2015, pp. 1–28. ISBN: 978-1-84973-671-8.

[39] I. Akhatov, N. Vakhitova, A. Topolnikov, K. Zakirov, B. Wolfrum, T. Kurz, O. Lindau, R. Mettin, and W. Lauterborn. “Dynamics of laser-induced cavitation bubbles.” In: *Experimental Thermal and Fluid Science* 26.6 (2002), pp. 731–737. ISSN: 0894-1777.

[40] Donald F Swinehart. “The beer-lambert law.” In: *Journal of chemical education* 39.7 (1962), p. 333.

[41] Frank M. Sogandares and Edward S. Fry. “Absorption spectrum (340–640 nm) of pure water. I. Photothermal measurements.” In: *Appl. Opt.* 36.33 (Nov. 1997), pp. 8699–8709.

[42] R. Thiéry and L. Mercury. “Explosivity Conditions of Aqueous Solutions.” In: *Journal of Solution Chemistry* 38.7 (July 2009), pp. 893–905. ISSN: 1572-8927.

[43] Alfred Vogel, Kester Nahen, Dirk Theisen, Reginald Birngruber, Robert J. Thomas, and Benjamin A. Rockwell. “Influence of optical aberrations on laser-induced plasma formation in water and their consequences for intraocular photodisruption.” In: *Appl. Opt.* 38.16 (June 1999), pp. 3636–3643.

[44] Mikio Hino, Masaki Sawamoto, and Shuji Takasu. “Experiments on transition to turbulence in an oscillatory pipe flow.” In: *Journal of Fluid Mechanics* 75.2 (1976), 193–207.

[45] Alexander Shapiro, Gershon Grossman, and David Greenblatt. “Simplified Transition and Turbulence Modeling for Oscillatory Pipe Flows.” In: *Energies* 14.5 (Mar. 2021), p. 1410. ISSN: 1996-1073.

[46] Debopam Das and Jaywant H. Arakeri. “Transition of unsteady velocity profiles with reverse flow.” In: *Journal of Fluid Mechanics* 374 (1998), 251–283.

[47] Milad Mohammadzadeh, Fenfang Li, and Claus-Dieter Ohl. “Shearing flow from transient bubble oscillations in narrow gaps.” In: *Phys. Rev. Fluids* 2 (1 Jan. 2017), p. 014301.

[48] C. Y. Wang. “Analytic Solutions for Pulsatile Flow Through Annular, Rectangular and Sector Ducts Filled with a Darcy–Brinkman Medium.” In: *Transport in Porous Media* 112.2 (Mar. 2016), pp. 409–428. ISSN: 1573-1634.

[49] C. Poelma, J. M. Mari, N. Foin, M.-X. Tang, R. Krams, C. G. Caro, P. D. Weinberg, and J. Westerweel. “3D Flow reconstruction using ultrasound PIV.” In: *Experiments in Fluids* 50.4 (Apr. 2011), pp. 777–785. ISSN: 1432-1114.

[50] P. Merkli and H. Thomann. “Transition to turbulence in oscillating pipe flow.” In: *Journal of Fluid Mechanics* 68.3 (1975), 567–576.

[51] David M. Eckmann and James B. Grotberg. “Experiments on transition to turbulence in oscillatory pipe flow.” In: *Journal of Fluid Mechanics* 222 (1991), 329–350.

[52] B. R. Ramaprian and Shuen-Wei Tu. “An experimental study of oscillatory pipe flow at transitional Reynolds numbers.” In: *Journal of Fluid Mechanics* 100.3 (1980), 513–544.

[53] R. Akhavan, R. D. Kamm, and A. H. Shapiro. “An investigation of transition to turbulence in bounded oscillatory Stokes flows Part 1. Experiments.” In: *Journal of Fluid Mechanics* 225 (1991), 395–422.

[54] C. R. LODAHL, B. M. SUMER, and J. FREDSØE. “Turbulent combined oscillatory flow and current in a pipe.” In: *Journal of Fluid Mechanics* 373 (1998), 313–348.

[55] Islam Ramadan, Ahmed El-Rahman, Abdelmaged Ibrahim Essawey, and Ehab Abdel-Rahman. “Transition to Turbulence in Oscillating Flows.” In: July 2017.

[56] Tandiono Tandiono, Evert Klaseboer, Siew-Wan Ohl, Dave Siak-Wei Ow, Andre Boon-Hwa Choo, Fenfang Li, and Claus-Dieter Ohl. “Resonant stretching of cells and other elastic objects from transient cavitation.” In: *Soft Matter* 9 (36 2013), pp. 8687–8696.

[57] Philippe Marmottant and Sascha Hilgenfeldt. “Controlled vesicle deformation and lysis by single oscillating bubbles.” In: *Nature* 423.6936 (May 2003), pp. 153–156. ISSN: 1476-4687.

[58] Say Hwa Tan, Florine Maes, Benoît Semin, Jérémy Vrignon, and Jean-Christophe Baret. “The Microfluidic Jukebox.” In: *Scientific Reports* 4.1 (Apr. 2014), p. 4787. ISSN: 2045-2322.

[59] Julien Rapet, Pedro A. Quinto-Su, and Claus-Dieter Ohl. “Cavitation Inception from Transverse Waves in a Thin Liquid Gap.” In: *Phys. Rev. Appl.* 14 (2 Aug. 2020), p. 024041.

[60] Vincenzo Andrea Montagna, Stefano Palagi, Giovanna Adele Naselli, Carlo Filippeschi, and Barbara Mazzolai. “Cavitation-driven Deformable Microchambers Inspired by Fast Microscale Movements of Ferns.” In: *Advanced Functional Materials* 33.39 (2023), p. 2214130.

[61] W.-P. Breugem. “The effective viscosity of a channel-type porous medium.” In: *Physics of Fluids* 19.10 (2007), p. 103104.

[62] Qunte Dai and Luwei Yang. “LBM numerical study on oscillating flow and heat transfer in porous media.” In: *Applied Thermal Engineering* 54.1 (2013), pp. 16–25. ISSN: 1359-4311.

[63] A.-R.A. Khaled and K. Vafai. “The role of porous media in modeling flow and heat transfer in biological tissues.” In: *International Journal of Heat and Mass Transfer* 46.26 (2003), pp. 4989–5003. ISSN: 0017-9310.

6

CRYSTALLIZATION VIA LASER-INDUCED BUBBLE PAIRS IN A MICROCHANNEL

This chapter demonstrates a novel crystallization route from supersaturated aqueous solutions of a model inorganic salt, potassium permanganate ($KMnO_4$) arising from interaction between laser-induced micro-bubble pairs. "Jets" of fast-moving liquid emerge due to bubble-bubble interaction along the axis connecting the bubble centres. This jets enable crystallization at much lower laser energies and solution supersaturations compared to crystallization involving a single bubble. There is an increase in the crystal nucleation kinetics with jet velocity and is attributed to the shear induced by the impingement of the jet over the liquid surrounding the bubble. The proposed theory for crystallization employs classical nucleation theory with the effect of shear embodied into the kinetic prefactor. Furthermore, the evolution of the jet is numerically simulated using the axisymmetric Boundary Integral Element Method to determine the characteristic scaling laws for jet velocity based on the bubble-bubble standoff distance, channel diameter and laser energy. The findings contribute to the interdisciplinary field of primary nucleation control of crystallization from solution using laser-induced cavitation.

This chapter is based on the article:
N. Nagalingam et al. "Laser-induced crystal nucleation facilitated by microjets emerging from interaction of thermocaviation bubble pairs under confinement." In: *(submitted)* (2024).

6.1 Introduction

The potential of single-bubble motion to induce strong localized flows and its associated stress has been realized in engineering [1, 2] and biomedical applications [3, 4]. The interaction of a bubble with its surrounding is mediated via flow of the liquid surrounding the bubble [5] and shockwaves generated during bubble formation and collapse [6]. As long as the environment around the bubble is sufficiently spherically symmetric, the bubble will retain a spherical shape throughout its lifetime. However, asymmetries in the bubble's environment can lead to anisotropic bubble dynamics, and even formation of microjets [7]. These thin jets of fast-moving liquid emerge from the gas-liquid interface owing to the impulse generated. Jetting consequently leads to transport of fluid and species away from the location of bubble inception.

Common methods to induce microjets include generating the bubbles near rigid boundaries, near free surfaces or near other bubbles [8, 9]. The jet emerging from bubble formation close to a rigid boundary can often lead to surface destruction [10, 11], and should therefore be avoided. Jet formation near free interface [12] may be more suitable, but free interfaces are hardly present in continuously functioning synthetic or physiological systems. Thus, inducing jets through interaction between multiple laser-induced bubbles, due to its more versatile and less invasive nature for controlling the jet properties, has found its application in microrheology [13], single-cell poration [9, 14], mechanotransduction [15] and particle manipulation [16].

This chapter shows how controlling microjets through bubble interactions can be applied to control crystallization. In particular, a novel route to crystallization of salts is demonstrated employing aqueous solutions of $KMnO_4$ via laser-induced bubble pairs in a microchannel, Fig. 6.1. Intriguingly, no crystal formation was observed with only a single bubble, even when the laser energy was doubled to accelerate the crystal nucleation kinetics [17]. Thus, the crystallization observed with bubble pairs is attributed to the formation of the microjets that have directed fluid and species transport over short distances away from the location of bubble inception. This article first discusses the experiments and demonstrates the role of jet velocity in crystallization using classical nucleation theory. The latter discusses a boundary integral element method which complement the observed influence of laser energy and geometry parameters (bubble-bubble standoff distance, capillary diameter, bubble size) on jet velocity. This numerical model can be used to engineer the system for any capillary geometries and fluid properties.

6.2 Materials and Methods

Optical setup

For sample illumination a white LED light (KL1500, Zeiss) was used. An infinity corrected 10x objective (Plan Fluor, Nikon) with 0.3 numerical aperture was used for laser 1. A 8x objective (Planapochromat, Carl Zeiss) with 0.1 numerical aperture was used for laser 2. The 10x objective was also used for imaging with resolution $\approx$ 2 μm/px for high-speed camera (FASTCAM NOVA S16, Photron) and $\approx$ 0.74 μm/px for low-speed camera (Imager Pro LX 16M, LaVision). Both the laser 1 and 2 were pulsed Nd:YAG lasers with the configurations listed in Table 6.1.

Table 6.1: Laser parameters.

Parameter	Laser 1	Laser 2
Model	Nano L 90-100	Powerlite DLS 8000
Wavelength	532 nm	532 nm
Pulse duration	5 ns	$7-9$ ns
Diameter at source	4 mm	9 mm
Diameter at objective	8 mm	3 mm
TEM_{00}	yes	no

Solution preparation

Ultrapure water (18.2 MΩ cm, ELGA Purelab) was used to prepare the supersaturated $KMnO_4$ (223468, Sigma-Aldrich) solutions in a 8 ml vial (SF8, BGB). A solubility of 0.076 g/g-H_2O at 298 K for $KMnO_4$ was used [18, 19]. After preparation, the solution was stirred at 1000 rpm over a hot plate maintained at 333 K for one hour to accelerate the dissolution. Then the solution was placed in the oven maintained at 323 K overnight ($>$ 12 hours) for complete dissolution. During experiments the vials were placed over a hot plate maintained at 333 K and constantly stirred at 1000 rpm.

6.3 Results and Discussions

6.3.1 Experiments

The formation of bubble pairs are achieved using two 532 nm lasers with $5-9$ ns pulse width integrated via a delay generator. The vapor bubbles B_1 and B_2 are formed

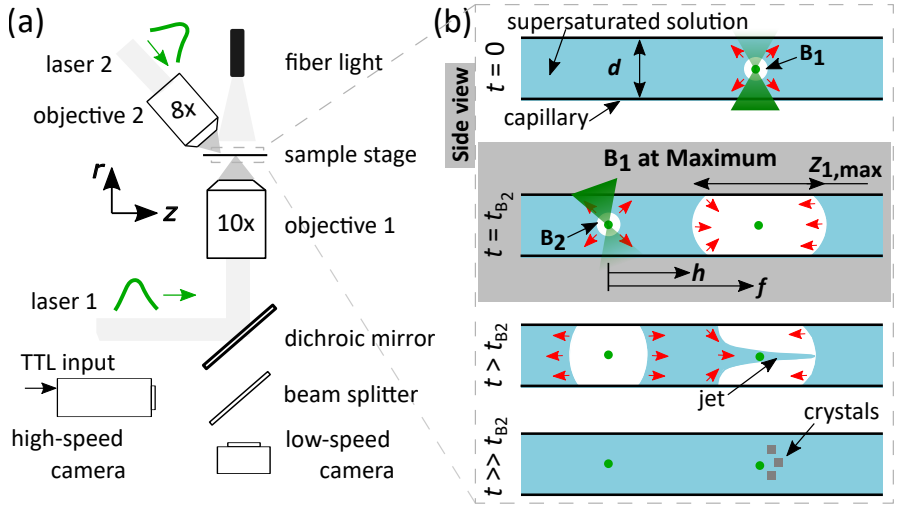

Figure 6.1: Sketch of the experimental setup. (a) Optical paths. (b) Bubble pair generation. Bubble B_2 is formed when B_1 is at its maximum size, $Z_{1,max}$. Theoretically, $h = f - Z_{1,max}$, where f is the distance between the laser foci.

using the lasers 1 and 2, respectively, as illustrated in Fig. 6.1. The parameters governing the dynamic bubble size and jet properties are the absorbed laser energy for the two bubbles, E_1 and E_2, which correlate to their maximum sizes, $Z_{1,max}$ and $Z_{2,max}$, the standoff distance, h, and the time delay (phase difference) between the initiation of the bubbles. Throughout this work the bubbles are maintained out-of-phase [20], where the second bubble is formed only when the first bubble is at $Z_{1,max}$. The respective time of formation of the bubbles 1 and 2 is denoted using t_{B_1} and t_{B_2}, with $t_{B_1} = 0\,\mu s$. The h is a parameter defined only at $t = t_{B_2}$, and can be controlled either by adjusting the distance between the laser foci or by changing the energy supplied to B_1 as it dictates $Z_{1,max}$. All the supplied laser energy is absorbed, owing to the high absorption coefficient of the solution $> 1000\,cm^{-1}$. Appendix E.1 details the experimental protocol used.

Figure 6.2 (a,c) shows the representative images from experiments demonstrating the formation of a microjet and subsequent crystals. The high-speed camera operating at 112500 frames per second (fps) captures the bubble and jet dynamics, while the low-speed camera recording at 3 fps captures the crystal growth. The experiments are for aqueous $KMnO_4$ solution with supersaturation in the bulk $S_\infty = 1.5$ relative to the solubility of 0.076 g/g of water at 298 K [18]. Figure 6.2 (b) highlights the formation of B_2 at $t_{B_2} = 240\,\mu s$ as B_1 reaches its maximum size. Consequently, as B_2 continues to grow the formation of a microjet within B_1 is noticed along the axis connecting the bubble centers. This fast-moving jet pierces the right end side of B_1, creating new bubbles. After the collapse of B_1 and B_2, the residual bubble(s) either coalesce or

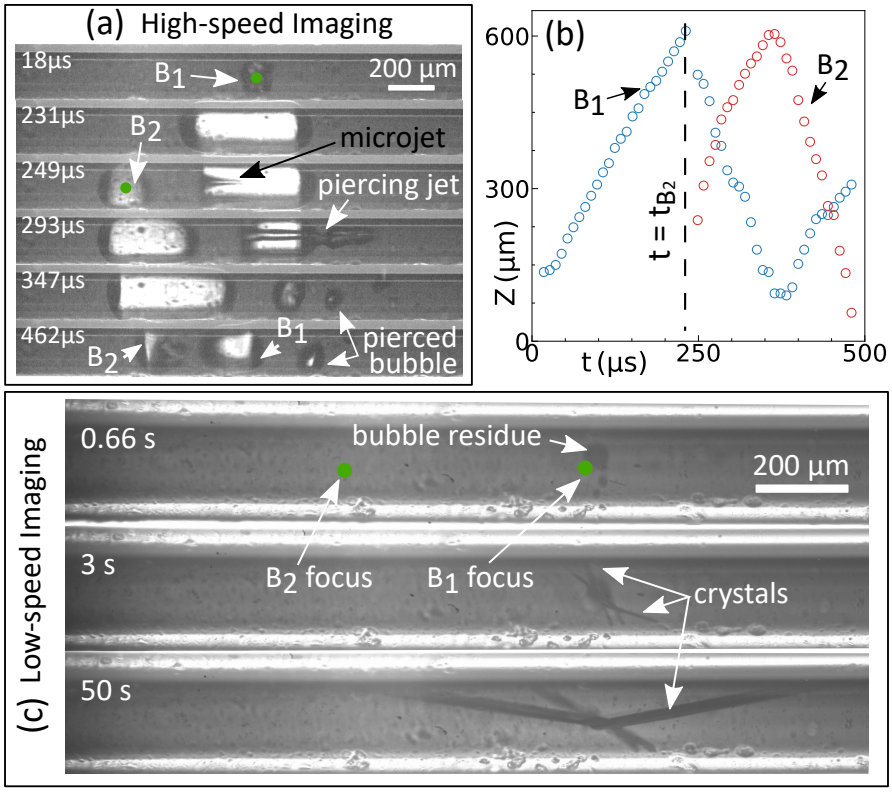

Figure 6.2: Bubble-bubble interaction with subsequent crystallization. (a) Illustration of the formation of bubble pair and a microjet. The images were recorded using a high-speed camera at 112500 fps. (b) Dynamic bubble sizes from (a). Bubble B_2 is formed when B_1 reaches its maximum size at $t = t_{B_2}$. (c) Low-speed camera images captured at 3 fps showing the growth of $KMnO_4$ crystals.

dissolve over a milliseconds-to-second time range. The crystals of observable size are then recorded surrounding the residual bubble over seconds. Under identical experimental conditions, no crystal was observed if only B_1 is formed. Moreover, even when twice the laser energy was supplied to B_1 (with no B_2) to enforce enhanced crystal nucleation kinetics [17], no crystal was observed (see Appendix E.2). Therefore the crystal formation is attributed to the presence of microjet and therefore have analyzed the jet velocity in relation to the onset of crystallization in more detail.

Figure 6.3 shows the representative images for jet evolution at different time instances. The velocity v_j of the jet tip is determined based on the rate of change of jet tip position with time. The plot illustrates the temporal jet tip velocity for a chosen h for three different laser energies E_2 of B_2. Based on the tip velocity, the jets have different appearances and are categorized into three types: (i) pinch-off: jet breaks

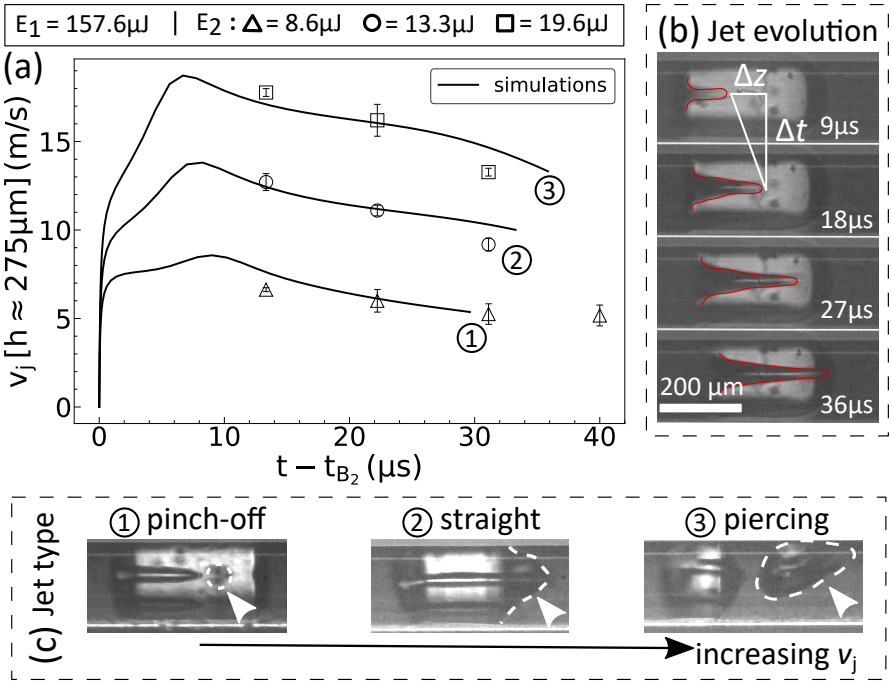

Figure 6.3: Jet evolution and type. (a) Temporal jet tip velocity for three different B_2 laser energies, E_2. (b) Illustration of jet displacement over time. (c) Different jet types based on the velocities. The white dashed lines in images from left to right represent the jet breakup (pinch-off), the deformed B_1 interface, and the pierced bubble, respectively. The circled numbers 1, 2 and 3 respectively correspond to the different jet tip velocities in (a).

into droplet(s); (ii) straight: jet does not break up before it reaches the opposite end of B_1, and therefore will deform the incident vapor-liquid interface but will not pierce it; and (iii) piercing: the jet pierces the opposite end of B_1 leading to the creation of new bubble(s). The tendency of a jet to breakup is evaluated using the Weber number $We = \rho_L v_j^2 r_j/\sigma_{gl}$, with ρ_L the liquid density, r_j the jet radius and σ_{gl} the surface tension. Jetting is reported to occur for $We > 4$ [21, 22]. In this work, We ranges between $4 - 65$, satisfying the necessary condition for jet formation and breakup. However, as the distance the jets can travel within B_1 is limited to $Z_{1,max}$, jets with relatively higher velocities possess sufficient momentum to reach the right side end of B_1 before breaking up, while the jets with lower velocities breakup (pinch-off) due to the Rayleigh instability [21]. The observed velocity range ($4 - 8$ m/s) of jet pinch-off is in agreement with the reported satellite-free drop generation range [23]. Arguably, the jet could increase the solute transport due to the transfer of momentum, favoring crystal nucleation [24]. However, this is a mere hypothesis and further experimental

evidence with different solution supersaturation and channel diameter is necessary for a quantitative estimate.

Figure 6.4 shows the jet velocities for a range of supersaturations $S_\infty = \{1.5, 1.3, 1.2\}$ and channel diameter $d = \{200, 200, 300\}$ µm, respectively, for varying

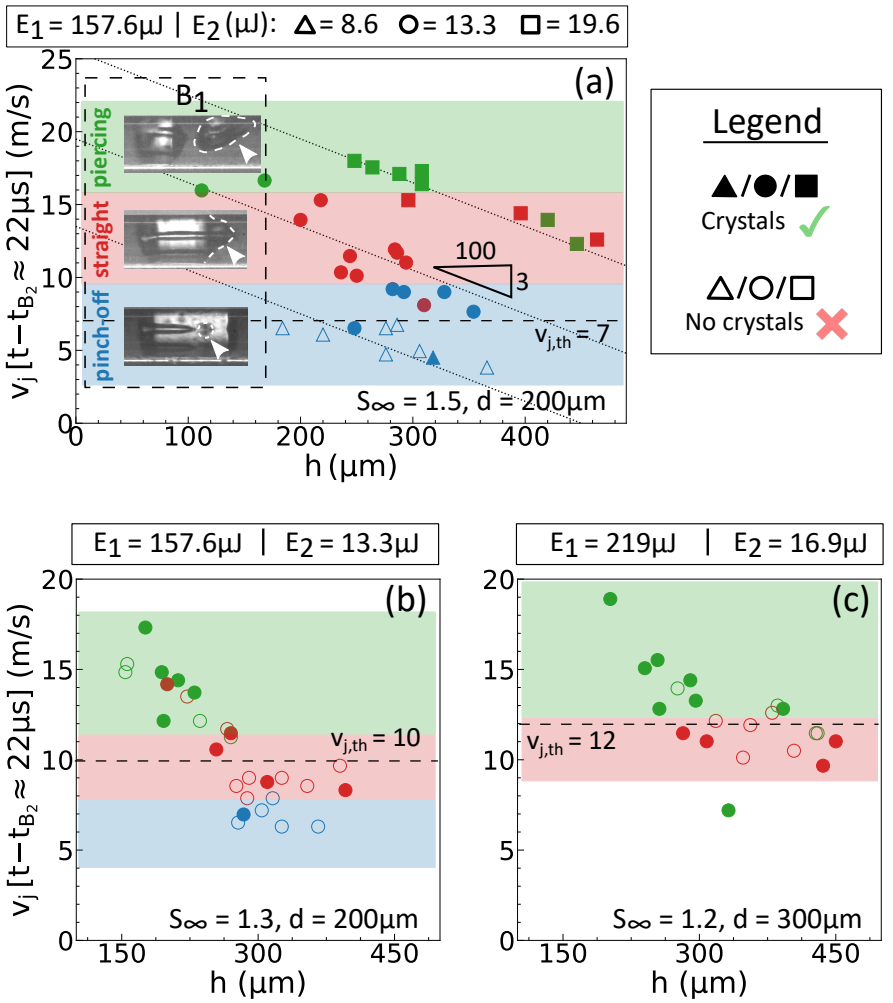

Figure 6.4: Jet velocities versus crystallization. (a-c) Jet velocities over different stand-off distance (h) at a given time $t - t_{B_2}$. The color of the markers represent the type of jet as annotated using the respective colors. In addition, the appropriate zones of each jet type are shaded using the respective colors with illustrative images of B_1. The markers with and without face colors represent the experiments with and without crystallization, respectively. The slopes of the fit lines represented with dotted line are -0.03. $v_{j,th}$ is the threshold velocity for crystal formation above which the crystallization probability is $\geqslant 0.5$. The crystallization is determined with a fixed observation time of 2 minutes from the laser irradiation.

h and E_2. The representative velocity for each jet is chosen at $t - t_{B_2} = 22\,\mu s$ as it closely matches the incident jet velocity over the opposite end of B_1. From the plotted data $v_j \propto E_2/h$, consistent with others [25]. In addition, there is an increase in the crystallization probability with jet velocity. Overall, the results suggest a dependence of crystallization probability on jet velocity, solution supersaturation and channel diameter, with no influence of jet type. Therefore a characteristic jet velocity for crystallization is defined to compare between different systems. The threshold jet velocity for crystal formation, $v_{j,th}$, is defined as the value above which the cumulative crystallization probability is greater than 50 %. The cumulative probability is calculated as the number of trials which crystallized (within an observation time of 2 minutes) to the total number of trials. There is an increase in $v_{j,th}$ with decreasing supersaturation. Furthermore, upon increasing d from 200 to 300 μm while maintaining $S_\infty = 1.3$, a steep rise in the number of crystals formed isobserved (> 20, see Appendix E.2). This indicates an increasing crystal nucleation tendency with increasing channel diameter. Therefore, the trials in Fig. 6.4 (c) in 300 μm channel were performed with much lower supersaturation ($S_\infty = 1.2$) to appropriately estimate the $v_{j,th}$.

The impingement of a jet over the liquid surrounding the bubble can create shear/strain [14], thereby altering the nucleation kinetics [26]. However the exact crystal nucleation mechanism is still under debate, shrouded in speculations involving enhanced mass transfer, shear-induced molecular alignment and agitation-enhanced cluster aggregation [27]. From classical nucleation theory, the nucleation rate, J, which is the number of nuclei formed per unit volume per unit time, is expressed as [28],

$$J = \Lambda S \exp\left[-B/\log^2 S\right], \tag{6.1}$$

where S is the local supersaturation and B is a dimensionless thermodynamic parameter given by $B = 16\pi v_0^2 \sigma_{sl}^3/(3k_B^3 T^3)$. Here v_0 is molecular volume, σ_{sl} is solute-solution interfacial tension, k_B is Boltzmann's constant and T is the temperature. Λ is the $S-$independent kinetic parameter for homogeneous nucleation. The influence of nucleation rate due to liquid shear is accounted for in Λ with empirical evidence showing a power law dependence, $\Lambda \propto \dot{\gamma}^n$ [29–33], in which $\dot{\gamma}$ is the shear rate. In addition, for aqueous glycine Forsyth at al. [34] demonstrated the Λ to positively scale with the solution container's surface area A_{sur} as $\Lambda \propto \dot{\gamma} A_{sur}$. Combining the relations, $\Lambda \propto (v_j/d)^n d$, with $\dot{\gamma} \sim v_j/d$ and $A_{sur} \sim \pi d$ over unit length of the channel. This relation thus provides the relationship to the governing parameters accounted for in the pre-exponential kinetic factor Λ while maintaining the thermodynamic parameters B and S constant.

By definition, J can be expressed as $N/(t_{obs}V)$, where N is crystal count, t_{obs} is observation time and V the channel volume. The crystallization threshold criterion is

established as, $N \approx 1$, with a fixed observation time of $t_{obs} = 2\,\text{min}$. This approximation is valid in all the performed experiments which crystallized close to the threshold as the average crystal count was 1 (refer Appendix E.2). Therefore, near the crystallization threshold, this makes J only a function of channel volume, $J \propto 1/(\pi d^2 L)$. Since a constant channel length (L) is maintained throughout this work,

$$J/\Lambda \propto d^{-3}(\nu_{j,th}/d)^{-n} = \mathfrak{C} S \exp\left[-B/\log^2 S\right]. \tag{6.2}$$

$\mathfrak{C}$ is a constant whose value is based on N, t_{obs}, L, temperature and solute-solvent properties [28]. The thermal penetration depth in the liquid surrounding the bubble calculated using the lifetime of the bubbles is $O(10\,\mu m)$. However, the momentum penetration depth due to jet impingement calculated using the Newton's approximation of impact depth [35] is $O(100\,\mu m)$. Therefore, the effect of the local temperature variations in liquid surrounding the bubble is neglected in Eq. 6.2 with $T = 298\,K$ throughout the analysis. Correspondingly, the change in S due to T is neglected. By rearranging Eq. 6.2,

$$-\log[d^3(\nu_{j,th}/d)^n S] = -B/\log^2 S + \log \mathfrak{C}. \tag{6.3}$$

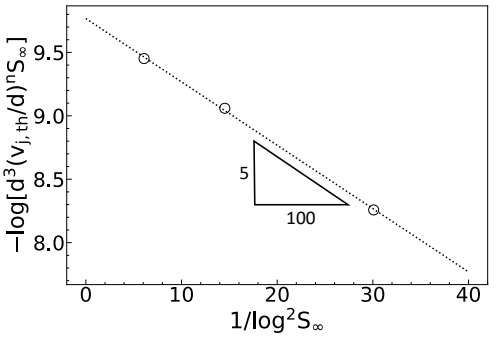

Figure 6.5: Calculation of solute-solution interfacial tension. The plot shows the estimates from Eq. 6.3. Appropriate values for the variables are supplied for the parameters discussed in this work, $S = \{1.5, 1.3, 1.2\}$ and $d = \{200, 200, 300\}\,\mu m$, respectively. The slope corresponds to the value of B in Eq. 6.3, with which the solute-solution interfacial tension σ_{sl} is estimated. The coefficient of determination for the fit line is $R^2 = 0.999$.

Figure 6.5 shows the estimates by substituting the appropriate values of variables in Eq. 6.3. The value of the index $n = 1.5$ is chosen such that the coefficient of determination for the linear fit line is $R^2 \approx 1$. This chosen value for n is in agreement with the empirically observed $1-3$ range from literature [29–34], see Appendix E.3. Using the obtained slope in the value for B, $\sigma_{sl} = 3.1\,mJ/m^2$ is calculated and is in close agreement with $3.16\,mJ/m^2$ estimated using the Mersmann relation [36]. See Appendix E.4 for the calculation of σ_{sl}.

The above analysis demonstrates the influence of jet velocity on crystallization using classical nucleation theory. The proposed theory for crystallization suggests a threshold jet velocity dependent on the solution supersaturation and channel diameter. Therefore, an analytical or numerical model is necessary to estimate the jet velocity based on the control parameters involving laser energy and channel geometry. Although previous work [37] suggests an analytical expression for the peak jet velocity, $v_{j,pk}$, a numerical model is necessary to estimate the temporal change in jet velocity. This temporal jet velocity elucidates the incident velocity of the jet onto the opposite end side of B_1.

6.3.2 Numerical simulations

The liquid momentum in response to evolving bubbles is solved using an axisymmetric Boundary Integral Element Method. This allows the simulation of interactions between the two bubbles perfectly centered along the channel axis and estimation of the temporal evolution of the jet velocity. To decrease the code runtime the computational domain is reduced by simulating the bubble-bubble interaction only using the near side of B_1, see Fig. 6.6 (a). This resembles B_2 interacting with a meniscus, with the option to define the initial B_1 interface curvature using a contact angle. A numerical model for bubble-meniscus interaction in a channel partially filled with liquid exists [37], but that model fails to predict the influence of change in channel diameter. Moreover, bubble initialization in the existing model employs a pressure pulse that cannot be directly related to experiments.

In studies involving bubble-meniscus interaction in a channel, the contact angle of the meniscus with the wall is observed to influence the jet velocity due to flow focusing. The velocity is reported to decrease with increasing contact angle [25, 37]. Thus, the initiation of the B_1 interface requires an estimate of its contact angle with the channel wall. Using the angles measured from experiments an initial contact angle of 30° is imposed, consistent with others using borosilicate glass [38, 39]. The gas inside the bubble is assumed to consist of non-condensables and water vapor. The partial pressure due to the non-condensable gas is assumed to undergo a polytropic process with $\Upsilon = 1.25$ as the polytropic index [40]. Thus, the gas pressure over the liquid at the interface is written as [41],

$$p_l = p_c + p_0(V_0/V_b)^{\Upsilon} - \sigma_{gl}\kappa. \tag{6.4}$$

where p_c is the saturated vapor pressure of the condensable gas, V_b is the instantaneous bubble volume, p_0 and V_0 are the initial non-condensable gas pressure and bubble volume, respectively. $\kappa = 0.5(\kappa_1 + \kappa_2)$ is the mean local curvature computed using the following equations for an axisymmetric surface [42]: $\kappa_1 = r'z'' -$

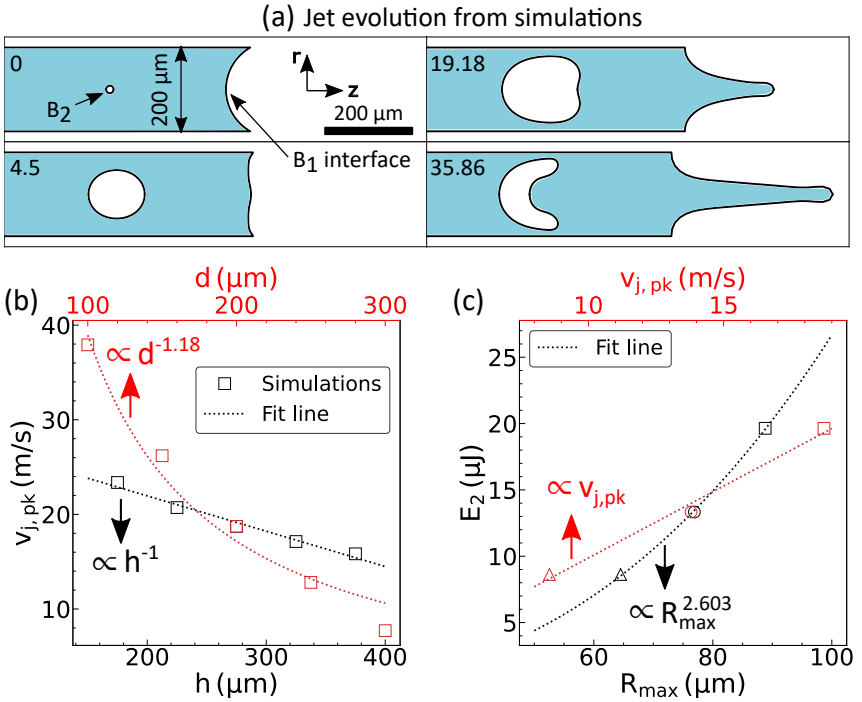

Figure 6.6: Simulations: jet evolution and validation. (a) An illustration from the Boundary Integral Element simulations for $E_2 = 19.64\,\mu J$ in Fig. 6.3. The numbers in the top left of each frame represent the time in µs. (b) Peak jet velocity ($v_{j,pk}$) as a function of stand-off distance (h, bottom black scale) and channel diameter (d, top red scale) from simulations. (c) Simulated $v_{j,pk}$ (top red scale) and R_{max} (bottom black scale) as a function of absorbed laser energy in experiments, E_2. The average standard error over mean for E_2 is $\pm 0.3\,\mu J$. R_{max} is the maximum radius of the bubble when simulated in an unbound liquid domain - with no channel or B_1. The three data points correspond to the examples from Fig. 6.3.

$z'r''$ and $\kappa_2 = z'/r$. The superscripts $'$ and $''$ denote the first and second derivatives with respect to Γ, which is the arc length of the piecewise smooth surface comprising the bubble surface, free surface and rigid boundary.

The liquid is treated as inviscid and incompressible and the flow induced by the bubble motion as irrotational. Using the theory for potential flow, the potential ϕ is related to the velocity vector $\mathbf{u}$ as $\mathbf{u} = \nabla\phi$, which itself satisfies the Laplace equation,

$$\nabla^2\phi = 0, \tag{6.5}$$

in the flow domain Ω. For a sufficiently smooth function ϕ defined over the piecewise smooth surface Γ, Green's integral formula for a three-dimensional space is written as [43],

$$c(p)\phi(p) = \int_\Gamma \frac{\partial}{\partial n}(\phi(q))\ \frac{1}{|p-q|}d\Gamma - \int_\Gamma \phi(q)\ \frac{\partial}{\partial n}\left(\frac{1}{|p-q|}\right) d\Gamma, \quad (6.6)$$

where p is the field point anywhere in $\Omega + \Gamma$, $q \in \Gamma$ and n is the outward unit normal. With $c(p) = 2\pi\ \forall\ p \in \Gamma$, choosing p over Γ results in a solution for either ϕ or $\partial\phi/\partial n$ on Γ if the other is specified. Following a Lagrangian framework, the kinematic and dynamic boundary conditions on the bubble surface are written as,

$$\Delta r = (\partial\phi/\partial r)\,\Delta t, \quad \Delta z = (\partial\phi/\partial z)\,\Delta t, \quad \text{and} \quad (6.7)$$

$$\Delta\phi = \left[\frac{1}{2}|\boldsymbol{\nabla}\phi|^2 + \frac{p_\infty - p_l}{\rho_L}\right]\Delta t, \quad (6.8)$$

where p_∞ is the pressure at $z \to \infty$.

With $\Delta p = p_\infty - p_c$, the following characteristic scales are used to non-dimensionalize the associated parameters: $R_{max}(\rho_L/\Delta p)^{1/2}$ for time, $R_{max}(\Delta p/\rho_L)^{1/2}$ for potential and $(\Delta p/\rho_L)^{1/2}$ for velocity. The length is non-dimensionalized using R_{max}, which is the maximum radius of the spherical bubble when simulated in an unbounded liquid domain - with no channel walls or B_1. Correspondingly, the change in potential on the B_1 and B_2 surface is given by [44, 45],

$$\Delta\widehat{\phi} = \left[1 + \frac{1}{2}|\widehat{\mathbf{u}}|^2 - \zeta(V_0/V_b)^\Upsilon + \widehat{\sigma}_{gl}\widehat{\kappa}\right]\Delta\widehat{t} \quad \text{and} \quad (6.9)$$

$$\Delta\widehat{\phi} = \left[\frac{1}{2}|\widehat{\mathbf{u}}|^2 + \widehat{\sigma}_{gl}\widehat{\kappa}\right]\Delta\widehat{t}, \quad (6.10)$$

respectively. Where $\zeta = p_0/\Delta p$ is the strength parameter and $\widehat{\sigma}_{gl} = \sigma_{gl}/(R_{max}\Delta p)$ is the surface tension parameter. The superscript $\widehat{}$ denotes the dimensionless form of the parameters.

The numerical solution procedure to Eq. 6.6 can be found in Appendix E.5. An illustration of the results from a simulation is shown in Fig. 6.6 (a). The jet evolution with B_2 is similar to experiments from Figs. 6.2 (a) and 6.3 (b). However, the lifetime of bubble B_2 in the simulation ($\approx 36\,\mu s$) is smaller compared to experiments [$O(100\,\mu s)$]. The deviation is attributed to the neglection of viscous effects and capillary forces between the interface of B_1 and the wall. Yet, in Fig. 6.6 (b), the model accurately predicts the inverse linear dependence of peak jet velocity ($v_{j,pk}$) on h with -0.037 slope and a power law dependence on d with -1.18 index, consistent with the previous observations [25]. Furthermore, the value of the slope is in agreement with the experimental observations from Fig. 6.4 (a).

The bubble initialization requiring p_0 and V_0 is theoretically related to the potential energy of the bubble with $p_0 V_0 \propto R_{max}^3$ [46]. In all the analysis $\zeta = 313$, with the non-dimensionalized initial radius $R_0/R_{max} = 0.1$. The chosen value for ζ is within the $100 - 500$ range for exploding bubbles [40], with the change in value within this range having negligible effect on bubble/jet dynamics, similar to others [47]. Appendix E.5 discusses the validation of the initial conditions together with the analytical equation for the estimation of ζ. It is essential to note that only two of the three dimensionless parameters ζ, R_0/R_{max} and Υ can be chosen independently. In Fig. 6.6 (c) the R_{max} from simulations directly correlates to the laser energy from experiments. The determined power law fit index from $E_2 \propto R_{max}^{2.603}$ is consistent with the reported empirical relation for energy difference above a threshold laser energy [48]. Furthermore, the obtained linear relation of $v_{j,pk} \propto E_2$ agrees with the literature [37]. The numerical model discussed thus quantitatively captures the bubble-bubble interaction.

6.4 Conclusions

In summary, a novel route to crystallization of salts is demonstrated via microjets formed due to bubble-bubble interaction in supersaturated solutions of aqueous $KMnO_4$. This technique enables primary control over crystal nucleation at lower laser energies and solution supersaturation compared to crystallization via a single bubble. The crystal formation in experiments is correlated to the jet velocities using classical nucleation theory. The proposed scaling relations for jet velocity with absorbed laser energy, stand-off distance and channel diameter using numerical simulations agree with the experiments performed and with literature. A threshold jet velocity only above which crystal formation is significant is reported to be a function of solution supersaturation and channel diameter. This threshold velocity increases with decreasing supersaturation and channel diameter. While the field of laser-induced crystallization via cavitation bubbles remain shrouded in speculations involving photochemistry, shockwaves and solute accumulation at the vapor-liquid interface [49, 50], this findings suggest a new alternate route via bubble-bubble hydrodynamic interaction. The proposed route to crystallization thus will assist the study of spatiotemporal control of the crystal nucleation process using lasers [49] and ultrasound [51].

REFERENCES

[1] Siew-Wan Ohl and Claus-Dieter Ohl. "Acoustic Cavitation in a Microchannel." In: *Handbook of Ultrasonics and Sonochemistry*. Singapore: Springer Singapore, 2016, pp. 99–135. ISBN: 978-981-287-278-4.

[2] Nagaraj Nagalingam, Vikram Korede, Daniel Irimia, Jerry Westerweel, Johan T. Padding, Remco Hartkamp, and Hüseyin Burak Eral. "Unified framework for laser-induced transient bubble dynamics within microchannels." In: *Scientific Reports* 14.1 (Aug. 2024), p. 18763.

[3] James A. Rooney. "Hemolysis Near an Ultrasonically Pulsating Gas Bubble." In: *Science* 169.3948 (1970), pp. 869–871.

[4] Zhenzhen Fan, Haiyan Liu, Michael Mayer, and Cheri X. Deng. "Spatiotemporally controlled single cell sonoporation." In: *Proceedings of the National Academy of Sciences* 109.41 (2012), pp. 16486–16491.

[5] Ed Zwaan, Séverine Le Gac, Kinko Tsuji, and Claus-Dieter Ohl. "Controlled Cavitation in Microfluidic Systems." In: *Phys. Rev. Lett.* 98 (25 June 2007), p. 254501.

[6] Outi Supponen, Takahito Akimura, Tomoya Minami, Tomoki Nakajima, Satoshi Uehara, Kiyonobu Ohtani, Toshiro Kaneko, Mohamed Farhat, and Takehiko Sato. "Jetting from cavitation bubbles due to multiple shockwaves." In: *Applied Physics Letters* 113.19 (Nov. 2018), p. 193703. ISSN: 0003-6951.

[7] J R Blake and D C Gibson. "Cavitation Bubbles Near Boundaries." In: *Annual Review of Fluid Mechanics* 19.1 (1987), pp. 99–123.

[8] Outi Supponen, Danail Obreschkow, Marc Tinguely, Philippe Kobel, Nicolas Dorsaz, and Mohamed Farhat. "Scaling laws for jets of single cavitation bubbles." In: *Journal of Fluid Mechanics* 802 (2016), 263–293.

[9] G. N. Sankin, F. Yuan, and P. Zhong. "Pulsating Tandem Microbubble for Localized and Directional Single-Cell Membrane Poration." In: *Phys. Rev. Lett.* 105 (7 Aug. 2010), p. 078101.

[10] Leen van Wijngaarden. "Mechanics of collapsing cavitation bubbles." In: *Ultrasonics Sonochemistry* 29 (2016), pp. 524–527. ISSN: 1350-4177.

[11] Claus-Dieter Ohl, Manish Arora, Rory Dijkink, Vaibhav Janve, and Detlef Lohse. "Surface cleaning from laser-induced cavitation bubbles." In: *Applied Physics Letters* 89.7 (Aug. 2006), p. 074102. ISSN: 0003-6951.

[12] P. B. Robinson, J. R. Blake, T. Kodama, A. Shima, and Y. Tomita. "Interaction of cavitation bubbles with a free surface." In: *Journal of Applied Physics* 89.12 (June 2001), pp. 8225–8237. ISSN: 0021-8979. eprint: https://pubs.aip.org/aip/jap/article-pdf/89/12/8225/19255147/8225_1_online.pdf.

[13] P. A. Quinto-Su, X. H. Huang, S. R. Gonzalez-Avila, T. Wu, and C. D. Ohl. "Manipulation and Microrheology of Carbon Nanotubes with Laser-Induced Cavitation Bubbles." In: *Phys. Rev. Lett.* 104 (1 Jan. 2010), p. 014501.

[14] Fang Yuan, Chen Yang, and Pei Zhong. "Cell membrane deformation and bioeffects produced by tandem bubble-induced jetting flow." In: *Proceedings of the National Academy of Sciences* 112.51 (2015), E7039–E7047.

[15] Fenfang Li, Chen Yang, Fang Yuan, Defei Liao, Thomas Li, Farshid Guilak, and Pei Zhong. "Dynamics and mechanisms of intracellular calcium waves elicited by tandem bubble-induced jetting flow." In: *Proceedings of the National Academy of Sciences* 115.3 (2018), E353–E362.

[16] Jaclyn Lautz, Georgy Sankin, Fang Yuan, and Pei Zhong. "Displacement of particles in microfluidics by laser-generated tandem bubbles." In: *Applied Physics Letters* 97.18 (Nov. 2010), p. 183701. ISSN: 0003-6951.

[17] Nagaraj Nagalingam, Aswin Raghunathan, Vikram Korede, Christian Poelma, Carlas S. Smith, Remco Hartkamp, Johan T. Padding, and Hüseyin Burak Eral. "Laser-Induced Cavitation for Controlling Crystallization from Solution." In: *Phys. Rev. Lett.* 131 (12 Sept. 2023), p. 124001.

[18] William M Haynes. *CRC handbook of chemistry and physics*. CRC press, 2014.

[19] Gregory P Baxter, Arthur C Boylston, and Robert A Hubbard. "THE SOLUBILITY OF POTASSIUM PERMANGANATE." In: *Journal of the American Chemical Society* 28.10 (1906), pp. 1336–1343.

[20] Fang Yuan, Georgy Sankin, and Pei Zhong. "Dynamics of tandem bubble interaction in a microfluidic channel." In: *The Journal of the Acoustical Society of America* 130.5 (Nov. 2011), pp. 3339–3346. ISSN: 0001-4966.

[21] Wim van Hoeve, Stephan Gekle, Jacco H. Snoeijer, Michel Versluis, Michael P. Brenner, and Detlef Lohse. "Breakup of diminutive Rayleigh jets." In: *Physics of Fluids* 22.12 (Dec. 2010), p. 122003. ISSN: 1070-6631.

[22] Brian Derby. "Inkjet Printing of Functional and Structural Materials: Fluid Property Requirements, Feature Stability, and Resolution." In: *Annual Review of Materials Research* 40.1 (2010), pp. 395–414.

[23] Paul Delrot, Miguel A. Modestino, Fran çois Gallaire, Demetri Psaltis, and Christophe Moser. "Inkjet Printing of Viscous Monodisperse Microdroplets by Laser-Induced Flow Focusing." In: *Phys. Rev. Appl.* 6 (2 Aug. 2016), p. 024003.

[24] Huaiyu Yang, Xi Yu, Vishal Raval, Yassir Makkawi, and Alastair Florence. "Effect of Oscillatory Flow on Nucleation Kinetics of Butyl Paraben." In: *Crystal Growth & Design* 16.2 (2016), pp. 875–886.

[25] Yoshiyuki Tagawa, Nikolai Oudalov, Claas Willem Visser, Ivo R. Peters, Devaraj van der Meer, Chao Sun, Andrea Prosperetti, and Detlef Lohse. "Highly Focused Supersonic Microjets." In: *Phys. Rev. X* 2 (3 July 2012), p. 031002.

[26] Anatolii V. Mokshin, Bulat N. Galimzyanov, and Jean-Louis Barrat. "Extension of classical nucleation theory for uniformly sheared systems." In: *Phys. Rev. E* 87 (6 June 2013), p. 062307.

[27] Rosalind J. Allen, Chantal Valeriani, Sorin Tănase-Nicola, Pieter Rein ten Wolde, and Daan Frenkel. "Homogeneous nucleation under shear in a two-dimensional Ising model: Cluster growth, coalescence, and breakup." In: *The Journal of Chemical Physics* 129.13 (Oct. 2008), p. 134704. ISSN: 0021-9606.

[28] D. Kashchiev and G. M. van Rosmalen. "Review: Nucleation in solutions revisited." In: *Crystal Research and Technology* 38.7-8 (2003), pp. 555–574.

[29] Carol Forsyth, Paul A. Mulheran, Claire Forsyth, Mark D. Haw, Iain S. Burns, and Jan Sefcik. "Influence of Controlled Fluid Shear on Nucleation Rates in Glycine Aqueous Solutions." In: *Crystal Growth & Design* 15.1 (2015), pp. 94–102.

[30] Sander Stroobants, Manly Callewaert, Marzena Krzek, Sudha Chinnu, Pierre Gelin, Iwona Ziemecka, James F. Lutsko, Wim De Malsche, and Dominique Maes. "Influence of Shear on Protein Crystallization under Constant Shear Conditions." In: *Crystal Growth & Design* 20.3 (2020), pp. 1876–1883.

[31] Jin Liu and Åke C. Rasmuson. "Influence of Agitation and Fluid Shear on Primary Nucleation in Solution." In: *Crystal Growth & Design* 13.10 (Oct. 2013), pp. 4385–4394. ISSN: 1528-7483.

[32] Felice De Santis, Roberto Pantani, and Giuseppe Titomanlio. "Effect of shear flow on spherulitic growth and nucleation rates of polypropylene." In: *Polymer* 90 (2016), pp. 102–110. ISSN: 0032-3861.

[33] Cedric Devos, Anja Vananroye, Ruth Cardinaels, Christos Xiouras, Tom Van Gerven, and Simon Kuhn. "The interplay between nucleation and patterning during shear-induced crystallization from solution in a parallel plate geometry." In: *Soft Matter* 19 (31 2023), pp. 5896–5906.

[34] Carol Forsyth, Iain S. Burns, Paul A. Mulheran, and Jan Sefcik. "Scaling of Glycine Nucleation Kinetics with Shear Rate and Glass–Liquid Interfacial Area." In: *Crystal Growth & Design* 16.1 (2016), pp. 136–144.

[35] Joe Henry Marsden, Guy Norman Taylor Levin, Jacob Eddison, and Darshan Vigneswara. “P6_3 Bulletproof T-Shirts.” In: *Physics Special Topics* 16.1 (2017).

[36] A. Mersmann. “Calculation of interfacial tensions.” In: *Journal of Crystal Growth* 102.4 (1990), pp. 841–847. ISSN: 0022-0248.

[37] Ivo R. Peters, Yoshiyuki Tagawa, Nikolai Oudalov, Chao Sun, Andrea Prosperetti, Detlef Lohse, and Devaraj van der Meer. “Highly focused supersonic microjets: numerical simulations.” In: *Journal of Fluid Mechanics* 719 (2013), 587–605.

[38] John Canning, Hadrien Weil, Masood Naqshbandi, Kevin Cook, and Matthieu Lancry. “Laser tailoring surface interactions, contact angles, drop topologies and the self-assembly of optical microwires.” In: *Opt. Mater. Express* 3.2 (Feb. 2013), pp. 284–294.

[39] Hirotaka Maeda, Tomoyuki Sakai, and Fuuga Matsuura. “Influence of structural change by heat treatment on the wettability of borosilicate glass.” In: *International Journal of Applied Glass Science* 13.4 (2022), pp. 549–553.

[40] R. H. Cole. *Underwater Explosions*. Princeton University Press, 1948.

[41] J. P. Best and A. Kucera. “A numerical investigation of non-spherical rebounding bubbles.” In: *Journal of Fluid Mechanics* 245 (1992), 137–154.

[42] Abdolrahman Dadvand, Mohammad T. Shervani-Tabar, and Boo Cheong Khoo. “A note on spark bubble drop-on-demand droplet generation: simulation and experiment.” In: *The International Journal of Advanced Manufacturing Technology* 56.1 (Sept. 2011), pp. 245–259.

[43] Bachok Bin Taib. “Boundary integral method applied to cavitation bubble dynamics.” PhD thesis. University of Wollongong, 1985.

[44] Abdolrahman Dadvand, Boo Cheong Khoo, Mohammad T. Shervani-Tabar, and Saman Khalilpourazary. “Boundary element analysis of the droplet dynamics induced by spark-generated bubble.” In: *Engineering Analysis with Boundary Elements* 36.11 (2012), pp. 1595–1603. ISSN: 0955-7997.

[45] Bao-Yu Ni, A-Man Zhang, Qian-Xi Wang, and Bin Wang. “Experimental and numerical study on the growth and collapse of a bubble in a narrow tube.” In: *Acta Mechanica Sinica* 28.5 (Oct. 2012), pp. 1248–1260. ISSN: 1614-3116.

[46] SASCHA HILGENFELDT, MICHAEL P. BRENNER, SIEGFRIED GROSSMANN, and DETLEF LOHSE. “Analysis of Rayleigh–Plesset dynamics for sonoluminescing bubbles.” In: *Journal of Fluid Mechanics* 365 (1998), 171–204.

[47] EVERT KLASEBOER, SIEW WAN FONG, CARY K. TURANGAN, BOO CHEONG KHOO, ANDREW J. SZERI, MICHAEL L. CALVISI, GEORGY N. SANKIN, and PEI ZHONG. "Interaction of lithotripter shockwaves with single inertial cavitation bubbles." In: *Journal of Fluid Mechanics* 593 (2007), 33–56.

[48] Vasan Venugopalan, Arnold Guerra, Kester Nahen, and Alfred Vogel. "Role of Laser-Induced Plasma Formation in Pulsed Cellular Microsurgery and Micromanipulation." In: *Phys. Rev. Lett.* 88 (7 Feb. 2002), p. 078103.

[49] V. Korede and N. Nagalingam, Frederico Marques Penha, Noah van der Linden, Johan T. Padding, Remco Hartkamp, and Huseyin Burak Eral. "A Review of Laser-Induced Crystallization from Solution." In: *Crystal Growth & Design* 23.5 (2023), pp. 3873–3916.

[50] Teruki Sugiyama and Shun-Fa Wang. "Manipulation of nucleation and polymorphism by laser irradiation." In: *Journal of Photochemistry and Photobiology C: Photochemistry Reviews* 52 (2022), p. 100530. ISSN: 1389-5567.

[51] Judy Lee, Kyuichi Yasui, Muthupandian Ashokkumar, and Sandra E. Kentish. "Quantification of Cavitation Activity by Sonoluminescence To Study the Sonocrystallization Process under Different Ultrasound Parameters." In: *Crystal Growth & Design* 18.9 (2018), pp. 5108–5115.

7

CONCLUSIONS AND RECOMMENDATIONS

An overview of the findings from this dissertation is presented in this chapter and the research objectives set in Chapter 1 are reflected upon. Finally, some recommendations for future work are provided.

கான முயலெய்த அம்பினில் யானை
பிழைத்தவேல் ஏந்தல் இனிது

"The spear that missed an elephant is worth holding
than the arrow that hit a hare"
(Verse 772, Thirukkural)

7.1 Conclusions

This dissertation contributes to settle the discussion on the origin of non-photochemical laser-induced nucleation (NPLIN) by providing quantification of the cavitation bubble emerging upon light irradiation - a previously hypothesized phenomenon that has proved to be difficult to visualize experimentally due to the small length and time scales involved. The experiments presented in this dissertation fix the position of bubble(s) formation by focusing the laser light with 532/1064 nm wavelength and <10 ns pulse duration. The study begins with the role of a single spherical bubble in NPLIN, later extended to bubble-bubble interactions. The experimental observations are complemented by concomitant numerical studies for parameter value estimation, such as local concentration and temperature, necessary to quantify crystallization using classical nucleation theory (CNT). The findings serve to *a priori* predict the NPLIN activity of a solution, based on the laser intensity and physicochemical properties of the solute, solvent and intrinsic impurities.

7.1.1 The experimental setup - Low-cost fluorescence microscope

A low-cost customizable microscope using optomechanical components in conjunction with a pulsed laser was constructed to primarily study laser-induced microbubble dynamics in Chapter 2. Sample experiments within in-house fabricated microfluidic channels were performed to validate the system. The setup offers flexibility in the design and costs approximately 65 % less compared to its commercial analogues.

7.1.2 Crystallization from solution using a single unbound spherical bubble

Combining high-speed video microscopy and 1-D finite element simulations, Chapter 3 demonstrated that cavitation initiated due to absorbed laser energy within supersaturated aqueous KCl solutions can trigger crystal nucleation. The solution absorption of the employed laser light (532 nm) is enhanced by intentionally adding impurity ($KMnO_4$) comparable to the NPLIN experiments in literature. The supplied laser energy is correlated to the maximum bubble radius (R_{max}), necessary to validate the bubble evolution in simulations. The numerical results suggest a momentary [$O(\mu s)$] spike in the solute supersaturation at the vapor-liquid interface to promote nucleation during bubble growth. The supersaturation emerges due to the high solvent evaporation rates during the initial growth of the bubble and therefore increases with increasing laser intensity and supersaturation in the bulk. A threshold (minimum) laser energy for crystal nucleation function of supersaturation in the bulk is recorded, similar to what is found in the literature. These are surprising results for a few reasons.

Firstly, the model solute studied, KCl has increasing solubility with increasing temperature, hence heating the supersaturated solution is expected to increase solubility, thus inhibiting crystallization from solution. The results are contradicting this basic expectation. Secondly, the work suggests a phenomenon that can be harnessed to produce crystals using laser-induced cavitation below the solution's optical breakdown threshold. This is distinct from cavitation induced crystallization experiments via multiphoton absorption using focused ultrashort laser pulse (~fs) that might involve photochemistry.

Chapter 4 extends the findings to other solutes such as NaCl and NH_4Cl with different laser wavelength (1064 nm), including KCl. Preliminary results using KCl indicated no difference in the crystallization probabilities as a function of R_{max} when compared to the results from Chapter 3 which employed a 532 nm laser. This suggests the underlying mechanism to primarily depend on R_{max} - the characteristic bubble size. Furthermore, analytical relations as a function of R_{max} and solute-solvent properties are derived for solute concentration and temperature at the vapor-liquid interface to estimate the supersaturation during the bubble lifetime. With an empirical correlation from literature for R_{max} surrounding an impurity, these analytical relations serve as a basis to rationalize the observed NPLIN (in)activity of different solutions in literature experimented using the classical technique in vials with unfocused laser. The solutions from literature include aqueous KCl, NH_4Cl, KBr, and CH_4N_2O, all subjected to a single unfocused laser pulse and probabilities determined by counting the number of vials that crystallized after a fixed observation time. Thus, the developed analytical framework will help to *a priori* predict the NPLIN activity of a solution based on the laser energy, and physicochemical properties of solute, solvent and intrinsic impurities.

7.1.3 Geometrically confined bubble(s) and crystallization from bubble-bubble interaction

While Chapters 3 and 4 involve studies of unbounded three-dimensional spherical bubbles, continuously functioning synthetic or physiological systems are mostly geometrically confined. Chapter 5 establishes unified theoretical (analytical) relations with experiments that characterize the fluid flow surrounding a single bubble within quasi-1D channel geometries. The study associates the dynamic bubble size and lifetime to the laser energy supplied in microchannels with different cross-sectional shapes, sizes, and lengths. In addition, the results inform on scaling laws for momentary flow distortions (instabilities), even for low Reynolds numbers ($Re < 1000$), that emerge from channel walls due to the oscillating nature of the flow.

The work thus extends the fundamental understanding of laser-induced forward transfer (LIFT) to arbitrary geometries with potential applications to complex or supersaturated liquids under confinement together with insights on flow transition. The adapted technique using laser allows for precise, rapid, and highly frequent flow control even in complex networks with only need for optical access to the liquid. The proposed stability diagram confirms a critical Womersley number ($Wo \approx 7$) for the onset of instabilities due to flow oscillation, while the instability growth is characterized using a dimensionless convective timescale of the flow.

Chapter 6, combining experiments, classical nucleation theory, and boundary integral element simulations, demonstrates a novel route to crystallization of salts from supersaturated solution via laser-induced bubble pairs in circular microchannels. The model solute studied, $KMnO_4$, inherently absorbs the supplied 532 nm laser pulse(s) thus avoiding the need for any external absorbing agent. With laser energy, inter-bubble distance, channel diameter and solution supersaturation as control parameters, the results show an increase in the crystal nucleation kinetics with the velocity of microjets resulting from the hydrodynamic interaction between bubbles. While the field of laser-induced crystallization via cavitation bubbles remains shrouded in speculations involving photochemistry, shockwaves and solute accumulation at the vapor-liquid interface, this finding suggest a new alternate route via bubble-bubble hydrodynamic interaction. The intense shear created by the jet as it impinges the liquid surrounding the bubble is demonstrated to influence crystal nucleation. In addition, the findings presented also enable crystallization at much lower laser energies and solution supersaturation compared to laser-induced crystallization via a single bubble in a microchannel. This avoids any potential photochemistry due to large laser intensities and extends the solution stability due to relatively low supersaturation. Furthermore, the study on the jets within microchannels contributes to the interdisciplinary field of advanced drug delivery, mechanotransduction, and vesicles/cells rheology in cardiovascular flows, via acoustic and optical cavitation.

7.2 Recommendations

Although Chapters 3 and 4 studied the NPLIN via single spherical bubbles, only aqueous solutions were discussed. Thus the proposed experiments and models (numerical and analytical) should be put to test for non-aqueous solvents, e.g., carbamazepine in acetonitrile/methanol [1] and sulfathiazole in Water/Ethanol [2] mixtures. This will further ensure the validity of the underlying NPLIN mechanism and the robustness of the models. The non-aqueous solutes will also provide insights on the polymorph selectivity using lasers in addition to aqueous glycine - one of the most iterated compound in NPLIN for studying polymorphism.

With continuously operated crystallizer/seed generator as end target, the developed models to predict NPLIN should be adapted to various channel geometries and solutions. Thus the effect of channel walls and bubble-bubble interactions on bubble dynamics and crystallization should be further validated. This dissertation however is a pioneer on the influence of bubble-bubble hydrodynamic interaction on crystallization within microchannels.

REFERENCES

[1] Aziza Ikni, Bertrand Clair, Philippe Scouflaire, Stéphane Veesler, Jean Michel Gillet, Nouha El Hassan, Françoise Dumas, and Anne Spasojević-De Biré. "Experimental demonstration of the carbamazepine crystallization from non-photochemical laser-induced nucleation in acetonitrile and methanol." In: *Crystal Growth & Design* 14.7 (2014), pp. 3286–3299. ISSN: 15287505.

[2] Wenjing Li, Aziza Ikni, Philippe Scouflaire, Xiaoxuan Shi, Nouha El Hassan, Pascale Gémeiner, Jean Michel Gillet, and Anne Spasojević-De Biré. "Non-Photochemical Laser-Induced Nucleation of Sulfathiazole in a Water/Ethanol Mixture." In: *Crystal Growth & Design* 16.5 (2016), pp. 2514–2526. ISSN: 15287505.

PART II APPENDICES

A

APPENDIX TO CHAPTER 2

A.1 Bill of materials summary

The spreadsheet containing the bill of materials (Bill of materials.xlsx) can be found in the repository: https://doi.org/10.4121/f2fd9286-c77b-4a94-a570-2306b5a0fc56. The materials are mentioned in the same order as presented in the following section. An additional spreadsheet containing the description of the materials (Description of materials.xlsx) is also provided in the repository. For convenience the component name and the corresponding part number is presented in Table A.S1. Note that the material costs furnished might vary with different suppliers, time period and the location of purchase.

Table A.S1: Component part numbers.

Designator	Component	Designator	Component
Part #1	Nano L 50-50 PIV laser	Part #31	Lab jack
Part #2	Optical breadboard	Part #32	Linear translation stage
Part #3	Allen key set	Part #33	Damped post
Part #4	Dichroic filter	Part #34	Post mounting clamp
Part #5	Kinematic fluorescence filter cube	Part #35	3-Axis travel stage
Part #6	Cage assembly rod	Part #36	Slide holder
Part #7	Cage system iris diaphragm	Part #37	Mounted LED
Part #8	Cage plate (objective)	Part #38	LED driver
Part #9	20x objective	Part #39	Pyroelectric energy sensor
Part #10	Threading adapter (objective)	Part #40	Oscilloscope
Part #11	Notch filter	Part #41	FASTCAM NOVA S16 camera
Part #12	Tube lens	Part #42	BNC coaxial cable
Part #13	Cage plate (tube lens)	Part #43	Digital delay generator
Part #14	Lens tube	Part #44	Alignment laser
Part #15	Threading adapter (tube lens)	Part #45	Alignment laser cable
Part #16	Cage cube	Part #46	Alignment laser collimator

Part #17	Rectangular silver mirror	Part #47	Detector card
Part #18	Cage assembly rod	Part #48	Shearing interferometer
Part #19	Cage plate (lens)	Part #49	Polydimethylsiloxane (PDMS) - base and curing agent
Part #20	Drop-in cage mount	Part #50	Form 3+ printer
Part #21	Achromatic doublet lens	Part #51	#1 cover glass (24x60 mm)
Part #22	Right-angle kinematic mirror mount	Part #52	Spin coater
Part #23	Round beamsplitter	Part #53	Precision tips
Part #24	Nd:YAG laser mirror	Part #54	Laser safety glasses
Part #25	Mirror mount	Part #55	Red dye
Part #26	Optical post	Part #56	Rhodamine B dye
Part #27	Right angle post clamp	Part #57	Red-fluorescent particles
Part #28	Pedestal post holder	Part #58	Flow control system
Part #29	Clamping fork	Part #59	Test target
Part #30	Cap screw		

A.2 Build instructions

The optical train is constructed predominantly using 30 mm cage components. The setup is built starting with the dichroic filter and subsequently branched in three directions namely the objective branch, tube lens branch, and the laser guidance with telescope branch as depicted in Fig. A.S1. Additionally, some laser mirrors are used to guide the laser path from the source and therefore this might vary in each case. The details of mountings for each of the components are given in the respective links provided in the bill of materials.

Microscope construction

1. First, mount the laser (Part #1) on the optical breadboard (Part #2) with the help of Allen keys (Part #3). Allocate sufficient space for the remaining components of the setup.

2. Place the dichroic filter (Part #4) inside the kinematic fluorescence filter cube (Part #5) and position it accordingly such that it is inclined at 45° to the incident laser beam. The coated side should face the incoming laser light as shown in Fig. A.S1 (a).

3. Using the help of cage assembly rods (Part #6), assemble the cage system iris diaphragm (Part #7) followed by the cage plate (Part #8) for the objective on the side of the reflected laser light as depicted in Fig. A.S1 (b).

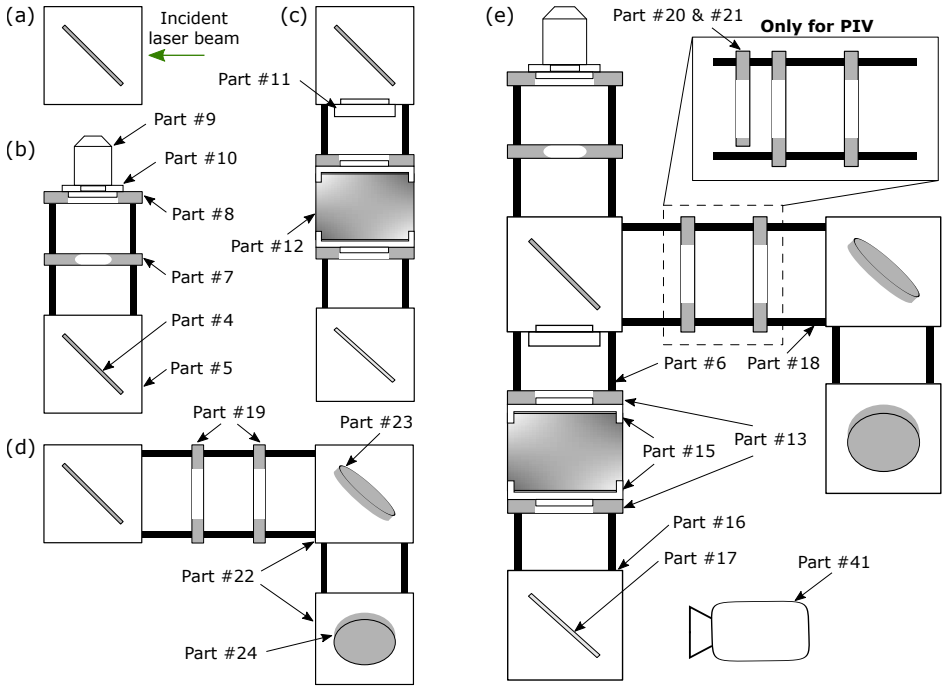

Figure A.S1: Sketches of: (a) dichroic filter in a cage, (b) sub-assembly of the objective branch, (c) sub-assembly of the tube lens branch, (d) sub-assembly of laser guidance and telescope branch, and (e) complete assembly of the microscope.

4. Screw the 20x objective (Part #9) to its cage plate while making use of the threading adapter (Part #10) in order to match the screw threads. In the current setup, the objective has a NA = 0.5 and focal length, $f_{obj} = 10\,mm$. The calculated pupil diameter of the objective is, $2\,(NA)\,f_{obj} = 10\,mm$.

5. On the opposite side of the kinematic fluorescence filter cube, secure the notch filter (Part #11) in the emission filter port with the engraved transmission arrow pointing away from the dichroic filter.

6. Following this, sandwich the tube lens (Part #12) between the two cage plates (Part #13) with the aid of threading adapters (Part #15) and then attach this sub-assembly to the cage assembly rods (as indicated in Fig. A.S1 (c)) beneath the notch filter making sure that the transmission arrow points away from the notch filter. The required magnification ($= f_{tubelens}/f_{objective}$) is achieved by choosing the tube lens with the right focal length ($f_{tubelens}$).

   In order to achieve a magnification of 20x, the tube lens with $f_{tubelens} = 200\,mm$ is chosen.

7. At the bottom, connect the cage cube (Part #16) containing the rectangular mirror (Part #17) inclined at 45° to the incident light with the cage assembly rods.

8. On the laser incident side of the kinematic filter cube, fasten the cage assembly rods (Part #18) and attach two cage plates (Part #19) for lenses as in Fig. A.S1 (d). The use of lens is required only if there is a need for varying the laser source beam diameter as shown in Fig. 2.1 in the main text. One of the cage plates is secured whereas the other is left free to slide so that adjustments can be made depending on the focal length of the lenses used. Additionally, a drop-in cage mount (Part #20) holding the achromatic doublet lens (Part #21) is mounted as shown in Fig. A.S1 (e) only while performing the PIV experiments.

9. Take a couple of right-angle kinematic mirror mounts (Part #22) each encompassing a round beamsplitter (Part #23) and a round laser mirror (Part #24) respectively and connect them using the cage assembly rods. Insert this subassembly to the other end of the cage assembly rods extending from the kinematic filter cube as represented in Fig. A.S1 (d). The distance between the two mirror mounts can be adjusted for varying the height based on the laser source position by adding or removing the cage assembly rods.

10. In order to erect the setup upright, secure the right angle kinematic mirror mount to the optical breadboard with the help of optical posts (Part #26), right angle post clamp (Part #27), pedestal post holder (Part #28), clamping fork (Part #29) and cap screw (Part #30). Place the lab jack (Part #31) beneath the cage cube for support as portrayed in Fig. 2.2 in the main text.

11. Alongside the setup, clamp the linear translation stage (Part #32) to the breadboard and mount the damped post (Part #33) on top of it (refer Fig. 2.2 in the main text - side view). Insert the post mounting clamp (Part #34) through the damped post and tighten it. By making use of the optical posts and right angle post clamp, set up the 3-axis travel stage (Part #35). Connect the slide holder (Part #36) to the travel stage using an optical post and ensure that it remains on top of the objective by adjusting the height. The linear travel stage facilitates a larger translation in the horizontal direction whereas the 3-axis travel stage helps with smaller translations in all three directions. In addition, the post mounting clamp provides a rotational degree of freedom to the slide holder.

12. With the support of an optical post, post holder, clamping fork and cap screw, place the mounted LED (Part #37) on top of the slide holder (refer Fig. 2.2 in the main text - side view). Connect the cable from the LED light to the LED

driver (Part #38) and power the LED driver using the power source. The LED driver controls the light intensity.

13. Similarly, align the energy sensor (Part #39) above the beamsplitter to measure the energy of each laser pulse. The output of the sensor is connected to the oscilloscope (Part #40) which reads the measured output voltage. The energy can be calculated from the voltage using the calibration curve of the energy sensor provided by the manufacturer for the laser wavelength used.

14. Finally, position the camera (Part #41) in-line with the cage cube as shown in Fig. A.S1 (e). Link the camera and laser by means of a BNC cable (Part #42) to the digital delay generator (Part #43). The camera is triggered to record starting with 5 image frames before pulsing the laser so as to image the initial condition of the sample just before laser irradiation.

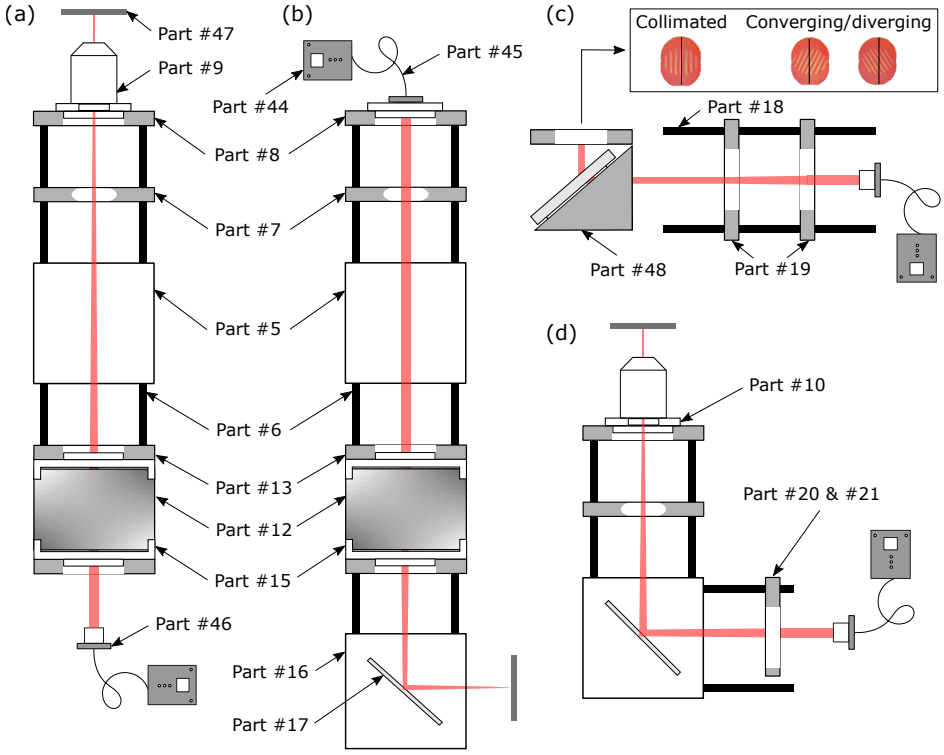

Figure A.S2: Illustrations of (a) the alignment of objective and tube lens, (b) the alignment of camera, (c) the alignment of lenses, and (d) the alignment of doublet lens for PIV.

Alignment of the optical components

During the construction of the microscope, the objective, tube lens and camera are initially positioned based on the design specifications provided by the manufacturer. The working distance of the tube lens is used as the distance between the tube lens and the camera. While, the distance between the objective and tube lens is calculated using [1], $f_{\text{tubelens}}(\Xi_2 - \Xi_1)/\Xi$, where Ξ_1 is the objective exit pupil diameter, Ξ_2 is the tube lens entrance pupil diameter and Ξ is the camera's sensor size.

However, in practice, an alignment laser (Part #44) is used for the purpose of aligning these components precisely [2]. This laser is first passed through the tube lens towards the objective as shown in Fig. A.S2 (a). During this process, the dichroic and notch filters are removed temporarily so as to allow the transmission of the laser. The position of either the objective or the tube lens is varied such that the alignment laser exiting the objective's front lens remains collimated at any distance further from the objective. This is ensured with the help of a detector card (Part #47). The above procedure allows us to determine the exact position of the tube lens relative to the objective or vice versa. The same alignment procedure can also be followed for non-infinity corrected objectives. However, for non-infinity corrected objectives a very precise positioning of the objective relative to the tube lens is required to overcome the drawbacks due to potential loss in the image quality. On the other hand, infinity-corrected objectives allow the positioning of additional optical components such as dichroic and notch filters between the objective and camera without causing any aberrations or distortions.

In a similar manner, the precise position of the camera is determined to obtain a sharp image. First, the objective is unscrewed from the cage plate temporarily and the alignment laser is placed such that it passes through the kinematic fluorescence filter cube (without the dichroic filter) towards the direction of tube lens. The point where the tube lens focuses the alignment laser is found using the detector card as depicted in Fig. A.S2 (b). The camera sensor is mounted exactly at this marked position. In this configuration, an additional mirror is used in between the tube lens and the camera to guide the light - allowing us to position the camera horizontally (stable orientation).

In the case of using a pair of lenses (as a Galilean telescope) to vary the source beam diameter, the lenses are initially placed at a distance equal to the sum of their focal lengths. In order to fix this distance accurately and ensure whether the beam remains collimated in the far field, the lenses are positioned in between the alignment laser and the shearing interferometer (Part #48) as shown in Fig. A.S2 (c). The laser light passing through the lenses forms an interference fringe pattern on the diffuser plate (or shear plate) of the shearing interferometer. When the fringes are parallel to the ruled reference line marked in the diffuser plate, the beam is collimated, and hence this distance between the lenses can be maintained while performing the experiments.

Alignment for PIV experiment

For performing the PIV experiment, a doublet lens is placed in between the right-angle kinematic mirror mount with the beamsplitter and the kinematic fluorescence filter cube containing the dichroic filter. The focal length of the doublet lens is chosen such that:

$$\textit{focal length of doublet lens} = \textit{focal length of objective lens} \times \textit{demagnification},$$
$$\textit{demagnification} = \textit{diameter of laser beam} / \textit{field number},$$

where the desired *field number* is the diameter of the view field. The position of the doublet lens is determined such that the beam from the alignment laser passing through the doublet lens remains collimated when it leaves the objective as represented in Fig. A.S2 (d).

B

APPENDIX TO CHAPTER 3

B.1 Bubble incidence in experiments

Figure A.S1 shows the probability of bubble incidence observed in experiments with ultrapure water (18.2 MΩ cm, ELGA Purelab) and aqueous $KMnO_4$ (3.26 mg per 100 g of water). Since water has no absorbance to 532 nm light the observed bubble formation is attributed to the non-linear absorption with the possibility of plasma formation.

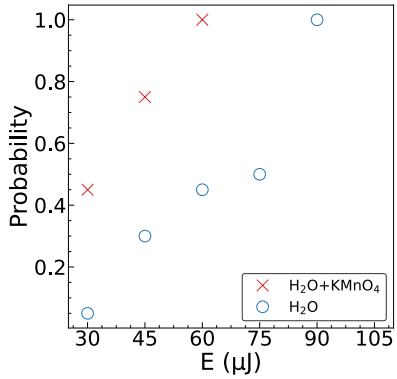

Figure A.S1: Probability of bubble incidence in experiments. The results are averaged over 20 trials.

B.2 Solubility

The solubility measurements were conducted using an equipment (Crystalline, Technobis Crystallization Systems) that measures the turbidity (transmissivity) of the solution to estimate the solubility line (clear point). The experiments were performed using 8 ml HPLC vials stirred at 700 rpm subjected to a heating rate of 0.1 K/min. The clear point is estimated as when the solution reaches 100 % transmission. The experimentally measured solubility from this work is presented in Fig. A.S2. The

solubility of KCl (without $KMnO_4$) was measured to be 35.97 g/100 g-H_2O at 298 K, used for estimating supersaturation in the bulk.

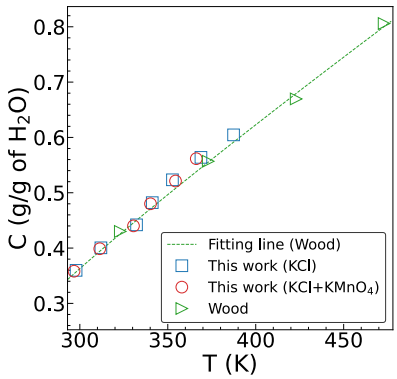

Figure A.S2: KCl solubility estimated using turbidity measurements. Each data point corresponds to an average of 3 trials (except T = 388 K, which contains one). The experimental results from this work are compared with those reported by Wood [3].

The solubility data from Wood [3] is best fit using the relation $(280.54 + 3.97\,(T - 273)^{0.92}) \times 10^{-3}$, where T is the temperature in Kelvin.

B.3 Predicted Bubble Sizes in NPLIN

In relation to the impurity heating mechanism proposed for NPLIN, the size of microbubbles hypothesized to appear around heated nano-impurities is predicted using an empirical relation from literature [4] employing Mie theory [5]. Comparing the predicted bubble size to those observed in this work provides a sanity check.

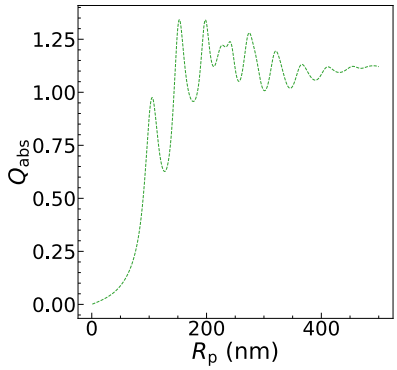

Figure A.S3: Absorption efficiency estimated using Mie theory [5]. The value for the complex refractive index is $2.3456 + i\,0.0926$ (at 532 nm) [6].

The elemental analysis of KCl from the manufacturer indicates the element iron (Fe) as the major impurity ($\leqslant$ 3 ppm). The relationship between the vapor bubble radius and the insoluble iron nanoparticle (Fe_3O_4 - one of the most common states of Fe) radius is empirically approximated as $R_{max} \propto (Q_{abs} R_p^2 I_0)^{(1/3)}$ [4]. R_p is the radius of the nanoparticle, I_0 is the laser intensity and Q_{abs} the absorption efficiency calculated using Mie theory [5] (see Fig. A.S3). The experiments by Kacker et al. [7] used a filter with pore size of 0.45 μm and reported a minimum laser energy threshold of $\approx 5\,MW/cm^2$ [8], for KCl crystallization with $S_\infty = 1.048$. In calculations, therefore a nanoparticle radius of 225 nm is used and the vapor bubble radius is estimated to be 170 μm, when compared to a 141 μm radius bubble formed using 50 nm nanoparticles and 790 MW/cm^2 laser intensity [4]. By roughly extrapolating the experimental data from this work to $S_\infty = 1.048$, the estimated bubble size should be a sufficient condition for crystallization.

B.4 Experimental validation

Does the bubble stay hemispherical ?

As the experimental setup does not allow imaging the bubble from side view, it is not possible to quantify how much the bubble deviates from the hemispherical shape. The bubble nucleates close to the bottom surface ($<$ 10 μm) because this is where the laser is focused. After nucleation, the bubble growth is fast and inertia-driven. To test the validity of the hemispherical assumption, two potential disturbances that can affect the bubble shape is analyzed, without which the overall appearance of the shape of the bubble would be of a hemispherical cap during the entire growth and collapse process [9]. The arguments are as follows:

• Viscous boundary layer over cover glass: In reality, there may be some degree of deformation at the vapor-liquid interface near the cover glass (bottom surface), but because of the inertial character of the growth-collapse of the bubble, any wall-tension induced deformation is expected to remain relatively localized (relative to the size of the bubble) close to the cover glass. For illustration, the experiment with largest bubble lifetime is chosen ($t_{osc} = 72$ μs, refer Fig. 5 in main text) since the length scale for the diffusive growth of the viscous boundary layer is proportional to t_{osc} following the relation $\sqrt{(1.72^2 \mu_L t_{osc}/\rho_L)}$ [10]. Where μ_L and ρ_L are the solution's dynamic viscosity and density respectively. The calculated length scale is 13.4 μm. Therefore the deformation should be relatively localized when compared to the corresponding bubble size ($R_{max} = 325$ μm, refer Fig. 5 in main text), supporting the hemispherical bubble assumption.

• Buoyancy: It is necessary to quantify whether a bubble can become spherical over time as it can be driven away from the cover glass due to buoyancy. Therefore the terminal velocity (v_{rise}) in the presence of buoyancy force is calculated assuming the bubble is spherical, $v_{rise} = 2R_{max}^2(\rho_L - \rho_V)g/(9\mu_L)$. Where g is the acceleration due to gravity and the density of vapor, $\rho_V \ll \rho_L$. Taking $R_{max} = 325\,\mu m$ (estimated maximum bubble size in this work), the calculated v_{rise} is 0.26 m/s. Therefore for the corresponding bubble lifetime $t_{osc} = 72\,\mu s$, the length scale of bubble rise is 18.72 μm (5.76 % of R_{max}), supporting the hemispherical bubble assumption.

Can the hemispherical bubble in experiments be analyzed as a sphere ?

Below it is verified if the bubbles in the experiments behave similar to a sphere due to the plane of symmetry offered by the cover glass of the microfluidic device (refer Fig. 1 in main text). This claim is validated by comparing the lifetime of the hemispherical bubbles against the theory for spherical bubbles using Rayleigh collapse time [11].

Figure 2 (b) (in the main text) displays a clear increase in the maximum radius (R_{max}) and lifetime of the bubble (t_{osc}) with the supplied laser energy (E). Theoretically, the dynamics of hemispherical bubble is compared to an unbound spherical bubble using the time that the bubble takes to collapse from its maximum radius to zero, known as the Rayleigh collapse time (t_{col}). For an unbound spherical bubble [11],

$$t_{col}/R_{max} = 0.91468\,[\rho_L/(p_\infty - p_V)]^{1/2}, \tag{A.S1}$$

where $\rho_L = 1175\,kg/m^3$ is the density of the solution, $p_\infty = 1.013$ bar is the ambient pressure and p_V is the vapor pressure within the bubble. If the bubble is assumed to be saturated, p_V can be estimated by quantifying the temperature surrounding the bubble during its collapse. The temperature following the collapse of a laser-induced vapor bubble has been measured by Quinto-Su et al. [12]. By fitting a curve to their data, the temperature rise is found to have a power law dependence on laser energy ($\propto E^{0.5}$). By extrapolating this reported energy range ($E = 1 - 7\,\mu J$) to the experiments in this work ($E = 30 - 60\,\mu J$) where R_{max} is within the field of view, the temperature rise is estimated to be $19 - 27$ K, relative to a room temperature of 298 K. This temperature is assumed to be surrounding the bubble during its collapse and the corresponding p_V is determined based on the saturation pressure of water. In the experiments of this work, the ratio t_{col}/R_{max} is calculated to be 103.52 ± 8.6 ms/m, which is in good agreement with the estimated value of 104.58 ± 1.31 ms/m for an unbound spherical bubble.

B.5 Morphologies

Three different morphologies of KCl were observed in the experiments, represented in Fig. A.S4. The morphologies can be classified based on the number of significant dimensions: cube - three, rectangle - two and needle - one. To get better insight on

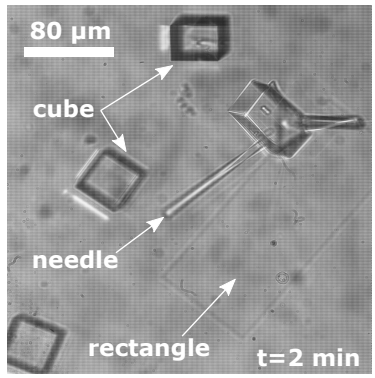

Figure A.S4: Illustration of KCl crystal morphologies observed in experiments.

the probability of occurrence of each of the morphology, the morphology chances is calculated. The morphology chance is defined as the ratio of number of trials in which a certain morphology is spotted to the number of trials that crystallized. Fig. A.S5 shows the recorded chances from experiments for each of the morphologies.

There is an increase in the probability of finding a rectangle or needle with the increase in bulk supersaturation and laser energy. The increase in the nucleation rate (number of nuclei formed per unit volume per unit time) is non-linear with respect to the local supersaturation (the supersaturation at the vapor-liquid interface in this case) [13]. Therefore, the amount of solute available in the bulk per nucleus is expected to decrease with increasing laser energies or vapor-liquid interface supersaturation. This explanation is also in agreement with the reported morphological changes based on solute mass transfer [14, 15].

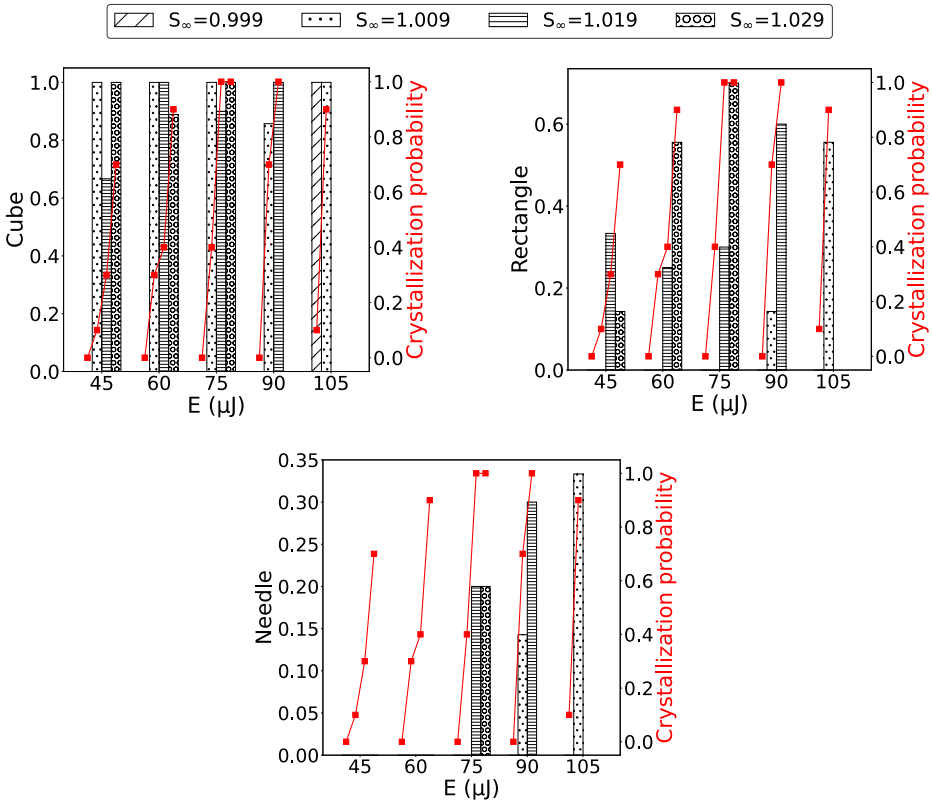

Figure A.S5: The bars represent the morphology chances from experiments and the red line represents the crystallization probability. $S = S_\infty$ - the supersaturation in the bulk. The crystallization probability is the number of trials that crystallized to the total number of trials performed. The reported data are for a fixed observation time of 2 minutes from the time of the laser pulse.

B.6 Simulations: Parameters, Boundary Conditions and Validation

The vapor bubble is approximated as a lumped system and initialize the model with radius $R(t = 0) = 0.5\,\mu m$. This initial radius was chosen based on the calculated laser spot size and the objective's depth of field, discussed in Materials and Methods of main text. At $t = 0$, the vapor bubble is assumed to be saturated at a temperature of $T_V = 650\,K$ - the spinodal temperature of a saturated NaCl solution [16]. The initial temperature profile of the solution surrounding the vapor bubble is established using $T(\xi) = T_\infty + (T_V - T_\infty)\exp\left[-(\xi/\delta_T)^{25}\right]$, where T_∞ is the ambient temperature, δ_T is the thermal boundary layer thickness and $\xi = r - R$, is the radial distance from the interface. A high exponent of 25 is used to approximate a step function while avoiding numerical instabilities near $\xi \approx \delta_T$. In this model, the change in R due to phase change

is neglected at the vapor-liquid interface. This is justified due to negligible effect of phase change on the liquid velocity, $(dm_V/dt)/(\rho_L A_V) \ll dR/dt$, in simulations.

While the momentum equation (Rayleigh–Plesset) is an ordinary differential equation that is solved without the need for meshes, the heat and mass transfer is solved in the frame of reference of the moving vapor-liquid interface. The simulations were performed with COMSOL Multiphysics (version 5.6) using equation-based modeling functionality [17]. Since all the governing equations under consideration are in spherically symmetric coordinates, the analyses are performed in one dimension.

Parameters

• Supersaturation (S) and Solubility ($C_{sat,298}$): solubility of KCl, $C_{sat,298} = 0.3597$ g/g-H_2O at 298 K. Therefore, KCl supersaturation in the bulk $S_\infty = C_\infty$ [concentration in g/g-H_2O] / $C_{sat,298}$ [solubility at 298 K].

• Latent heat of vaporization of the solution (H_L): estimated using the empirical relation $H_L = (2230.1 - 280\, C|_{r=R})$ kJ/kg, from the work by Lunnon [18].

• Thermal conductivity of the solution (k): in the work by Ozbek et al. [19], an empirical correlation equation for aqueous NaCl with molality (m) 5 mol/kg was reported to be $k = -5.693 \times 10^{-6}(T-273)^2 + 1.519 \times 10^{-3}(T-273) + 0.5574$ W/(m K). For simplicity, the value is assumed to be constant with $k = 0.625$ W/(m K), since its change between $273 - 523$ K is less than 5 %.

• Density of the solution (ρ_L): was measured to be 1173.3 kg/m^3 with a density meter (DMA5000, Anton Paar) using a solution with $S_\infty = 1$. In simulations, the density was assumed to be independent of temperature and supersaturation, with $\rho_L = 1175$ kg/m^3.

• Specific heat capacity of the solution (c_{pL}): was measured experimentally to be 3000 J/(kg K) by Toner et al. [20] for an aqueous KCl solution with molality (m) 4.62 mol/kg.

• Dynamic viscosity of solution (μ_L): assumed to be constant (0.984 mPa s) [21] - independent of temperature and pressure. Note that the contribution in the Rayleigh-Plesset equation by the viscosity $(4\mu_L/R)(dR/dt)$ is two orders of magnitude less than $(p_V - p_\infty)$ for all conditions studied in this work.

• Surface tension of solution (σ_{gl}): assumed to be constant (0.079 N/m) [22] - independent of temperature and pressure. Note that the contribution in the Rayleigh-Plesset equation by the surface tension $2\sigma_{gl}/R$ is two orders of magnitude less than $(p_V - p_\infty)$ for all conditions studied in this work.

• Diffusivity of KCl (D): reported to be 1.92×10^{-9} m^2/s at 298 K [23]. Within the solution, D is estimated as a function of temperature to scale according to the Stokes–Einstein equation, $D \propto T/\mu_L$. The dynamic viscosity as a function of temperature is estimated using the empirical equation from the work by Kestin et al. [24].

• Specific heat capacity of vapor (c_{pV}): the specific heat capacity of superheated steam at high pressure (650 K and 220 bar) is calculated to be 2990.81 J/(kg K) using the empirical equation by Schmidt [25]. The specific heat of saturated steam at 323 K is 1948.24 J/(kg K). Since, H_L is an order of magnitude higher than $c_{pV}(T_V - T_\infty)$ in the energy equation for vapor, and in addition, the temperature of the vapor is also governed by the heat convected by the solution surrounding the bubble, c_{pV} is approximated to be constant, 2500 J/(kg K).

• Saturation pressure of the solution (p_s): estimated using the empirical relation $p_s = p^\circ_{sat}(1 - 33\, C|_{r=R}/M_{KCl})$, from the work by Leopold et al. [26]. Here p°_{sat} is the saturation pressure of water, C is the concentration of KCl in the solution (in g/g-H_2O) and M_{KCl} the molar mass of KCl.

• $\widehat{C}$ is the concentration of KCl in the solution in g/g of solution. $\widehat{C} = C/(1 + C)$.

• Other constants: specific gas constant, $R_g = 461.52$ J/(kg K). Ambient pressure, $p_\infty = 1.013$ bar. Ambient temperature, $T_\infty = 298$ K. Molar mass of KCl = 74.55 g/mol.

Meshing

A finer mesh for the solution domain is established closer to the vapor-liquid interface compared to the farther surroundings. A rough estimate for the penetration depth of solute elements is calculated using $\sqrt{4Dt_{osc}}$, where t_{osc} is the vapor bubble lifetime. Using this, the calculated solute penetration depth at 298 K for a 100 μs bubble is 0.88 μm. A uniform grid size of 50 nm is established over a distance of 2 μm from the vapor-liquid interface. Then the next 198 μm length is divided into 1200 grid cells distributed using an arithmetic sequence with an element ratio of 5 [17]. The equations are solved using a time step (Δt) of 1 ns. With α as the solution's thermal diffusivity and h as the minimum grid size, the maximum value for $\sqrt{4\alpha\Delta t}/h$ and $\sqrt{4D\Delta t}/h$ is 0.53 and 0.2, respectively.

Figure A.S6 shows the obtained grid convergence for the values presented in Table A.S1.

Table A.S1: Grid values. In all the cases the grid cells inside the domain with 198 μm was distributed using an arithmetic sequence with an element ratio of 5 [17].

	h (nm)	Δt (ns)	Number of cells (initial 2 μm)	Number of cells (farther 198 μm)
Type 1	12.5	0.05	160	4800
Type 2	50	1	40	1200
Type 3	200	20	10	300
Type 4	500	100	4	120

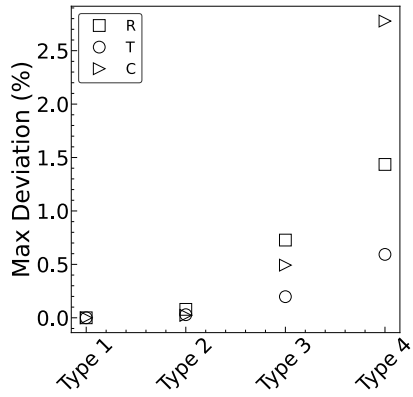

Figure A.S6: Grid convergence study. The simulations were performed for the grid values mentioned in Table A.S1. For all the cases, $\sqrt{4\alpha\Delta t}/h \in [0.48, 0.6]$ and $\sqrt{4D\Delta t}/h \in [0.16, 0.2]$. The maximum deviation percentage was calculated at $t = 7\,\mu s$ with respect to the values from Type 1. R is the position of the vapor-liquid interface from the laser focal spot (center), and T and C are the temperature and solute concentration, respectively, in the liquid domain (200 µm long) surrounding the vapor bubble. The deviations were calculated with the values from Type 1 as the reference.

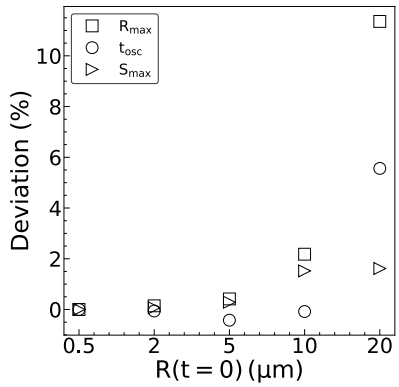

Figure A.S7: Sensitivity analysis for different initial radii of the bubble in simulations. The deviation is calculated using the reference values from $R(t = 0) = 0.5\,\mu m$ ($R_{max} = 228\,\mu m$). The simulations are for $E = 43.14\,\mu J$ and $S_\infty = 1.019$ (at 298 K). The value of $\delta_T(\mu m) \in \{25.5, 24, 21, 16.3, 8.35\}$ correspond to $R(t = 0) \in \{0.5, 2, 5, 10, 20\}$, respectively.

Boundary conditions

• For the heat transfer within the solution, Dirichlet conditions are applied at either end, with $T = T_V$ at the vapor-liquid interface and $T = T_\infty$ at the exterior domain of the simulation.

• For the mass transfer within the solution, a Neumann condition is applied at the vapor-liquid interface, with the solute flux given by $(dm_V/dt)C_\infty/(\rho_L A_V)$, and a Dirichlet condition $C = C_\infty$ at the exterior domain of the simulation.

• Sensitivity analysis of the key parameters, such as: R_{max}, t_{osc} and S_{max} for different $R(t = 0)$ was performed. A small effect on the parameters ($< 12\%$) was observed, even when $R(t = 0)$ is increased by a factor of 40, Fig. A.S7. The analyses were performed by fixing the $E = 43.14\,\mu J$ and $S_\infty = 1.019$ (at 298 K). The value of δ_T is changed with $R(t = 0)$ to maintain the E constant. This demonstrates the efficiency of the model and validity of the boundary conditions. Especially, it emphasizes the only tunable parameter in simulations, δ_T, as a parameter that characterizes the energy surrounding the initial bubble (similar to laser energy in experiments) and is not explicitly a fudge factor.

Energy parameter δ_T

δ_T characterizes the initial thermal energy surrounding the bubble to be used for growth in the simulations. Since only the dynamic bubble radius from experiments is matched to simulations, the energy supplied by the laser is indirectly related to the δ_T from simulations. Analytically the energy supplied in the simulations can be calculated as,

$$E_{sim} = m_V(H_L + c_{pV}(T_V - T_\infty)) + 4\pi\rho_L c_{pL} \int_0^\infty (R(t = 0) + r)^2 (T_V - T_\infty) \exp\left[-(r/\delta_T)^{25}\right] dr. \tag{A.S2}$$

The values for the variables in Eq. A.S2 are chosen at $t = 0$, and therefore excludes the kinetic energy. Energy surrounding a hemisphere is $E = E_{sim}/2$. The dependence of R_{max} on E from simulations is represented in Fig. 5 of the main text.

In the experiments, since the bubble momentarily goes out of the field of view for higher energies ($E \geqslant 75\,\mu J$), for all cases, the experiments are numerically simulated by matching the bubble's lifetime (t_{osc}). This approach to plotting experiments against simulations is rationalized using the Rayleigh collapse time equation, $t_{osc}/R_{max} = 1.83\,[\rho_L/(p_\infty - p_V)]^{1/2}$, which relates the bubble lifetime (t_{osc}) and maximum bubble size (R_{max}). As the initial thermal energy surrounding the bubble is what dictates its dynamics, the energy value from the numerical model is determined using Eq. A.S2.

Effect of initial bubble pressure

While the thermal energy surrounding the bubble influences the R_{max}, the initial bubble pressure would influence dR/dt close to formation. In simulations, violating

the current assumption of a saturated bubble at $t = 0$, the bubble was intentionally supplied with very high pressure of 2000 bar. Thus, while saturated vapor bubble in a supersaturated aqueous solution has 192 bar @ 650 K [16], the condition is changed to 500-2000 bar @ 650 K. The maximum temperature of the liquid surrounding the bubble was maintained 650 K - the spinodal temperature limit [16]. In addition, the initial bubble radius, $R(t=0)$, was changed from 0.5μm to 5μm to increase the mechanical energy ($E_{bubble} \propto p_V V_V$) [27]. The model is less sensitive for $R(t = 0) = 0.5 - 5\ \mu m$ (refer Fig. A.S7), provided the same thermal energy is supplied surrounding the bubble. The results are presented in Fig. A.S8.

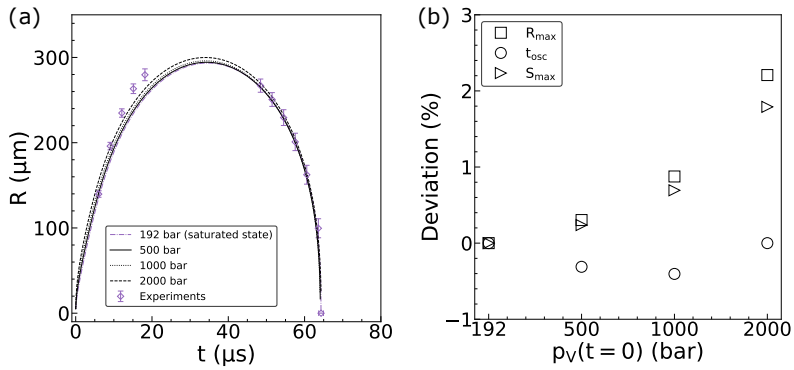

Figure A.S8: (a) Sensitivity analysis for different initial pressure of the bubble in simulations. The experiment is for $E = 75\ \mu J$. The simulations are for $\delta_T = 28\ \mu m$ with $R(t = 0) = 5\ \mu m$. (b) The deviation is calculated using the reference values from 192 bar.

As the bubble pressure is increased at $t = 0$ a decrease in deviation in dynamic bubble size (R) is noticed between the experiments and simulation. Such high initial bubble pressures [$O(1000\ bar)$] can exist only if non-linear absorption is involved with potential plasma formation [28]. The argument is in agreement with the experimental observation on the increase in probability of bubble formation for $E \geqslant 75\ \mu J$ in absence of $KMnO_4$, reported in Section B.1. As the dR/dt increases the rate at which the pressure drops within the bubble increases. Consequently, the difference between the bubble pressure and the saturation pressure of the liquid at the interface increases leading to increased solvent evaporation rates, estimated using Hertz-Knudsen equation [29]. Thus the increase in initial vapor pressure reduces the mismatch in R between experiments and simulations, with a consequent increase in the interface peak supersaturation (S_{max}). The observed increase in S_{max} further validates the proposed nucleation hypothesis based on solute accumulation at the interface.

Solute and heat conservation

The conservation of solute mass is shown in Fig A.S9. When the solution evaporates, the dissolved solute is assumed to remain in the liquid phase. Therefore, at any time instant, the solute mass that was dissolved in the evaporated solvent ($m_V C_\infty$) should be equal to the excess solute present in the solution ($\int_R^\infty 4\pi r^2 \rho_L (\widehat{C} - \widehat{C}_\infty) dr$). Fig A.S10 shows the corresponding mass flux density of the solvent at the vapor-liquid interface.

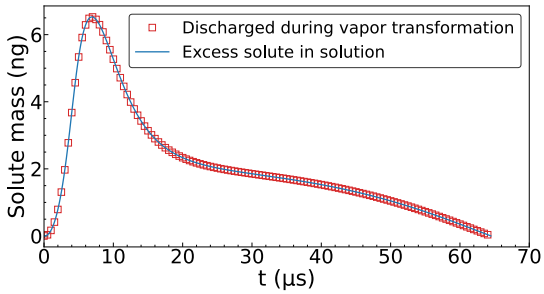

Figure A.S9: Solute conservation. The represented data from simulations is for $\delta_T = 32.5$ μm (E = 88.2 μJ - for a hemispherical vapor bubble) and $S_\infty = 1.019$.

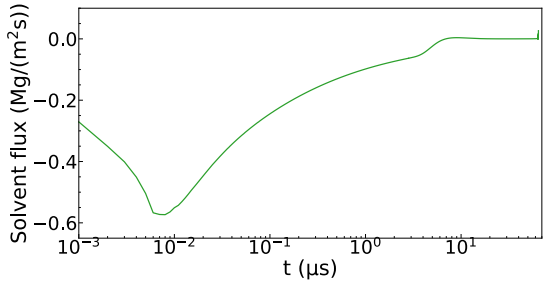

Figure A.S10: Solvent mass flux density at the vapor-liquid interface. The negative sign indicates evaporation. The represented data from simulations is for $\delta_T = 32.5$ μm (E = 88.2 μJ - for a hemispherical vapor bubble) and $S_\infty = 1.019$.

Due to the action of non-conservative force as a consequence of solution viscosity ($\propto 4\mu_L \dot{R}/(\rho_L R)$), the total energy is not conserved. Moreover, the force due to surface tension ($\propto 2\sigma_{gl}/(\rho_L R)$) and external force due to ambient pressure (p_∞) are expected to do negative work on the system during bubble expansion and positive work during the collapse, Fig. A.S11. The total energy equals the sum of sensible heat (vapor and liquid), latent heat (vapor) and kinetic energy of the solution at any time instant. At the start of the process, the thermal energy of the liquid decreases due to evaporation. Correspondingly, an increase in the energy content of the vapor and the kinetic en-

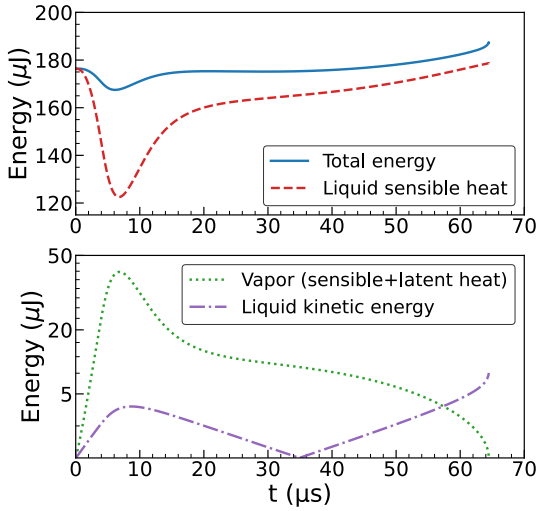

Figure A.S11: Energy trends. The represented data from simulations is for $\delta_T = 32.5\,\mu m$ ($E = 88.2\,\mu J$ - for a hemispherical vapor bubble).

ergy of the solution are seen. As expected, these trends reverse in magnitude during condensation.

B.7 Solute-solution interfacial tension calculation

The rate of nucleation (the number of nuclei formed per unit time per unit volume) is expressed using [13],

$$J \propto S \exp\left[-16\pi v_0^2 \sigma_{sl}^3/(3k_B^3 T^3 \log^2(S))\right]. \tag{A.S3}$$

Table A.S2 provides the values used for calculation.

From the numerical simulations performed, the maximum supersaturation (S_{max}) was found to occur between $458 - 464$ K. Thus, the σ_{sl} from Eq. A.S3 was calculated to be $3.7^{+0.47}_{-0.65}$ mJ/m^2 using the average temperature of 461 K and the slope value of $12.75 \pm 5.53 \times 10^{-3}$ obtained from Figure 5 (a) in the main text.

Mersmann calculated a simple relation for the solute-solution interfacial tension based on thermodynamics as [31],

$$\sigma_{sl} \propto T \log\left(\frac{\rho_{KCl}}{\widehat{C}\,\rho_L}\right). \tag{A.S4}$$

The values for the parameters are taken from Table A.S2. $\widehat{C}$ is the solute concentration in g/g of solution. During the event when maximum supersaturation at the vapor-liquid

Table A.S2: Physical and derived parameter values for aqueous KCl solution.

Parameter	Description	Value
ν_0	Solute molecular volume	6.238×10^{-29} m^3
k_B	Boltzmann constant	1.381×10^{-23} m^{2}kg/(s^{2}K)
B	Gradient(slope) for $\log(J/S)$ vs $1/\log^2(S)$ [Eq. A.S3]	6.02 ± 3.95
ρ_{KCl}	Solute density	1989 kg/m^3
ρ_L	Solution density (at 25 °C)	1175 kg/m^3
ρ_L	Solution density. Obtained by curve fit using the data from Ref. [30] (T in K)	$(-4.41/(48.28 + T - 273)) + 1.24$ g/m^3
M_{KCl}	Molar mass of solute	74.55 g/mol
N_A	Avogadro constant	6.023×10^{23} mol^{-1}

interface occurs: using the values of $\widehat{C} = 0.46$ g/g and $\rho_L = 1221$ kg/m^3 at 461 K, the calculated value is $\sigma_{sl} = 3.51$ mJ/m^2 for 298 K.

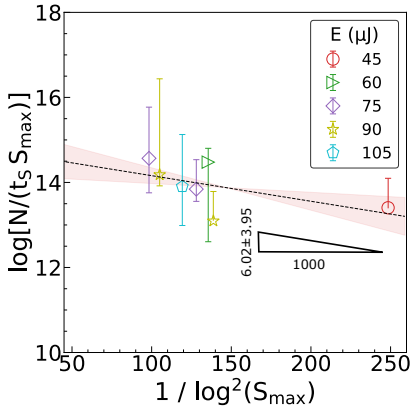

Figure A.S12: Relation between the experimentally observed median of crystal count (N is the median only in this case) and simulated peak supersaturation (S_{max}). $N/t_s \propto J$, where t_s is the time for which $S > 1$ in simulations and J the nucleation rate. The error bars represent the interquartile ranges.

Figure A.S12 shows the slope obtained when the median of the crystal count observed in experiments is taken into account for calculation. By using the value of this slope in Eq. A.S3, the σ_{sl} value is estimated to be $2.88^{+0.53}_{-0.86}$ mJ/m^2 (at $\approx 458 - 464$ K). This obtained value, when calculated for 298 K (2.73 mJ/m^2), is in excellent agreement with the σ_{sl} values reported for supersaturated KCl solutions, $2.73 - 2.91$ mJ/m^2

[32–34]. From the analysis, the median value of the crystal count from experiments closely estimates the σ_{sl} values reported for supersaturated KCl solutions, compared to mean values. The reasoning lies in the statistical approach since, in this work, the recorded data is skewed for each data point (10 trials each). Therefore median is a good measure of central tendency.

B.8 Miscellaneous Calculations

Estimate of the R_{max} *in experiments*

In literature, the lifetime of the bubble (t_{osc} - time taken for one oscillation) is roughly estimated as [35, 36], $t_{osc} = 2\,t_{col}$. Thus from Eq. A.S1, the R_{max} in experiments can be estimated using t_{osc}. The p_V in the equation is estimated assuming saturated conditions where the temperature is obtained by extrapolating the values for the reported energy range ($E = 1 - 7$ μJ) by Quinto-Su et al. [12].

Shock waves

Explosive formation of a cavitation bubble or its implosion (collapse) can lead to transient high-pressure environment (shockwaves, ~GW/cm^2) surrounding the bubble [27, 37]. These emitted shock waves would compress the liquid as it propagates outwards and decays over time. The significance of shock wave in crystal nucleus formation is determined to eliminate its possibility and further strengthen the mechanism based on evaporation leading to supersaturation spike at the vapor-liquid interface.

The change in chemical potential $(\Delta\mu)_{\Delta p}$ of the solution due to pressure changes is quantitatively estimated using [38],

$$(\Delta\mu)_{\Delta p} = \Delta V_m \Delta p - \Delta S_m \Delta T. \tag{A.S5}$$

Where ΔV_m and ΔS_m are the change in the volume and entropy per mole of the solute. Conditions under which $(\Delta\mu)_{\Delta p} > 0$ should result in an increase in crystallization probability due to the shock wave. For simplicity, the solution properties is assumed to be that of water and the equation of state of water is used to calculate the changes [39], refer Table A.S3. For example, the parameter values calculated for $\Delta p = 1$ GPa are $\Delta V_m = 37.02\,\mu m^3$/mole, $\Delta S_m = 15.61$ J/(K mole) and $\Delta T = 36$ K.

Venugopalan et al. [27] measured the size and shape of the laser-induced plasma together with the pressure of the emitted shock wave. In Section B.4, the theoretically calculated diameter and length of the laser spot are 0.762 μm and 1.71 μm, respectively. For simplicity, the plasma is assumed to be spherical and the initial plasma diameter is taken to be 1.236 μm. Since the experimentally measured plasma volume

Table A.S3: Equation of state of water from shock wave measurements. The equations for ΔS_m, ΔV_m and ΔT are obtained by curve fitting the values from Rice et al. [39] for $\Delta p \in \{0, 1.5\,\text{GPa}\}$. The Δp in the equations are in units of GPa.

Parameter	Description	Value
ΔV_m	Change in molar volume	$0.1786\, M_{KCl} \Delta p^{0.5019} / C_\infty$ [μm^3/mole]
ΔS_m	Change in molar entropy	$0.0753\, M_{KCl} \Delta p^{1.844} / C_\infty$ [J/(K mole)]
ΔT	Change in temperature	$36\, \Delta p$ [K]

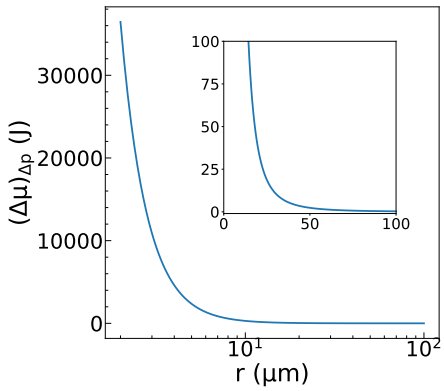

Figure A.S13: The change in solution's chemical potential due to pressure ($(\Delta\mu)_{\Delta p}$) at different positions from the laser focal spot (as the shock wave propagates). The curve starts at $r = 2\,\mu m$, the initial radius of the speculated plasma.

was found to be larger than the theoretical volume by a factor of ≈ 16 [27], in this work, the calculations for initial plasma diameter is corrected to 4 μm.

Figure A.S13 shows the calculated value of $(\Delta\mu)_{\Delta p}$ at different radial positions from the laser focal spot (bubble center). In this calculation, the pressure was assumed to radially decay with r^{-2}, with the pressure at the vapor-liquid / plasma-liquid interface to be 1 GPa [27, 28]. The $(\Delta\mu)_{\Delta p}$ is found to sharply decrease in the vicinity of plasma/vapor bubble ($\lesssim 40\,\mu m$). Although $(\Delta\mu)_{\Delta p} > 0$ favors the formation of a crystal nucleus, the length scale is comparable to that of the thermal boundary layer thickness (δ_T). Therefore, no formation of crystals is expected due to shockwaves because of the lower supersaturation ratio associated with higher temperatures. From Fig. A.S1, the probability of plasma formation is significant close to 90 μJ, which corresponds to δ_T value of $\approx 32.5\,\mu J$ (Figs. A.S9 and A.S10). As a result, although pressure waves might favor the crystal nucleus formation, the absorbed energy by the liquid from the incident laser would decrease the supersaturation and hence the nucleation probability. Recent evidence on the difference in crystal size distribution

between shock wave and direct laser-induced crystallization [40] also suggests a mechanism other than shock wave is at play.

C

APPENDIX TO CHAPTER 4

C.1 Experimental protocol

For each trial the warm solution from the hot plate is freshly loaded to the microwell using a micropipette. The warmth prevents spontaneous nucleation while handling. First a 500 μL of solution is transferred following which 100 μL of silicone oil (378321, Sigma-Aldrich) is pipetted over it to prevent evaporation. The step by step experimental procedure during each trails are detailed in Table A.S1.

Table A.S1: Experimental protocol

Description of the event sequence	**Timestamp (minutes)**
1. Fill the microwell with supersaturated solution and silicone oil	at 0
2. Place the filled microwell over sample stage in microscope and allow it to cool down. The LED light is switched off during this process.	$0-5$
3. Scan the microwell bottom end to end to check if there are any crystals formed. If no crystals then align the microwell with its centre directly above the objective.	$5-8.5$
4. Trigger few laser pulses with shutter closed to warm up the laser, and prepare the camera and oscilloscope to wait for trigger. The laser is shot at ≈ 9 min.	$8.5-9$
6. The high-speed camera records for ≈ 100 μs, while the low-speed camera continues recording until 30 s. After 30 s the LED is switched off together with the low-speed camera. The light is switched back on at 11 min and a snapshot of the image is saved to determine crystallization probability and crystal count.	$9-11$
7. The microwell bottom is scanned end to end to check for crystal(s).	>11

C.2 Derivation of analytical relation

Temperature

This analysis assumes the interface and bubble temperature to be equal. To estimate the change in temperature of the interface, the energy balance of the bubble and the solution surrounding it is written as follows,

$$E_B = K.E. + Q + m_V c_{pV} \Delta T. \tag{A.S1}$$

The left-hand side is the potential energy of bubble determined using $E_B = 4\pi R_{max}^3 p_\infty/3$ [41], K.E. is the kinetic energy of the surrounding liquid, and the second and third term on the right-hand side is the heat content of the liquid and vapor respectively. m_V is the vapor mass, c_{pV} is the vapor specific heat capacity at constant pressure, ΔT is the change in temperature relative to the ambient temperature (298 K) and p_∞ is the ambient pressure. By analyzing the above equation at the maximum bubble size, one can substitute $K.E. = 0$ and $m_V = 4\pi R_{max}^3 \rho_V/3$, where ρ_V is the vapor density. Thus Eq. A.S1 can be rewritten as,

$$\lambda_T 4\pi R_{max}^3 p_\infty/3 = Q + 4\pi R_{max}^3 \rho_V c_{pV} \Delta T/3. \tag{A.S2}$$

λ_T is a constant of proportionality. During the bubble evolution a thermal boundary layer develops in the liquid surrounding the bubble. The layer thickness is proportional to the thermal penetration depth $\sqrt{\alpha \Delta t}$, where α is the thermal diffusivity of liquid and Δt is the time taken by the bubble to expand to its maximum size. As the temperature gradient in the boundary layer drives Q, using the Fourier law one can relate [42]

$$Q \approx k_L \frac{\Delta T}{\sqrt{\alpha \Delta t}} 4\pi R_{max}^2 \Delta t = \sqrt{k_L \rho_L c_{pL} \Delta t}\; 4\pi R_{max}^2 \Delta T. \tag{A.S3}$$

k_L is the thermal conductivity, ρ_L is the density and c_{pL} is the specific heat capacity at constant pressure respectively for the liquid. By substituting the relation for Q in Eq. A.S2, one gets

$$\Delta T \approx \frac{\Delta T_{ad}}{(1 + \sqrt{\Delta t/\Delta t_Q})}, \tag{A.S4}$$

similar to Dular et al. [42]. $\Delta T_{ad} = \lambda_T p_\infty/(\rho_V c_{pV})$, is the adiabatic ($Q = 0$) change in temperature and $\Delta t_Q = (\rho_V c_{pV} R_{max})^2/(9 k_L \rho_L c_{pL})$ is a characteristic time of heat transfer. Since $\Delta t \gg \Delta t_Q$ in all the discussed cases, one can simplify

$$\Delta T \approx \Delta T_{ad} \sqrt{\Delta t_Q/\Delta t}. \tag{A.S5}$$

In case of cavitation with pulsed laser in water, the time for bubble expansion and collapse is approximately equal [43]. The condition for symmetric bubble expansion and collapse satisfies primarily due to two reasons, (i) the source energy for cavitation is supplied at much smaller timescales (nanoseconds) compared to bubble life (microseconds) and (ii) negligible damping effect provided by water due to its moderate viscosity. Thus the time for bubble expansion, Δt, is determined using the Rayleigh collapse time as [11],

$$\Delta t = 0.915 R_{max} \left(\rho_L / p_\infty\right)^{1/2}. \tag{A.S6}$$

By substitution the above relation in Eq. A.S5 and further simplifying it, one gets

$$\Delta T \approx \frac{\lambda_T p_\infty^{5/4}}{3\sqrt{0.915 k_L c_{pL} \rho_L^{3/2}}} \sqrt{R_{max}}. \tag{A.S7}$$

Concentration

Similar to heat flow for change in temperature, this subsection discusses the derivation for solute flow for change in concentration at the interface. The solute balance in the liquid surrounding the bubble is written as follows,

$$\frac{4}{3}\pi R_{max}^3 \rho_V C_\infty \propto \rho_L D \frac{\Delta \widehat{C}}{\sqrt{D\Delta t}} 4\pi R_{max}^2 \Delta t. \tag{A.S8}$$

C_∞ is the solute concentration in the bulk and D is the mass diffusivity. The hat $\widehat{\ }$ symbol over the solute concentration C denotes the units in g/g of solution, with $\widehat{C} = C/(1+C)$. $\Delta\widehat{C} = \widehat{C} - \widehat{C}_\infty$, is the added concentration (due to evaporation) in the liquid volume surrounding the interface. The left-hand side of the above equation corresponds to the mass of solute that was previously dissolved in the liquid that now exists as vapor. While the right-hand side is analogous to the Fourier law for heat transfer discussed in detail in the previous subsection. Eq. A.S8 can be rewritten as,

$$\frac{4}{3}\pi R_{max}^3 \rho_V C_\infty = \lambda_C \rho_L D \frac{\Delta \widehat{C}}{\sqrt{D\Delta t}} 4\pi R_{max}^2 \Delta t, \tag{A.S9}$$

where λ_C is a constant of proportionality. By substituting the value of Δt in the above equation and further simplifying it, one gets

$$\frac{C}{1+C} = \frac{C_\infty}{1+C_\infty} + \frac{\lambda_C C_\infty \rho_V p_\infty^{1/4} \sqrt{R_{max}}}{3\sqrt{0.915 D \rho_L^{5/2}}}. \tag{A.S10}$$

The density of the vapor bubble can be approximately estimated using the ideal gas law as, $\rho_V = p_V/(R_g T)$, where R_g is the specific gas constant of vapor. The vapor

pressure can be calculated as, $p_V = a_w p_V^\circ$ [44], in which a_w is the water activity and p_V° is the vapor pressure of pure water. The water activity in turn can be calculated as, $a_w = 1 - \Gamma C/M$ [26, 45]. Γ is the relative molar vapor pressure lowering that depends on the solute and M is the molar mass of the solute. The values of Γ for each solute discussed in this work is summarised in the section: solution properties under Table A.S2. By substituting the relation for ρ_V in Eq. A.S10, one gets

$$\frac{C}{1+C} = \frac{C_\infty}{1+C_\infty} + \frac{\lambda_C C_\infty (1 - \Gamma C/M) p_V^\circ p_\infty^{1/4} \sqrt{R_{max}}}{3 R_g T \sqrt{0.915 D \rho_L^{5/2}}}. \tag{A.S11}$$

C.3 Solution properties

Figure A.S1 (a) shows the solubility of the salts discussed in this work measured using the change in turbidity (Crystal16, Technobis Crystallization Systems), using 1.5 ml vials constantly stirred at 700 rotations per minute.

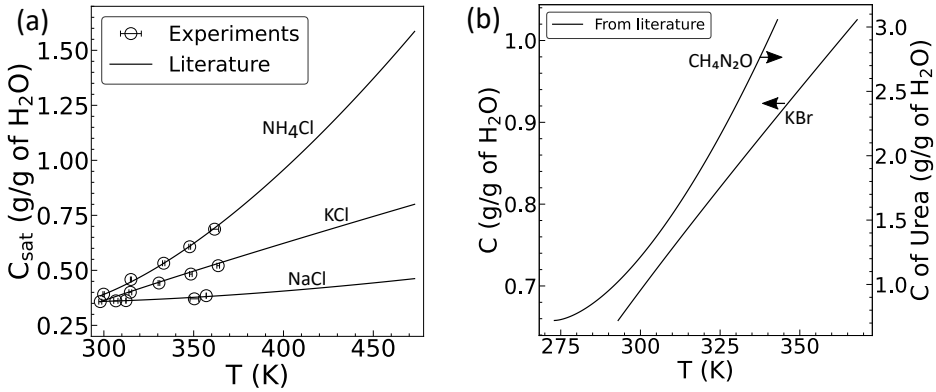

Figure A.S1: (a) Solubility data from experiments performed in this work against the data from literature [3, 46]. (b) Solubility data from literature [47, 48]. The equations for the fit line to the data from literature are tabulated in Table A.S2.

The solute-solution interfacial tension σ_{sl} is calculated using the thermodynamic equation proposed by Mersmann [31] as,

$$\sigma_{sl} \propto T \left(\frac{\rho_S}{M}\right)^{2/3} \log\left(\frac{\rho_S}{\widehat{C}\,\rho_L}\right). \tag{A.S12}$$

Where T is the temperature in K, ρ_S is the crystal density, M molar mass of solute, ρ_L is the solution density, and $\widehat{C} = C/(1+C)$ is the weight fraction in g/g of solution. By substituting the respective values from Table A.S3 in the above relation, one can calculate the σ_{sl} for a solute relative to $\sigma_{sl} = 2.2\,\mathrm{mJ/m^2}$ for KCl [8, 34] at 298 K.

Table A.S2: Aqueous Solution Properties. The saturation concentration C_{sat} as a function of temperature T in K. $C_{sat,298}$ is the saturation solubility at 298 K. Γ is the relative molar vapor pressure lowering. The solubility relations are illustrated in Fig. A.S1.

Solute	**$C_{sat,298}$ (g/g-H_2O)**	**$C_{sat}(T)$ (g/g-H_2O)**	**T range**	**Γ (g/mol)**
NH_4Cl	0.3879	$0.333 + 3.68 \times 10^{-4}\,(T-273)^{1.535}$ [46]	$283-477$	28.4 [49]
KCl	0.3578	$0.2805 + 3.97 \times 10^{-3}\,(T-273)^{0.92}$ [3]	$273-473$	32.8 [26, 45]
NaCl	0.3593	$0.355 + 1.77 \times 10^{-5}\,(T-273)^{1.644}$ [3]	$273-473$	40.5 [26, 45]
CH_4N_2O	1.1553	$0.72 + 2.277 \times 10^{-3}\,(T-273)^{1.632}$ [47]	$273-343$	11.64 [49]
KBr	0.6843	$0.5403 + 7.693 \times 10^{-3}\,(T-273)^{0.91}$ [48]	$273-373$	33.5 [50]

Table A.S3: Aqueous Solution Properties. The properties are for $S = 1$ and at 298 K. ρ_S is the crystal density. The solution (liquid) properties are: ρ_L - density; k_L - thermal conductivity; $c_{p,L}$ - specific heat capacity; D - mass diffusivity. [a]The value was calculated using the analytical relation from ref. [19].

Solute	**ρ_S (kg/m^3)**	**ρ_L (kg/m^3)**	**k_L (W/m K)**	**c_{pL} (J/kg K)**	**D (m^2/s)**
NH_4Cl	1527	1080 [51]	0.47 [51]	3200 [52]	2.25×10^{-9} [53]
KCl	1989	1178 [30]	0.544 [54]	3000 [20]	1.92×10^{-9} [23]
NaCl	2165	1200 [30]	0.566 [54]	3200 [20]	1.5×10^{-9} [23]
CH_4N_2O	1335	1146 [55]	0.45[a]	3022 [55]	0.7×10^{-9} [56]
KBr	2750	1380 [57]	0.5 [58]	2315 [59]	2.4×10^{-9} [60]

D

APPENDIX TO CHAPTER 5

D.1 Dynamic bubble size, bubble lifetime and bubble energy

Determining X

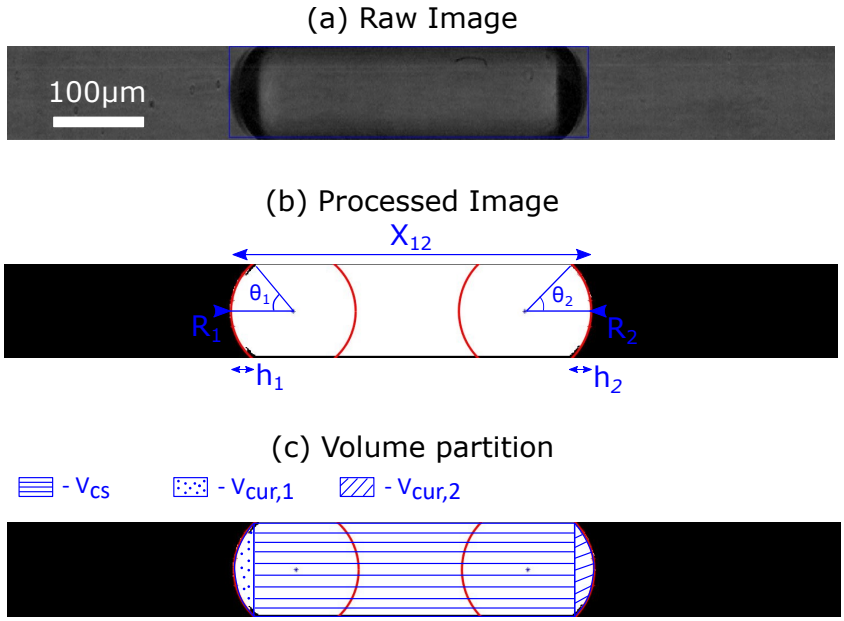

Figure A.S1: (a) Raw image from experiments. (b) Processed image. X_{12} is the distance between the extreme bubble ends. R_1 and R_2 are the radius of curvature for the left and right ends respectively. h_1 and h_2 are the width of the curvature for the left and right ends respectively.

Fig. A.S1 illustrates the image processing technique adapted to determine the bubble size. To eliminate the effects of curvatures on the estimation of X, the bubble volume is calculated first. The total volume of a vapor bubble, $V_b = V_{cs} + V_{cur,1} + V_{cur,2}$, can be expressed using the summation of the portions as expressed in Fig. A.S1.

Where V_{cs} is the cross-section volume and V_{cur} is the curvature volume. The effective bubble length incorporating the curvature effects over the bubble ends is $X = V_b/A$.

The volume $V_{cs} = A(X_{12} - h_1 - h_2)$, where A is the cross-section area of the channel. $A = \pi d^2/4$ for circular cross-section, and $A = a\,b$ for square/rectangular cross-section. d is the channel's hydraulic diameter and, a and b are the cross-section's edge lengths with $b \leqslant a$. The calculation of volume V_{cur} requires the consideration of the curvature.

Circular cross-section: The bubble volume is

$$V_b = A\,(X_{12} - h_1 - h_2) + \sum_{i=1}^{2} \pi h_i\,(3d^2/4 + h_i^2)/6, \tag{A.S1}$$

where,

$$h_i = R_i\,(1 - \cos(\theta_i)) \quad \text{and} \quad \theta_i = \sin^{-1}(d/(2R_i)). \tag{A.S2}$$

Refer to Fig. A.S1 for all the other notations discussed in the section.

Square/Rectangle cross-section: The volumetric flow rate due to a curvature can be expressed as $\dot{V}_{cur} = A U_{mean,cur}$, where $U_{mean,cur}$ is the average velocity. The average velocity for a rectangular channel is calculated as [61],

$$U_{mean,cur} = \frac{a^2 \Delta p}{4 l_L \mu_L} \frac{\sin(\alpha_n)\beta_n}{AR\,\alpha_n^3} \left[AR - \frac{\tanh(\alpha_n AR)}{\alpha_n} \right]. \tag{A.S3}$$

Where $\alpha_n = \left(n - \frac{1}{2}\right)\pi$, $\beta_n = \frac{2(-1)^{n+1}}{\alpha_n}$ and $AR = b/a$. Furthermore, the velocity at the channel axis ($r = 0$) is [61],

$$U_{r=0} = \frac{a^2 \Delta p}{4 l_L \mu_L} \sum_{n=1}^{\infty} \frac{\beta_n}{\alpha_n^2} \left[1 - \frac{1}{\cosh(\alpha_n AR)} \right]. \tag{A.S4}$$

For square channels, $AR = 1$, since $a = b$. Furthermore, Eqs. A.S3 and A.S4 can be solved to obtain the velocity ratio, $U_{ratio} = U_{mean,cur}/U_{r=0} = 0.477$, which is independent of the channel's hydraulic diameter or the cross-sectional edge lengths. Thus $\dot{V}_{cur}$ can be calculated as, $\dot{V}_{cur} = 0.477\,A U_{r=0}$. Since $a = b = d$, the cross-section area is $A = d^2$. Analogous to $\dot{V}_{cur}$, the V_{cur} is calculated by substituting $U_{r=0}$ with h_i. The substitution leads to, $V_{cur,i} = 0.477\,h_i d^2$. Thus for square channels,

$$V_b = A\,(X_{12} - h_1 - h_2) + \sum_{i=1}^{2} 0.477\,h_i d^2. \tag{A.S5}$$

In this work, the two rectangular channels employed are with $AR = 0.5$ and 0.2667 for 50×100 (in μm) and 80×300 (in μm) channels, respectively. Below the results are presented for rectangular channels similar to square:

$$V_b = A\,(X_{12} - h_1 - h_2) + \sum_{i=1}^{2} 0.502\, h_i\, a\, b \quad \text{for } d_h = 66.7\,\mu\text{m, and} \tag{A.S6}$$

$$V_b = A\,(X_{12} - h_1 - h_2) + \sum_{i=1}^{2} 0.558\, h_i\, a\, b \quad \text{for } d_h = 126\,\mu\text{m.} \tag{A.S7}$$

Bubble lifetime and energy

The non-dimensionalized plots (unscaled) for dynamic bubble size are represented in Figs. A.S2-A.S4. Similarly, the non-dimensionalized plots (unscaled) for bubble lifetime and energy against its maximum size are represented in Fig. A.S5.

While the exact solution to the Lambert W function in Eq. 5.3 of the main manuscript accurately captures the experiments, below the approximation to help solve the equation with regular/popular functions is provided. The following are the approximate relations:

$$W_0(\psi) = \sum_{n=1}^{\infty} \frac{(-n)^{n-1}\psi^n}{n!},\ |\psi| \leqslant \frac{1}{e} \text{ and} \tag{A.S8}$$

$$W_{-1}(\psi) \approx \log(-\psi) - \log(-\log(-\psi)) + \log(-\log(-\psi))/\log(-\psi)... \tag{A.S9}$$

Where $\psi = -e^{-(1+\widehat{X}_{max})}$. Figure A.S6 shows the solution to the above equations for n upto 3 with

$$\widehat{t}_{osc} = W_0(\psi) - W_{-1}(\psi). \tag{A.S10}$$

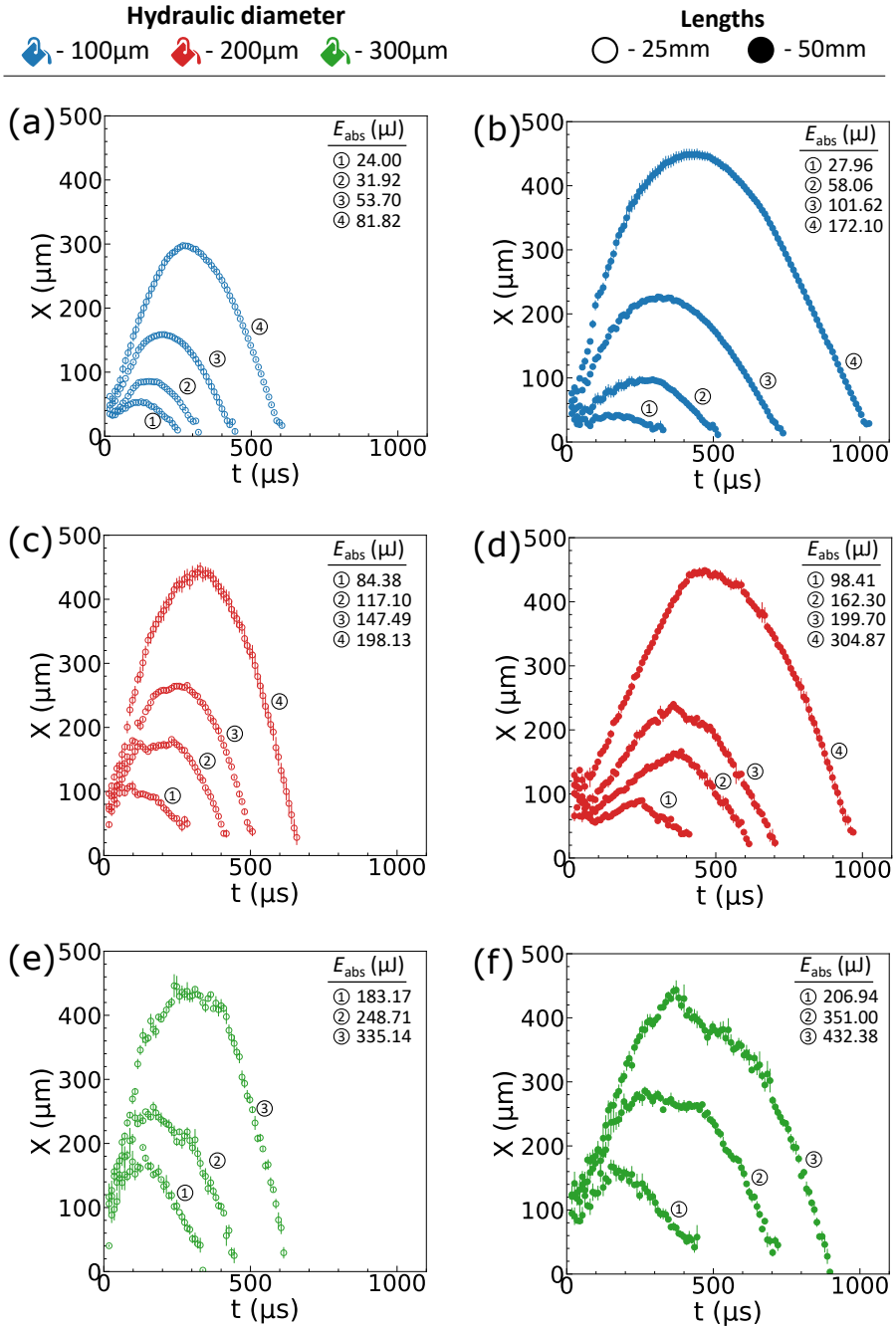

Figure A.S2: (a-f) Bubble size (X) against time (t) for a channel with circular cross-section. The colors represent the dimension; the markerfacecolors represent the channel length. The error bars represent the standard error over 5 trials.

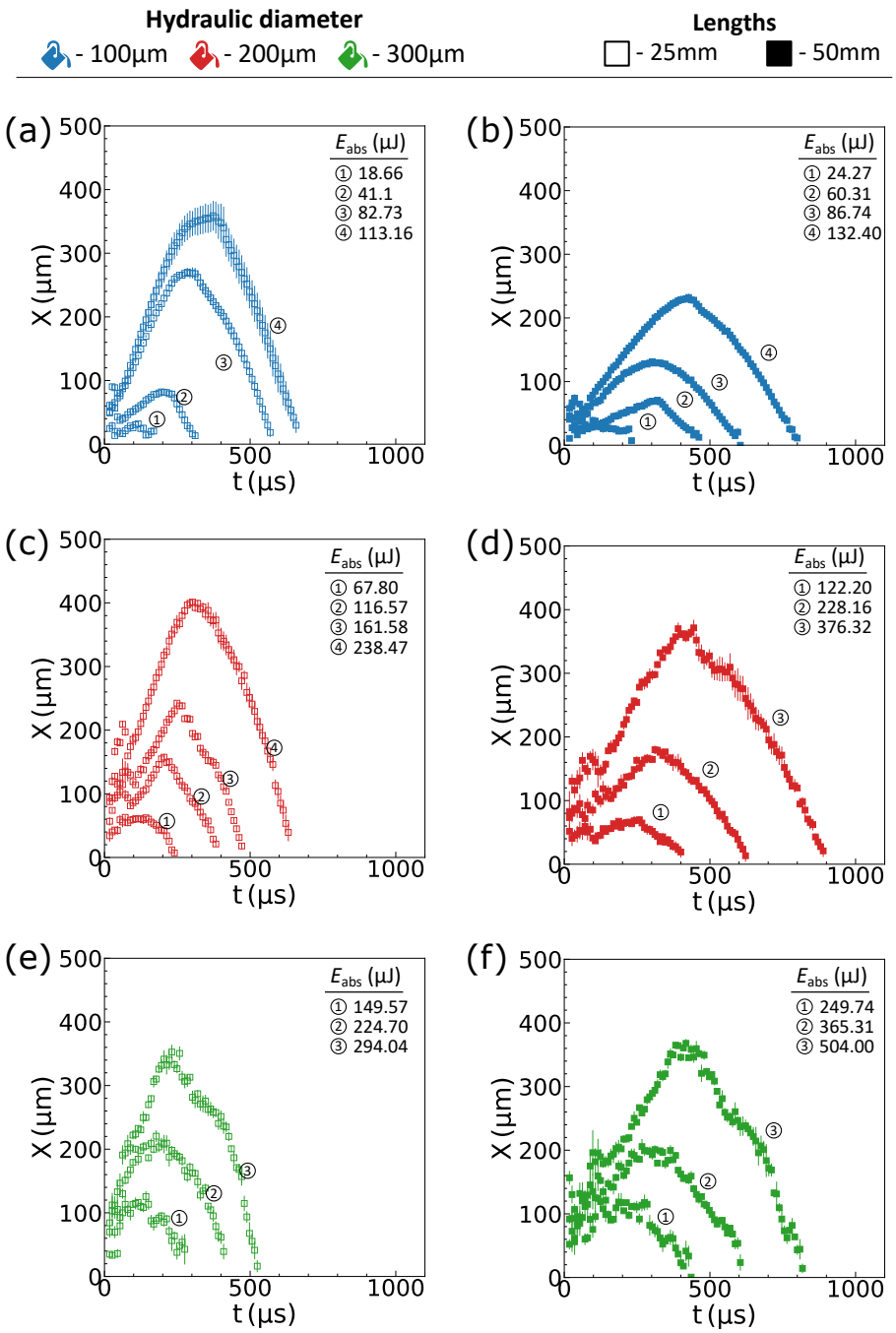

Figure A.S3: (a-f) Bubble size (X) against time (t) for a channel with square cross-section. The colors represent the dimension; the markerfacecolors represent the channel length. The error bars represent the standard error over 5 trials.

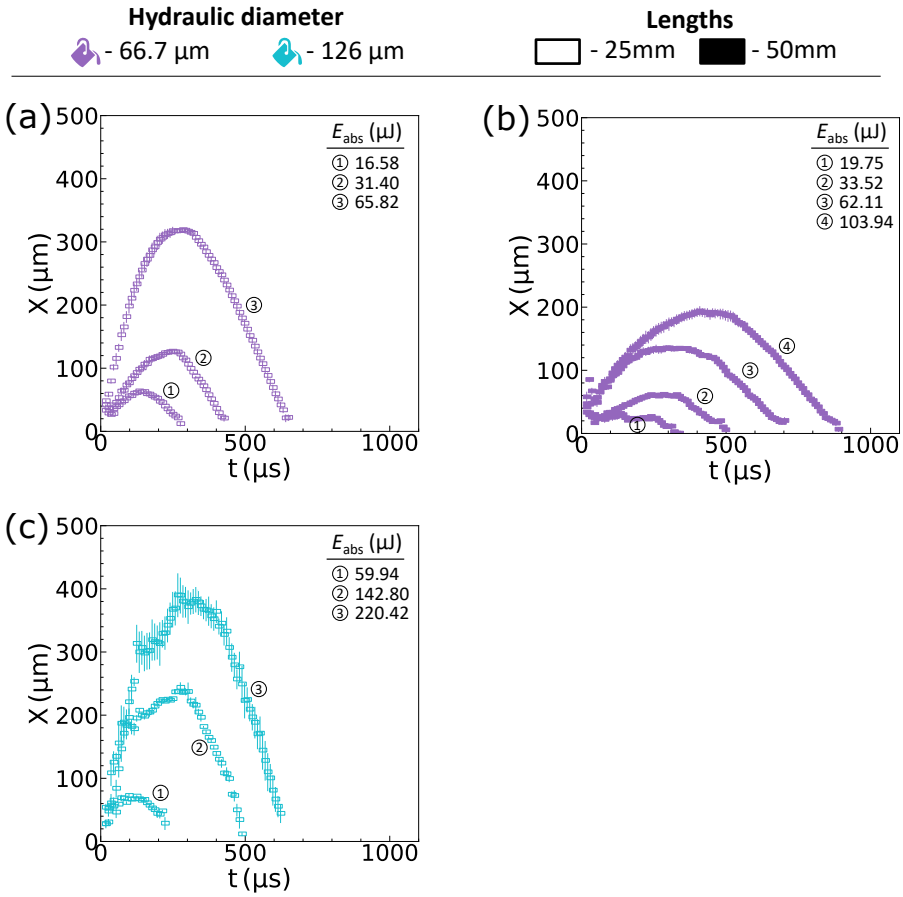

Figure A.S4: (a-c) Bubble size (X) against time (t) for a channel with rectangular cross-section. The colors represent the dimension; the markerfacecolors represent the channel length. The error bars represent the standard error over 5 trials.

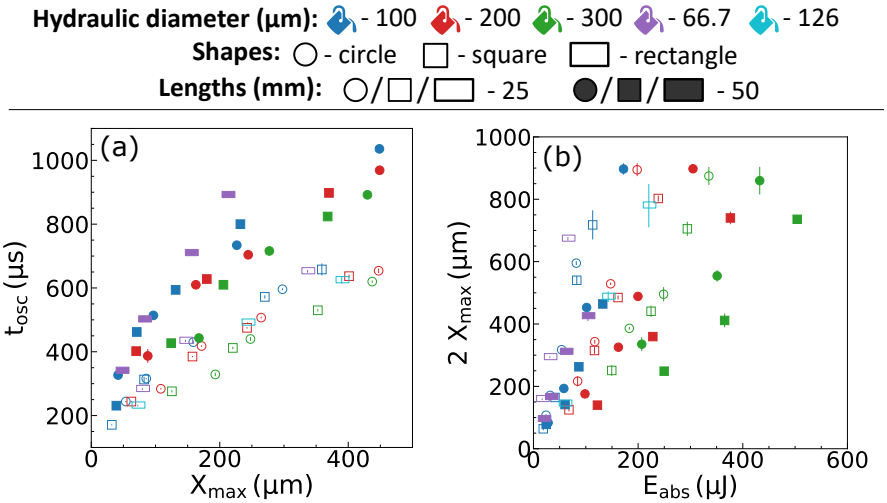

Figure A.S5: (a) The lifetime (t_{osc}) against maximum size (X_{max}) of the bubble. (b) The maximum bubble size (X_{max}) against the laser energy absorbed by the liquid (E_{abs}). The marker shapes represent the shape of the cross-section; the colors represent the dimension; the markerfacecolors represent the channel length. The error bars represent the standard error over 5 trials.

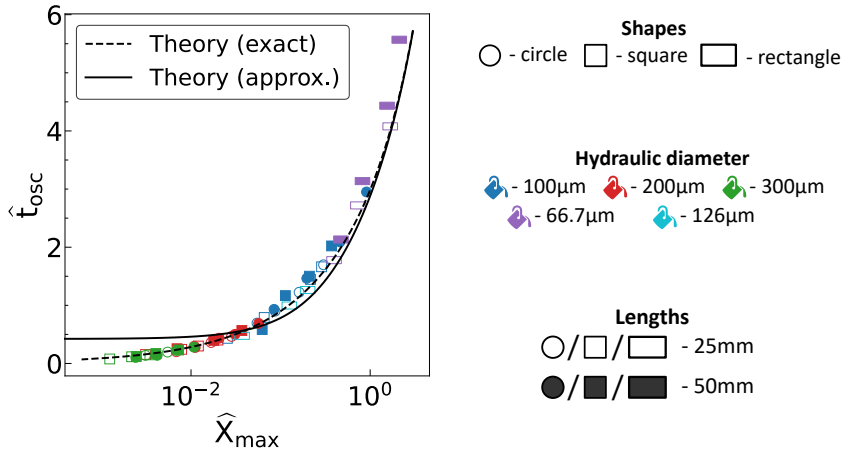

Figure A.S6: The approximate solution to Eq. A.S10 employing Eqs. A.S8 and A.S9 is represented using the continuous line, while the exact solution to Eq. A.S10 is represented using dashed line. The approximate solution is with n upto 3 in Eq. A.S8. The markers are the experiments performed.

D.2 Laser energy absorbed by the liquid and threshold energy for bubble formation

The channel's geometry, such as, wall thickness, material, cross-section shape and dimension can influence the laser energy available for the liquid to absorb. For energy calibration, the energy transmitted through the channel (E_{trans}) was measured. An energy ratio is denoted as, ϵ_{geom}, estimated by measuring the energy difference without the channels and channels filled with water. Therefore, if E_{supp} is the energy supplied to the channel, then for channels filled with water, $E_{trans} = \epsilon_{geom} E_{supp}$. The channels filled with water was used as reference to measure energy absorbed in experiments since water is transparent to 532 nm wavelength and matches the refractive index of the aqueous dye (referred to as liquid).

For experiments with the aqueous dye, a portion or a whole the energy, $\epsilon_{geom} E_{supp}$, will be absorbed based on the absorption coefficient of the liquid and the distance the light will travel through the liquid. Therefore the energy transmitted through the channel with the liquid is, $E_{trans} = \epsilon_L \epsilon_{geom} E_{supp}$, where ϵ_L is the transmission ratio of the liquid. Therefore using the Beer–Lambert law [62], the absorbance (A_{abs}) of the liquid is calculated as,

$$A_{abs} = -\log_{10}(\epsilon_L) = -\log_{10}(E_{trans}/(\epsilon_{geom} E_{supp})). \tag{A.S11}$$

Furthermore, the absorbance can be written as, $A_{abs} = \beta\, d_L$, where β is the absorption coefficient and d_L is the distance the light will travel through the liquid. d_L is equal to the hydraulic diameter (d) for circular and square channels. For rectangles it is the shorter edge length of the cross-section. Since the red dye (RD81, Sigma-Aldrich) concentration in the liquid is consistent through this work (0.5 wt %), therefore β is a constant. The β of the liquid is estimated experimentally by measuring the transmitted light as, $\beta = A_{abs}/d_L$. Figure A.S7 shows the estimation of β from experiments using the A_{abs} against d_L line slope. The estimated value is $86.54\,cm^{-1}$.

For $r \in [-d_L/2, d_L/2]$ is the radial position from the channel's geometric centre, the laser energy absorbed at the laser focal spot is required to estimate the threshold energy for bubble formation. An estimation for the transmitted energy as a function of r can be represented as, $E_{trans} = 10^{-\beta(d_L/2+r)} \epsilon_{geom} E_{supp}$. By further differentiating it,

$$dE_{trans} = -\epsilon_{geom} E_{supp} \beta \log(10) 10^{-\beta(d_L/2+r)}\, dr. \tag{A.S12}$$

In the above expression for $r > d_L/2$ is where the energy meter is positioned to calibrate the transmitted energy. Thus $r = 0$ correspond to the position of the laser spot, and $dE_{trans}(r = 0)$ is the energy absorbed at the laser spot. This absorbed energy will be used for sensible and latent heat of the liquid, resulting in the energy balance,

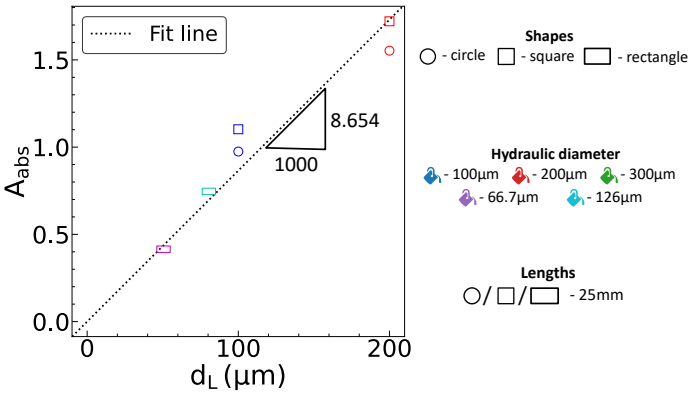

Figure A.S7: The absorbance of the liquid (A_{abs}) against the distance the light travels through the liquid (d_L). The slope represents the absorption coefficient. The marker shapes represent the shape of the cross-section and the colors represent the dimension.

$dE_{trans}(r = 0) = -\pi w_0^2 \rho_L (c_{pL}\Delta T + H_L)\, dr$. Where $2w_0$ is the laser spot diameter, c_{pL} is the liquid specific heat, ΔT is the rise in temperature and H_L the latent heat of vaporization. Thus the energy at the laser spot can be expressed as,

$$\epsilon_{geom} E_{supp} = \frac{\pi w_0^2 \rho_L (c_{pL}\Delta T + H_L)}{\beta \log(10) 10^{-\beta (d_L/2)}}. \tag{A.S13}$$

In other words, the total energy absorbed by the liquid, E_{abs}, can be theorized as follows,

$$E_{abs} = (1 - \epsilon_L)\epsilon_{geom} E_{supp} = (1 - 10^{-\beta d_L}) \frac{\pi w_0^2 \rho_L (c_{pL}\Delta T + H_L)}{\beta \log(10) 10^{-\beta (d_L/2)}}. \tag{A.S14}$$

In the above theoretical expression for the absorbed laser energy, by substituting the values of properties of the liquid the threshold energy for bubble formation (E_{th}) is theoretically calculated. For a bubble to form, the spinodal temperature of water is used as the necessary condition - temperature at which the water explosively turns into vapor. Thus as the water reaches the spinodal temperature (577 K) [16], $E_{th} = E_{abs}$. Since the laser pulse width is 4 ns, the energy from the laser is transferred to the liquid within a short amount of time, which in turn vaporizes the liquid.

D.3 Analytical solution to oscillating flow with sinusoidal pressure gradient

The equations discussed in this section are adapted from Wang [61].

Circular channels

The velocity profiles within a channel with circular cross-section is as follows,

$$U(r,t) = \frac{(\Delta p/\Delta x)d^2}{4\mu_e\sigma^2}[1 + c_1 I_0(2\sigma r/d) + c_2 K_0(2\sigma r/d)]\ \exp(i\omega t), \quad \text{(A.S15)}$$

where, $\sigma = \sqrt{k + i\widehat{\omega}}$ and

$$c_1 = \frac{K_0(-\sigma) - K_0(\sigma)}{I_0(-\sigma)K_0(\sigma) - I_0(\sigma)K_0(-\sigma)},\ c_2 = \frac{I_0(\sigma) - I_0(-\sigma)}{I_0(-\sigma)K_0(\sigma) - I_0(\sigma)K_0(-\sigma)}. \quad \text{(A.S16)}$$

The I_n and K_n are the modified Bessel functions, and $\Delta p/\Delta x = p_\infty/l_L$ is the pressure gradient along channel axis. Thus the flow is governed by two parameters, a non-dimensional frequency, $\widehat{\omega} = \rho_L d^2\omega/(4\phi\mu_e)$, and a porous medium factor, $k = \mu_L/(\mu_e D)$. D is the Darcy number, μ_e is the effective viscosity and ϕ the channel porosity. For pure fluid flows, $D \to \infty$, $\mu_L = \mu_e$ and $\phi = 1$ [63]. Thus the transient mean flow velocity is,

$$U(t) = \frac{4}{\pi d^2}\int_0^{d/2} U(r,t)\,2\pi r dr = \frac{2\,(\Delta p/\Delta x)}{\mu_e\sigma^2}\,\mathbb{R}\Big\{[0.5 + c_1 I_1(\sigma)/\sigma]\ \exp(i\omega t)\Big\}, \quad \text{(A.S17)}$$

where $\mathbb{R}$ is the real part of a complex number.

Figure A.S8 (a) shows the predicted velocity profiles for an oscillating flow with pressure gradient $p_\infty \cos(\omega t)/l_L$. The representative solution is for $d = 300\,\mu m$, $L = 50\,mm$ and $t_{osc} = 892\,\mu s$. Figure A.S8 (b) illustrates the velocity profiles along the channel's radial direction.

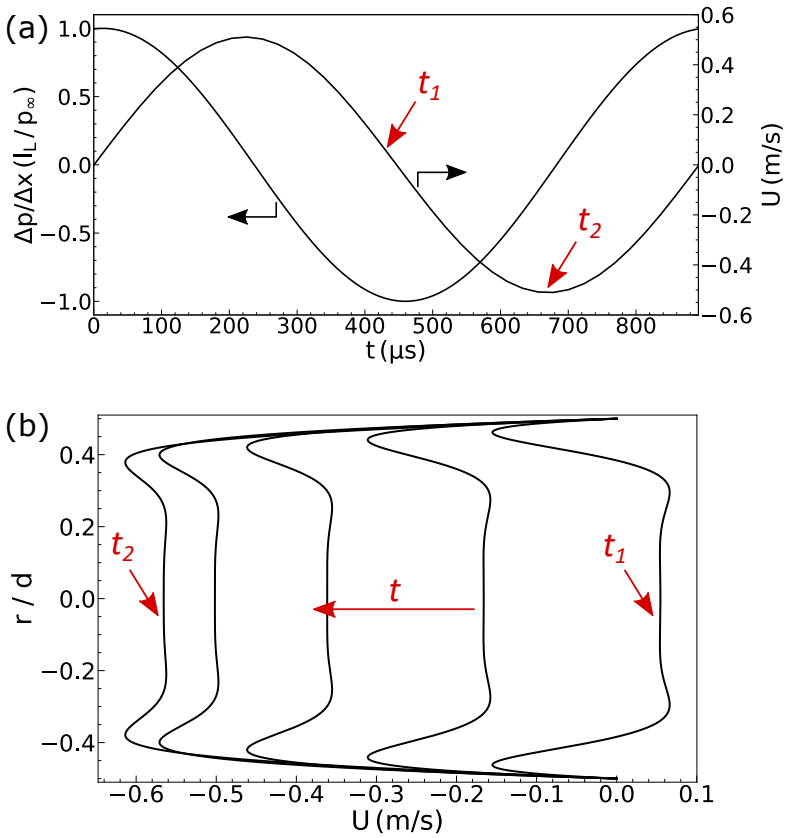

Figure A.S8: (a) This representative analytical solution is for $d = 300\,\mu m$, $L = 50\,mm$ and $t_{osc} = 892\,\mu s$. U is the mean flow velocity. (b) The corresponding velocity profiles along the channel's radial direction (r) for the solution from (a). t_1 and t_2 are chosen time window to represent the flow. The direction of t represents the progress in time. The gradient in the velocity at the channel walls suggest a deceleration of the flow following the mean flow reversal (at the start of bubble collapse).

E

APPENDIX TO CHAPTER 6

E.1 Experimental protocol

Experimental protocol

For each trial the solution is freshly loaded to a new channel. The warm solution from the hot plate is transferred using a micro-pipette. The warmth prevents spontaneous nucleation while handling. Once the supersaturated solution is transferred, the channel ends are covered using droplets of silicone oil (378321, Sigma-Aldrich) to prevent evaporation. The step by step experimental procedure during each trails is detailed in Table A.S1.

Table A.S1: Experimental protocol

Description of the event sequence	**Timestamp (minutes)**
1. Fill the channel with supersaturated solution	at 0
2. Place the filled channel over sample stage in microscope and allow it to cool down. The LED light is switched off during this process.	$0-2$
3. Scan the channel end to end to check if there are any crystals formed. If no crystals then align the channel with its mid along length over the objective.	$2-6$
4. Trigger few laser pulses with shutter closed to warm up the lasers.	$6-6.5$
5. Prepare the camera and oscilloscope to wait for trigger. The laser is shot at ≈ 7 min.	$6.5-7$
6. The high-speed camera records for 3 seconds, while the low-speed camera continues recording until 2 min. After 5^{th} second the intensity of LED is kept at minimum as the large exposure time of low-speed camera allows in more light.	$7-9$
7. The channel is scanned end to end to check for crystal(s).	$9-11$

E.2 Crystal count

Single bubble

Figure A.S1 illustrates B_1 formation (with no B_2) in a 200 μm channel. No crystal formation was observed post the bubble collapse within the standard observation time of 2 minutes. The laser energy supplied is $E_1 = 304.75$ μJ, which is approximately twice the laser energy supplied for B_1 in 200 μm channel in the main text.

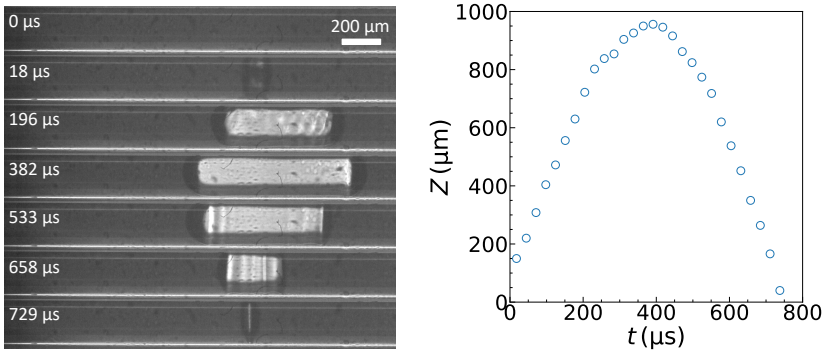

Figure A.S1: B_1 formation with no B_2. No crystals were recorded after a fixed observation time of 2 minutes from laser irradiation. The laser energy supplied is $E_1 = 304.75$ μJ.

Bubble pair experiments within 300 μm channel

Figure A.S2 illustrates the crystal formation in experiments for $S = 1.3$ within 300 μm channel. The experiments involved formation of bubble pairs with $E_1 = 219$ μJ and $E_1 = 16.9$ μJ, similar to the experiments from the main text. In total the experiment was repeated 8 times out of which 5 trials resulted in > 20 crystals and the other 3 trails resulted in $2 - 3$ crystals.

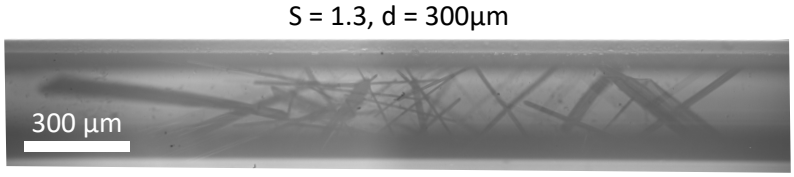

Figure A.S2: Illustration of crystal formation after a fixed observation time of 2 minutes from laser irradiation.

The crystal count for experiments reported in Fig. 4 of main text

The crystal count recorded in experiments are reported in Fig. A.S3. The results are for the experiments reported in Fig. 4 of the main text. The markers are adapted from Fig. 4 in the main text. The crystals were recorded after a fixed observation time of 2 minutes from laser irradiation.

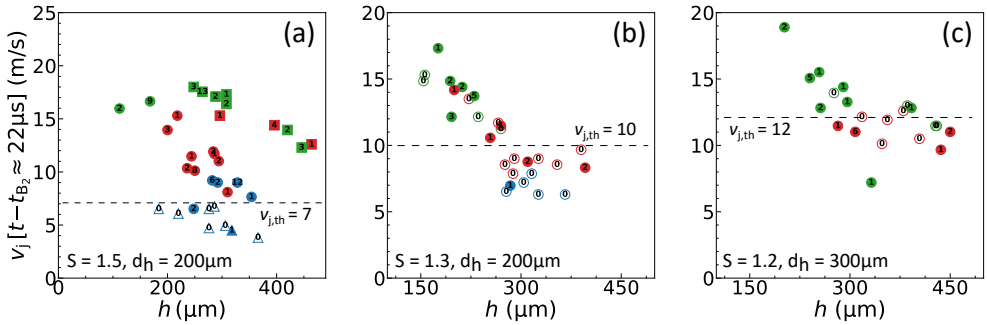

Figure A.S3: (a-c) The recorded crystal count for experiments from Fig. 4 of main text. The markers are adapted from Fig. 4 in main text. The crystals were recorded after a fixed observation time of 2 minutes from laser irradiation.

E.3 Index n values from literature

Table A.S2 contains the index value n from the relation $J \propto \dot{\gamma}^n$ (in main text) referenced from literature.

Table A.S2: Empirically observed n values from literature. $\dot{\gamma}$ is the shear rate.

n	Compound	$\dot{\gamma}$ (1/s)	Reference
1.443	lysozyme	$0-10$	[64]
1.226	butyl paraben	$0-200$	[65]
3.029	isotactic polypropylene	$0-8$	[66]
2.08	paracetamol	$0-200$	[67]
1	glycine	$10-1000$	[68, 69]

E.4 Solute-solution interfacial tension calculation

Table A.S3 provides the values required for calculation of solute-solution interfacial tension σ_{sl} with $B = 16\pi v_0^2 \sigma_{sl}^3/(3k_B^3 T^3)$.

Mersmann proposed a simple relation for the solute-solution interfacial tension calculation from thermodynamics as [31],

$$\sigma_{sl} \propto T \left(\frac{\rho_{KMnO_4}}{M}\right)^{2/3} \log\left(\frac{\rho_{KMnO_4}}{\widehat{C}\,\rho_L}\right). \tag{A.S1}$$

Where T is the temperature, ρ_{KMnO_4} is the solute density, M molar mass of solute, ρ_L is the solution density, and $\widehat{C}$ is the weight fraction in g/g of solution. By substituting the respective values from Tables A.S3 and A.S4 in the above relation, the σ_{sl} for $KMnO_4$ is calculated relative to $\sigma_{sl} = 2.2\,mJ/m^2$ for KCl [8, 34]. The calculated value of σ_{sl} for $KMnO_4$ is $3.16\,mJ/m^2$ at 298 K.

Table A.S3: Physical parameter values for aqueous $KMnO_4$ solution.

Parameter	Description	Value
B	Gradient(slope) [Fig. 4 from main text]	0.05
v_0	Solute molecular volume	9.71×10^{-29} m^3
k_B	Boltzmann constant	1.381×10^{-23} $m^2kg/(s^2K)$
T	Temperature	298 K
ρ_{KMnO_4}	Solute density	2700 kg/m^3
$\rho_{L\text{-}KMnO_4}$	Solution density (at 298 K)	1060 kg/m^3
M_{KMnO_4}	Molar mass of solute	158.03 g/mol
N_A	Avogadro constant	6.023×10^{23} mol^{-1}

Table A.S4: Physical parameter values for aqueous KCl solution.

Parameter	Description	Value
v_0	Solute molecular volume	6.238×10^{-29} m^3
ρ_{KCl}	Solute density	1989 kg/m^3
$\rho_{L\text{-}KCl}$	Solution density (at 298 K)	1175 kg/m^3
M_{KCl}	Molar mass of solute	74.55 g/mol

E.5 Boundary Integral Element Method (BIEM) solution procedure

For an axisymmetric problem with cylindrical coordinates (r, θ, z), all the variables are independent of the rotation angle and therefore can be expressed as [70, 71],

$$\frac{1}{|p-q|}dS = \frac{4r(\xi)}{D}\left[\left(\frac{dz}{d\xi}\right)^2 + \left(\frac{dr}{d\xi}\right)^2\right]^{\frac{1}{2}} K(k)d\xi \tag{A.S2}$$

and,

$$\frac{\partial}{\partial n}\left(\frac{1}{|p-q|}\right)dS = \frac{4r(\xi)}{D^3}\left\{\left[\frac{dz}{d\xi}(r(\xi)+r_i) - \frac{dr}{d\xi}(z(\xi)-z_i) - \frac{2}{k^2(\xi)}\frac{dz}{d\xi}r_i\right]\frac{E(k)}{1-k^2(\xi)} + \frac{2}{k^2(\xi)}\frac{dz}{d\xi}r_i K(k)\right\}d\xi. \tag{A.S3}$$

With each elements of the boundary parameterized by $\xi \in [0,1]$, $p = (r_i, z_i)$ and $q = (r(\xi), z(\xi))$. $D = [(r(\xi)+r_i)^2 + (z(\xi)-z_i)^2]^{\frac{1}{2}}$ and $k = 2\sqrt{r(\xi)r_i}/D$. $K(k)$ and $E(k)$ are the complete elliptic integrals of the first and second kind respectively, approximated by the polynomial expansion [72],

$$K(k) = P(\eta) - Q(\eta)\ln(\eta) \tag{A.S4}$$

$$E(k) = R(\eta) - S(\eta)\ln(\eta). \tag{A.S5}$$

P, Q, R and S are tabulated polynomials of fourth-order, and $\eta = 1 - k^2$.

When the point under consideration (p) lies within the interval of integration, logarithmic singularity in $K(k)$ and $E(k)$ exists at $\eta = 0$. In addition, a special case exists when this point lies over the axisymmetric axis. The detailed calculations required for these cases are reported in thesis by Taib [71].

Numerical integration

The integral equation is solved numerically along the surface Γ as [70, 73],

$$2\pi\phi_i = \sum_{j=1}^{N}\int_{S_j}\frac{\partial}{\partial n}(\phi_j)\ \frac{1}{|p_i-q_j|}d\Gamma - \sum_{j=1}^{N}\int_{S_j}\phi_j\ \frac{\partial}{\partial n}\left(\frac{1}{|p_i-q_j|}\right)d\Gamma. \tag{A.S6}$$

Since the bubble is deforming, it is necessary to have a continuously differentiable surface at each node points. For this purpose, the surface contour is approximated by a finite number of cubic elements as [74],

$$r(\xi) = a_j^r + b_j^r\xi + c_j^r\xi^2 + d_j^r\xi^3, \tag{A.S7}$$

$$z(\xi) = a_j^z + b_j^z\xi + c_j^z\xi^2 + d_j^z\xi^3. \tag{A.S8}$$

As either ϕ or $\partial\phi/\partial n$ is unknown over the surface, both the parameters are chosen to linearly vary within each surface element as,

$$\phi(\xi) = [(1-\xi)\ \xi] \begin{bmatrix} \phi_j \\ \phi_{j+1} \end{bmatrix} \tag{A.S9}$$

$$\frac{\partial\phi(\xi)}{\partial n} = [(1-\xi)\ \xi] \begin{bmatrix} (\partial\phi/\partial n)_j \\ (\partial\phi/\partial n)_{j+1} \end{bmatrix}. \tag{A.S10}$$

For each element, the integrals on the hight-hand side of the Eq.A.S6 can be evaluated as [75],

$$I_e = [k_1] \begin{bmatrix} \phi_j \\ \phi_{j+1} \end{bmatrix} - [k_2] \begin{bmatrix} (\partial\phi/\partial n)_j \\ (\partial\phi/\partial n)_{j+1} \end{bmatrix} \tag{A.S11}$$

with

$$[k_1] = \int_0^1 [(1-\xi)\ \xi] \ \frac{\partial}{\partial n}\left(\frac{1}{|p_i - q_j|}\right) d\xi \tag{A.S12}$$

$$[k_2] = \int_0^1 [(1-\xi)\ \xi] \ \frac{1}{|p_i - q_j|} d\xi. \tag{A.S13}$$

The global equations are obtained by summing the contributions from all elements. Thus

$$H_{i,j}\phi_j = G_{i,j}\left(\frac{\partial\phi}{\partial n}\right)_j,\ i,j = 1,2,3,...,N \tag{A.S14}$$

where

$$H_{i,j} = \sum [(k_1)_{i,j} + \delta_{i,j}\, c(p)],\ \text{where} \tag{A.S15}$$

$$\delta_{i,j} = 1\ \forall\ i = j\ \text{ and }\ \delta_{i,j} = 0\ \forall\ i \neq j, \tag{A.S16}$$

$$G_{i,j} = \sum (k_2)_{i,j}. \tag{A.S17}$$

Eq. A.S6 is composed of Fredholm integral equation of the first and second kind. During the time marching process, sawtooth instability over the moving boundary profile may appear due to the numerical solution to Fredholm integral equation of the first kind [73]. Therefore a five-point smoothing technique introduced by Longuet-Higgins and Cokelet [76] for equally spaced points is used,

$$f_i^* = f_i - \omega(f_{i-2} - 4f_{i-1} + 6f_i - 4f_{i+1} + f_{i+2}). \tag{A.S18}$$

Where $\omega = 1/16$, f_i is the quantity prior to smoothing and f_i^* is the smoothed quantity. Besides, the nodes of the moving boundaries after updation can become too close to (or too far from) each other, which may also cause numerical instabilities [77]. Therefore, the boundary is re-discretized after each time step.

Initialization

The computational domain has the B_1 interface on one end with the other end open. Gravity is neglected as the tube is horizontal and the vertical dimension (channel diameter) is $O(100\ \mu m)$. The initial B_1 interface curvature radius is defined using the contact angle of B_1 with the channel wall, θ. It is to be noted that this contact angle is dynamic during the simulations run and changes based on the fluid flow. The bubble B_2 with radius R_0 is positioned at distance h away from the B_1 interface.

The node that connects the B_1 interface to the channel wall is considered a part of both the interface and the channel wall. While solving the boundary integral equation, this common node is treated as a part of wall and impose $\partial\phi/\partial n = 0$ on it. The velocity of this common node along the wall ($\partial z/\partial t$) is computed using the gradient $\Delta\phi/\Delta z$ at this node with respect to the neighbouring node on wall.

Validation

The validity of most of the results are already shown in the Fig. 6 of the main text. Therefore, below only the validity of model with respect to the initial contact angle (θ) of B_1 is illustrated. The analytical expression for $v_{j,pk}$ is proposed by Peters et al. [78] as,

$$v_{j,pk} \propto \frac{\cos\theta(1+\psi\cos\theta)}{b\log\left(\frac{\sin\theta-b}{1-b}\right)+\sin\theta-1} \tag{A.S19}$$

where $b = 1 + h_0\cos\theta$. h_0 is a fitting parameter and ψ is a proportionality factor.

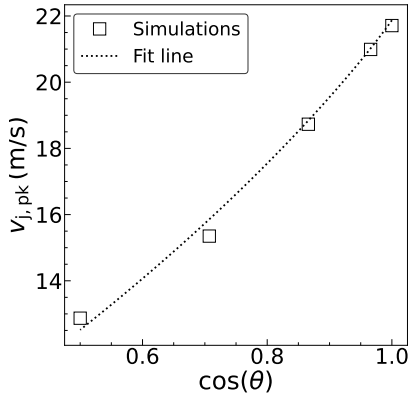

Figure A.S4: Influence of the jet velocity due to change in the initial contact angle. The simulations are for $d = 200\ \mu m$, $h = 275\ \mu m$ and $R_{max} = 88.8\ \mu m$. The fit line correspond to Eq. A.S19 with 11.75 as the constant of proportionality.

Figure A.S4 shows the relation between the peak jet velocity ($v_{j,pk}$) and the cosine of contact angle. The fit line is derived from Eq. A.S19 with 11.75 as the constant of proportionality and by substituting $h_0 = 0.26$ and $\psi = 0.84$ for $d = 200\,\mu m$ [78]. The model thus predicts the correlation same as the analytical expression from literature.

In addition, the change in $v_{j,pk}$ for $\zeta = 100 - 500$ was less than 5 % relative to $\zeta = 313$.

Analytical equation for ζ calculation

With the dimensionless initial radius of the bubble $\widehat{R}_0 = R_0/R_{max}$, the strength parameter is calculate as [73]

$$\zeta = \left[\widehat{R}_0^3 - 1 - \frac{3}{\widehat{\sigma}_{gl}}(1 - \widehat{R}_0^2)\right] \frac{(\Upsilon - 1)}{\widehat{R}_0^{3\Upsilon}(1 - \widehat{R}_0^{3(1-\Upsilon)})}. \tag{A.S20}$$

The above relation is derived from the Rayleigh–Plesset equation, using the boundary conditions $dR/dt = 0$ at $R = R_0$ and $R = R_{max}$. Thus Eq. A.S20 can be used to calculate ζ, which is used as one of the initial conditions provided the R_0/R_{max} and Υ are established.

REFERENCES

[1] Edmund Optics Worldwide. *Infinite conjugate tube length: Edmund Optics*. https://www.edmundoptics.com/knowledge-center/tech-tools/infinite-conjugate-tube-length/. [Online; accessed 10-May-2024].

[2] Rainer Heintzmann. "Practical guide to optical alignment." In: *Fluorescence Microscopy* (2013).

[3] James R Wood. "Thermodynamics of brine-salt equilibria — II. The system NaCl-KCl-H2O from 0 to 200°C." In: *Geochimica et Cosmochimica Acta* 40.10 (1976), pp. 1211–1220. ISSN: 0016-7037.

[4] Linglong Wang, Yingchun Wu, Xuecheng Wu, and Kefa Cen. "Measurement of dynamics of laser-induced cavitation around nanoparticle with high-speed digital holographic microscopy." In: *Experimental Thermal and Fluid Science* 121 (2021), p. 110266. ISSN: 0894-1777.

[5] Christian Matzler. "MATLAB functions for Mie scattering and absorption." In: *IAP Res Rep* 8 (July 2002).

[6] Marvin R Querry. *Optical constants*. Tech. rep. Missouri Univ-Kansas City, 1985.

[7] Rohit Kacker, Sanjana Dhingra, Daniel Irimia, Murali Krishna Ghatkesar, Andrzej Stankiewicz, Herman J. M. Kramer, and Huseyin Burak Eral. "Multiparameter Investigation of Laser-Induced Nucleation of Supersaturated Aqueous KCl Solutions." In: *Crystal Growth & Design* 18.1 (2018), pp. 312–317.

[8] Andrew J. Alexander and Philip J. Camp. "Single Pulse, Single Crystal Laser-Induced Nucleation of Potassium Chloride." In: *Crystal Growth & Design* 9.2 (2009), pp. 958–963.

[9] Outi Supponen. *Collapse phenomena of deformed cavitation bubbles*. Tech. rep. EPFL, 2017.

[10] George Keith Batchelor. *An introduction to fluid dynamics*. Cambridge university press, 1967.

[11] Lord Rayleigh. "VIII. On the pressure developed in a liquid during the collapse of a spherical cavity." In: *The London, Edinburgh, and Dublin Philosophical Magazine and Journal of Science* 34.200 (1917), pp. 94–98.

[12] Pedro A. Quinto-Su, Madoka Suzuki, and Claus-Dieter Ohl. "Fast temperature measurement following single laser-induced cavitation inside a microfluidic gap." In: *Scientific Reports* 4.1 (June 2014), p. 5445. ISSN: 2045-2322.

[13] D. Kashchiev and G. M. van Rosmalen. "Review: Nucleation in solutions revisited." In: *Crystal Research and Technology* 38.7-8 (2003), pp. 555–574.

[14] J. Kardum, Aleksandra Sander, and A Glasnoviae. "Batch Crystallization of KCl: the Influence of the Cooling and Mixing Rate on the Granulometric Properties of Obtained Crystals." In: *Chemical and Biochemical Engineering Quarterly* 19 (Mar. 2005).

[15] An-Chieh Cheng, Hiroshi Masuhara, and Teruki Sugiyama. "Evolving Crystal Morphology of Potassium Chloride Controlled by Optical Trapping." In: *The Journal of Physical Chemistry C* 124.12 (2020), pp. 6913–6921.

[16] R. Thiéry and L. Mercury. "Explosivity Conditions of Aqueous Solutions." In: *Journal of Solution Chemistry* 38.7 (July 2009), pp. 893–905. ISSN: 1572-8927.

[17] *Reference Manual*. COMSOL Multiphysics® v. 5.6. 2020.

[18] Robert G Lunnon. "The Latent Heat of Evaporation of Aqueous Salt Solutions." In: *Proceedings of the Physical Society of London* 25.1 (Dec. 1912), pp. 180–191.

[19] H Ozbek and S L Phillips. *Thermal conductivity of aqueous NaCl solutions from 20°C to 330°C*. Tech. rep. U.S. Department of energy, May 1979.

[20] Jonathan D. Toner and David C. Catling. "A Low-Temperature Thermodynamic Model for the Na-K-Ca-Mg-Cl System Incorporating New Experimental Heat Capacities in KCl, MgCl2, and CaCl2 Solutions." In: *Journal of Chemical & Engineering Data* 62.3 (2017), pp. 995–1010.

[21] Joseph Kestin, H. Ezzat Khalifa, and Robert J. Correia. "Tables of the dynamic and kinematic viscosity of aqueous KCl solutions in the temperature range 25–150°C and the pressure range 0.1–35 MPa." In: *Journal of Physical and Chemical Reference Data* 10.1 (1981), pp. 57–70.

[22] Orhan Ozdemir, Stoyan I. Karakashev, Anh V. Nguyen, and Jan D. Miller. "Adsorption and surface tension analysis of concentrated alkali halide brine solutions." In: *Minerals Engineering* 22.3 (2009), pp. 263–271. ISSN: 0892-6875.

[23] Y. C. Chang and A. S. Myerson. "The diffusivity of potassium chloride and sodium chloride in concentrated, saturated, and supersaturated aqueous solutions." In: *AIChE Journal* 31.6 (1985), pp. 890–894.

[24] Joseph Kestin, Mordechai Sokolov, and William A. Wakeham. "Viscosity of liquid water in the range 8°C to 150°C." In: *Journal of Physical and Chemical Reference Data* 7.3 (1978), pp. 941–948.

[25] E. S. Nowak and R. J. Grosh. *An analysis of specific heat data for water and water vapor in the critical region.* Tech. rep. 8. U.S. Department of energy, Oct. 1961.

[26] H. Geneva Leopold and John Johnston. "THE VAPOR PRESSURE OF THE SATURATED AQUEOUS SOLUTIONS OF CERTAIN SALTS." In: *Journal of the American Chemical Society* 49.8 (1927), pp. 1974–1988.

[27] Vasan Venugopalan, Arnold Guerra, Kester Nahen, and Alfred Vogel. "Role of Laser-Induced Plasma Formation in Pulsed Cellular Microsurgery and Micromanipulation." In: *Phys. Rev. Lett.* 88 (7 Feb. 2002), p. 078103.

[28] A. Vogel, S. Busch, and U. Parlitz. "Shock wave emission and cavitation bubble generation by picosecond and nanosecond optical breakdown in water." In: *The Journal of the Acoustical Society of America* 100.1 (1996), pp. 148–165.

[29] Jonathan Barrett and Charles Clement. "Kinetic evaporation and condensation rates and their coefficients." In: *Journal of Colloid and Interface Science* 150.2 (1992), pp. 352–364. ISSN: 0021-9797.

[30] V. L. Thurmond, R. W. Potter II, and M. A. Clynne. *The densities of saturated solutions of NaCl and KCL from 10 degrees to 105 degrees C*. Tech. rep. Report. U.S. Geological Survey, 1984.

[31] A. Mersmann. "Calculation of interfacial tensions." In: *Journal of Crystal Growth* 102.4 (1990), pp. 841–847. ISSN: 0022-0248.

[32] George W. Preckshot and George Granger Brown. "Nucleation of Quiet Supersaturated Potassium Chloride Solutions." In: *Industrial & Engineering Chemistry* 44.6 (1952), pp. 1314–1321.

[33] A. C. Chatterji and Ram Naresh Singh. "Nucleation from Quiet Supersaturated Solution of Alkali Halides. Part I. Chlorides, Bromides, Iodides of Potassium and Ammonium." In: *The Journal of Physical Chemistry* 62.11 (1958), pp. 1408–1411.

[34] Amir Faravar and Mehrdad Manteghian. "An Empirical Technique for Prediction of Nucleation Mechanism and Interfacial Tension of Potassium Chloride Nanoparticles." In: *International Journal of New Chemistry* 6.1 (2019), pp. 43–57. ISSN: 2645-7237.

[35] Bing Han, Karsten Köhler, Kerstin Jungnickel, Robert Mettin, Werner Lauterborn, and Alfred Vogel. "Dynamics of laser-induced bubble pairs." In: *Journal of Fluid Mechanics* 771 (2015), 706–742.

[36] Kaustubh R. Rau, Pedro A. Quinto-Su, Amy N. Hellman, and Vasan Venugopalan. "Pulsed Laser Microbeam-Induced Cell Lysis: Time-Resolved Imaging and Analysis of Hydrodynamic Effects." In: *Biophysical Journal* 91.1 (2006), pp. 317–329. ISSN: 0006-3495.

[37] Robert Hickling. "Transient, High-Pressure Solidification Associated with Cavitation in Water." In: *Phys. Rev. Lett.* 73 (21 Nov. 1994), pp. 2853–2856.

[38] Nasrin Mirsaleh-Kohan, Andrew Fischer, Bernard Graves, Mehdi Bolorizadeh, Dilip Kondepudi, and Robert N. Compton. "Laser Shock Wave Induced Crystallization." In: *Crystal Growth & Design* 17.2 (2017), pp. 576–581.

[39] Melvin H. Rice and John M. Walsh. "Equation of State of Water to 250 Kilobars." In: *The Journal of Chemical Physics* 26.4 (1957), pp. 824–830.

[40] Yusron Darojat, Abdulaziz Aljalal, Khaled Gasmi, Isam H. Aljundi, Nasrin Mirsaleh-Kohan, and Watheq Al-Basheer. "Laser-Induced Shockwave Crystallization in Supersaturated Solutions and Conceivable Clustering in Undersaturated Aqueous Potassium Nitrate Solutions." In: *ACS Omega* 7.43 (2022), pp. 38400–38408.

[41] W. Hentschel and W. Lauterborn. "Acoustic emission of single laser-produced cavitation bubbles and their dynamics." In: *Applied Scientific Research* 38.1 (Jan. 1982), pp. 225–230. ISSN: 1573-1987.

[42] Matevž Dular and Olivier Coutier-Delgosha. "Thermodynamic effects during growth and collapse of a single cavitation bubble." In: *Journal of Fluid Mechanics* 736 (2013), 44–66.

[43] W Lauterborn. "Laser-induced cavitation." In: *Acta Acustica united with Acustica* 31.2 (1974), pp. 51–78.

[44] Hidetoshi Kuramochi, Hidetaka Noritomi, Daisuke Hoshino, and Kunio Nagahama. "Measurements of Vapor Pressures of Aqueous Amino Acid Solutions and Determination of Activity Coefficients of Amino Acids." In: *Journal of Chemical & Engineering Data* 42.3 (1997), pp. 470–474.

[45] Ri A Robinson. "The vapour pressures of solutions of potassium chloride and sodium chloride." In: *Trans. R. Soc. NZ* 75.2 (1945), pp. 203–217.

[46] Huang Lin and Vishal Lagad. "Evaluating Ammonium Chloride Corrosion Potential with Water Partial Pressure." In: vol. All Days. NACE CORROSION. Mar. 2017, NACE–2017–8960.

[47] LA Pinck and Mary A Kelly. "The Solubility of Urea in Water." In: *Journal of the American Chemical Society* 47.8 (1925), pp. 2170–2172.

[48] *Solubility Table of Compounds in Water*. 2023.

[49] Graham Edgar and W. O. Swan. “THE FACTORS DETERMINING THE HYGROSCOPIC PROPERTIES OF SOLUBLE SUBSTANCES. I. THE VAPOR PRESSURES OF SATURATED SOLUTIONS.” In: *Journal of the American Chemical Society* 44.3 (1922), pp. 570–577.

[50] WH McCoy and WE Wallace. “Activity Coefficients in Concentrated Aqueous KCl-KBr Solutions at 25° 1, 2.” In: *Journal of the American Chemical Society* 78.9 (1956), pp. 1830–1833.

[51] Mihaela Stefan-Kharicha, Abdellah Kharicha, Johann Mogeritsch, Menghuai Wu, and Andreas Ludwig. “Review of Ammonium Chloride–Water Solution Properties.” In: *Journal of Chemical & Engineering Data* 63.9 (2018), pp. 3170–3183.

[52] V. P. Korolev. “H2O-NH4Cl system: Is there a thermodynamic response to the nucleation point?” In: *Journal of Structural Chemistry* 55.5 (Sept. 2014), pp. 858–862. ISSN: 1573-8779.

[53] A. W. Nienow, R. Unahabhokha, and J. W. Mullin. “Diffusion and mass transfer of ammonium and potassium chloride in aqueous solution.” In: *Journal of Applied Chemistry* 18.5 (1968), pp. 154–156.

[54] I. M. Abdulagatov and U. B. Magomedov. “Thermal conductivity of aqueous solutions of NaCl and KCI at high pressures.” In: *International Journal of Thermophysics* 15.3 (May 1994), pp. 401–413. ISSN: 1572-9567.

[55] E. P. Jr. Egan and B. B. Luff. “Heat of Solution, Heat Capacity, and Density of Aqueous Urea Solutions at 25° C.” In: *Journal of Chemical & Engineering Data* 11.2 (1966), pp. 192–194.

[56] L. S. Sorell and A. S. Myerson. “Diffusivity of urea in concentrated, saturated and supersaturated solutions.” In: *AIChE Journal* 28.5 (1982), pp. 772–779.

[57] K. RIDGWAY and M. E. AULTON. “The kinetics of crystallization of potassium bromide from aqueous solution.” In: *Journal of Pharmacy and Pharmacology* 23.S1 (1971), 111S–120S.

[58] Ilmutdin M. Abdulagatov, Lala A. Akhmedova-Azizova, and Nazim D. Azizov. “Thermal Conductivity of Binary Aqueous NaBr and KBr and Ternary H2O + NaBr + KBr Solutions at Temperatures from (294 to 577) K and Pressures up to 40 MPa.” In: *Journal of Chemical & Engineering Data* 49.6 (2004), pp. 1727–1737.

[59] V. I. Klopov, A. M. Kolker, and G. A. Krestov. “Heat capacity and structure of concentrated solutions of potassium bromide in mixtures of water and isopropyl alcohol.” In: *Journal of Structural Chemistry* 16.2 (Mar. 1975), pp. 276–279. ISSN: 1573-8779.

[60] RH Stokes. “The diffusion coefficients of eight uni-univalent electrolytes in aqueous solution at 25.” In: *Journal of the American Chemical Society* 72.5 (1950), pp. 2243–2247.

[61] C. Y. Wang. “Analytic Solutions for Pulsatile Flow Through Annular, Rectangular and Sector Ducts Filled with a Darcy–Brinkman Medium.” In: *Transport in Porous Media* 112.2 (Mar. 2016), pp. 409–428. ISSN: 1573-1634.

[62] Donald F Swinehart. “The beer-lambert law.” In: *Journal of chemical education* 39.7 (1962), p. 333.

[63] W.-P. Breugem. “The effective viscosity of a channel-type porous medium.” In: *Physics of Fluids* 19.10 (2007), p. 103104.

[64] Sander Stroobants, Manly Callewaert, Marzena Krzek, Sudha Chinnu, Pierre Gelin, Iwona Ziemecka, James F. Lutsko, Wim De Malsche, and Dominique Maes. “Influence of Shear on Protein Crystallization under Constant Shear Conditions.” In: *Crystal Growth & Design* 20.3 (2020), pp. 1876–1883.

[65] Jin Liu and Åke C. Rasmuson. “Influence of Agitation and Fluid Shear on Primary Nucleation in Solution.” In: *Crystal Growth & Design* 13.10 (Oct. 2013), pp. 4385–4394. ISSN: 1528-7483.

[66] Felice De Santis, Roberto Pantani, and Giuseppe Titomanlio. “Effect of shear flow on spherulitic growth and nucleation rates of polypropylene.” In: *Polymer* 90 (2016), pp. 102–110. ISSN: 0032-3861.

[67] Cedric Devos, Anja Vananroye, Ruth Cardinaels, Christos Xiouras, Tom Van Gerven, and Simon Kuhn. “The interplay between nucleation and patterning during shear-induced crystallization from solution in a parallel plate geometry.” In: *Soft Matter* 19 (31 2023), pp. 5896–5906.

[68] Carol Forsyth, Paul A. Mulheran, Claire Forsyth, Mark D. Haw, Iain S. Burns, and Jan Sefcik. “Influence of Controlled Fluid Shear on Nucleation Rates in Glycine Aqueous Solutions.” In: *Crystal Growth & Design* 15.1 (2015), pp. 94–102.

[69] Carol Forsyth, Iain S. Burns, Paul A. Mulheran, and Jan Sefcik. “Scaling of Glycine Nucleation Kinetics with Shear Rate and Glass–Liquid Interfacial Area.” In: *Crystal Growth & Design* 16.1 (2016), pp. 136–144.

[70] BB Taib, G Doherty, and JR Blake. “High order boundary integral modelling of cavitation bubbles.” In: *Proceedings of 8th Australasian Fluid Mechanics Conference*. Vol. 52. 1983.

[71] Bachok Bin Taib. “Boundary integral method applied to cavitation bubble dynamics.” PhD thesis. University of Wollongong, 1985.

[72] Cecil Hastings Jr, Jeanne T Wayward, and James P Wong Jr. *Approximations for digital computers*. Vol. 2040. Princeton University Press, 2015.

[73] Abdolrahman Dadvand, Boo Cheong Khoo, Mohammad T. Shervani-Tabar, and Saman Khalilpourazary. "Boundary element analysis of the droplet dynamics induced by spark-generated bubble." In: *Engineering Analysis with Boundary Elements* 36.11 (2012), pp. 1595–1603. ISSN: 0955-7997.

[74] Richard H Bartels, John C Beatty, and Brian A Barsky. *An introduction to splines for use in computer graphics and geometric modeling*. Morgan Kaufmann, 1995.

[75] Gerard P. Lennon, Philip L.-F. Liu, and James A. Liggett. "Boundary integral equation solution to axisymmetric potential flows: 1. Basic formulation." In: *Water Resources Research* 15.5 (1979), pp. 1102–1106.

[76] Michael Selwyn Longuet-Higgins and ED Cokelet. "The deformation of steep surface waves on water-I. A numerical method of computation." In: *Proceedings of the Royal Society of London. A. Mathematical and Physical Sciences* 350.1660 (1976), pp. 1–26.

[77] Mohammad T. Shervani-Tabar, Abdolrahman Dadvand, Boo Cheong Khoo, and M. R. H. Nobari. "A numerical and experimental study of a collapsing bubble-induced droplet ejector." In: *Theoretical and Computational Fluid Dynamics* 23.4 (July 2009), pp. 297–316. ISSN: 1432-2250.

[78] Ivo R. Peters, Yoshiyuki Tagawa, Nikolai Oudalov, Chao Sun, Andrea Prosperetti, Detlef Lohse, and Devaraj van der Meer. "Highly focused supersonic microjets: numerical simulations." In: *Journal of Fluid Mechanics* 719 (2013), 587–605.

PART III

ACKNOWLEDGMENTS

நெல்லுக்கு இறைத்த நீர் வாய்க்கால் வழி ஓடிப் புல்லுக்கும்
ஆங்கே பொசியுமாம் - தொல் உலகில் நல்லார் ஒருவர் உளரேல்
அவர் பொருட்டு எல்லார்க்கும் பெய்யுமாம் மழை

"An irrigated paddy field collectively does good to the grass in the soil bund.
Likewise, if a good man lives in this world...
it rains for his sake and does good to every one ."

(Avvaiyar)

First I would like to thank Dr. Burak Eral for providing me this opportunity to work at this interdisciplinary project with the option to perform both experiments and numerical studies. Together I would also like to thank Prof. dr. Johan T. Padding and Dr. Remco Hartkamp for their supervision. I enjoyed a lot of freedom and support during the project period which really helped me to remain focused on the objective. Not to mention the conversations during regular group lunches at the cafeteria and lunch meetings which I really enjoyed.

My thanks to supporting staffs Ing. Michel van den Brink and Ing. Edwin Overmars for their help with the resources and logistics. Special thanks to my coauthors in publications Dr. Daniel Irimia, Dr. Herman Kramer, Prof. dr. Antoine van der Heijden, Dr. Carlos Smith, Prof. dr. Christian Poelma, Prof. dr. Jerry Westerweel, and Dr. Jan Groenewold for sharing their technical expertise.

My thanks to the members of LightX user committee for their productive discussions; Dr. Jörn Gebauer (Bayer AG), Dr. Clemens Bothe (Bayer AG), Dr. Jana Sonnenschein (Bayer AG), Dr. Bart Zwijnenburg (Nobian B.V.), Dr. Rob Geertman (Janssen Pharmaceutica), Dr. Andreas Sieber (Lonza Group), and Ir. John Nijenhuis (TU Delft). Special thanks to Nederlandse Organisatie voor Wetenschappelijk Onderzoek for making this project possible.

Many thanks to Rumen Georgiev, M.Sc., Ir. Vikram Korede, Dr. MengMeng Zhang and Dr. Frederico Marques Penha for quality discussions and equipment training. My thanks to my master students Ir. Aswin Raghunathan, Ir. Xiuzi Baolin and Adithya Vignesh for their support with the experiments. Thanks to my colleagues Ir. Suryaprakash Senthil kumar, An Qi, M.Sc., Ir. Arvind Pari, Esaar Butt, M.Sc., Ir. Udhav Gawandalkar, Heng Li, M.Sc., and Ir. Teja Donepudi for creating a pleasant work environment.

I am also grateful to the department management assistants Leslie van Leeuwen, Linda Starrenburg, Caroline Legierse and Eveline van der Veer for their administrative support.

I would like to apologise in advance if I have missed to thank someone. Last but certainly not the least, I would like to express my sincere gratitude to my family members for their endless support.

While nothing really starts nor ends, it is only our perception that changes over time. Learning, hardship and prosperity inevitably occur the moment one is born until death. However one's mental conditioning demands time and experience.

Nagaraj Nagalingam
September, 2024

RESEARCH DATA

Laser-Induced Cavitation for Controlling Crystallization from Solution

Author: N. Nagalingam

Delft University of Technology,
Department of Process and Energy,
Faculty of Mechanical Engineering.
Leeghwaterstraat 39, 2628 CB,
Delft. The Netherlands.

Description

This dataset contains data collected using experiments, numerical simulations and theory at Delft University of Technology, as reported in the dissertation of Nagaraj Nagalingam available at : http://repository.tudelft.nl/. This work was funded by LightX project under NWO Open Technology Programme (project number 16714).

This data is being made public both to act as supplementary data for the dissertation and in order for other researchers to use this data in their own work, under the condition that the source publication is appropriately cited. The data set is available at the 4TU.Centre for Research Data via: https://doi.org/10.4121/f2fd9286-c77b-4a94-a570-2306b5a0fc56. The data set is provided in .xlsx format. Each file contains the data presented in a specific figure in a chapter. Each filename corresponds with the figure of which it contains the data.

CURRICULUM VITÆ

Nagaraj NAGALINGAM

19 OCTOBER 1993 Born in Thevaram, India.

WORK EXPERIENCE

2015-2017: Lead Application Engineer in Research and Development,
Turbo Energy Private Limited Chennai, India.

AUG'18-NOV'18: Project Intern,
Zero Emission Fuels B.V. Delft, Netherlands.

MAR'15-MAY'15: Project Intern,
Mettur Thermal Power Station, Salem, India.

EDUCATION

NOV'19-MAY'24: PhD Research Scholar,
Process & Energy Department, Delft University of Technology, The Netherlands.

2017-2019: Ms. in Mechanical Engineering,
Process & Energy Department, Delft University of Technology, The Netherlands.

2011-2015: B. Tech in Mechanical Engineering,
Vellore Institute of Technology, Vellore, India.

LIST OF PUBLICATIONS

* denotes equal contribution.

Publications within this dissertation

[1] V. Korede* and N. Nagalingam*, F. M. Penha, N. van der Linden, J. T. Padding, R. Hartkamp, and H. B. Eral. "A Review of Laser-Induced Crystallization from Solution." In: *Crystal Growth & Design* 23.5 (2023), pp. 3873–3916.

[2] N. Nagalingam* and A. Raghunathan*, V. Korede, E. F. J. Overmars, S. Hung, R. Hartkamp, J. T. Padding, C. S. Smith, and H. B. Eral. "Low-cost fluorescence microscope with microfluidic device fabrication for optofluidic applications." In: *HardwareX* 14 (2023), e00415.

[3] N. Nagalingam, A. Raghunathan, V. Korede, C. Poelma, C. S. Smith, R. Hartkamp, J. T. Padding, and H. B. Eral. "Laser-Induced Cavitation for Controlling Crystallization from Solution." In: *Phys. Rev. Lett.* 131 (12 Sept. 2023), p. 124001. [selected as Editor's Suggestion]

[4] N. Nagalingam, J. Groenewold, V. Korede, P. Cui, A. E. D. M. van der Heijden, H. J. M. Kramer, J. T. Padding, R. Hartkamp, and H. B. Eral. "General Framework for Non-photochemical Laser-Induced Crystallization via Cavitation." In: *(under preparation)* (2024).

[5] N. Nagalingam, V. Korede, D. Irimia, J. Westerweel, J. T. Padding, R. Hartkamp, and H. B. Eral. "Unified framework for laser-induced transient bubble dynamics within microchannels." In: *Scientific Reports* 14.1 (Aug. 2024), p. 18763.

[6] N. Nagalingam, A. Vignesh, V. Korede, A. E. D. M. van der Heijden, H. J. M. Kramer, R. Hartkamp, J. T. Padding, and H. B. Eral. "Laser-induced crystal nucleation facilitated by microjets emerging from interaction of thermocaviation bubble pairs under confinement." In: *(submitted)* (2024).

Publications outside this dissertation

[1] V. Korede, F. M. Penha, V. de Munck, L. Stam, T. Dubbelman, N. Nagalingam, M. Gutta, P. Cui, D. Irimia, A. E. D. M. van der Heijden, H. J.M. Kramer, and

H. B. Eral. “Design and Validation of a Droplet-based Microfluidic System To Study Non-Photochemical Laser-Induced Nucleation of Potassium Chloride Solutions.” In: *Crystal Growth & Design* 23.8 (2023), pp. 6067–6080.

[2] V. Korede, M. Veldhuis, F. M. Penha, N. Nagalingam, P. Cui, A. E. D. M. Van der Heijden, H. J. M. Kramer, and H. B. Eral. “Effect of Laser-Exposed Volume and Irradiation Position on Nonphotochemical Laser-Induced Nucleation of Potassium Chloride Solutions.” In: *Crystal Growth & Design* 23.11 (2023), pp. 8163–8172.

[3] P. Cui* and V. Korede*, P. van Tooren, N. Nagalingam, R. Wang, Q. Yin, A. E. D. M. van der Heijden, H. J. M. Kramer, and H. B. Eral. “Influence of Nanoparticle Properties on Non-Photochemical Laser-Induced Nucleation.” In: *(to be submitted)*, (2024).


TUDelft